# Progression of multiple sclerosis: The role of microglia and neurons

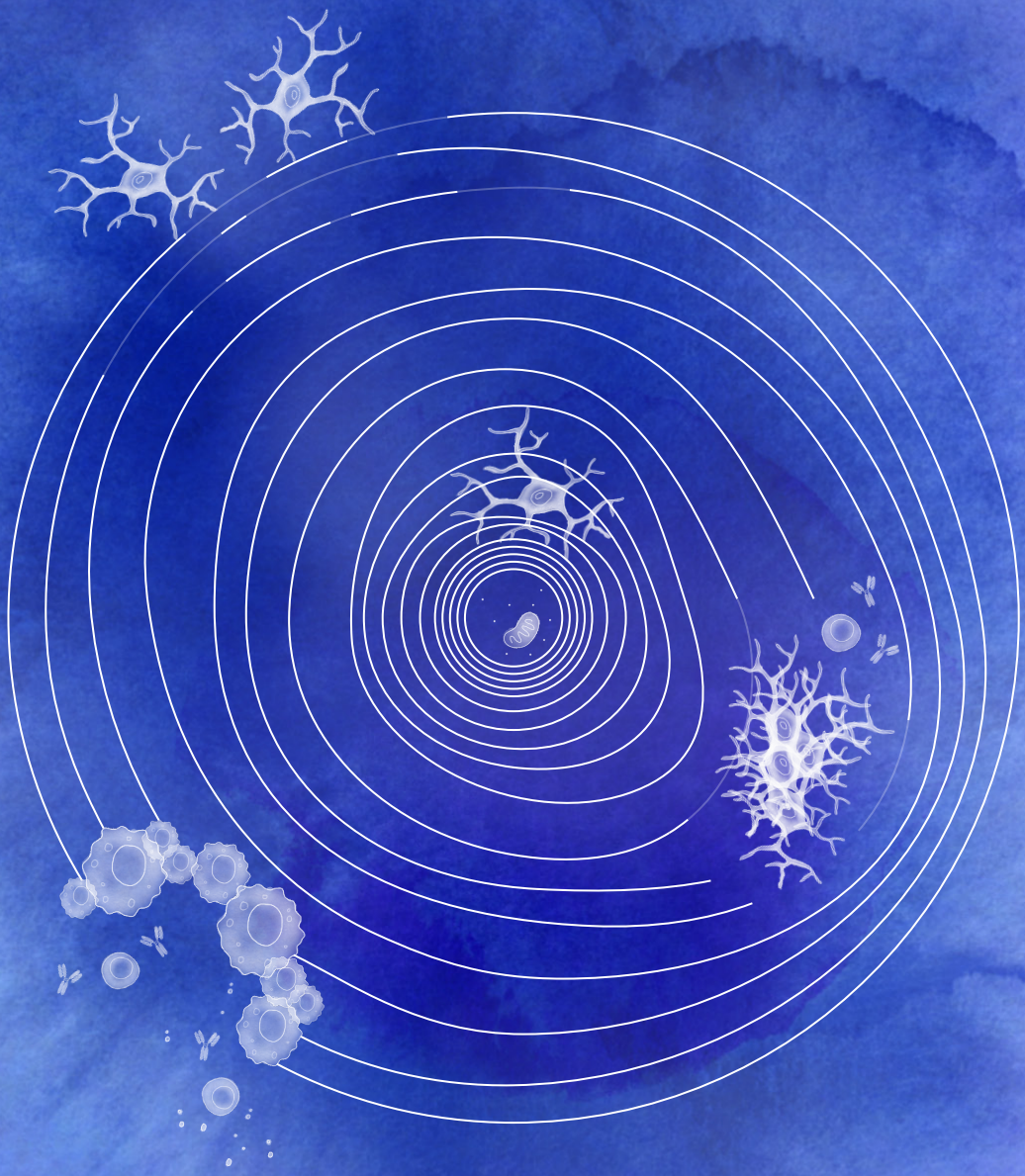

Aletta van den Bosch

# Progression of multiple sclerosis: The role of microglia and neurons

A.M.R. van den Bosch

The studies described in this thesis were funded by Stichting MS Research and by MoveS. Financial support for publication of this thesis was kindly provided by Stichting MS Research and by the Graduate School of Neurosciences Amsterdam Rotterdam (ONWAR).

**Cover design**
Charlotte van den Bosch (charlottevandenbosch.com). Front cover design illustrates the dynamic and intricate processes of lesion formation, expansion, and repair.



Provided by thesis specialist Ridderprint, ridderprint.nl
Printing: Ridderprint
Layout and design:Michèle Duquesnoy, persoonlijkproefschrift.nl

**ISBN**
978-94-6506-418-5

Progression of multiple sclerosis: The role of microglia and neurons

ACADEMISCH PROEFSCHRIFT

ter verkrijging van de graad van doctor
aan de Universiteit van Amsterdam
op gezag van de Rector Magnificus
prof. dr. ir. P.P.C.C. Verbeek
ten overstaan van een door het College voor Promoties ingestelde commissie,
in het openbaar te verdedigen in de Agnietenkapel
op donderdag 7 november 2024, te 10.00 uur

door Aletta Marthe Roswitha van den Bosch
geboren te Boxmeer

***Promotiecommissie***

| | | |
|---|---|---|
| *Promotor:* | prof. dr. I. Huitinga | Universiteit van Amsterdam |
| *Copromotores:* | dr. J. Hamann | Universiteit van Amsterdam |
| | dr. J.J.F.M. Smolders | Erasmus Universiteit Rotterdam |
| *Overige leden:* | prof. dr. P.J. Lucassen | Universiteit van Amsterdam |
| | prof. dr. P. van der Valk | Vrije Universiteit Amsterdam |
| | prof. dr. B.M.J. Uitdehaag | Vrije Universiteit Amsterdam |
| | prof. dr. M.H.P. Kole | Universiteit Utrecht |
| | dr. J. Mulder | Karolinska Institutet |
| | dr. M. Absinta | Università Vita-Salute San Raffaele |

Faculteit der Natuurwetenschappen, Wiskunde en Informatica

"Nothing in life is to be feared, it is only to be understood.
Now is the time to understand more, so that we may fear less"
*Marie Curie*

## TABLE OF CONTENTS

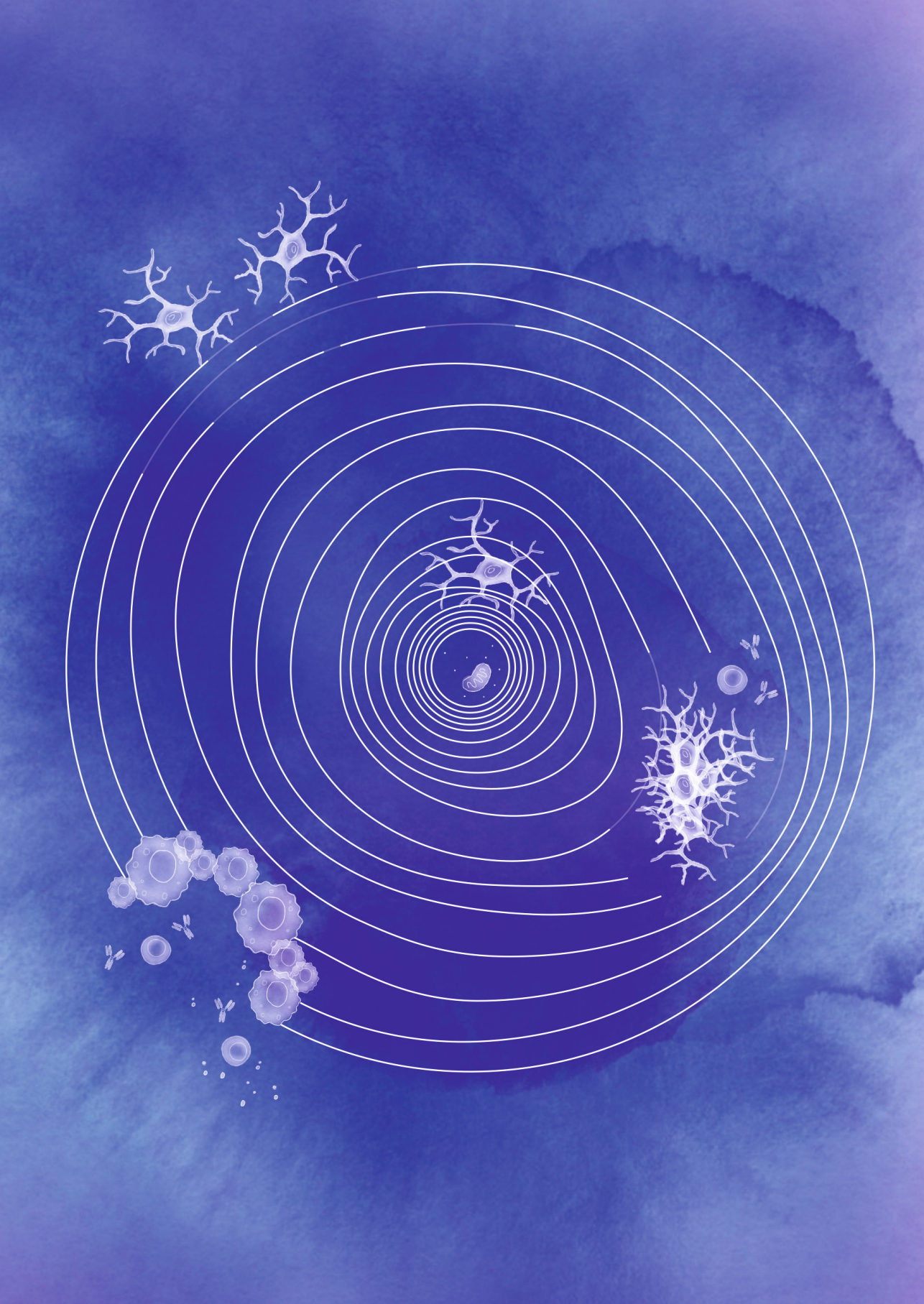

# Chapter 1

## Introduction and outline of the thesis

# MULTIPLE SCLEROSIS

## Diagnosis

Multiple sclerosis (MS) is the most prevalent neuroinflammatory disorder among young adults, affecting 2.8 million people worldwide [1,2]. Individuals with a genetic predisposition for the onset of MS are more vulnerable to penetrance of environmental risk factors [3]. To date, over 200 single-nucleotide polymorphisms (SNPs) have been associated with increased risk of MS. Most of the susceptibility associated genes are related to immunological pathways, and the major histocompatibility complex (MHC) region is the main genetic determinant [4]. Accordingly, disease-modifying therapies that reduce the relapse rate are immune-modulatory and target the adaptive immune system [5]. However, our understanding of the risk factors and mechanisms underlying disease progression remains limited, resulting in an unmet need for therapies capable of halting and reversing progression of MS [6].

People with MS have focal, demyelinating lesions throughout the central nervous system (CNS) [7], which can be detected by magnetic resonance imaging (MRI) [8]. Moreover, more than 95% of people with MS have immunoglobulin (Ig) G oligoclonal bands in the cerebrospinal fluid (CSF), persisting throughout the course of the disease and indicating continuous intrathecal antibody production [9]. Diagnostic criteria for MS include evidence of grey matter (GM) or white matter (WM) lesions in at least two separate areas of the (CNS) that occurred at different time points. In some settings, oligoclonal bands can substitute for demonstration of lesions in time [10].

MS is a highly heterogenic disease, both clinically and pathologically [11]. During life, pathological disease progression manifests as progressive loss of walking ability and is reflected by biomarkers such as MRI [8] and soluble biomarkers in blood and CSF [12]. The rate of disability progression is variable between patients and is largely unpredictable. Traditionally, people with MS have been categorized as distinct clinical phenotypes, i.e. relapsing-remitting, secondary progressive, or primary progressive. However, accumulating evidence suggests that the clinical course of MS is better considered as a continuum, reflected by concurrent pathophysiological processes that vary across individuals over time [6]. The formation of new focal demyelinating lesions and ongoing inflammation and demyelination are pathophysiological processes that contribute to progression of MS which we investigated in this thesis. Unravelling of the molecular mechanisms of various pathophysiological processes contributing to MS progression may lead to the identification of new therapeutic interventions and to the validation of biomarkers that can predict the disease course.

**MS lesion pathology**

MS lesions can occur throughout the CNS and are histologically characterized by focal inflammation and demyelination. A number of classification systems have been introduced, among which the Bö/Trapp system, the De Groot/Van der Valk modification, the Lucchinetti/Lassmann/Brück system, the Vienna consensus, and, most recently, the Kuhlmann system [13–18]. The Bö Trapp system focused on microglia density, stratifying between active, chronic active (or mixed active/inactive), and inactive lesions. The Lucchinetti/Lassmann/Brück system further subdivided active and chronic active lesions based on oligodendrocyte destruction and on the presence of myelin degradation products within the microglia into early or late demyelinating lesions. The De Groot/Van der Valk modification combined these two systems, and furthermore described clusters of microglia as pre-active lesions (or nodules). The Vienna consensus included inflammation based on both microglia and perivascular infiltrates and on active demyelination based on myelin degradation products, distinguishing between entire lesions or plaque margins. The Kuhlman classification system combined the former classification systems, while reducing complexity by not stratifying for early or late demyelination, and included the presence of remyelination,. This unified classification system serves as a fundamental framework for categorising MS lesions based on histopathological similarities of the myelin and microglia, aiming to provide a cohesive understanding of MS pathology [19]. Nonetheless, it is important to recognize that beyond this classification system the biological landscape of MS lesions is likely far more intricate and multifaceted. Each MS lesion subtype may harbour numerous additional biologically relevant characteristics, contributing to considerable heterogeneity within and across lesion types.

Based on the classification system described by Kuhlmann *et al* (2017) [19], various lesion types can be distinguished, as shown in **figure 1**. In the WM, reactive sites and four types of lesions are defined: active, mixed active/inactive (mixed), inactive, and remyelinated lesions. Reactive sites are regions with no demyelination and with accumulation of microglia and/or macrophages (hereafter microglia). Active lesions have partial demyelination and an accumulation of microglia. Mixed lesions have a demyelinated, hypocellular core and a border with accumulation of microglia. For active and mixed lesions, the microglia are scored as ramified, ameboid, or foamy. Inactive lesions have a demyelinated, hypocellular core with a lower density of microglia/macrophages compared to the normal-appearing WM (NAWM). Remyelinated lesions have sparsely myelinated axons with a similar microglia density the NAWM. Inactive lesions and remyelinated lesions are considered as two possible end-points for MS lesion development [11]. In the GM, three types of lesions are defined based on their location: subpial, intra-cortical, and leuko-cortical lesions. Subpial

lesions are lesions spanning the first layers of the cortex that can extend towards but not into the WM. Those without clear demyelination of the first layer of the cortex that do not extend into the WM are classified as intra-cortical lesions. Cortical lesions that extend into the WM are classified as leuko-cortical lesions.

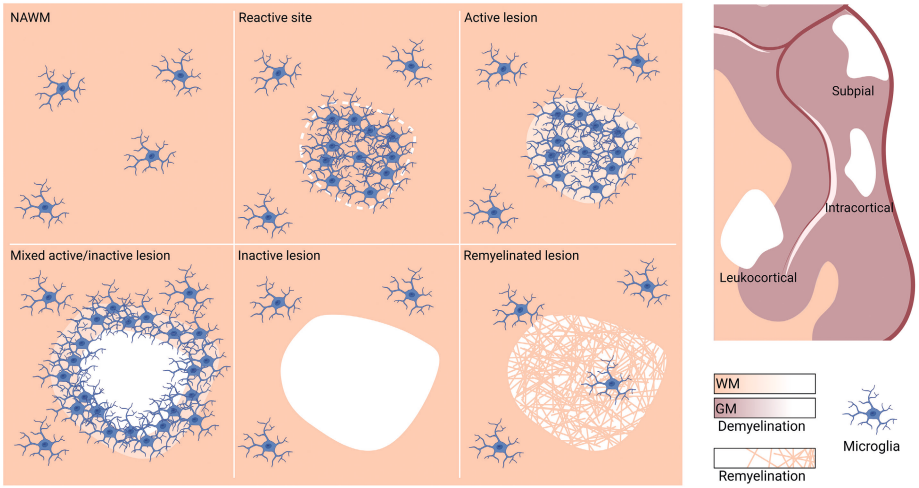


**Figure 1:** Schematic presentation of characterisation of MS lesions in the WM and GM based on activated microglia and myelin, according to Kuhlmann *et al.* (2017). NAWM: normal-appearing white matter, WM: white matter, GM: cortical grey matter.

For each donor, the reactive site load, lesion load, proportion of active, mixed, inactive, and remyelinated lesions, the cortical lesion rate, and the microglia/macrophage activity score can be calculated [11]. These donor characteristics vary between donors and are clinically relevant: the lesion load and the proportion of mixed lesions positively correlate with clinical severity [11]. Likely, different lesion types have a different propensity for ongoing tissue damage or repair, and consequently, they will vary in the likelihood of becoming either a scar that becomes an inactive lesion, or a remyelinated lesion. Understanding the upstream and downstream mechanisms that determine whether lesions will continue to expand, become inactive, or remyelinate can help identify new therapeutic targets to halt disease progression. Simultaneously, these insights may provide biomarkers to better predict the clinical disease course.

## PROGRESSION OF MS

### Lesion formation

Molecular changes in the brain tissue preceding MS lesion formation may serve as triggers for their formation. In this thesis, we aim to gain insight into these alterations in the NAWM and normal-appearing GM (NAGM), as this is likely to provide valuable understanding of key mechanisms driving the initiation of MS lesion formation.



Neuronal cell bodies and their dendrites lie in the GM, and their associated axons reach into the WM. These axons are myelinated by oligodendrocytes. The myelin sheath is characterized by a multilamellar structure of multiple lipid-rich plasma membranes, as shown in **figure 2**, that enables rapid saltatory conduction. The charge of phospholipids and sphingolipids ensures compact wrapping of the myelin sheaths [20]. Each myelin internode becomes flanked by nodes of Ranvier [21].

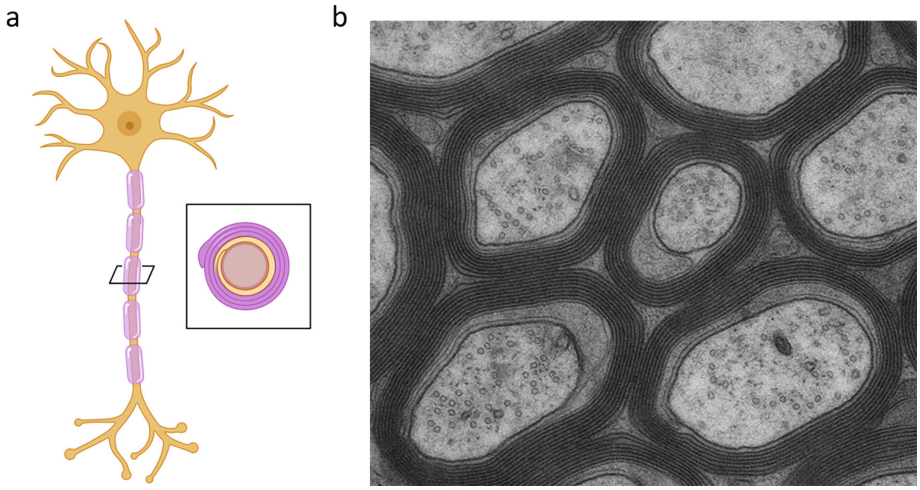


**Figure 2:** a) Animation of a neuron and it's axon in yellow, with the multilamellar myelin in pink, created with Biorender.com. b) Electron microscope cross section image of the axons of the mouse optic nerve. Oligodendrocytes wrap around axons, forming multilaminar lipid-rich myelin sheaths. Copyright by Prof. K.A. Nave, MPI for Experimental Medicine, Göttingen. Adapted from https://www.mpg.de/5786721/glial-cells-metabolites.

Myelin collected from post-mortem MS brains is phagocytosed more efficiently compared to myelin from healthy control donors [22], indicating that the myelin itself in MS is fundamentally altered, which may trigger demyelination. Previously,

compared to myelin of healthy control donors, changes in the molecular composition of myelin membranes and structural organisation have been observed. Wheeler *et al.* showed a perturbed lipid metabolism that resulted in a disturbed lipid composition with an increase in phospholipids and decrease of sphingolipids [20]. Musse *et al.* showed deamination of the myelin basic protein. Both changes in lipid composition have been modelled and predicted to result in an increased repulsive force between myelin sheaths, which may impact the saltatory conduction [20,23]. In the NAWM, there is a higher presence of oxidized phospholipids (oxPLs) compared to healthy control WM [24]. Microglia bind to oxPLs through scavenger receptors and Fcγ receptors, leading to internalisation and, depending on the volume, transition to foamy cell, and through Toll-like and complement receptors, triggering pro-inflammatory signal transduction [25,26]. Therefore, in the NAWM in MS, oxPLs can trigger demyelination and sustained inflammation.

Microglia are yolk-sac-derived myeloid cells that populate the brain during embryonic development [27,28]. They are the phagocytes of the CNS and play crucial roles in various physiological processes. Homeostatic microglia are involved in neurodevelopment and regulation of myelin integrity, immune surveillance, remodelling of myelin and synapses, and vascular regulation [29,30]. In MS, microglia play a significant role in disease pathogenesis. Activated microglia are highly dynamic and can be both pro-degenerative or pro-regenerative, depending on stimuli from the cellular (micro)environment [29,31]. Microglial immune activity is controlled through seclusion from the circulation, cell-bound and soluble restraining factors, and transcriptional regulators. These immune checkpoint mechanisms control microglial function by efficiently and tightly regulating microglial responses to inflammation [32]. Microglia in the WM and GM have distinct characteristics, which may partially be attributed to neuronal membrane-bound immune checkpoint molecules, such as CD200 and CD47 [33–35]. Microglia have a highly diverse morphology which dynamically changes, as visualized in **figure 3**, with distinct states of activation [30]. Resting, homeostatic microglia have a ramified morphology. Upon activation and uptake of debris, microglia can become more rounded and ameboid or even foamy after excessive lipid uptake. Furthermore, microglia in the NAWM can form small clusters, or nodules. It is hypothesized that a subset of these nodules may progress into MS lesions, depending on stimuli from their (micro)environment [36,37]. In the NAWM compared to healthy WM, microglia downregulate homeostatic markers, including P2RY12 and TMEM119, and upregulate pro-inflammatory mediators [38]. Moreover, microglia in the NAWM already have an increased expression of genes associated with lipid-metabolism, which is further upregulated in MS lesions. Microglia in the NAGM have an increased expression of genes

associated with glycolysis and iron homeostasis, possibly reflecting microglia reacting to iron depositions [35].

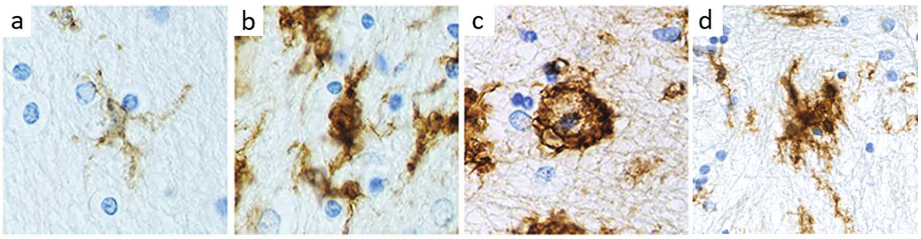


**Figure 3**: HLA-DR immunohistochemistry showing microglia with a) ramified, b) ameboid and c) foamy morphology, and d) a cluster of ramified microglia forming a nodule. Adapted from Hendrickx *et al.*, 2017, J. Neuroimmunol, doi: 10.1016/j.jneuroim.2017.04.007.

T and B cells are lymphocytes essential for the adaptive immune response. In contrast to myeloid cells, these cells respond on specific, unique antigens rather than molecular patterns. When activated, T and B cells proliferate and effector molecules, such as cytokines. Activated cytotoxic T cells release cytotoxic molecules and engage death receptors on the surface of target cells. B cells activated by antigens bound to their B cell-receptor can develop into specific antibody-secreting cells [39]. In the healthy CNS, low numbers of T and B cells populate the perivascular space. However, in MS, in particular T and B cells are triggered to infiltrate the parenchyma in association with local inflammation [40]. In the NAWM, there is an increase in the number of T and B cells compared to healthy control WM, both perivascular as well as parenchymal, and an increase in the number of antibody-secreting cells resulting in an elevated production of immunoglobulins [39,40,42]. In the NAGM, only few lymphocytes are found. However, in the meninges, larger numbers of B cells persist and can contribute to meningeal inflammation, which is associated with altered microglia morphology and function [41]. IgG produced by clonally-expanded plasmablasts from the WM and CSF of MS patients can bind myelin and trigger rapid demyelination *in vitro*. Possibly, myelin in MS is opsonized by IgG, which may lead to the more efficient phagocytosis by microglia [22]. The pro-inflammatory cytokines and immunoglobulins released by T and B cells can activate microglia, which can then become pro-inflammatory, and contribute to demyelination and MS pathology [43].

In summary, the NAWM and the NAGM are not so normal. Many early changes are seen in myelin composition, microglia activity, and lymphocyte accumulation,

which can have detrimental effects on overall CNS homeostasis and may even lead to the initiation of MS lesion formation.

**Lesion expansion and failure of remyelination**

In line with the broad clinical spectrum of MS, the pathological manifestation of the disease is also highly heterogeneous between and within patients [11,44,45]. Mechanisms driving this donor and lesion heterogeneity are not yet fully understood. Serial MRI studies have shown that MS lesions during life are highly dynamic; in expanding lesions both demyelination and remyelination are observed, giving rise to high variability of lesions [46,47]. Inflammatory and demyelinating lesion activity is widely present even in the late stage of the disease. In post-mortem tissue, the majority of lesions are either active or mixed, and the proportion of mixed lesions is correlated with clinical disease severity [11]. Remyelination, on the other hand, can also be extensive in MS, with wide heterogeneity between donors [48].

There is also heterogeneity regarding the presence of B- and T-cell infiltrates in MS lesions. In some donors, B cells infiltrate the parenchyma in WM MS lesions, with the highest number of B cells found in active lesions [49,50]. Donors with B-cell infiltration have a more severe clinical disease, higher proportion of mixed lesions, and a higher number of T cells [49]. In some donors, perivascular cuffing of T cells is observed. These donors have more mixed lesions and a higher lesion load [51]. The number of B and T cells in lesions is further associated with axonal damage [50].

Many active and some mixed lesions have the potential to remyelinate [52], however, the myelin repair is often incomplete and therefore insufficient. Mechanisms underlying remyelination failure are not yet completely understood. In active lesions, failure to remyelinate occurs despite the presence of mature oligodendrocytes due to lack of myelin sheath formation. In mixed lesions, there is oligodendrocyte loss, and a hostile tissue environment (inflammatory microglia and lymphocytes) may play a role in remyelination failure [52]. The lack of remyelination in mixed lesions may be due to a block of the ability of oligodendrocyte progenitor cells (OPCs) to differentiate and start remyelinating [53]. Senescence and oxidative stress in OPCs with limited antioxidant capacity may be underlying the differentiation impairment and therefore underlying remyelination failure [54,55]. Although myelin internalisation by microglia fuels demyelination, the removal of damaged myelin also promotes remyelination, as myelin inhibits OPC differentiation [56].

Uptake of myelin debris by microglia can induce an anti-inflammatory phenotype that is beneficial to repair. However, excessive internalization of myelin may

drive foamy microglia towards a more pro-inflammatory phenotype [57]. This may indicate that active and mixed lesions containing ramified microglia may be more prone to remyelination while those with foamy microglia may be more inclined towards expansion.

## POST-MORTEM MS BRAIN RESEARCH



Post-mortem brain research is often limited by tissue availability and quality. All tissue used in this thesis was obtained by the Netherlands Brain Bank (NBB). At the NBB, tissue from human brain donors with a variety of neurological and psychiatric disorders and of non-diseased donors is collected. The rapid autopsy program of the NBB ensures high-quality tissue, which combined with the extensive pathological and clinical data obtained per donor enables high quality scientific research. Brain donors sign up to the NBB during life. Of each donor, a detailed summary of the medical record and a neuropathological summary is made by trained medical staff. When the donor passes away, their body is transported to the Amsterdam UMC, location VUmc, where the autopsy takes place within 4-10 hours. Tissue is dissected following a standard protocol and an additional protocol according to the clinical diagnosis. For MS donors, lesions are dissected based on post-mortem MRI guidance in collaboration with the department of Radiology, Amsterdam UMC. For each dissected MS tissue block, the tissue is characterized for MS pathology. To date, 5,393 tissue blocks of a total of 251 MS donors have been characterized. Of each donor, the reactive site load, lesion load, cortical lesion rate, proportion of different MS lesion types, and microglia/macrophage activity score has been calculated [11,19,58]. The pathological characterization per donor in combination with their clinical variables is crucial to interpret the biological relevance of pathological findings.

During my PhD, together with collaborators, I was able to apply state-of-the-art quantitative techniques that have only scarcely been applied to human tissue before. We performed electron microscopy, high-resolution immunohistochemistry visualized with stimulated emission depletion microscopy (STED), single molecule array (SIMOA) on CSF and plasma samples, bulk next-generation RNA sequencing on laser micro-dissected tissue, and spatial transcriptomics using the Stereo-seq platform. Single nucleotide polymorphisms (SNPs) of MS donors were identified through genome-wide association studies (GWAS). These techniques allowed us to identify mechanisms driving MS lesion formation, lesion expansion, and failure of remyelination.

## OUTLINE OF THE THESIS

The aim of the thesis is to unravel mechanisms of pathological progression in MS, specifically focussing on the role of microglia and neurons. Identification of key drivers in ongoing local-inflammation, neurodegeneration, and remyelination failure, has enabled the discovery of new therapeutic targets to prevent further damage or promote repair.

In part 1 of this thesis, entitled *loss of microglia homeostasis can lead to initiation of lesion formation,* we aim to identify key players in the formation of new lesions.

In **chapter 2**, we investigated the expression of the check-point molecules CD200 and CD47 and their receptors in the GM to unravel their putative role in MS lesion formation. We combined quantitative immunohistochemistry with qPCR to explore the expression of CD200 and CD47, and their receptors CD200R and SIRPα, in NAGM, cortical lesions, and in peri-lesion cortical regions.

In **chapter 3**, we studied possible early mechanisms of lesion formation by investigating the axon-myelin unit in NAWM in MS in relation to inflammation. We combined quantitative immunohistochemistry with electron microscopy, to investigate the amount of activated and phagocytic microglia and the amount of parenchymal and perivascular lymphocytes, the organization of the nodes of Ranvier, the density and diameter of axons, the area of the peri-axonal space, the diameter and compactness of myelin, and the frequency and size of axonal mitochondria.

In **chapter 4**, we explored a possible role of microglia nodules in the NAWM in lesion formation in MS. We combined immunohistochemistry with RNA sequencing of laser capture-dissected microglia nodules. We measured association of microglia nodules with presence of nearby T cells and B cells, immunoglobulin production, activation of the complement cascade, activation of lipid metabolism, phagocytosis of oxidized phospholipids, and shape of the axonal mitochondria network.

In part 2 of this thesis, entitled *lesions with foamy microglia are neuro-destructive and lesions with ramified microglia are regenerative*, we aim to unravel the regenerative and degenerative capacity of different types of lesions, stratifying between active and mixed lesions with ramified or foamy microglia.

In **chapter 5**, we identified three independent dimensions of pathology in MS using a data-driven approach, utilizing quantitative and qualitative

neuropathology data and clinical data. This enabled disentangling of different pathophysiological processes happening simultaneously in MS brains, which together determine clinical features of MS patients.

In **chapter 6**, we investigated the biomarker neurofilament light chain (NfL) in the CSF to identify the pathological correlate of NfL levels to better estimate disease activity and thereby disease course in people with MS. We combined a SIMOA assay with quantitative pathology of all fully characterized MS donors with CSF available of the Netherlands Brain Bank to study the correlation of NfL with the proportion and activity of lesion types.



In **chapter 7**, we performed high-resolution spatial transcriptomics combined with immunohistochemistry, to investigate the de- and regenerative capacity of mixed lesions with a border with ramified microglia compared to those with a border with foamy microglia within donors. We focussed on the centre, border, and peri-lesion regions, to study cell-type specific roles in de- or regeneration and in lesion expansion.

In part 3 of this thesis, entitled *genetic susceptibility for clinical severity is associated with more severe pathology*, we aim to biologically validate the severity locus SNP rs10191329 in the *DYSF-ZNF638* locus and investigate the pathological implications of this SNP using immunohistochemistry and bulk nuclear RNA sequencing.

In **chapter 8**, we contributed to a study of the International Multiple Sclerosis Genetics Consortium on the genetics of disability progression in MS. The consortium identified a SNP in the *DYSF/ZNF638* locus that was associated with clinical disease progression. In this chapter, we aimed to provide a biological validation of this SNP, by genotyping all MS donors of the NBB for the risk variant and by comparing pathological characteristics of donors carrying this risk variant to those without.

In **chapter 9**, we further elaborated on the pathological implications of the risk variant in the *DYSF/ZNF638* locus by combining immunohistochemistry and RNA sequencing of single cell types. We compared the neuronal density in the NAGM, the axonal density, and the degree of acute axonal stress in the NAWM, the localization and amount of dysferlin and ZNF638 in and around WM lesions, and the gene expression profile of oligodendrocytes and neurons.

In **chapter 10**, the findings and conclusions described in this thesis are discussed.

## REFERENCES


1. *The Multiple Sclerosis International Federation. Atlas of MS, 3rd edition* (2020).
2. Walton, C. *et al.* Rising prevalence of multiple sclerosis worldwide: Insights from the Atlas of MS, third edition. *Mult. Scler. J.* 26, 1816–1821 (2020).
3. Olsson, T., Barcellos, L. F. & Alfredsson, L. Interactions between genetic, lifestyle and environmental risk factors for multiple sclerosis. *Nat. Rev. Neurol.* 13, 26–36 (2016).
4. Nourbakhsh, B. & Mowry, E. M. Multiple sclerosis risk factors and pathogenesis. *Contin. Lifelong Learn. Neurol.* 25, 596–610 (2019).
5. Rommer, P. S. *et al.* Immunological Aspects of Approved MS Therapeutics. *Front. Immunol.* 10, 1–24 (2019).
6. Kuhlmann, T. *et al.* Multiple sclerosis progression: time for a new mechanism-driven framework. *Lancet Neurol.* 22, 78–88 (2023).
7. Lassmann, H. Multiple sclerosis pathology. *Cold Spring Harb. Perspect. Med.* 8, 1–15 (2018).
8. Hemond, C. C. & Bakshi, R. Magnetic resonance imaging in multiple sclerosis. *Cold Spring Harb. Perspect. Med.* 8, 1–21 (2018).
9. Franciotta, D., Salvetti, M., Lolli, F., Serafini, B. & Aloisi, F. B cells and multiple sclerosis. *Lancet Neurol.* 7, 852–858 (2008).
10. Thompson, A. J. *et al.* Diagnosis of multiple sclerosis: 2017 revisions of the McDonald criteria. *Lancet Neurol.* 17, 162–173 (2018).
11. Luchetti, S. *et al.* Progressive multiple sclerosis patients show substantial lesion activity that correlates with clinical disease severity and sex: a retrospective autopsy cohort analysis. *Acta Neuropathol.* 135, 511–528 (2018).
12. Ziemssen, T., Akgün, K. & Brück, W. Biomarkers in multiple sclerosis. *J. Neuroinflammation* 9, 1–11 (2019).
13. Bö, L. *et al.* Detection of MHC class II-antigens on macrophages and microglia, but not on astrocytes and endothelia in active multiple sclerosis lesions. *J. Neuroimmunol.* 51, 135–146 (1994).
14. Lassmann, H., Raine, C. S., Antel, J. & Prineas, J. W. Immunopathology of multiple sclerosis: Report on an international meeting held at the Institute of Neurology of the University of Vienna. *J. Neuroimmunol.* 86, 213–217 (1998).
15. Lucchinetti, C. *et al.* Heterogeneity of multiple sclerosis lesions: Implications for the pathogenesis of demyelination. *Ann. Neurol.* 47, 707–717 (2000).
16. Trapp, B. D. *et al.* Axonal Transection in the Lesions of Multiple Sclerosis. *N. Engl. J. Med.* 338, 278–285 (1998).
17. Van Der Valk, P. & De Groot, C. J. A. Staging of multiple sclerosis (MS) lesions: Pathology of the time frame of MS. *Neuropathol. Appl. Neurobiol.* 26, 2–10 (2000).
18. Van Waesberghe, J. H. T. M. *et al.* Axonal loss in multiple sclerosis lesions: Magnetic resonance imaging insights into substrates of disability. *Ann. Neurol.* 46, 747–754 (1999).
19. Kuhlmann, T. *et al.* An updated histological classification system for multiple sclerosis lesions. *Acta Neuropathol.* 133, 13–24 (2017).
20. Wheeler, D., Bandaru, V. V. R., Calabresi, P. A., Nath, A. & Haughey, N. J. A defect of sphingolipid metabolism modifies the properties of normal appearing white matter in multiple sclerosis. *Brain* 131, 3092–3102 (2008).

21. Cohen, C. C. H. *et al.* Saltatory Conduction along Myelinated Axons Involves a Periaxonal Nanocircuit. *Cell* 180, 311-322.e15 (2020).
22. Hendrickx, D. A. E., Schuurman, K. G., van Draanen, M., Hamann, J. & Huitinga, I. Enhanced uptake of multiple sclerosis-derived myelin by THP-1 macrophages and primary human microglia. *J. Neuroinflammation* 11, 1–11 (2014).
23. Musse, A. A., Boggs, J. M. & Harauz, G. Deimination of membrane-bound myelin basic protein in multiple sclerosis exposes an immunodominant epitope. *Proc. Natl. Acad. Sci. U. S. A.* 103, 4422–4427 (2006).
24. Haider, L. *et al.* Oxidative damage in multiple sclerosis lesions. *Brain* 134, 1914–1924 (2011).
25. Freigang, S. The regulation of inflammation by oxidized phospholipids. *Eur. J. Immunol.* 46, 1818–1825 (2016).
26. Miller, Y. I., Chang, M. K., Binder, C. J., Shaw, P. X. & Witztum, J. L. Oxidized low density lipoprotein and innate immune receptors. *Curr. Opin. Lipidol.* 14, 437–445 (2003).
27. Perdiguero, E. G. *et al.* Tissue-resident macrophages originate from yolk sac-derived erythro-myeloid progenitors. *Nature* 518, 547–551 (2015).
28. Dendrou, C. A., Fugger, L. & Friese, M. A. Immunopathology of multiple sclerosis. *Nat. Rev. Immunol.* 15, 545–558 (2015).
29. Distéfano-Gagné, F., Bitarafan, S., Lacroix, S. & Gosselin, D. Roles and regulation of microglia activity in multiple sclerosis: insights from animal models. *Nat. Rev. Neurosci.* 24, 397–415 (2023).
30. Paolicelli, R. C. *et al.* Microglia states and nomenclature: A field at its crossroads. *Neuron* 110, 3458–3483 (2022).
31. Jiang, Z., Jiang, J. X. & Zhang, G. X. Macrophages: A double-edged sword in experimental autoimmune encephalomyelitis. *Immunol. Lett.* 160, 17 (2014).
32. Deczkowska, A., Amit, I. & Schwartz, M. Microglial immune checkpoint mechanisms. *Nat. Neurosci.* 21, 779–786 (2018).
33. Prins, M. *et al.* Pathological differences between white and grey matter multiple sclerosis lesions. *Ann. N. Y. Acad. Sci.* 1351, 99–113 (2015).
34. Koning, N., Swaab, D. F., Hoek, R. M. & Huitinga, I. Distribution of the immune inhibitory molecules CD200 and CD200R in the normal central nervous system and multiple sclerosis lesions suggests neuron-glia and glia-glia interactions. *J. Neuropathol. Exp. Neurol.* 68, 159–167 (2009).
35. van der Poel, M. *et al.* Transcriptional profiling of human microglia reveals grey–white matter heterogeneity and multiple sclerosis-associated changes. *Nat. Commun.* 10, 1–13 (2019).
36. Hendrickx, D. A. E., van Eden, C. G., Schuurman, K. G., Hamann, J. & Huitinga, I. Staining of HLA-DR, Iba1 and CD68 in human microglia reveals partially overlapping expression depending on cellular morphology and pathology. *J. Neuroimmunol.* 309, 12–22 (2017).
37. Singh, S. *et al.* Microglial nodules in early multiple sclerosis white matter are associated with degenerating axons. *Acta Neuropathol.* 125, 595–608 (2013).
38. Zrzavy, T. *et al.* Loss of 'homeostatic' microglia and patterns of their activation in active multiple sclerosis. *Brain* 140, 1900–1913 (2017).
39. Bogers, L. *et al.* Selective emergence of antibody-secreting cells in the multiple sclerosis brain. *eBioMedicine* 89, 104465 (2023).
40. van Langelaar, J., Rijvers, L., Smolders, J. & van Luijn, M. M. B and T Cells Driving Multiple Sclerosis: Identity, Mechanisms and Potential Triggers. *Front. Immunol.* 11, 1–12 (2020).

41. van Olst, L. *et al.* Meningeal inflammation in multiple sclerosis induces phenotypic changes in cortical microglia that differentially associate with neurodegeneration. *Acta Neuropathol.* 141, 881–899 (2021).
42. Smolders, J. *et al.* Tissue-resident memory T cells populate the human brain. *Nat. Commun.* 9, 4593 (2018).
43. van der Poel, M., Hoepel, W., Hamann, J., Huitinga, I. & Dunnen, J. den. IgG Immune Complexes Break Immune Tolerance of Human Microglia. *J. Immunol.* 205, 2511–2518 (2020).
44. Frischer, J. M. *et al.* Clinical and Pathological Insights into the Dynamic Nature of the White Matter Multiple Sclerosis Plaque. *Ann Neurol* 78, 710–721 (2015).
45. Metz, I. *et al.* Pathologic heterogeneity persists in early active multiple sclerosis lesions. *Ann. Neurol.* 75, 728–738 (2014).
46. Calvi, A. *et al.* Slowly expanding lesions relate to persisting black-holes and clinical outcomes in relapse-onset multiple sclerosis. *NeuroImage Clin.* 35, 103048 (2022).
47. Weber, C. E. *et al.* Long-term dynamics of multiple sclerosis iron rim lesions. *Mult. Scler. Relat. Disord.* 57, 103340 (2022).
48. Patani, R., Balaratnam, M., Vora, A. & Reynolds, R. Remyelination can be extensive in multiple sclerosis despite a long disease course. *Neuropathol. Appl. Neurobiol.* 33, 277–287 (2007).
49. Fransen, N. L. *et al.* Absence of B Cells in Brainstem and White Matter Lesions Associates With Less Severe Disease and Absence of Oligoclonal Bands in MS. *Neurol. Neuroimmunol. NeuroInflammation* 8, 1–11 (2021).
50. Frischer, J. M. *et al.* The relation between inflammation and neurodegeneration in multiple sclerosis brains. *Brain* 132, 1175–1189 (2009).
51. Fransen, N. L. *et al.* Tissue-resident memory T cells invade the brain parenchyma in multiple sclerosis white matter lesions. *Brain* 143, 1714–1730 (2020).
52. Heß, K. *et al.* Lesion stage-dependent causes for impaired remyelination in MS. *Acta Neuropathol.* 140, 359–375 (2020).
53. Kuhlmann, T. *et al.* Differentiation block of oligodendroglial progenitor cells as a cause for remyelination failure in chronic multiple sclerosis. *Brain* 131, 1749–1758 (2008).
54. Koutsoudaki, P. N., Papadopoulos, D., Passias, P. G., Koutsoudaki, P. & Gorgoulis, V. G. Cellular senescence and failure of myelin repair in multiple sclerosis. *Mech. Ageing Dev.* 192, 111366 (2020).
55. Spaas, J. *et al.* Oxidative stress and impaired oligodendrocyte precursor cell differentiation in neurological disorders. *Cell. Mol. Life Sci.* 78, 4615–4637 (2021).
56. Kotter, M. R., Li, W. W., Zhao, C. & Franklin, R. J. M. Myelin impairs CNS remyelination by inhibiting oligodendrocyte precursor cell differentiation. *J. Neurosci.* 26, 328–332 (2006).
57. Grajchen, E., Hendriks, J. J. A. & Bogie, J. F. J. The physiology of foamy phagocytes in multiple sclerosis. *Acta Neuropathol. Commun.* 6, 124 (2018).
58. Van Der Valk, P. & De Groot, C. J. A. Staging of multiple sclerosis (MS) lesions: Pathology of the time frame of MS. *Neuropathol. Appl. Neurobiol.* 26, 2–10 (2000).

# Part

# Loss of microglia homeostasis can lead to initiation of lesion formation

1

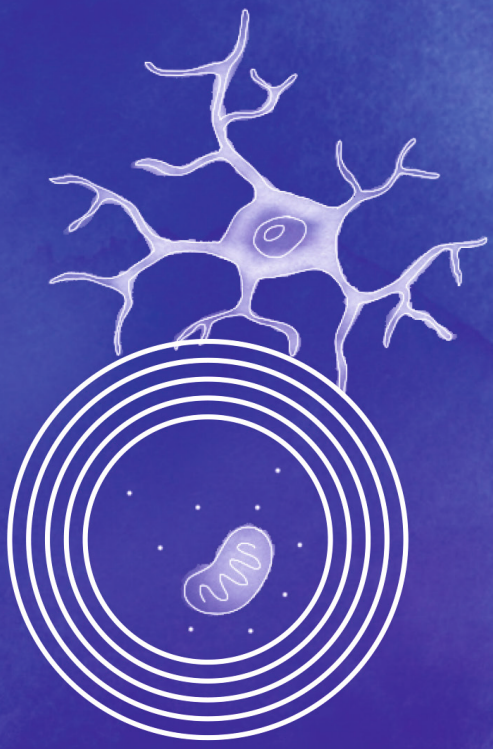

# CHAPTER 2

# Cortical CD200-CD200R and CD47-SIRPα expression is associated with multiple sclerosis pathology

Aletta M.R. van den Bosch[1], Dennis Wever[1], Pleun Schonewille[1], Sabine L. Schuller[1], Joost Smolders [1,2], Jörg Hamann[1,3] and Inge Huitinga[1,4]

[1]Neuroimmunology Research Group, Netherlands Institute for Neuroscience, Amsterdam, The Netherlands; [2]MS Center ErasMS, Departments of Neurology and Immunology, Erasmus Medical Center, Rotterdam, The Netherlands; [3]Amsterdam Institute for immunology and Infectious Diseases, Amsterdam University Medical Center, Amsterdam, The Netherlands; [4]Swammerdam Institute for Life Sciences, University of Amsterdam, Amsterdam, The Netherlands

*Brain Communications. 2024 Aug; 6(4): fcae264*

## ABSTRACT

Control of microglia activity through CD200–CD200R and CD47–SIRPα interactions has been implicated in brain homeostasis. Here, we assessed CD200, CD47, CD200R and SIRPα expression with qPCR and immunohistochemistry in multiple sclerosis (MS) normal-appearing cortical grey matter (NAGM), normal-appearing white matter (NAWM), cortical grey matter (GM) lesions and peri-lesional GM, and compared this to control GM and white matter (WM), to investigate possible altered control of microglia in MS. We assessed CD200, CD47, CD200R and SIRPα RNA and protein expression. In MS NAGM, CD200 expression is lower compared to control GM, specifically in cortical layers 1 and 2, and CD200 expression in NAGM negatively correlates with the cortical lesion rate. Interestingly, (NA)GM and (NA)WM CD200 expression is positively correlated, and NAGM CD200 expression negatively correlates with the proportion of active and mixed WM lesions. In GM lesions, CD200 and CD47 expression is lower compared to NAGM and peri-lesional GM. CD200R expression is lower in MS NAGM, whereas SIRPα was increased in and around GM lesions. Taken together, our data indicates that CD200 and CD47 play a role in GM MS lesion formation and progression, respectively, and that targeting CD200 pathways may offer therapeutic avenues to mitigate MS pathology in both WM and GM.

## INTRODUCTION

Multiple sclerosis (MS) is a chronic inflammatory disorder characterised by focal demyelinating lesions and neuroaxonal damage across the central nervous system (CNS)[1,2]. Within cortical normal-appearing grey matter (NAGM) of people with MS, diffuse neurodegeneration, microglia activation, and macrophage infiltration is found, with variability observed among individuals[3]. In MS NAGM compared to healthy grey matter (GM), microglia exhibit upregulated gene expression associated with iron accumulation and inflammation[4], increased density, and altered morphology[5]. Large areas of the cortical GM can be effected by MS, and the majority of patients have cortical GM lesions at autopsy[6–10]. Based on their location in the cortex, GM lesions are divided in subpial, intracortical and leukocortical lesions[11]. GM lesions and peri-lesional GM demonstrate increased apoptotic neuron counts and reduced neuronal density, contributing to the pathological characteristics of MS[12,13]. Although the clinical consequences of GM demyelination are not yet fully understood, the extent of GM demyelination has been correlated with disability and cognitive impairment in people with MS[9,14,15].

The interaction between neurons and microglia plays a role in microglia homeostasis, modulating microglia activity through both cell-surface interactions and soluble molecules[16,17]. Combinations of inhibitory and stimulatory signals regulate microglia activity[18]. In the healthy CNS, neurons actively maintain microglia in a quiescent, ramified state[19]. CD200 and CD47 are immunoglobulin superfamily glycoproteins. CD200 is highly expressed by neurons, and to a lesser extent by oligodendrocytes, whereas CD47 is expressed by neurons, oligodendrocytes and astrocytes[20]. Binding of CD200 and CD47 to their receptors CD200R and SIRPα, respectively, on microglia, results in maintaining microglia in a ramified, anti-phagocytic state[21–24]. Interestingly, in major depressive disorder, increased expression of CD200 and CD47 is thought to regulate an immune-suppressed microglial phenotype[25].

In MS, neuron–microglia communication is disrupted[17]. Previously, we found checkpoint molecules CD200 and CD47 are expressed lower in and around white matter (WM) lesions in post-mortem MS brain tissue compared to normal appearing white matter (NAWM)[26,27]. In experimental autoimmune encephalomyelitis (EAE) mice, decreased CD200 levels manifest during the presymptomatic phase[28], and knock-out of CD200 elicited an accelerated microglial response, more severe pathology, and a more rapid onset of EAE[22,29,30]. Conversely, administering a CD200R agonist (CD200-Fc) during the chronic EAE phase mitigate disease severity, demyelination, axonal damage, and microglial clustering within the CNS[31]. Blocking CD47 *in vitro* promotes myelin

phagocytosis[32], and intraperitoneal administration of antibodies against CD47 in late-stage EAE intensified disease severity and enhanced immune activation, leading to elevated immune cell proliferation and heightened production of inflammatory cytokines in spleen and lymph nodes[32]. To date, it is not yet known what the expression levels of CD200, CD47, CD200R and SIRPα in NAGM, GM lesions and peri-lesional GM are, and their roles in lesion formation and disease severity are yet to be elucidated.

This study describes the expression of CD200, CD200R, CD47 and SIRPα in MS and control (NA)GM, GM lesions, and peri-lesional GM. Furthermore, we correlated this to clinical and pathological hallmarks. We hypothesize that lower expression of CD200 and CD47 within the MS GM instigates an exaggerated microglial response, impeding remyelination processes, amplifying pathological cascades, and thereby exacerbating the severity of the disease. Ultimately, the restoration or augmentation of CD200–CD200R and CD47–SIRPα interactions may emerge as a promising avenue for the potential treatment of MS.

## METHODS

### Donors and sample collection

Frozen post-mortem brain tissue samples of the superior or medial temporal gyrus of n=30 non-demented control donors and n=34 MS donors, and fresh tissue samples of the lateral parietal sulcus and NAWM of the pyramid tract in 4% PFA of 1 MS donor were provided by the Netherlands Brain Bank (www.brainbank.nl). All donors provided informed consent for brain autopsy and for the use of material and clinical data for research purposes in compliance with national ethics guidelines. MS pathology was confirmed by a certified neuropathologist. MS and control donors were matched for age, sex, post-mortem delay, pH of the CSF, and weight of the brain, and donor demographics are summarised in **Table 1.** For MS donors, disease duration was calculated as years between initial symptom onset to death. Ranked scores on three pathologically and clinically relevant dimensions of disease progression were previously calculated based on data accessible via the Netherlands Neurogenetics Database (NND)[33,34]. Lesion parameters were calculated as previously described[8,35]. In standard locations of the brainstem, the reactive site load was calculated as the number of reactive sites identified, and the lesion load was calculated as the sum of all lesions present. The proportion of active, mixed, inactive and remyelinated lesions throughout the CNS were calculated by dividing the number of lesions of that lesion type by the sum of active, mixed, inactive and remyelinated lesions. The cortical lesion rate was

calculated by dividing the number of cortical lesions present throughout the CNS by the number of tissue blocks containing cortex.

**Table 1:** Donor demographics

| Parameter | Control (n=30) | MS (n=32) | P-value |
|---|---|---|---|
| Age (years) | 73.10 ± 12.26 | 70.26 ± 10.23 | n.s. |
| Sex | 22 F/8 M | 16 F/16 M | n.s. |
| PMD (min) | 396.50 ± 101.19 | 502.74 ± 100.20 | 1.2e-4 |
| pH CSF | 6.55 ± 0.41 | 6.45 ± 0.25 | n.s. |
| Weight of the brain (g) | 1,242.19 ± 112.98 | 1,201.38 ± 134.53 | n.s. |

*CSF, cerebrospinal fluid; F, female; M, male; PMD, post-mortem delay*



## RNA isolation and qRT-PCR

For each tissue block, GM was dissected with a scalpel in the cryostat and two 20 µm sections were made. GM was separated from WM, and GM was collected in 500 µl of Trisure (Bioline, London, England). Tissue was dissociated by vortexing rigorously and the samples were stored at -80°C until RNA isolation. Samples were incubated with 200 µl chloroform for 2 min and spun down at 10,000 rpm for 10 min. The aqueous phase was collected, and an equal amount of cold isopropanol was added together with 1 µl glycogen. The samples were left to precipitate at -20°C for an hour and spun down at 10,000 rpm for 10 min. The supernatant was discarded, and the samples were air-dried. The pellet was reconstituted in 20 µl RNase free water and incubated at 55°C for 10 min. RNA concentration and purity were measured on the NanoDrop (Thermo Fisher, Waltham, MA, USA). Complementary DNA (cDNA) was synthesised with the Quantitect Reverse Transcription Kit (Qiagen, Hilden, Germany). Samples of 12 µl with 1,000 ng RNA were incubated with 2 µl of gDNase at 42°C for 5 min and subsequently incubated with 6 µl of cDNA master mix at 42°C for 30 min and at 95°C for 3 min. cDNA samples were diluted 1:20 in RNase free water and stored at -20°C. Quantitative reverse transcription PCR (qRT-PCR) was performed in duplo using the primers indicated in **Table 2**. The samples were diluted 1:1 with the SYBR Green PCR Master Mix (Applied Biosystems, Waltham, MA, USA) and 2 µM primer mix per reaction. For each gene of interest, the primer mix contained 2 µM forward primer and 2 µM reverse primer (Sigma-Aldrich, St. Louis, MO, USA). The QuantStudio PCR system 96-well apparatus (Thermo Fisher) was used for the amplification. For each reaction, the cycle threshold (CT) was assessed. Samples containing lesions as assessed with immunohistochemistry (IHC) (n=11 MS samples) or samples where genes of interest were not detected with qPCR were excluded (n=2 control, n=6 MS samples). The average CT of each duplicate

reaction was subtracted by the CT of the average of the two housekeeping genes (ΔCT). The ΔCT was subtracted by the average ΔCT of the control group (ΔΔCT) and the -ΔΔCT was calculated per gene per donor.

**Table 2:** qPCR primers

| Primer | Forward sequence (5'–3') | Reverse sequence (5'–3') |
|---|---|---|
| *CD200* | CCAGGAAGCCCTCATTGTGA | TCTCGCTGAAGGTGACCATGT |
| *CD47* | ATGGAGCTCTAAACAAGTCCACTGT | TGTGAGACAGCATCACTCTTATCCAT |
| *CD200R1* | GAGCAATGGCACAGTGACTGTT | GTGGCAGGTCACGGTAGACA |
| *SIRPA* | GTCTGGAGCAGGCACTGA | GGACTCGCAGGTGAAGCT |
| *GAPDH* | TAGTCGCCGTGCCTACCAT | CCTGCTGCCTTCCTTGGA |
| *EEF1A1* | AAGCTGGAAGATGGCCCTAAA | AAGCGACCCAAAGGTGGAT |

**Immunohistochemistry**

Fresh tissue was fixed for 24 hours in 4% PFA after autopsy, and tissue blocks were submerged in 30% before being frozen at -80°C. Tissue sections of 8 µm thickness of the frontal gyrus or 20 µm thickness of the lateral parietal sulcus and pyramid tract were cut using a cryostat. Antibodies and their corresponding fixation buffers were selected as detailed in **Table 3.** For optical density (OD) analysis, dilution series were made to ensure that the staining had not reached saturation and the staining would develop in a controlled, time-dependant manner, which is necessary to distinguish subtle changes in protein expression. The OD values over the dilution series and the OD values of the chosen primary antibody over incubation time of DAB is shown in **Suppl. Fig. 1**. Sections used for different stainings were sequential, and all MS and control sections per staining were stained simultaneously. For fresh-frozen sections, sealed frozen sections were allowed to reach room temperature for 30–45 min and then fixed for 15 min using 4% paraformaldehyde or 10 min using ice-cold acetone. Acetone-fixed tissue was air-dried for 40 min. For free-floating immunofluorescent stainings, sections were washed with PBS. Subsequently, sections were treated with 3% hydrogen peroxide ($H_2O_2$) in phosphate buffered saline (PBS) + 0.5% TritonX for 20 min before being incubated with blocking buffer (PBS + 10% normal horse serum + 1% bovine serum albumin + 0.5% TritonX) for 1 hour to block aspecific binding. Primary antibodies were incubated overnight at 4°C. For all DAB stainings and for immunofluorescent staining of axons (neurofilament heavy chain (NFH)), biotinylated secondary antibodies were incubated for one hour and incubated with avidin-biotin complex (ABC; Vector Laboratories, Newark, CA, USA) 1:800 in PBS for 45 min. For CD200R, staining was enhanced with biotinylated tyramide 1:7,500 + 0.001% $H_2O_2$ in 0.05 M borate buffered saline for 10 min and incubated with ABC 1:800 in PBS for 45 min. For

all DAB-visualised stainings, sections were incubated with 3-3'-diaminobenzidin (DAB) for 10 min to visualize the staining, followed by counterstaining with haematoxylin and dehydration using increasing ethanol concentrations and xylene. All immunofluorescent stainings were incubated with the appropriate fluorophore-conjugated antibodies. DAPI 1:1,000 was incubated for 10 min for nuclei staining, and quenching of autofluorescence was performed with 0.1% Sudan Black in 70% ethanol for 10 min. Imaging of was performed using the Axio Scan Z1 (ZEISS, Oberkochen, Germany) microscope at a magnification of 20x. Immunofluorescent imaging was performed with confocal microscopy on a stimulated emission depletion (STED) microscope at 63x magnification, creating z-stacks of steps of 0.5 µm.



Cell-types expected to express CD200, CD200R, CD47 and SIRPα were found on the website of the Human Protein Atlas, www.proteinatlas.org, based on integrative omics and single-cell transcriptomics of human tissue[20,36], and on the website of Brain RNA-Seq, www.brainrnaseq.org, based on cell type-specific RNA sequencing after immunopanning[37].

**Table 3:** IHC antibodies

| Antibody | Company (cat#) | Clone | Dilution | Fixation buffer |
|---|---|---|---|---|
| HLA | Abcam (ab7856) | CR3/43 | 1:1,000 | 4% PFA |
| PLP | Biorad (MCA8396) | PLC1 | 1:1,500 | 4% PFA |
| CD200 | Biorad (MCA1960T) | OX-104 | 1:80,000, 1:400# | 4% PFA |
| CD200R | Serotec (MCA2282) | OX-108 | 1:150+, 1:100+# | Acetone |
| CD47 | Serotec (MCA911) | BRIC126 | 1:30,000, 1:800# | 4% PFA |
| Iba1 | Wako (019-19741) | Polyclonal | 1:100# | 4% PFA/Acetone |
| MBP | Millipore (AB980) | Polyclonal | 1:100 | 4% PFA |
| NF-H | Thermo Fisher (18934-1) | Polyclonal | 1:100+ | 4% PFA |
| SIRPα | Atlas (HPA054437) | Polyclonal | 1:400, 1:100+# | 4% PFA |
| NeuN | Sigma (MAB377) | A60 | 1:500 | 4% PFA |

*PFA: paraformaldehyde. +enhanced staining, #IF staining*

**Immunohistochemistry analysis**

Staining analysis was conducted with QuPath (version 0.4.4). Of all sections, the human leukocyte antigens (HLA) and myelin proteolipid protein (PLP) stainings were assessed to confirm absence of pathology in control samples and to annotate regions with GM lesions as well as the adjacent peri-lesional GM defined as 100 µm expansion from GM lesions in MS samples. No control donor

showed abnormal myelination or microglia activation. For the control donors, a GM region of interest (ROI) was annotated where all layers of the cortex were visible on the neuronal nuclei (NeuN) staining. For MS donors, a NAGM ROI was annotated as far away from GM lesions as possible with intact myelination and where all layers of the cortex were present and visible on the NeuN staining.

ROIs were imported into the NeuN images. Based on the NeuN staining, cortical layers were annotated in the ROIs. The first layer of the cortex was recognised by a low neuronal density. The second layer of the cortex was recognised by a high density of small neurons. The third layer of the cortex was recognised by a lower density of neurons and presence of pyramidal cells. The fourth layer of the cortex was recognised by a high density of small neurons. The fifth layer of the cortex was recognised by a lower density of neuronal cells including large pyramidal cells. The transition from the fifth to the sixth layer of the cortex was recognised by a small rim with a relative increase of the neuronal density. Positive cells were quantified with cell detection and normalised to the size of the ROI.

The annotation of the ROIs including the annotation of the cortical layers were imported into the CD200, CD47 and SIRPα stainings. For CD200, NAWM was additionally annotated. Tissue gaps were eliminated using a thresholder, and for CD200 and CD47, the mean OD was calculated per ROI. For SIRPα, cells were annotated via nuclei staining-based detection, and within each annotation the number of cells with a DAB intensity exceeding twice the average DAB intensity of that annotation was quantified relative to the area of the annotation. Given that lesions and peri-lesional GM appeared across diverse cortical layers, and the quantification of CD200, CD47 and SIRPα indicated layer-specific expression, OD or cell density calculations were normalised against NAGM within the same layers. For CD200R, as there were only very few $CD200R^+$ cells and these were not homogeneously spread throughout the tissue and there was some background staining, the number of $CD200R^+$ cells were counted manually in lesions and peri-lesional GM as previously defined as well as in the entire section for NAGM.

**Statistical analysis**

All statistics were performed in RStudio Desktop (2023.06.1; Rstudio, Boston, MA) using key packages lme4, car, plyr and ggpubr. Missing values were ignored. For IHC, groups were tested with a quasipoisson generalised linear model, statistically correcting for neuronal density when comparing GM lesions with peri-lesional GM or with NAGM. When more than two conditions were compared multiple testing correction was performed with false-discovery rate.

For qPCR data, a two-sided T-test was performed. Correlations were tested with Pearson's correlation coefficient. Tests were considered significant if $p<0.05$.

## RESULTS

### Lower neuronal density in GM lesions

As visualised in**. 1A-B**, neuronal density was quantified with a NeuN staining, and layers were separated based on the shape and density of neurons. In MS (n=30) and controls (n=27, the neuronal density in the whole GM was 327.94 ± 74.36 and 342.23 ± 97.94 neurons/mm$^2$ respectively, with the highest neuronal density in layer 2 and layer 4. The neuronal density was not different in MS compared to controls in any of the cortical layers or in the whole (NA)GM (**Fig. 1C**). In GM lesions (n=13) compared to NAGM (n=30), the neuronal density was lower in layer 2, 3, 4 and 6 of the cortex (layer 2 NAGM: 492.60 ± 171.57, lesion: 347.30 ± 121.04, p= 9.9e-3; layer 3 NAGM: 293.59 ± 104.28, lesion: 224.11 ± 75.01, p=0.03; layer 4 NAGM: 599.51 ± 184.66, lesion: 388.93 ± 107.99, p=1.2e-3; layer 6 NAGM: 326.02 ± 96.16, lesion: 196.93 ± 52.55, p=0.02). In peri-lesional GM (n=14) compared to NAGM (n=30), neuronal density was lower in layer 4 (layer 4 NAGM: 599.51 ± 184.66, peri-lesional: 408.50 ± 132.32, p=1.2e-4; **Fig. 1D**).

### Expression of inhibitory receptor–ligand pairs in the NAGM

Expression of CD200, CD200R, CD47 and SIRPα in (NA)GM was quantified with qRT-PCR and IHC. The expression of CD200, CD200R, CD47 and SIRPα was not correlated to the neuronal density (data not shown). As visualised in **Fig. 2A-D**, RNA expression of both *CD200* and *CD200R* was lower in MS NAGM (n=15) compared to control GM (n=26) (*CD200*: -ΔΔCT CON: 0.00 ± 1.82, -ΔΔCT MS: -1.00 ± 1.05, p=0.03; *CD200R*: -ΔΔCT CON: 0.00 ± 2.40, -ΔΔCT MS: -2.19 ± 1.18, p=3.6e-4). No difference in RNA expression was observed for *CD47* or *SIRPA*. According to the Human Protein Atlas (v.23.0.proteinatlas.org) [20,36] and the Brain RNA-Seq database [37], CD200 and CD47 are highly expressed by neurons and to a lower extent by oligodendrocytes. CD47 is furthermore also expressed by astrocytes[20,36,37]. CD200R is very lowly expressed by microglia, T and B cells, neurons, astrocytes and oligodendrocytes[20,36,37]. SIRPα is expressed by microglia and barely by T and B cells, neurons, astrocytes and oligodendrocytes[20,36,37]. With immunofluorescence, we show that CD200 and CD47 both were abundantly expressed in NAGM and to a lesser extent in NAWM in a similar pattern. The staining was highly intense and so diffuse that cellular localization was difficult to interpret. Therefore, we stained NAWM in the pyramid tract, where lower expression of CD200 and CD47 enables visualisation of cellular localisation. We found faint but distinct colocalization of CD200 with myelin and axons.

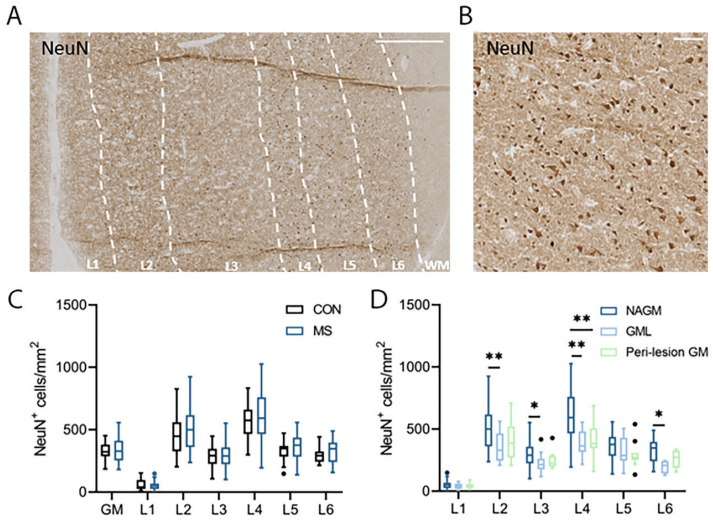


**Figure 1: Neuronal density in the (NA)GM in MS and controls.** A) Immunohistochemistry of NeuN in NAGM in MS, with delineation of the cortical layers (L1-L6) and WM based on neuronal density and neuron shape, scale bar 500 µm. B) Higher magnification of NeuN staining, scale bar 100 µm. C) There was no difference in neuronal density in MS NAGM (n=30) compared to control GM (n=27). D) Neuronal density is lower in GM lesions (n=13) and peri-lesional GM (n=14) compared to NAGM (n=30) in lesions spanning layers 2, 3, 4, and 6 of the cortex and in peri-lesional regions in layer 4. GM = grey matter, GML = grey matter lesion, NAGM = normal-appearing grey matter, WM = white matter. Box plots indicate the median. * $p < 0.05$, ** $p < 0.01$, *** $p < 0.001$. Significance was tested with a quasi-poisson generalized linear model, correcting for multiple testing with FDR if comparing multiple groups.

Myelin also frequently stained strongly positive for CD47, which might originate from myelin-forming oligodendrocytes. Infrequently, $CD47^+$ axonal fragments were found (**Fig. 2E-J**). CD200R as well as SIRPα were co-localised with the microglia/macrophage marker Iba1 (**Fig. 2K-L**). $CD200R^+Iba1^-$ cells were rare, while $SIRP\alpha^+Iba1^-$ cells were observed more frequently.

Representative DAB immunohistochemical stainings for CD200, CD47, CD200R and SIRPα are visualised in **Fig. 2M-P**. The majority of CD200 was found extracellularly, and occasionally $CD200^+$ neuronal cell bodies could be identified. CD200 was visually higher in the (NA)GM than in the adjacent WM. In the (NA)GM, the lowest amount of CD200 was found in layer 1 and 2 of the cortex, which in MS, but not in controls, was significantly lower compared to layers 3, 4, 5 and 6 (MS L1: OD 0.35 ± 0.04 and L2: OD 0.37 ± 0.04 vs L3: OD 0.42 ± 0.04, $p<0.0001$, $p=5.0e-4$, respectively, L4: OD 0.43 ± 0.05, $p<0.0001$, $p<0.0001$, respectively, L5: OD 0.42 ± 0.05, $p<0.0001$, $p=2.0e-4$, respectively, L6: OD 0.41 ± 0.05, $p<0.0001$, $p=2.5e-3$, respectively). In MS (n=19) compared to

controls (n=19), no difference in OD of CD200 was found when the whole GM was compared, however there was a significantly lower OD of CD200 in layer 1 and 2 (layer 1 controls: 0.39 ± 0.07, MS: 0.35 ± 0.04, p=0.03; layer 2 controls: 0.41 ± 0.08, MS: 0.37 ± 0.04, p=0.04). In the other layers, no difference was found (**Fig. 2Q**).

CD47 was found abundantly expressed extracellularly throughout the (NA)GM and sporadically on neuronal cell bodies, like CD200. CD47 expression visually was lower in WM than in the (NA)GM. OD of CD47 was similar in layer 1 and layer 2 and was significantly higher per consecutive layer except from layer 4 to layer 5 in both control GM as well as MS NAGM (CON L1: 0.59 ± 0.04, L2: 0.59 ± 0.03, L1 vs L2 p=*n.s.*, L3: 0.61 ± 0.03, L2 vs L3 p=0.03, L4: 0.63 ± 0.03, L3 vs L4 p=0.03, L5: 0.65 ± 0.03, L4 vs L5 p=*n.s.*, L6: 0.66 ± 0.04, L5 vs L6 p=0.01; MS L1: 0.58 ± 0.04, L2: 0.58 ± 0.04, L1 vs L2 p=*n.s.*, L3: 0.61 ± 0.04, L2 vs L3 p=9.9E$^{-3}$, L4: 0.63 ± 0.04, L3 vs L4 p=0.02, L5: 0.64 ± 0.04, L4 vs L5 p=*n.s.*, L6: 0.66 ± 0.04, L5 vs L6 p=*n.s.*). No difference was found in CD47 OD (**Fig. 2R**).

For CD200R, the number of positive cells, likely microglia and macrophages, was quantified in the whole (NA)GM with no distinction between layers. CD200R$^+$ cells were only found sporadically. The majority of CD200R$^+$ cells were found perivascular, but sporadically CD200R$^+$ cells were found in the parenchyma. There was a small but significant lower number of CD200R$^+$ cells/mm$^2$ in NAGM (n=24) compared to control GM (n=21) (control GM: 1.60 ± 1.44, MS NAGM: 0.75 ± 0.67, p=9.2e-3, **Fig. 2S**). SIRPα, similarly to CD47, gradually increased from layer 1 to layer 6 in both MS and controls, similarly to CD47, but this was not significant in either controls or MS. Strong SIRPα expression was found on round parenchymal cells, which are likely microglia and lymphocytes, and low SIRPα expression was found on neurons. No difference was found in the (NA)GM or in the layers in MS (n=31) compared to controls (n=25) (**Fig. 2T**).

**Lower expression of CD200–CD200R and CD47–SIRPα in GM lesions and peri-lesional GM**

In GM lesions (n=16), CD200 was lower compared to NAGM (n=19) (fold change OD: 0.92 ± 0.08, p=0.02, **Fig. 3A**). CD200 expression in peri-lesional GM (n=16) was like in NAGM (n=19). CD47 was lower in GM lesions (n=24) (fold change GM lesions compared to NAGM: 0.93 ± 0.01, p=2.0e-4) and near-significantly lower in peri-lesional GM (n=24) compared to NAGM (n=24) (fold change peri-lesional GM compared to NAGM: 0.96 ± 0.01, p=0.05, **Fig. 3B**). There was no difference in the number of CD200R$^+$ cells/mm$^2$ in NAGM (n=24), GM lesions (n=18), or peri-lesional GM (n=18) (**Fig. 3C**). SIRPα expression was increased in GM lesions (n=17) compared to NAGM (n=31) (fold change GM lesions compared to NAGM: 5.96 ± 9.55, p=0.01), and further increased in peri-lesional region (n=15) (fold change peri-lesional compared to NAGM: 7.65 ± 5.92, p=6.1e-4, **Fig. 3D**).

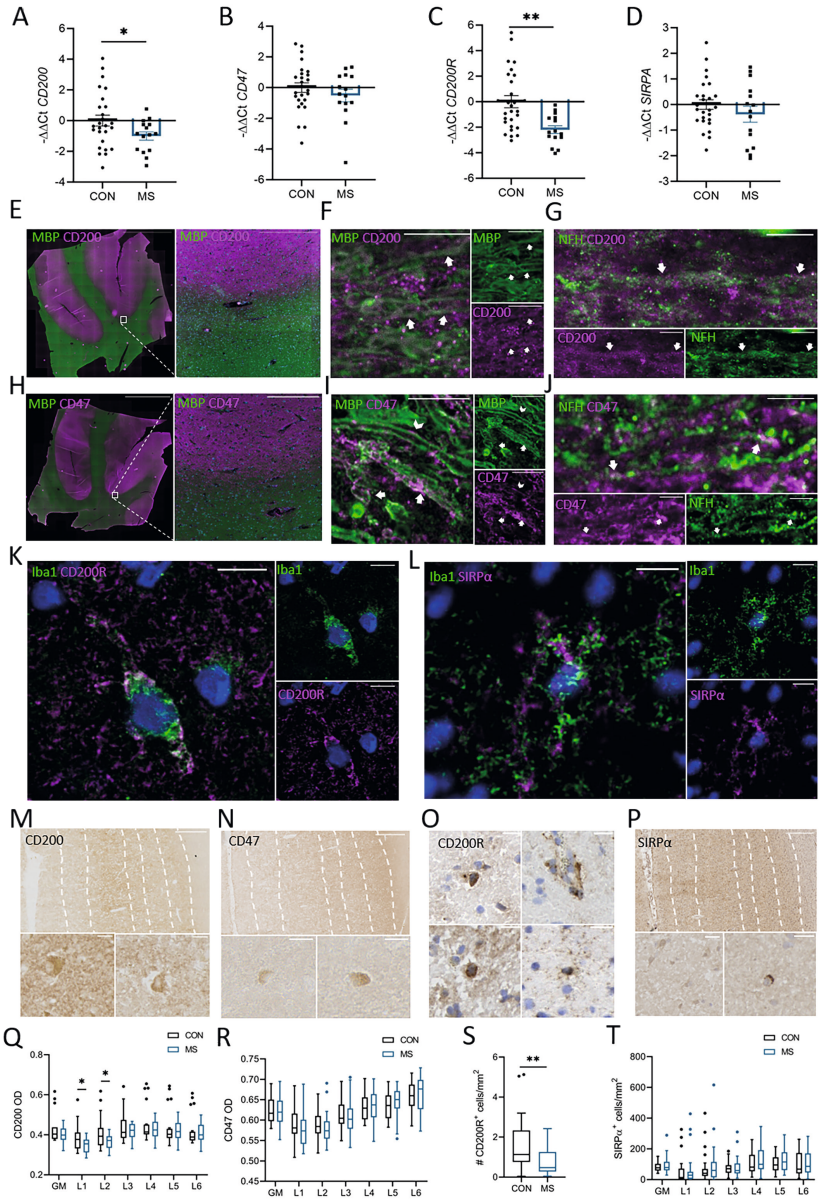


**Figure 2: Gene and protein expression of CD200, CD47, CD200R, and SIRPα in NAGM.** Gene expression in NAGM of MS compared to GM of controls as measured with qRT-PCR (MS n = 15, CON n = 26) was A) lower for *CD200*, B) comparable for *CD47*, C) lower for *CD200R* and D) comparable *SIRPA*. E) Immunofluorescent staining of CD200 and MBP shows that CD200 expression was abundant in NAGM and low in NAWM. Scale bar on the overview image is 1 cm and on the zoomed image is 250 µm. F) CD200 expression co-localised with MBP$^+$ myelin as indicated with arrows; scale bar is set at 10 µm. G) CD200 expression co-localised with NFH$^+$ axons as indicated with arrows; scale bar is set at 5 µm. H) CD47 expression was, like CD200, abundant in NAGM and

lower in NAWM. Scale bar on the overview image is 1 cm and on the zoomed image is 250 µm. I) CD47 strongly co-localised with some MBP$^+$ myelin, as indicated with the arrows, and was sometimes localised adjacent to the myelin, on the outer layer, as indicated with the arrowhead. Scale bar is set at 10 µm. J) Occasionally, CD47 co-localised with NFH$^+$ axons, scale bar is set at 5 µm. K) CD200R was expressed by Iba1$^+$ microglia, scale bar is set at 10 µm. L) SIRPα was expressed by Iba1$^+$ microglia, scale bar is set at 10 µm. DAB stainings showed M) mainly extracellular deposition and sporadic expression on neurons for CD200, N) mainly extracellular deposition and sporadic expression on neurons for CD47, O) sporadic positive staining of cells for CD200R, and P) light positive neurons and some darker stained round cells for SIRPα. Scale bars are set at 20 µm. In MS NAGM compared to control GM, there was a Q) lower CD200 OD in cortical layers 1 and 2 (MS n = 19, CON n = 19), R) comparable CD47 OD (MS n = 31, CON n = 28), S) lower number of CD200R$^+$ cells/mm$^2$ (MS n = 24, CON n = 21), and T) comparable number of SIRPα$^+$ cells/mm$^2$ (MS n = 31, CON n = 25). GM = grey matter, NAGM = normal-appearing grey matter, OD = optical density. Box plots indicate the median. IHC = immunohistochemistry. * $p < 0.05$, ** $p < 0.01$, *** $p < 0.001$. Significance was tested with a quasi-poisson generalized linear model.



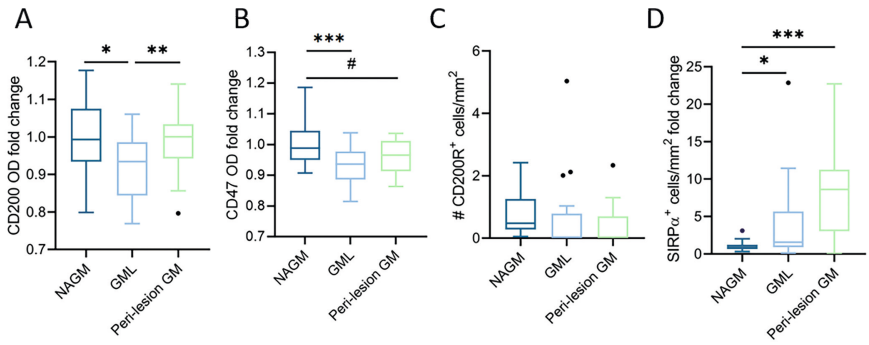


**Figure 3: Distribution of CD200, CD47, CD200R and SIRPα in GM lesions and peri-lesional GM.** A) CD200 OD was lower in GM lesions (n=16) compared to NAGM and peri-lesional GM (n=19). B) CD47 OD was lower in GM lesions (n=24) compared to NAGM (n=24). C) There was no difference in number of CD200R$^+$ cells/mm$^2$ in GM lesions (n=24) or peri-lesional GM (n=18) compared to NAGM (n=18). D) In GM lesions (n=17) and peri-lesional GM (n=15), there was an increase in the number of SIRPα$^+$ cells/mm$^2$ compared to the NAGM (n=31). GM = grey matter, GML = grey matter lesion, NAGM = normal-appearing grey matter, OD = optical density. Box plots indicate the median. * $p < 0.05$, ** $p < 0.01$, *** $p < 0.001$, # $p = 0.05$. Significance was tested with a quasi-poisson generalized linear model, correcting for neuronal density and for multiple testing with FDR.

**Neuronal density and CD200 expression in NAGM correlate with MS donor pathology**

In NAGM, neuronal density negatively correlated to the reactive site load (p=0.04, r=-0.37, **Fig. 4A**) and to the lesion load (n=30) (p=9.2e-3, r=-0.47, **Fig. 4B**). The neuronal density of NAGM negatively correlated with the disease duration (p=0.01, r=-0.48, **Fig. 4C**), also after correction for age (p=0.05). Recently, exploratory factor analysis identified three pathologically and clinically relevant dimensions of disease progression[33]. Although the correlations were not statistically significant, there was a noticeable trend towards a negative correlation with demyelination and immune cell activity (dimension 1), no correlation with microglia (re)activity and possibly lesion initiation (dimension 2) and a trend towards a positive correlation with loss of lesion activity and scar formation (dimension 3) (**Fig. 4D-F**). These trends could indicate a negative association between CD200 and ongoing microglia activation and demyelination. The OD of CD200 in NAGM (n=19) was correlated to the OD of CD200 in NAWM (p=1.3e-3, r=0.50, **Fig. 4G**). CD200 NAGM OD negatively correlated with the cortical lesion rate (p=6.5e-3, r=-0.62, **Fig. 4H**). CD200 NAGM OD furthermore correlated negatively with the proportion of active lesions (p=7.9e-4, r=-0.70, **Fig. 4I**), mixed active/inactive lesions (p=0.02, r=-0.53, **Fig. 4J**)**,** was correlated positively with the proportion of inactive lesions (p=2.1e-4, r=0.75, **Fig. 4K**), and was not correlated to the proportion of remyelinated lesions (p=0.35, r=-0.23, **Fig. 4L**). The OD of CD47, the number of SIRPα$^+$ cells/mm$^2$ and the number of CD200R$^+$ cells/mm$^2$ were not correlated to any pathological characteristics. The OD of CD200 and CD47 and the number of SIRPA$^+$ cells or CD200R$^+$ cells per mm$^2$ were not correlated to disease duration.

## DISCUSSION

GM lesions have a pathogenesis that differs from the pathogenesis of WM lesions. In contrast to WM lesions, there are only few T cells that infiltrate the parenchyma. Also, there are fewer microglia, and these microglia tend to be less pro-inflammatory[6,9,38,39]. Neuronal cell bodies in GM expressing CD200 and CD47 may be in part responsible for keeping the microglia in the cortical GM in a more homeostatic state as compared to WM. The binding of CD200 and CD47 to their respective microglial receptors has immunosuppressive effects, maintaining microglia in a ramified, anti-phagocytic state[19,26]. Here, we investigate the RNA and protein expression of the immune-inhibitory ligands C200 and CD47 and of their respective receptors, CD200R and SIRPα, in NAGM, GM lesions and peri-lesional GM, and relate these to pathological features of the donors, with the aim of unveiling mechanisms involved in microglia activation and MS related pathology.

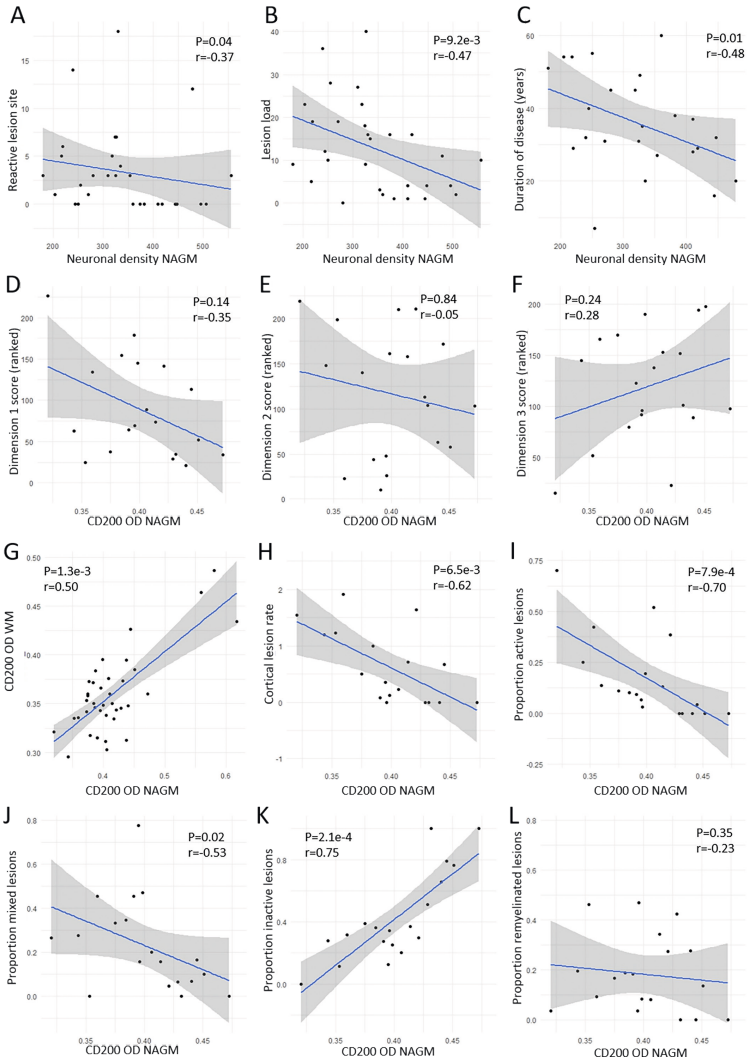


**Figure 4: Neuronal density and CD200 OD of NAGM in MS correlate with pathology.** Neuronal density was negatively correlated to A) the reactive site load, B) the lesion load and C) the disease duration (n=30). CD200 OD in NAGM showed D) a trend towards a negative correlation with demyelination and immune cell activity (dimension 1), E) no correlation with microglia (re) activity and possibly lesion initiation (dimension 2) and F) a trend towards a positive correlation with loss of lesion activity and scar formation (dimension 3). G) The OD of CD200 in WM was positively correlated to the OD of CD200 in GM (n=19). CD200 OD was negatively correlated to H) the cortical lesion rate, H) the ratio of leukocortical lesions, I) the proportion of active lesions and J) the proportion of mixed active/inactive lesions (n=19). CD200 OD was positively correlated to K) the proportion of inactive lesions and was not correlated to L) the proportion of remyelinated lesions (n=19). NAGM = normal-appearing grey matter, OD = optical density, WM = white matter. Significance was tested with a Spearman's correlation.

Although comparable neuronal density between MS and control (NA)GM, GM lesions and peri-lesional GM exhibited lower neuronal density, which is similar to what was previously found[12,13]. Decreased peri-lesional neuronal density indicates that neuronal damage extends beyond de demyelinated region of the lesion. As CD200, CD200R, CD47 and SIRPα are all to some extent expressed by neurons, the altered expression of these proteins in lesions and peri-lesional GM might be influenced by the lower neuronal density. Therefore, we corrected for the neuronal density in the statistical model. This does not, however, correct for loss of neuronal processes and synapses, which may influence the data. The neuronal density negatively correlated with both the lesion load and the duration of disease, also after correction for age, which may be due to dying back of neurons.

From RNA sequencing studies, it is known that CD200 and CD47 are expressed by neurons and, more so for CD47, by oligodendrocytes[20,36,37]. CD47 is furthermore also expressed by astrocytes. Our immunohistochemical stainings show a pattern for CD200 and CD47 that is highly intense in the (NA)GM and less intense in the (NA)WM, and we additionally show that both, CD200 and CD47, are co-expressed with myelin and axons. Additionally, we show that CD47 is localised adjacent to myelin. CD200R mRNA and protein are lowly expressed[20,27,36,37], mainly by microglia, whereas microglia robustly express SIRPα[20,36,37]. Both receptors are also expressed by T and B cells, neurons, astrocytes and oligodendrocytes, indicating their diverse effects[20,36,37]. Here, with IHC, we validated that CD200R and SIRPα are indeed expressed by microglia. The low mRNA expression of CD200R indicate either a very low basic protein presence or expression by only a small fraction of cells. Indeed, we found that only very few microglia expressed CD200R, and it is possible that we cannot accurately quantify all $CD200R^{+}$ microglia with IHC. SIRPα, in line with its more abundant mRNA expression, was found on a larger number of microglia.

The CD200R cytoplasmic tail bears three tyrosine residues, which, upon CD200–CD200R interaction, undergo phosphorylation, initiating downstream inhibitory protein responses via Dok1 and Dok2. This leads to the downregulation of pro-inflammatory cytokines, including TNF, IFN-γ and IL-1, alongside upregulation of anti-inflammatory cytokines, such as IL-10 and TGF-β, consequently inhibiting phagocytosis[40]. The upstream mechanisms of CD200 regulation are not yet fully understood and need further investigation. In Alzheimer's disease, a loss of CD200 expression is hypothesised to contribute to chronic inflammation[41]. Notably, we found that CD200 and CD200R gene expression was lower in MS NAGM compared to control GM, and CD200 OD was lower in cortical layers 1 and 2. Similar to what we previously found in WM lesions[26], CD200 OD was lower in GM lesions compared to NAGM, even when correcting for neuronal

density, and not in peri-lesional GM compared to NAGM. Interestingly, here we show that there was a negative correlation between the OD of CD200 in NAGM and the cortical lesion rate. The lower expression of CD200 in NAGM and in GM lesions may indicate a decrease of control of pro-inflammatory cytokines and phagocytosis, therefore lower CD200 may lead to the cortex being more vulnerable to initiation of lesion formation. Previously, we have shown that that presence of GM lesions was associated with more extensive MS pathology in WM[8]. We found that CD200 OD in NAGM correlated with the CD200 OD in NAWM that could point to a donor-related lower CD200 expression relating to both GM and WM related pathology. Despite lacking statistical significance, the directionality of the correlation between CD200 in NAGM and three recently identified dimensions of disease progression[33] indicates that CD200 expression is negatively associated with ongoing microglia activity and demyelination. In line with this, here we show that lower CD200 OD in GM is associated with more actively demyelinating MS pathology in WM: CD200 OD of NAGM is negatively correlated with the proportion of active and mixed active/inactive, and positively correlated with the proportion of inactive lesions. It remains elusive if CD200 expression is associated with GM lesion activity, as inflammatory cortical demyelination is mainly associated with lymphocyte infiltration in the meninges[42], which have for the majority been removed during autopsy.



Previously, it has been shown that in EAE, a mouse model for autoimmune inflammatory diseases of the CNS, subcutaneous administration of a dimeric CD200R fusion protein (CD200R-Fc) that interacts with CD200R1 as agonist, can prevent demyelination and reduce symptom burden[31]. In a rat model for chronic constriction injury of the sciatic nerve, intrathecal CD200R-Fc application attenuated activation of microglial cells, decreased proinflammatory cytokine messenger RNA levels and increased anti-inflammatory cytokine messenger RNA levels[43]. In human renal cells *in vitro*, CD200R-Fc attenuated the inflammatory response to lipopolysaccharide[44]. Rat monoclonal antibodies agonistic for human CD200R as well as CD200R-Fc administered *in vitro* to mouse peritoneal cells, human peripheral blood cells, human dendritic cells and a human monocyte cell line activated with IFN-y inhibits pro-inflammatory cytokine production, especially after further cross-linking of the agonists[45]. Polyethylene glycol-modified DNA aptamer is also a CD200R1 agonist and can suppress the induction of cytotoxic T lymphocytes in human and murine allogeneic-mixed lymphocyte cultures[46]. We hypothesize that elevated expression of CD200 may lead to resolution of microglia activation, thereby potentially inhibiting smouldering lesion activity. The lack of correlation between CD200 OD of NAGM and the proportion of remyelinated lesions, indicates that CD200 upregulation will likely not inhibit microglia activity supporting remyelination. Additionally, as oligodendrocytes express CD200,

myelin may also express CD200, which could directly inhibit phagocytosis of myelin. Lastly, as microglia activation precedes MS lesion formation[47], and CD200 suppresses activation of microglia, activation of the CD200–CD200R pathway could be an interesting therapeutic target to decrease overall microglia activation and may limit the formation of new lesions. There are also facts that question this hypothesis, in particular the very low expression of CD200R by microglia and recent data showing that IFN-α can rewire CD200R signalling to become proinflammatory[48]. The biological role of CD200R therefore needs further investigation.

SIRPα contains intracellular immunoreceptor tyrosine-based inhibitory motifs (ITIMs), which, upon phosphorylation due to CD47 binding, recruit phosphatases like SH2-domain-containing protein tyrosine phosphatase (SHP-2) leading to inhibition of phagocytosis through deactivation of the motor protein myosin IIA[23,24]. Myosin significantly influences phagocytosis by modulating actin filaments[49,50]. Recently, SIRPα-Fc and less potently CD47-Fc were shown to have anti-inflammatory effects[51]. *In vitro* administration of SIRPα-Fc and high concentrations of CD47-Fc to a macrophage cell line suppressed inflammatory cytokine secretion in a cross-linking dependent manner, similar to the effect observed with CD200R-Fc. *In vivo*, intraperitoneally administered SIRPα-Fc showed anti-chemotactic effects on neutrophils and monocytes. In an experimental arthritis model, SIRPα-Fc reduced arthritis severity by ameliorating joint inflammation via inhibition of neutrophil and monocyte infiltration[51]. In line with this, *in vivo* administration of Miap410, a CD47-blocking antibody, in EAE impaired resolution of CNS inflammation[52]. We here show that CD47 is highly expressed in the (NA)GM. In NAWM of the pyramid tract, we additionally show that CD47 can co-localize with myelin or be found adjacent to myelin. CD47 gene expression and OD as well as and SIRPα gene expression and positive cell density showed no significant differences between MS and control donors. However, CD47 OD was significantly lower in GM lesions compared to NAGM, and near-significantly lower in peri-lesional GM, which together suggests a role in lesion progression. In contrast, there was an increase in the number of $SIRP\alpha^+$ cells/$mm^2$ in GM lesions as well as in peri-lesional GM, possibly reflecting a neuroprotective response or an increase in microglia in these lesions. Taken together, CD47 is not likely associated with the initiation of GM lesion formation, however it may be involved in expansion of GM lesions. Therefore, possibly CD47 and/or SIRPα may represent interesting therapeutic targets to reduce the expansion of GM lesions.

In conclusion, we show that downregulated CD200 expression in MS NAGM is associated with increased cortical lesion rate and more severe WM pathology of the donors. Meanwhile, CD47 is downregulated in GM lesions and in peri-

lesional GM, implicating its involvement in lesion progression. These findings provide more insight in the mechanisms behind GM lesion formation and progression and underscore the putative therapeutic potential of checkpoint molecules in mitigating pathological progression in both the white and GM.

**Data availability**
All gene expression data as well as IHC data is available upon reasonable request. The script for data analysis is provided as supplementary material.

**Acknowledgements**
We are grateful to the brain donors and their families for their commitment to the Netherlands Brain Bank donor program. We thank Dr. Inge Holtman and Alyse de Boer for providing data obtained from exploratory factor analysis for correlations with neuropathological dimensions.

**Funding**
Funding for this research was obtained from MoveS inspiration Grant 17-975 and MS Research grant 19-1079.

**Competing interest**
Authors declare no competing interests.

## REFERENCES


1. Lassmann H, Van Horssen J, Mahad D. Progressive multiple sclerosis: Pathology and pathogenesis. *Nat Rev Neurol*. 2012;8(11):647-656. doi:10.1038/nrneurol.2012.168
2. Dendrou CA, Fugger L, Friese MA. Immunopathology of multiple sclerosis. *Nat Rev Immunol*. 2015;15(9):545-558. doi:10.1038/nri3871
3. Lassmann H. Pathogenic mechanisms associated with different clinical courses of multiple sclerosis. *Front Immunol*. 2019;10(JAN):1-14. doi:10.3389/fimmu.2018.03116
4. van der Poel M, Ulas T, Mizee MR, et al. Transcriptional profiling of human microglia reveals grey–white matter heterogeneity and multiple sclerosis-associated changes. *Nat Commun*. 2019;10(1):1-13. doi:10.1038/s41467-019-08976-7
5. van Olst L, Rodriguez-Mogeda C, Picon C, et al. Meningeal inflammation in multiple sclerosis induces phenotypic changes in cortical microglia that differentially associate with neurodegeneration. *Acta Neuropathol*. 2021;141(6):881-899. doi:10.1007/s00401-021-02293-4
6. Bö L, Geurts JJG, Mörk SJ, Van Der Valk P. Grey matter pathology in multiple sclerosis. *Acta Neurol Scand*. 2006;113(SUPPL. 183):48-50. doi:10.1111/j.1600-0404.2006.00615.x
7. Albert M, Antel J, Brück W, Stadelmann C. Extensive cortical remyelination in patients with chronic multiple sclerosis. *Brain Pathol*. 2007;17(2):129-138. doi:10.1111/j.1750-3639.2006.00043.x
8. Luchetti S, Fransen NL, van Eden CG, Ramaglia V, Mason M, Huitinga I. Progressive multiple sclerosis patients show substantial lesion activity that correlates with clinical disease severity and sex: a retrospective autopsy cohort analysis. *Acta Neuropathol*. 2018;135(4):511-528. doi:10.1007/s00401-018-1818-y
9. Stadelmann C, Albert M, Wegner C, Brück W. Cortical pathology in multiple sclerosis. *Curr Opin Neurol*. 2008;21(3):229-234. doi:10.1097/01.wco.0000318863.65635.9a
10. Kutzelnigg A, Lucchinetti CF, Stadelmann C, et al. Cortical demyelination and diffuse white matter injury in multiple sclerosis. *Brain*. 2005;128(11):2705-2712. doi:10.1093/brain/awh641
11. Bø L, Vedeler CA, Nyland HI, Trapp BD, Mørk SJ. Subpial demyelination in the cerebral cortex of multiple sclerosis patients. *J Neuropathol Exp Neurol*. 2003;62(7):723-732. doi:10.1093/jnen/62.7.723
12. Peterson JW, Bö L, Mörk S, Chang A, Trapp BD. Transected neurites, apoptotic neurons, and reduced inflammation in cortical multiple sclerosis lesions. *Ann Neurol*. 2001;50(3):389-400. doi:10.1002/ana.1123
13. Klaver R, Popescu V, Voorn P, et al. Neuronal and Axonal Loss in Normal-Appearing Gray Matter and Subpial Lesions in Multiple Sclerosis. *J Neuropathol Exp Neurol*. 2015;74(5):453-458. doi:10.1097/NEN.0000000000000189
14. Calabrese M, Agosta F, Rinaldi F, et al. Cortical lesions and atrophy associated with cognitive impairment in relapsing-remitting multiple sclerosis. *Arch Neurol*. 2009;66(9):1144-1150. doi:10.1001/archneurol.2009.174
15. Tsouki F, Williams A. Multifaceted involvement of microglia in gray matter pathology in multiple sclerosis. *Stem Cells*. 2021;39(8):993-1007. doi:10.1002/stem.3374

16. Colonna M, Butovsky O. Microglia function in the central nervous system during health and neurodegeneration. *Annu Rev Immunol*. 2017;35:441-468. doi:10.1146/annurev-immunol-051116-052358
17. Szepesi Z, Manouchehrian O, Bachiller S, Deierborg T. Bidirectional Microglia–Neuron Communication in Health and Disease. *Front Cell Neurosci*. 2018;12(September):1-26. doi:10.3389/fncel.2018.00323
18. Li, Q and Barres B. Microglia and macrophages in brain homeostasis and disease. *Nat Rev Immunol*. 2018;18:225-242.
19. Biber K, Neumann H, Inoue K, Boddeke HWGM. Neuronal "On" and "Off" signals control microglia. *Trends Neurosci*. 2007;30(11):596-602. doi:10.1016/j.tins.2007.08.007
20. Karlsson M, Zhang C, Méar L, et al. A single–cell type transcriptomics map of human tissues. *Sci Adv*. 2021;7(31):1-10. doi:10.1126/sciadv.abh2169
21. Lehrman EK, Wilton DK, Litvina EY, et al. CD47 protects synapses from excess microglia-mediated pruning during development. *Neuron*. 2018;100(1):120-134. doi:10.1016/j.neuron.2018.09.017.CD47
22. Hoek RH, Ruuls SR, Murphy CA, et al. Down-regulation of the macrophage lineage through interaction with OX2 (CD200). *Science (80- )*. 2000;290(5497):1768-1771. doi:10.1126/science.290.5497.1768
23. Barclay AN, Van Den Berg TK. The interaction between signal regulatory protein alpha (SIRPα) and CD47: Structure, function, and therapeutic target. *Annu Rev Immunol*. 2014;32(October 2013):25-50. doi:10.1146/annurev-immunol-032713-120142
24. Logtenberg MEW, Scheeren FA, Schumacher TN. The CD47-SIRPα Immune Checkpoint. *Immunity*. 2020;52(5):742-752. doi:10.1016/j.immuni.2020.04.011
25. Scheepstra KWF, Mizee MR, van Scheppingen J, et al. Microglia Transcriptional Profiling in Major Depressive Disorder Shows Inhibition of Cortical Gray Matter Microglia. *Biol Psychiatry*. 2023;94(8):619-629. doi:10.1016/j.biopsych.2023.04.020
26. Koning N, Bö L, Hoek RM, Huitinga I. Downregulation of macrophage inhibitory molecules in multiple sclerosis lesions. *Ann Neurol*. 2007;62(5):504-514. doi:10.1002/ana.21220
27. Koning N, Swaab DF, Hoek RM, Huitinga I. Distribution of the immune inhibitory molecules CD200 and CD200R in the normal central nervous system and multiple sclerosis lesions suggests neuron-glia and glia-glia interactions. *J Neuropathol Exp Neurol*. 2009;68(2):159-167. doi:10.1097/NEN.0b013e3181964113
28. Valente T, Serratosa J, Perpiñá U, Saura J, Solà C. Alterations in CD200-CD200R1 system during EAE already manifest at presymptomatic stages. *Front Cell Neurosci*. 2017;11(May):1-15. doi:10.3389/fncel.2017.00129
29. Meuth SG, Simon OJ, Grimm A, et al. CNS inflammation and neuronal degeneration is aggravated by impaired CD200-CD200R-mediated macrophage silencing. *J Neuroimmunol*. 2008;194(1-2):62-69. doi:10.1016/j.jneuroim.2007.11.013
30. Chitnis T, Imitola J, Wang Y, et al. Elevated neuronal expression of CD200 protects Wlds mice from inflammation-mediated neurodegeneration. *Am J Pathol*. 2007;170(5):1695-1712. doi:10.2353/ajpath.2007.060677
31. Liu Y, Bando Y, Vargas-Lowy D, et al. CD200R1 agonist attenuates mechanisms of chronic disease in a murine model of multiple sclerosis. *J Neurosci*. 2010;30(6):2025-2038. doi:10.1523/JNEUROSCI.4272-09.2010
32. Han MH, Lundgren DH, Jaiswa S, et al. Janus-like opposing roles of CD47 in autoimmune brain inflammation in humans and mice. *J Exp Med*. 2012;209(7):1325-1334. doi:10.1084/jem.20101974

33. Boer A De, Bosch AM van den, Mekkes NJ, et al. Disentangling the heterogeneity of multiple sclerosis through identification of independent neuropathological dimensions. *Acta Neuropathol*. 2024;147(90). doi:10.1007/s00401-024-02742-w
34. Mekkes NJ, Groot M, Hoekstra E, et al. Identification of clinical disease trajectories in neurodegenerative disorders with natural language processing. *Nat Med*. 2024;30(4):1143-1153. doi:10.1038/s41591-024-02843-9
35. Harroud A, Stridh P, McCauley JL, et al. Locus for severity implicates CNS resilience in progression of multiple sclerosis. *Nature*. 2023;619(July). doi:10.1038/s41586-023-06250-x
36. Sjöstedt E, Zhong W, Fagerberg L, et al. An atlas of the protein-coding genes in the human, pig, and mouse brain. *Science (80- )*. 2020;367. doi:10.1126/science.aay5947
37. Zhang Y, Sloan SA, Clarke LE, et al. Purification and Characterization of Progenitor and Mature Human Astrocytes Reveals Transcriptional and Functional Differences with Mouse. *Neuron*. 2016;89(1):37-53. doi:10.1016/j.neuron.2015.11.013
38. De Stefano N, Matthews PM, Filippi M, et al. Evidence of early cortical atrophy in MS: Relevance to white matter changes and disability. *Neurology*. 2003;60(7):1157-1162. doi:10.1212/01.WNL.0000055926.69643.03
39. Prins M, Schul E, Geurts J, van der Valk P, Drukarch B, van Dam AM. Pathological differences between white and grey matter multiple sclerosis lesions. *Ann N Y Acad Sci*. 2015;1351(1):99-113. doi:10.1111/nyas.12841
40. Manich G, Recasens M, Valente T, Almolda B, González B, Castellano B. Role of the CD200-CD200R Axis During Homeostasis and Neuroinflammation. *Neuroscience*. 2019;405:118-136. doi:10.1016/j.neuroscience.2018.10.030
41. Walker DG, Dalsing-hernandez JE, Campbell NA, Lue L. Decreased expression of CD200 and CD200 receptor in Alzheimer's disease: A potential mechanism leading to chronic inflammation. *Exp Neurol*. 2009;215(1):5-19. doi:10.1016/j.expneurol.2008.09.003.Decreased
42. Lucchinetti CF, Popescu BFG, Bunyan RF, et al. Inflammatory Cortical Demyelination in Early Multiple Sclerosis. *N Engl J Med*. 2011;365(23):2188-2197. doi:10.1056/nejmoa1100648
43. Hernangómez M, Klusáková I, Joukal M, Hradilová-Svíženská I, Guaza C, Dubový P. CD200R1 agonist attenuates glial activation, inflammatory reactions, and hypersensitivity immediately after its intrathecal application in a rat neuropathic pain model. *J Neuroinflammation*. 2016;13(1):1-15. doi:10.1186/s12974-016-0508-8
44. Ding Y, Yang H, Xiang W, He X, Liao W, Yi Z. CD200R1 agonist attenuates LPS-induced inflammatory response in human renal proximal tubular epithelial cells by regulating TLR4-MyD88-TAK1-mediated NF-κB and MAPK pathway. *Biochem Biophys Res Commun*. 2015;460(2):287-294. doi:10.1016/j.bbrc.2015.03.026
45. Jenmalm MC, Cherwinski H, Bowman EP, Phillips JH, Sedgwick JD. Regulation of Myeloid Cell Function through the CD200 Receptor. *J Immunol*. 2006;176(1):191-199. doi:10.4049/jimmunol.176.1.191
46. Prodeus A, Sparkes A, Fischer NW, et al. A Synthetic Cross-Species CD200R1 Agonist Suppresses Inflammatory Immune Responses In Vivo. *Mol Ther Nucleic Acids*. 2018;12(September):350-358. doi:10.1016/j.omtn.2018.05.023
47. Bosch AMR van den, Poel M van der, Fransen NL, et al. Profiling of microglia nodules in multiple sclerosis reveals propensity for lesion formation. *Nat Commun*. 2024;15(1667):1-16. doi:10.1038/s41467-024-46068-3

48. van der Vlist M, Ramos MIP, van den Hoogen LL, et al. Signaling by the inhibitory receptor CD200R is rewired by type I interferon. *Sci Signal*. 2021;14(704):1-12. doi:10.1126/SCISIGNAL.ABB4324
49. Stendahl OI, Hartwig JH, Brotschi EA, Stossel TP. Distribution of actin-binding protein and myosin in macrophages during spreading and phagocytosis. *J Cell Biol*. 1980;84(2):215-224. doi:10.1083/jcb.84.2.215
50. Tsai RK, Discher DE. Inhibition of "self" engulfment through deactivation of myosin-II at the phagocytic synapse between human cells. *J Cell Biol*. 2008;180(5):989-1003. doi:10.1083/jcb.200708043
51. Xie MM, Dai B, Hackney JA, et al. An agonistic anti-signal regulatory protein α antibody for chronic inflammatory diseases. *Cell Reports Med*. 2023;4(8):101130. doi:10.1016/j.xcrm.2023.101130
52. Wang H, Newton G, Wu L, et al. CD47 antibody blockade suppresses microglia-dependent phagocytosis and monocyte transition to macrophages, impairing recovery in EAE. *JCI Insight*. 2021;6(21). doi:10.1172/jci.insight.148719

## SUPPLEMENTAL FIGURES

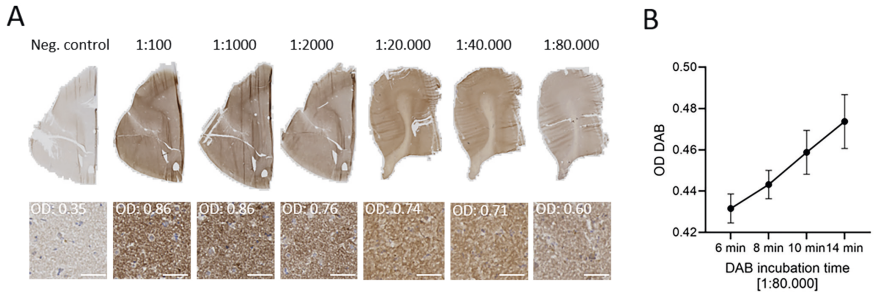


**Supplemental figure 1:** A) Serial dilutions of CD200 for optical density analysis, and B) optical density at [1:80,000] measured over DAB incubation time.

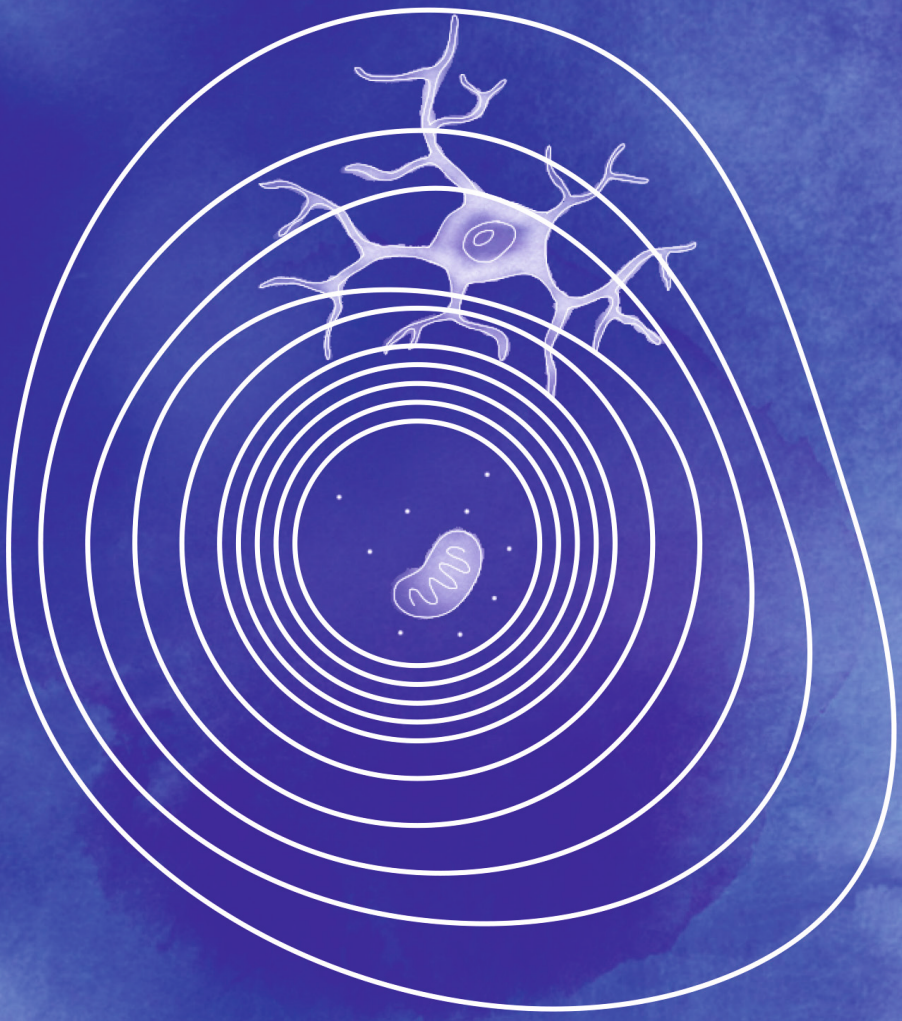

# CHAPTER 3

# Ultrastructural axon-myelin unit alterations in multiple sclerosis correlate with inflammation

Aletta M.R. van den Bosch[1], Sophie Hümmert[2], Anna Steyer[2], Torben Ruhwedel[2], Jörg Hamann[1,3], Joost Smolders[1,4], Klaus-Armin Nave[2], Christine Stadelmann[5], Maarten H. P. Kole[6,7], Wiebke Möbius[2*], Inge Huitinga[1,8*]

[1]Department of Neuroimmunology, Netherlands Institute for Neuroscience, Royal Netherlands Academy for Arts and Sciences, Amsterdam, The Netherlands, [2]Department of Neurogenetics, Max Planck Institute for Multidisciplinary Sciences, Göttingen, Germany, [3]Department of Experimental Immunology, Amsterdam institute for Infection and Immunity, Amsterdam UMC, Amsterdam, The Netherlands, [4]Department of Neurology and Immunology, MS center ErasMS, ErasmusMC, Rotterdam, The Netherlands, [5]Department of Neuropathology, University Medical Center Göttingen, Göttingen, Germany, [6]Department of Axonal Signaling, Netherlands Institute for Neuroscience, Royal Netherlands Academy for Arts and Sciences, Amsterdam, The Netherlands, [7]Cell Biology, Neurobiology and Biophysics, Department of Biology, Faculty of Science, University of Utrecht, Utrecht, The Netherlands, [8]Swammerdam Institute for Life Sciences, University of Amsterdam, Amsterdam, The Netherlands

[*]authors contributed equally

*Ann Neurol. 2023 Apr; 93(4):856-870*

## ABSTRACT

Changes in the normal-appearing white matter (NAWM) in multiple sclerosis (MS) may contribute to disease progression. Here, we systematically quantified ultrastructural and subcellular characteristics of the axon–myelin unit in MS NAWM and determined how this correlates with low-grade inflammation. Human brain tissue obtained with short post-mortem delay and fixation at autopsy enables systematic quantification of ultrastructural characteristics. In this study, we performed high-resolution immunohistochemistry and quantitative transmission electron microscopy to study inflammation and ultrastructural characteristics of the axon–myelin unit in MS NAWM (n = 8) and control white matter (WM) in the optic nerve. In the MS NAWM, there were more activated and phagocytic microglia cells ($HLA^{+}P2RY12^{-}$ and $Iba1^{+}CD68^{+}$) and more T cells ($CD3^{+}$) compared to control WM, mainly located in the perivascular space. In MS NAWM compared to control WM, there were, as expected, longer paranodes and juxtaparanodes and larger overlap between paranodes and juxtaparanodes. There was less compact myelin wrapping, a lower g-ratio, and a higher frequency of axonal mitochondria. Changes in myelin and axonal mitochondrial frequency correlated positively with the number of active and phagocytic microglia and lymphocytes in the optic nerve. These data suggest that in MS NAWM myelin detachment and uncompact myelin wrapping occurs, potassium channels are unmasked at the nodes of Ranvier, and axonal energy demand is increased, or mitochondrial transport is stagnated, accompanied by increased presence of activated and phagocytic microglia and T cells. These subclinical alterations to the axon–myelin unit in MS NAWM may contribute to disease progression.

## INTRODUCTION

Multiple sclerosis (MS) is a chronic inflammatory disease of the central nervous system (CNS), with focal demyelinated lesions throughout [1,2]. In early as well as advanced progressive MS, lesions arise from the normal-appearing white matter (NAWM) and there is substantial inflammatory activity. Compared to control white matter, in MS, the NAWM is affected by astrogliosis, axonal loss, increased oxidized phospholipids, lesion-like microglial activation, and reorganization of the paranodes and juxtaparanodal domains [3–8].

Little yet is known about the axons and myelin at the subcellular level in NAWM in MS and how these correlate with inflammation. The myelin sheath, characterized by a multilamellar structure of multiple lipid–rich plasma membranes surrounding the axons, enables rapid impulse propagation, known as saltatory conduction [9]. In the CNS, myelin sheaths are formed by oligodendrocytes wrapping and compacting multiple layers of membranes around the axon that become flanked by nodes of Ranvier. Myelin thickness is typically correlated to the axon caliber [10]. In between the axon and the innermost myelin layer lies the inner tongue, where myelin membrane incorporation occurs [11,12], and the extracellular peri-axonal space, which together with the myelinic channels is important for axonal metabolic support [9,13]. These areas, which are possibly critical to MS pathology, are only visible at the ultrastructural level.

In experimental animal models for MS, detachment of myelin from the axon occurs in the NAWM and increases over time [14]. Biochemically altering the myelin structure in mice elicits a demyelinating inflammatory immune response [15], suggesting altered organization of myelin relates to inflammation causing demyelinating lesions. In MS NAWM, disorganization of the nodes of Ranvier and myelin blistering have been observed [5,16,17], and myelin from MS donors obtained from the NAWM is phagocytosed more efficiently than myelin obtained from control donors [18]. In the NAWM of MS donors, a disturbed lipid composition due to a metabolic defect causes an increase in phospholipids and decrease of sphingolipids [19] and deimination of the myelin basic protein (MBP) [20] have been modelled to result in an increased repulsive force between myelin sheaths [19,20].

Here, we have systematically applied immunohistochemical (IHC) and transmission electron microscopy (TEM) methods on human optic nerve tissue to quantitatively analyze the characteristics and components of the axon and the myelin in the NAWM in MS at the ultrastructural level. To examine early myelin pathology in MS and the association of immune cell activation, we systematically correlated MS innate and adaptive immune parameters with these

NAWM characteristics. We show that in MS optic nerve NAWM, ultrastructural characteristics of the axon-myelin unit are altered. There is a disorganization of the nodes of Ranvier and potassium channels are unmasked, the myelin is less compact, and there are more axonal mitochondria axonal, and this correlates with an increased number of activated and phagocytic microglia and T cells. Together, these sub-clinical alterations may contribute to disease progression in MS.

## METHODS

### Donors and sample collection

Post-mortem optic nerve tissue of n=8 MS donors and n=8 healthy control donors was provided by the Netherlands Brain Bank (NBB, Amsterdam, The Netherlands, www.brainbank.nl). All donors provided informed consent for brain autopsy and for the use of material and clinical data for research purposes in compliance with national ethics guidelines. MS pathology was confirmed by a certified neuropathologist.

At autopsy, if no optic nerve lesions were visible by eye, the optic nerve was dissected at 1-cm distance of the optic chiasm, and each optic nerve sample was cut longitudinally. One half of the tissue was either fixed in formalin and embedded in paraffin (n=8) or fixed for 24 hours in 4% paraformaldehyde and cryo-protected in 30% sucrose prior to freezing (n=8) for high resolution IHC, and the other half of the tissue was fixed in a phosphate buffer with 2.5% glutaraldehyde, 4% paraformaldehyde, and 0.5% NaCl (n=16) for TEM. Axons in the optic nerve are bundled and oriented in the same direction, which allows for the study of axons cut either longitudinally or transverse. All longitudinal and sagittal sections were checked for demyelinated and reactive sites, and donors were excluded when these were present. Thus, optic nerves studied were considered lesion-free (NA)WM.

For MS donors, clinical disability milestones during the disease course were scored following the Kurtze's Expanded Disability Status Scale (EDSS) and the age at onset and the total duration of disease from onset of first symptoms were described. Disease severity score was calculated as 5 – log (years to EDSS6 + 1). For each MS donor, the lesion load and reactive site load, proportion of active lesions, mixed active/inactive lesions, inactive lesions, and remyelinated lesions, and the microglia macrophage activity score (MMAS) score was calculated as previously described[1,2].

**Sample preparation**
For high resolution IHC, 20-µm thick cryo-protected sections were cut longitudinally with a cryostat and stored in phosphate buffered saline (PBS) + 0.1% sodium azide until use. For TEM, samples were treated and contrasted using a modified reduced osmium/tetroxide-thiocarbohydrazide/osmium protocol [21]. Semi-thin (500 nm) and ultra-thin (60 nm) sections were cut transversally with an ultramicrotome. The region of interest was guided by 1:1 methylene blue/Azure II staining of semi-thin sections for 1 minute. Ultra-thin sections were mounted on copper grids.

**Immunohistochemistry**
For validation of the NAWM of all samples, 8-µm sections of the paraffin-embedded samples were deparaffinized and rehydrated in a xylene and ethanol series and 20-µm cryoprotected sections of the frozen sample were washed in PBS. All primary antibodies and antigen retrieval methods can be found in **Table 1**.



Sections were incubated with 3% $H_2O_2$ in PBS + 0.5% TritonX for 10 minutes. Aspecific binding was blocked with blocking buffer (PBS + 10% normal horse serum (NHS) + 1% bovine serum albumin (BSA) + 0.5% TritonX) for 1 hour, and primary antibodies were incubated overnight at 4°C at dilutions indicated in **Table 1**. Appropriate biotinylated secondary antibodies were incubated for 1 hour 1:400 in blocking buffer and avidin-biotin-complex 1:800 in PBS was incubated for 45 minutes. For HLA, PLP, APP and SMI32, the staining was visualized with DAB, and sections were counterstained with hematoxylin for 30 seconds and dehydrated in ethanol and xylene series. For Kv1.2, biotinylated tyramide was incubated 1:10,000 for 10 minutes, and avidin-biotin-complex 1:800 was incubated for 45 minutes. For all stainings, conjugated fluorophores 1:800 were incubated for 1 hour. Nuclei were stained with Hoechst (1:1.000) for 10 minutes and Sudan Black 0.1% in 70% ethanol was incubated for 10 minutes.

**Table 1:** Antibodies

| Primary antibody | Company (Cat#) | Dilution | Antigen retrieval |
|---|---|---|---|
| HLA | DAKO (M077501-2) | Frozen: 1:500<br>FFPE: 1:100 | Frozen: -<br>FFPE: PBS, pH7.6, 10 min, 700 W |
| PLP | BioRad (MCA839G) | Frozen: 1:6,000<br>FFPE: 1:500 | Frozen: -<br>FFPE: PBS, pH7.6, 10 min, 700 W |
| Kim1P | Kindly gifted by Prof. Dr. Heinz-Joachim Radzun, Göttingen | 1:5,000 | Citrate buffer, pH6, 10 min, 700 W |
| APP | EMD Millipore (MAB348) | 1:2,000 | - |
| SMI32 | Covance (LN# E11HF01669) | 1:1,000 | - |
| P2RY12 | Kindly gifted by Dr. Chotima Böttcher, Charité Berlin | 1:1,500 | - |
| Iba1 | Wako (019-19741) | 1:750 | - |
| CD68 | DAKO (M0814) | 1:750 | - |
| CD3 | DAKO (A0452) | 1:100 | Citrate buffer, pH6, 30 min, 80°C |
| CD3 | Abcam (ab699) | 1:50 | - |
| Laminin | Sigma (L9393) | 1:100 | - |
| CASPR | Abcam (ab34151) | 1:200 | Citrate buffer, pH6, 3 hours, 60°C |
| Kv1.2 | Alomone (APC-010) | 1:100 | Citrate buffer, pH6, 3 hours, 60°C |
| Tomm20 | Abcam (ab186735) | 1:200 | Citrate buffer, pH6, 30 min, 80°C |
| CD19 | Biolegend (115501) | 1:100 | Citrate buffer, pH6, 30 min, 80°C |
| CD138 | BioRad (MCA2459T) | 1:100 | Citrate buffer, pH6, 30 min, 80°C |
| SMI312 | Biolegend (837901) | 1:750 | Citrate buffer, pH6, 30 min, 80°C |

*Abbreviations: FFPE = formalin fixed paraffin embedded, PBS = phosphate buffered saline*

### Quantification of immunohistochemistry

For quantification of markers of Wallerian degeneration, scans of the APP and SMI32 staining were made (Axio slide scanner, 20 x magnification) and images were analyzed with Qupath. Donors were marked for presence of $APP^+$ axonal

fragments. For SMI32, the whole tissue section was outlined and a threshold mask was used to quantify the percentage of the tissue positive for dark SMI32 staining. For microglia activity and lymphocyte presence, scans were made of the optic nerve (Axio slide scanner, 20 x magnification). In Qupath, the whole tissue section was outlined, regions with aspecific staining were excluded, and the area of the tissue was measured. For microglia quantification in Qupath, the cell profiler was run on the DAPI signal, cell classifiers were created of the Iba1, CD68, P2RY12, TMEM119, and HLA signal, and composites were created to quantify the number of single or double positives. Distribution of microglia was assessed. For lymphocyte quantification, the number of $CD3^+$ T and $CD19^+$ B cells were counted. All measurements were normalized on the size of the tissue. For $CD3^+$ T cells, percentage of T cells localized in the perivascular space or parenchyma was assessed with laminin.



Quantification of the nodes of Ranvier was performed in ImageJ. The length of 345 control nodes and 257 MS nodes was measured, the length of 974 control paranodes and 692 MS paranodes were measured, and for the juxtaparanodes, the length and percentage of the paranode overlapping the juxtaparanodes were quantified of 82 control juxtaparanodes and 81 MS juxtaparanodes.

Mitochondria and axons were imaged in 3-6 regions of interest per donor at 100 x with the STED microscope (STEDYCON, Abberior Instruments GmbH, Göttingen, Germany). Images were analyzed on Imaris (v. 9.7, Bitplane AG, Zürich, Switzerland). In Imaris, the mitochondria and axons were reconstructed, and a filter removed all mitochondria that did not lie within the axon. The number of axonal mitochondria were measured, and the surface area of the axons and size of axonal mitochondria were measured. The frequency of mitochondria was calculated by calculating the number of mitochondria per $\mu m^2$ axon.

**Transmission electron microscopy**

Images were acquired at 5,000 x and 30,000 x magnification at random regions of interest (ROIs) with a transmission electron microscope (LEO EM912 Omega, Carl Zeiss Microscopy GmbH, Oberkochen, Germany) equipped with a dual speed, wide-angle 2K-CCD camera (TRS, Moorenweis, Germany) using iTEM (Olympus, Tokyo, Japan) and digitally edited with ImageJ version 2.1.0 [22].

Per donor, 119-268 myelinated axons were analyzed at 5,000 x magnification using a grid for unbiased quantification to characterize the g-ratio, myelin density, axon caliber, and inner tongue area. The diameter of the axon, the inner tongue, and the myelin sheath were calculated based on the area. The g-ratio was calculated by dividing the diameter of the axon with the diameter of the myelin sheath corrected for the inner tongue [11]. The myelin density was

calculated with a positive pixel classifier in QuPath [23]. Per donor, in six randomly selected images at 5,000 x magnification, the number of myelinated axons were counted and the number of myelinoid bodies, outfoldings, and mitochondria per axon was calculated. Additionally, of axons with visible mitochondria the percentage of the axon covered by the area of the mitochondria was calculated. Of 16-30 axons per donor, the peri-axonal space was measured at 30,000 x magnification. For the MS donors, the ultrastructural characteristics were correlated with the clinical and pathological MS characteristics.

**Statistical analysis**

Considering the small group size, correlations between continuous averages per donor were tested with Spearman correlation coefficient. Differences in donor demographics and averages of ultrastructural characteristics were tested between groups with a two-sided Student's T-test. If multiple measurements were made per donor for IHC or TEM characteristics, these were tested with a linear mixed-effect model correcting for within-donor measurements. All statistics were performed in RStudio Desktop (version 1.2.5033, Rstudio, Inc., Boston, MA, USA), using key packages ggplot2, lme4, car, plyr, ggpubr, and corrplot. P-values $<0.05$ were considered significant.

## RESULTS

**Donor demographics**

Donors with demyelination of the optic nerve or with reactive sites cwere excluded from the study, resulting in a cohort of n=8 control donors and n=8 MS donors. Microglia nodules were seen in both groups (**Fig. 1A-C**) and were avoided for quantification of ultrastructural characteristics. 6 control donors and 3 MS donors had cataract or macular degeneration and one MS donor had a prior history of optic neuritis in the contralateral optic nerve. As assessed with APP and SMI32, there was a comparable prevalence of Wallerian degeneration in controls compared to MS (**Fig. 1D-H**). Demographics and characteristics for disease severity and pathology of the MS donors are summarized in **Table 2**. In the IHC dataset, the groups were matched for age, post-mortem delay (PMD) and pH of the CSF, however there were significantly more control females than females with MS (CON: 100%, MS: 25%, p=0.03). In the TEM dataset MS donors were significantly younger than the control donors (CON: 85.88 ± 6.38 years, MS: 70.13 ± 7.22 years, p=4.1e-4) and there were less females with MS than control females (CON: 100% female, MS: 50% female, p=0.02). The cause of death of control donors was cancer (n=3), old age (n=1), infection (n=1), heart failure (n=1), palliative sedation (n=1) or euthanasia (n=1). The cause of death

of MS donors was infection (n=3), euthanasia (n=3), palliative sedation (n=1) or respiratory insufficiency (n=1).

**Table 2:** Donor demographics and characteristics of MS severity and pathology

| | IHC | | | TEM | | |
|---|---|---|---|---|---|---|
| | **CON (n=4)** | **MS (n=4)** | **p-value** | **CON (n=8)** | **MS (n=8)** | **p-value** |
| Age in years (SD) | 87.50 (7.94) | 72.25 (10.24) | n.s. | 85.88 (6.38) | 70.13 (7.22) | 4.1e-4 |
| Sex (F%) | 100% | 25% | 0.03 | 100% | 50% | 0.02 |
| PMD in hours (SD) | 6:41 (1:50) | 6:36 (1:37) | n.s. | 7:12 (1:34) | 6:59 (1:39) | n.s. |
| pH of CSF (SD) | 6.57 (0.21) | 6.60 (0.28) | n.s. | 6.58 (0.19) | 6.57 (0.26) | n.s. |
| Age at onset (SD) | - | 39.25 (13.45) | - | - | 37.38 (11.11) | - |
| DOD (SD) | - | 33.25 (11.15) | - | - | 32.88 (9.88) | - |
| Severity score (SD) | - | 2.35 (1.56) | - | - | 3.05 (1.28) | - |

*Abbreviations: CSF = cerebrospinal fluid, DOD = duration of disease, IHC = immunohistochemistry, PMD = post-mortem delay, SD = standard deviation, TEM = transmission electron microscopy. P-values calculated with unpaired two-sided T-test.*

## More active microglia and lymphocytes in MS NAWM

To determine activity of microglia of the NAWM of MS and control donors, the optic nerve was quantified for microglia activity as assessed with P2RY12/HLA and iba1/CD68. Lymphocyte presence was quantified with CD3, CD19, and CD138 staining. In MS compared to controls, there were similar numbers of microglia (Iba1$^+$CD68) and there were more activated, phagocytic microglia (Iba1$^+$CD68$^+$, CON: 234.55 ± 22.91 cells/mm$^2$, MS: 340.06 ± 45.65 cells/mm$^2$, p=0.01). Furthermore, there was a comparable number of homeostatic microglia (P2RY12$^+$HLA$^-$) and partially activated microglia (P2RY12$^+$HLA$^+$). Interestingly, there were more activated microglia (P2RY12$^-$HLA$^+$, CON: 257.06 ± 35.32 cells/mm$^2$, MS: 486.61 ± 133.11 cells/mm$^2$, p=0.04), despite the higher age of control patients. The microglia activity was homogeneously distributed throughout the optic nerve tissue. In MS compared to controls, there were more CD3$^+$ T cells (CON: 14.45 ± 2.23 cells/mm$^2$, MS: 29.70 ± 8.76 cells/mm$^2$, p=0.04). No cuffing, defined as more than one ring of perivascular CD3+ T cells [24], was observed in the tissue. As assessed with laminin, an equal percentage of the CD3$^+$ T cells were localized in the parenchyma in MS compared to controls (CON: 7.82%, MS: 11.57%) (**Fig. 1I-S**). Only 1 MS donor showed the presence of CD19$^+$ B cells

(data not shown). Thus, consistent with previous findings [25–27], the NAWM in MS is characterized by substantial activated immune cell infiltration and activated resident immune cells.

### Elongation and unmasking of ion channels at nodes of Ranvier in MS NAWM

With high resolution IHC, the organization of the nodes (75 per donor), paranodes (208 per donor), and juxtaparanodes (20 per donor) was quantified (illustration at **Fig. 2A**). Representative images of nodes and paranodes are visualized in **Fig. 2B**. In MS compared to controls, the length of the nodes was not different however the length of CASPR1 was longer (CON: 3.36 **± 0.52** µm, MS: **0.94 ±** 4.51 µm, p=0.03, **Fig. 2C-D**). A representative image of a non-overlapping paranode and juxtaparanode is shown in **Fig. 2E** with the corresponding intensity graph in **Fig. 2F**, and a largely overlapping paranode and juxtaparanode is visualized in **Fig. 2G** with the corresponding intensity graph in **Fig. 2H**. In MS compared to controls, the Kv1.2 ion channel-positive area was significantly longer (CON: 4.74 **± 0.52** µm, MS: 6.12 **± 1.11** µm, p=0.01), and the percentage of CASPR1-positive area overlapping with Kv1.2 staining is larger (CON: 34.50% **± %2.23**, MS: 49.30% **± %6.29**, p=7.12e-5, **Fig. 2I-J**). Thus, similar to others [5,17], here we showed that the nodes of Ranvier are disorganized as there is elongation of the paranodes and juxtaparanodes and increased overlap between the paranodal and juxtaparanodal regions.

**Figure 1: Inflammation occurring in the NAWM (p63). (A)** Luxol Fast Blue, **(B)** PLP, and **(C)** Kim1p stainings of the optic nerve shows no demyelination or reactive sites, besides from some nodules, with a scale bar of 400 nm. **(D)** $APP^+$ axonal fragments **(E)** were found in both control and MS tissue. **(F)** $SMI32^+$ axons were observed in both control as **(G)** MS tissue, and **(H)** the percentage of tissue that was $SMI32^+$ was comparable in control and MS tissue. **(I)** Iba1 (in green) and CD68 (in yellow) staining of a control optic nerve with an enlarged panel with an arrow pointing to an $Iba1^+CD68^-$ cell. **(J)** Iba1 (in green) and CD68 (in yellow) staining of an MS optic nerve with an enlarged panel with an arrow pointing to an $Iba1^+CD68^+$ cell. **(K)** In MS compared to controls, there are an equal amount of $Iba1^+$ microglia/$mm^2$ and more $Iba1^+CD68^+$ microglia/$mm^2$ (p=0.01). (**L**) HLA (in green) and P2RY12 (in yellow) staining of control optic nerve with two enlarged panels, with in the first panel an arrow pointing to a $P2RY12^+HLA^-$ cell and in the second panel an arrow pointing to a $P2RY12^+HLA^+$ cell. **(M)** HLA (in green) and P2RY12 (in yellow) staining of MS optic nerve with two enlarged panels, in the first panel an arrow pointing to a $P2RY12^+HLA^+$ cell and in the second panel an arrow pointing to a $P2RY12^-HLA^+$. **(N)** In MS compared to controls, there are equal numbers of $P2RY12^+HLA^-$ and $P2RY12^+HLA^+$ microglia/$mm^2$ and more $P2RY12^-HLA^+$ microglia/$mm^2$ (p=0.04). **(O)** CD3 (in yellow) staining of control optic nerve and **(P)** CD3 (in yellow) staining of MS optic nerve with arrows pointing to $CD3^+$ T cells. **(Q)** In MS compared to controls, there are more $CD3^+$ T cells/$mm^2$ (p=0.04). **(R)** As assessed with laminin (in green), $CD3^+$ T cells (in yellow) were found both in the perivascular space as well as in the parenchyma, and **(S)** the percentage of $CD3^+$ T cells in the parenchyma was similar in MS compared to controls.

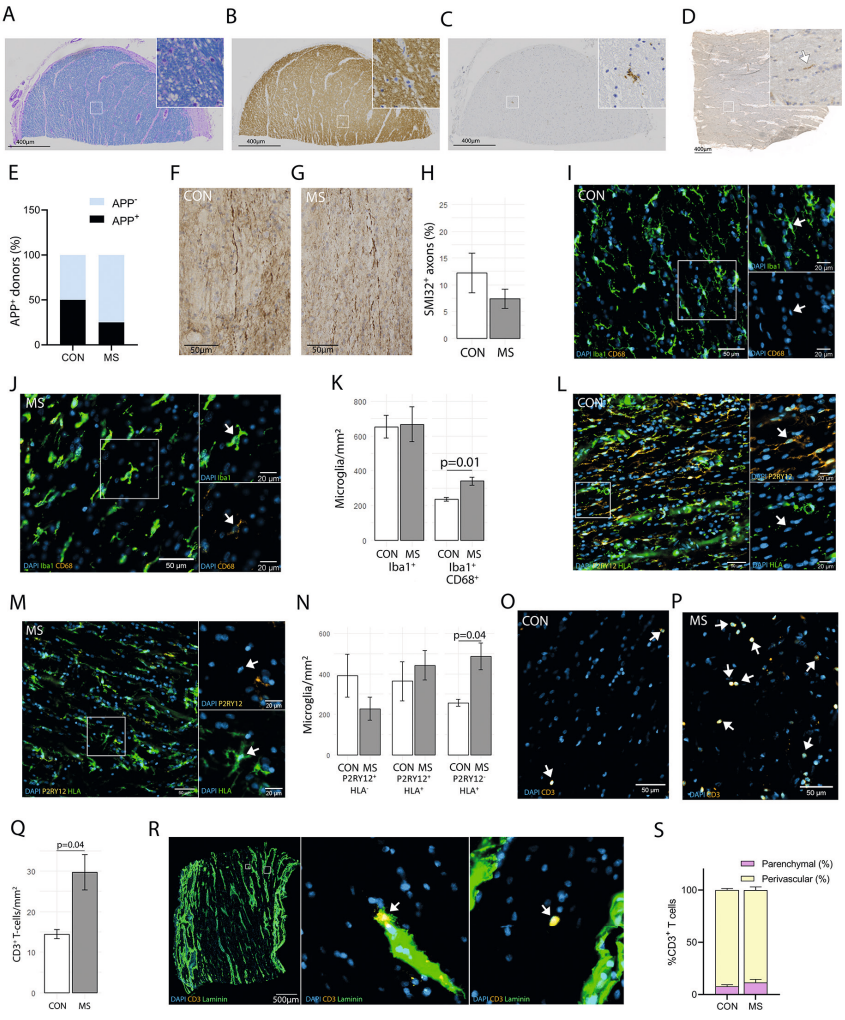
A
B
C
D
E
APP⁻
APP⁺
APP⁺ donors (%)
150
100
50
0
CON
MS
F
CON
50µm
G
MS
50µm
H
SMI32⁺ axons (%)
25
20
15
10
5
0
CON
MS
I
CON
DAPI Iba1 CD68
DAPI Iba1
DAPI CD68
20 µm
50 µm
J
MS
DAPI Iba1 CD68
DAPI Iba1
DAPI CD68
20 µm
50 µm
K
Microglia/mm²
800
600
400
200
0
p=0.01
CON MS
Iba1⁺
CON MS
Iba1⁺ CD68⁺
L
CON
DAPI P2RY12
DAPI HLA
20 µm
M
MS
DAPI P2RY12 HLA
DAPI P2RY12
DAPI HLA
20 µm
N
Microglia/mm²
600
400
200
0
p=0.04
CON MS
P2RY12⁺ HLA⁻
CON MS
P2RY12⁺ HLA⁺
CON MS
P2RY12⁻ HLA⁺
O
CON
DAPI CD3
50 µm
P
MS
DAPI CD3
50 µm
Q
p=0.04
CD3⁺T-cells/mm²
30
20
10
0
CON
MS
R
DAPI CD3 Laminin
500µm
DAPI CD3 Laminin
DAPI CD3 Laminin
S
Parenchymal (%)
Perivascular (%)
%CD3⁺ T cells
100
50
0
CON
MS

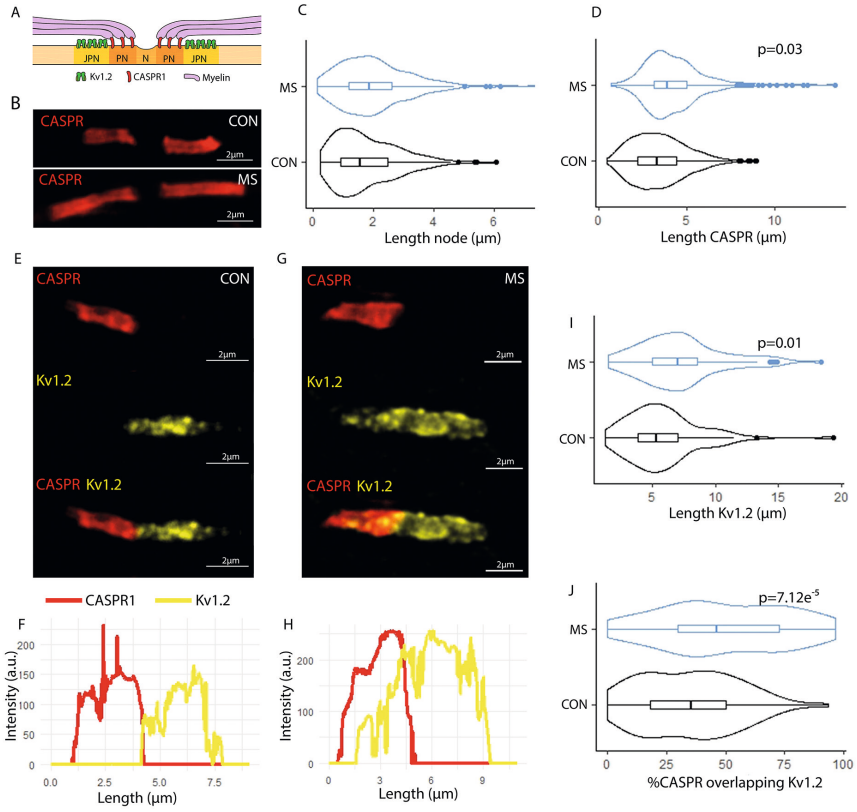


**Figure 2: Altered length and distribution of ion channels at the nodes of Ranvier. (A)** Illustrative image of nodal, paranodal, and juxtaparanodal area. (**B**) Control paranode (CASPR1) and MS paranode. **(C)** In MS, the length of the nodes is comparable to controls, and **(D)** the paranodes (CASPR1) are longer (p=0.03). (**E**) Control juxtaparanode (Kv1.2, yellow) and paranode (CASPR1, red) not overlapping, with (**F**) intensity plot. (**G**) MS juxtaparanode (Kv1.2, yellow) and paranode (CASPR1, red) with high overlap, with (**H**) intensity plot. In MS compared to controls, (**I**) the juxtaparanodes (Kv1.2) are longer (p=0.01) with (**J**) a higher percentage of overlap of paranodes (CASPR1) with juxtaparanodes (Kv1.2) (p=7.12e-5).

## Correlation between ultrastructural characteristics in MS NAWM

In **Fig. 3A-C**, representative TEM images are shown. All Spearman correlations between ultrastructural characteristics and age, post-mortem delay (PMD), and pH are visualized in **Fig. 3D**, with significant p-values indicated in text and correlation coefficients indicated in a color scale. The g-ratio, axon caliber, inner tongue area, axonal density, number of outfoldings, number of myelinoid bodies, coverage of the axon by mitochondria, mitochondria frequency, and peri-axonal space were not correlated to age, PMD, and pH of the CSF, and there were no sex differences. The axon caliber was positively correlated to the

g-ratio (**Fig. 3E**, p=0.01, r=0.63), the inner tongue area (p=0.02, r=0.57), and the number of outfoldings (p=2.5e-3, r=0.70). The axon caliber was negatively correlated to the axonal density (**Fig. 3F**, p=6.9e-5, r=-0.83) and the coverage of the axon by mitochondria (p=0.02, r=-0.56). The axonal density was negatively correlated with the number of outfoldings (p=0.01, r=-0.65) and positively correlated with the coverage of the axon by mitochondria (p=0.01, r=0.63).

**Ultrastructural alterations of the myelin in MS NAWM**

The ultrastructural characteristics based on 119-268 myelinated axons per donor, or 16-30 myelinated axons per donor for the peri-axonal space, were quantified with TEM and compared between MS and controls. The axon caliber was not different in MS NAWM compared to control WM (**Fig. 4A**). In MS NAWM, there was a significantly lower g-ratio compared to controls (CON: 0.53 **± 0.03**, MS: 0.50 **± 0.04**, p=0.03) and a lower myelin density (CON: 95.43% **± %1.47**, MS: 92.43% **± %3.01**, p=0.01) (**Fig. 4B-C**). The inner tongue area and peri-axonal space were not different in MS NAWM compared to control WM (**Fig. 4D-E**). The number of myelinoid bodies, axonal density, and the number of outfoldings were not different between MS and controls (**Fig. 4F-H**). Therefore, there are ultrastructural myelin alterations in MS as the myelin is less compact in MS NAWM compared to control WM.

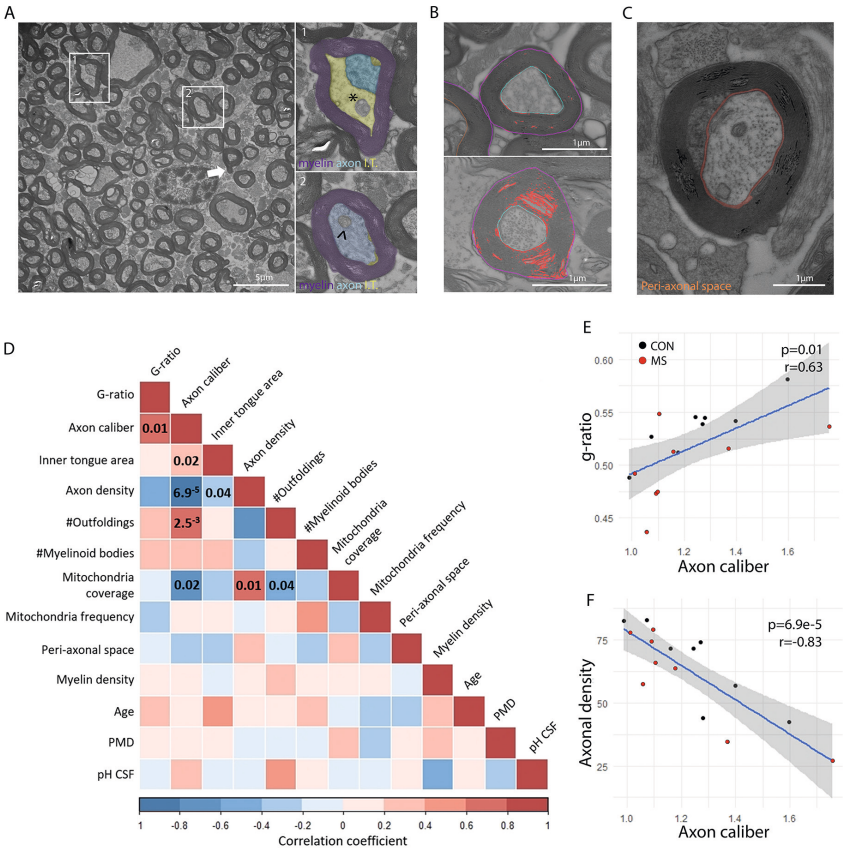


**Figure 3: Quantification of ultrastructural characterization of the NAWM in the optic nerve .** (**A**) TEM image of an MS optic nerve at 5,000 x with indicated a myelin outfolding indicated with a white arrow, axons in blue, inner tongues in yellow, myelin in purple, a myelinoid body with an asterisk, and a mitochondria indicated with an arrowhead. (**B**) Representative image of 5,000 x TEM image showing quantification of myelin density with the top panel showing a control myelin ring with high density and the lower panel showing MS myelin with low density. **(C)** Transmission electron microscope image at 30,000 x with the peri-axonal space in orange. (**D**) Correlation matrix of Spearman's correlations of ultrastructural characteristics measured with the TEM and donor demographics, showing that the axon calibre correlates positively to the g-ratio, the inner tongue area, and the number of outfoldings and negatively to the axon density. The axon density correlates negatively to the inner tongue area and the number of outfoldings and positively to the mitochondrial coverage of the axon. The number of outfoldings correlates negatively to the mitochondrial coverage of the axon. (**D**) The axon calibre correlates positively to the g-ratio (p=0.009, r=0.63) and (**E**) negatively to the axonal density (p=6.9e-5, r=-0.83).

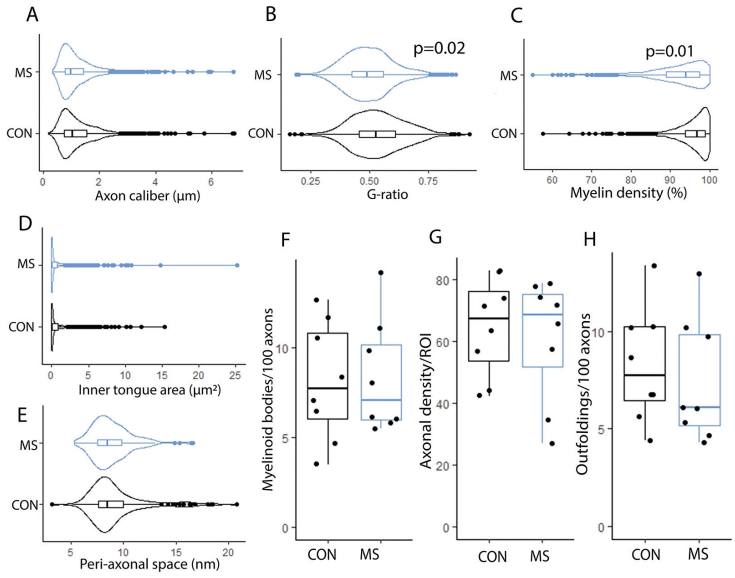


**Figure 4: Less compact myelin wrapping in MS NAWM.** In MS compared to controls, (**A**) the axon calibre was similar, (**B**) the g-ratio was smaller (p=0.02), (**C**) the myelin density was smaller (p=0.01), (**D**) the inner tongue area was similar, and (**E**) the peri-axonal space was similar. There were no differences between MS and controls in (**F**) amount of myelinoid bodies, (**G**) the axonal density, or (**H**) the amount of outfoldings.

## Increase of axonal mitochondria in MS NAWM

To fully appreciate the 3-dimentional (3D) shape of mitochondria, their frequency and size were studied with both TEM and high resolution IHC. As assessed with EM, in MS a higher percentage of axons containing mitochondria was visible (CON: 18.41% **± %5.68**, MS: 23.68% **± %3.72**, p<0.05), however in axons containing mitochondria the percentage mitochondrial coverage of the axons was not different between MS and controls (**Fig. 5A-C**). High resolution immunohistochemical stainings of axonal mitochondria were reconstructed in Imaris as visualized in **Fig. 5D**. Compared to healthy control WM, in MS axons in the NAWM contained more mitochondria (CON: 0.05 **± 0.01**, MS: 0.09 **± 0.01**, p=1.5e-4), however the surface area of the mitochondria was not different (**Fig. 5E-F**). This implies a higher axonal energy demand or a stagnated mitochondrial transport in MS NAWM compared to control WM.

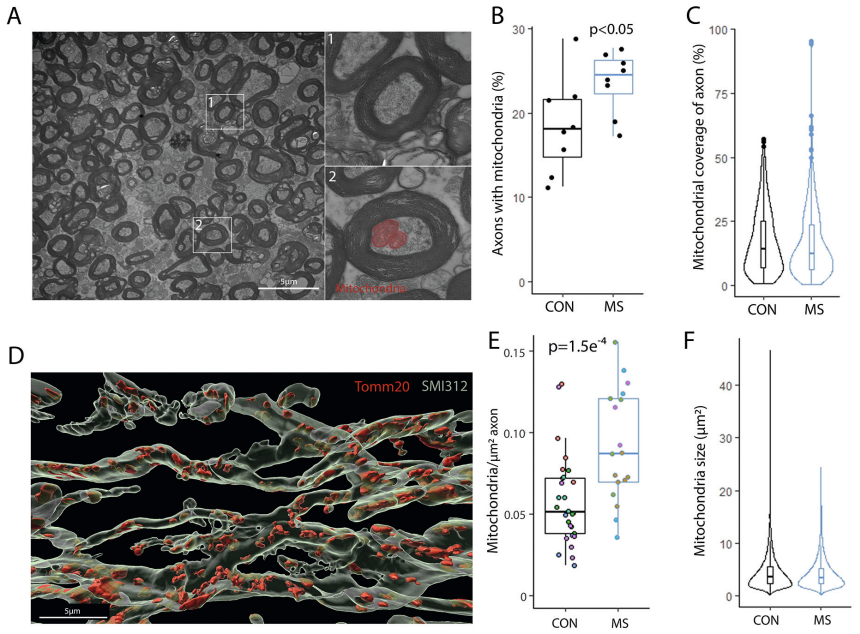


**Figure 5: Increased number of axonal mitochondria in MS NAWM.** (**A**) TEM image taken at 5,000 x with two enlarged panels, the top showing an axon with no mitochondria visible, the bottom showing an axon with mitochondria visible, shown in red. **(B)** In MS compared to controls, more axons contained mitochondria, and the **(C)** percentage of mitochondrial coverage of the axon was similar. **(D)** Reconstructed 3-D axons (SMI312 in green) and mitochondria (Tomm20 in red) of an MS donor. (**E**) In MS compared to controls, the mitochondria frequency was higher (p=1.5e-4) and **(F)** the surface area of the mitochondria is similar.

## Ultrastructural abnormalities correlate with microglia activity markers and T cell number

Ultrastructural characteristics as measured with TEM and IHC that were significantly different in MS compared to controls were tested for correlation with microglia activity and lymphocyte presence as visualized in **Fig. 6**. The g-ratio was near-significantly negatively correlated to the number of $P2RY12^{-}HLA^{+}$ activated microglia and the number of $CD3^{+}$ T cells (p=0.071, r=-0.67; p=0.071, r=-0.67) and was not correlated to the number of $Iba1^{+}CD68^{+}$ phagocytic microglia (p=0.120, r=-0.56, data not shown). The myelin density was negatively correlated to the number of $P2RY12^{-}HLA^{+}$ activated microglia (p=0.001, r=-0.93), the number of $Iba1^{+}CD68^{+}$ phagocytic microglia (p=0.007, r=-0.86) and the number of $CD3^{+}$ T cells (p=0.047, r=-0.74) (**Fig. 6A-C**). The axonal mitochondria frequency was positively correlated to the number of $P2RY12^{-}HLA^{+}$ activated microglia (p=0.015, r=0.81) and the number of $Iba1^{+}CD68^{+}$ phagocytic

microglia (p=0.047, r=0.71) (**Fig. 6D-E**), and was not correlated to the number of $CD3^+$ T cells. The paranode length was not correlated to the number of $P2RY12^-HLA^+$ activated microglia or the number of $Iba1^+CD68^+$ phagocytic microglia and was positively correlated to the number of $CD3^+$ T cells (p=0.015, r=0.81 (**Fig. 6F**). The juxtaparanode length was positively correlated to the number of $P2RY12^-HLA^+$ activated microglia (p=0.021, r=0.79) (**Fig. 6G**), was approaching a positive correlation to the number of $Iba1^+CD68^+$ phagocytic microglia (data not shown, p=0.058, r=0.69), and was positively correlated to the number of $CD3^+$ T cells (p=0.015, r=0.81) (**Fig. 6H**). The percentage overlap between the paranodes and juxtaparanodes was positively correlated to the number of $P2RY12^-HLA^+$ activated microglia (p=0.021, r=0.79), the number of $Iba1^+CD68^+$ phagocytic microglia (p=0.015, r=0.81) and the number of $CD3^+$ T cells (p=0.015, r=0.81) (**Fig. 6I-K**).

The g-ratio, myelin density, axonal mitochondria frequency, length of CASPR1, length of Kv1.2, and percentage overlap of CASPR1 with Kv1.2 were not correlated to the lesion load, MMAS score, severity score nor the percentage of $SMI32^+$ axons (data not shown).

## DISCUSSION

Here, we present the first systematic quantification of ultrastructural characteristics of the NAWM of control and MS donors using TEM and high-resolution IHC. In the NAWM of the optic nerve in MS compared to controls, we found an elongation of the paranodes and juxtaparanodes and an increased overlap of paranodes and juxtaparanodes, causing unmasking of the potassium channels, similar to previous findings in subcortical NAWM [5,17]. We further observed that the g-ratio is lower and that myelin is less compact, and that there is a higher frequency of mitochondria. The characteristics that are altered in MS are furthermore correlated positively with the number of active ($P2RY12^-HLA^+$) and phagocytic ($Iba1^+CD68^+$) microglia and the number of $CD3^+$ T cells present in the tissue. The loss of microglia homeostasis and presence of lymphocytes may be causal to alterations in the axon-myelin unit that could lead to more axonal mitochondria and possibly subsequently more free radicals that can oxidize the lipids, making the myelin more prone to phagocytosis and therefore predisposing the tissue for lesion formation.

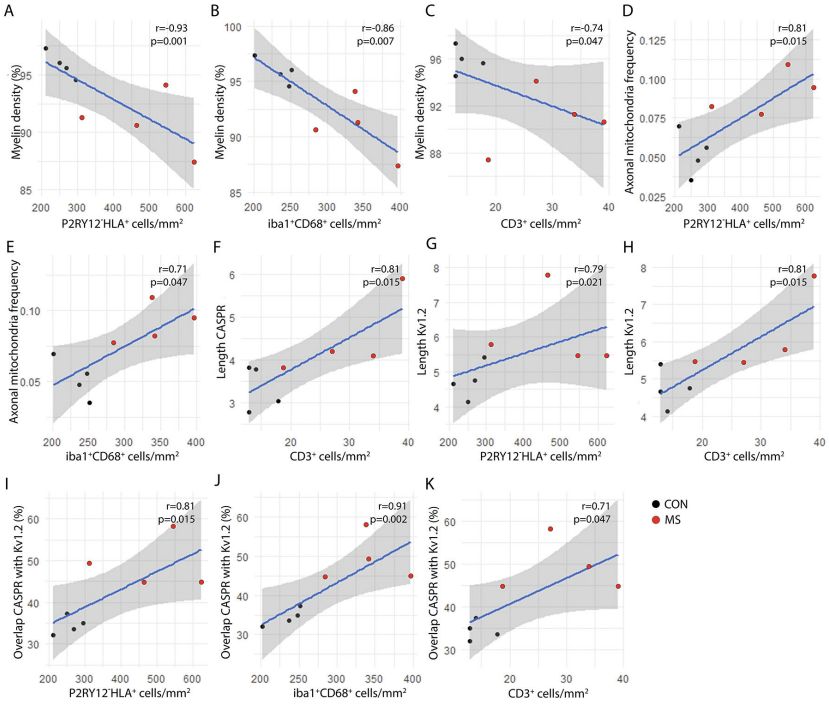


**Figure 6: Ultrastructural alterations are correlated to number of active and phagocytic microglia and number of T cells.** Spearman correlation tests of ultrastructural alterations and the number of activated microglia, phagocytic microglia and T cells. (**A**) Myelin density negatively correlated to the number of P2RY12$^-$HLA$^+$ cells/mm$^2$ (p=0.001, r=-0.93), (**B**) the number of Iba1$^+$CD68$^+$ cells/mm$^2$ (p=0.007, r=-0.86) and (**C**) the number of CD3$^+$ T cells/mm$^2$ (p=0.047, r=-0.74). Axonal mitochondria frequency positively correlated to (**D**) the number of P2RY12$^-$HLA$^+$ cells/mm$^2$ (p=0.015, r=0.81) and (**E**) the number of Iba1$^+$CD68$^+$ cells/mm$^2$ (p=0.047, r=0.71). CASPR1 length positively correlated to (**F**) the number of CD3$^+$ T cells/mm$^2$ (p=0.021, r=0.79). Kv1.2 length positively correlated to (**G**) the number of P2RY12$^-$HLA$^+$ cells/mm$^2$ (p=0.021, r=0.79) and (**H**) the number of CD3$^+$ T cells/mm$^2$ (p=0.015, r=0.81). The percentage overlap of CASPR1 with Kv1.2 positively correlated to (**I**) the number of P2RY12$^-$HLA$^+$ cells/mm$^2$ (p=0.015, r=0.81), (**J**) the number of Iba1$^+$CD68$^+$ cells/mm$^2$ (p=0.002, r=0.91) and (**K**) the number of CD3$^+$ T cells/mm$^2$ (p=0.047, r=0.71).

Ultrastructural and immunohistochemical characteristics of the NAWM were not confounded by donor demographics nor were they correlated with MS pathology throughout the CNS. Though the MS and control group differed in age and sex, no correlation between age and the data was found nor were there any sex-related differences in the data. In MS and control donors there was a similar prevalence of Wallerian degeneration and the percentage of SMI32$^+$ axons was not correlated to the data. Therefore, the data were not affected by Wallerian degeneration. Sampling bias was minimized by random selection of ROIs and using a grid for TEM axon analysis. Due to methodological

challenges of performing TEM on human tissue, not much yet is known about the ultrastructural characteristics of human WM. Here, potentially due to the short post-mortem delay and direct fixation at autopsy, tissue was well preserved enabling systematical quantification of ultrastructural characteristics. For ultrastructural characteristics quantified with IHC, all stainings were tripled with microglia staining to ensure exclusion of regions with small clusters of microglia as local pro-inflammatory sites may skew the data. Donors with macroscopically visible lesions in the optic nerve during autopsy and donors with focal lesion pathology in the sampled area of the optic nerve, as assessed with Kim1P, PLP, Bielschowsky, and Luxol Fast Blue staining, were excluded. Of the included donors, one MS donor had a history of optic neuritis in the opposing optic nerve, some control and some MS donors had cataract or macular degeneration, and no other donors had mentioning of optic neuritis in their clinical files.



In line with previous studies on subcortical WM on the nodes of Ranvier, in MS the length of the node was similar between MS and controls and in MS the paranode as well as the juxtaparanode were longer compared to controls, with a larger overlap of the paranode and the juxtaparanode [5,17,28–30]. We and others show that the extent of abnormalities at the nodes of Ranvier in the NAWM is correlated to the degree of microglial activation [30], and previously, it was shown that these alterations can be provoked *in vitro* by pro-inflammatory cytokines [5]. The unmasking of potassium channels may contribute to altered electrical properties of the axons [31] and altered potassium release can modulate microglia-node interactions [28].

In line with previous electron microscopy studies on non-human tissue [11,32,33], the axon caliber was positively correlated with the g-ratio, indicating that the myelin diameter corrected for the inner tongue is relative to the axonal diameter. Surprisingly, in MS, we found a smaller g-ratio compared to controls. As we found no difference in axon caliber, inner tongue area, or peri-axonal space between MS and controls, the altered g-ratio in MS can most likely be attributed to changes in the myelin itself. As the myelin density of MS donors is lower compared to control donors, it is likely that the smaller g-ratio in MS is due to less compact wrapping of the myelin. Previously, larger g-ratios were found in the normal-appearing grey matter of MS donors compared to controls, which was attributed to extensive remyelination [34]. Indeed, we did not observe remyelination in the NAWM of the optic nerves and the NAWM in MS seems to be affected pathologically different compared to the normal appearing grey matter. Moreover, an abnormal sphingolipid metabolism was found in MS NAWM [35–37], perhaps mediated by pro-inflammatory cytokines [38], and the increased lipid peroxidation products 4-HNE modified lysine and histidine

as well as deimination of myelin basic protein were modeled to result in an increase in the repulsive force between myelin layers, leading to decompaction of the myelin structure [19,20]. This altered sphingolipid metabolism may be the mechanism underlying the lower g-ratio and lower myelin compactness in MS that we have shown here. Myelin isolated from the NAWM was previously shown to be more efficiently phagocytosed by primary human microglia than control myelin [18], indicating that alterations in the myelin may predispose MS myelin for phagocytosis. We speculate that the less compact wrapping of the myelin, the detachment of the myelin at the paranode, and the unmasking of the potassium channels may underly a higher axonal energy demand.

Interestingly, in MS compared to controls, axons contained a higher number of mitochondria with comparable surface area, which was shown with TEM and as well as with 3D IHC. This implies that there is a higher energy demand of the axon in MS than controls or that the transport of mitochondria along the axon has stagnated, perhaps due to nodal pathology [5,30]. Although most mitochondria in axons are stationary, they will rapidly redistribute to sites of pathological stress [39]. During metabolic or environmental stress of a cell, mitochondrial fusion and fission help mitigate stress, create new mitochondria, and enable removal of damaged mitochondria [40]. If mitochondrial fragmentation occurs while surface area remains constant, this can result in a higher concentration of calcium, resulting in higher mitochondrial activity and more ATP production [41]. This improved calcium buffering capacity may provide a neuroprotective opportunity [42,43], however this could additionally lead to an increase of free radicals which, when in pathological amounts, can cause damage to the mitochondria itself and to the tissue surrounding it [44]. These radicals are additionally produced in large amounts by activated microglia, and mitochondrial injury is considered a key element of neurodegeneration in MS [45].

In line with previous studies in the NAWM of MS, there was a higher number of activated microglia ($P2RY12^{-}HLA^{+}$), phagocytic microglia ($Iba1^{+}CD68^{+}$) and $CD3^{+}$ T cells per square millimeter tissue compared to controls [25,27,46]. The percentage of parenchymal $CD3^{+}$ T cells was similar in controls and MS, which is in line with the localization of subcortical (NA)WM T cells [26]. The number of active and phagocytic microglia and $CD3^{+}$ T cells were accordingly correlated to ultrastructural characteristics of the NAWM in the same direction as these characteristics were affected in MS compared to controls. Previous studies have shown that pro-inflammatory cytokines that can be produced by these immune cells *in vitro* lead to elongation and disorganization of the nodes of Ranvier, and the extent of *ex vivo* lipid metabolism defect in MS is related to evidence of monocyte infiltrates [5,19]. As ultrastructural characteristics were not correlated to characteristics of MS pathology in the CNS of the donors, it is

likely that the abnormalities seen here in the NAWM of the optic nerve in MS are driven by pro-inflammatory cytokines produced by lymphocytes and active and phagocytic microglia rather than by Wallerian degeneration. However, it is also possible that ultrastructural abnormalities could lead to increased immune activity, therefore future research is necessary to elucidate any causalities. It should be noted that we cannot exclude the presence of lesions in tissue distally in the optic nerve, nor can we exclude the possibility that the smaller group size reduced the power thus far that no correlations could be found between ultrastructural characteristics and MS pathology or the severity score. It is likely that in MS at local inflammatory sites in the NAWM, such as microglia nodules or inflamed vessels, more ultrastructural axonal characteristics will be altered, and the interaction of immune cells and the axon-myelin unit may also be of importance. Future research should shed light on this.



Taken together, our data show ultrastructural changes in the NAWM of MS at the levels of the myelin and axon including a less compact myelin composition, disorganization of the nodes of Ranvier and increased axonal mitochondria frequency in progressive MS. Moreover, the changes correlated with chronic inflammation throughout the CNS. These changes may contribute to further MS progression.

**Data availability**

All images are stored at Groningen database (Nanotamy):
http://www.nanotomy.org/OA/vandenBosch2023ANA/index.html

**Acknowledgements**

We are grateful to the brain donors and their families for their commitment to the Netherlands Brain Bank donor program. We thank Houson Li (University of Göttingen), Jeen Engelenburg, Marlijn van der Poel, and Manon Vincenten (Netherlands institute for Neuroscience) for their intellectual input and technical help.

**Funding**

Funding for this research was obtained from MS Research grants 17-975 and 19-1079 (MoveS inspiration Grant), Vici grant 865.17.003 from the Netherlands Research Council (NWO), the ERC (MyeliNANO), and the Adelson Medical Research Foundation (AMRF).

**Potential conflicts of interest**

The authors have no conflicts of interest to declare

## REFERENCES


1. Kuhlmann, T. *et al.* An updated histological classification system for multiple sclerosis lesions. *Acta Neuropathol.* 133, 13–24 (2017).
2. Luchetti, S. *et al.* Progressive multiple sclerosis patients show substantial lesion activity that correlates with clinical disease severity and sex: a retrospective autopsy cohort analysis. *Acta Neuropathol.* 135, 511–528 (2018).
3. Allen, I. V. & McKeown, S. R. A histological, histochemical and biochemical study of the macroscopically normal white matter in multiple sclerosis. *J. Neurol. Sci.* 41, 81–91 (1979).
4. Allen, I. V., McQuaid, S., Mirakhur, M. & Nevin, G. Pathological abnormalities in the normal-appearing white matter in multiple sclerosis. *Neurol. Sci.* 22, 141–144 (2001).
5. Gallego-Delgado, P. *et al. Neuroinflammation in the normal-appearing white matter (NAWM) of the multiple sclerosis brain causes abnormalities at the nodes of Ranvier. PLoS Biology* vol. 18 (2020).
6. Ludwin, S. K. The pathogenesis of multiple sclerosis: Relating human pathology to experimental studies. *J. Neuropathol. Exp. Neurol.* 65, 305–318 (2006).
7. van der Poel, M. *et al.* Transcriptional profiling of human microglia reveals grey–white matter heterogeneity and multiple sclerosis-associated changes. *Nat. Commun.* 10, 1–13 (2019).
8. Haider, L. *et al.* Oxidative damage in multiple sclerosis lesions. *Brain* 134, 1914–1924 (2011).
9. Cohen, C. C. H. *et al.* Saltatory Conduction along Myelinated Axons Involves a Periaxonal Nanocircuit. *Cell* 180, 311-322.e15 (2020).
10. Fraher, J. & Dockery, P. A strong myelin thickness-axon size correlation emerges in developing nerves despite independent growth of both parameters. *J. Anat.* 193, 195–201 (1998).
11. Meschkat, M. *et al.* White matter integrity in mice requires continuous myelin synthesis at the inner tongue. *Nat. Commun.* 13, (2022).
12. Snaidero, N. & Simons, M. Myelination at a glance. *J. Cell Sci.* 127, 2999–3004 (2014).
13. Nave, K. A. & Werner, H. B. Myelination of the nervous system: Mechanisms and functions. *Annu. Rev. Cell Dev. Biol.* 30, 503–533 (2014).
14. Bando, Y. *et al.* Abnormal morphology of myelin and axon pathology in murine models of multiple sclerosis. *Neurochem. Int.* 81, 16–27 (2015).
15. Caprariello, A. V. *et al.* Biochemically altered myelin triggers autoimmune demyelination. *Proc. Natl. Acad. Sci. U. S. A.* 115, 5528–5533 (2018).
16. Luchicchi, A. *et al.* Axon-Myelin Unit Blistering as Early Event in MS Normal Appearing White Matter. *Ann. Neurol.* 89, 711–725 (2021).
17. Wolswijk, G. & Balesar, R. Changes in the 'expression and localization of the paranodal protein Caspr on axons in chronic multiple sclerosis. *Brain* 126, 1638–1649 (2003).
18. Hendrickx, D. A. E., Schuurman, K. G., van Draanen, M., Hamann, J. & Huitinga, I. Enhanced uptake of multiple sclerosis-derived myelin by THP-1 macrophages and primary human microglia. *J. Neuroinflammation* 11, 1–11 (2014).
19. Wheeler, D., Bandaru, V. V. R., Calabresi, P. A., Nath, A. & Haughey, N. J. A defect of sphingolipid metabolism modifies the properties of normal appearing white matter in multiple sclerosis. *Brain* 131, 3092–3102 (2008).

20. Musse, A. A., Boggs, J. M. & Harauz, G. Deimination of membrane-bound myelin basic protein in multiple sclerosis exposes an immunodominant epitope. *Proc. Natl. Acad. Sci. U. S. A.* 103, 4422–4427 (2006).
21. Webb, R. I. & Schieber, N. L. Volume Scanning Electron Microscopy: Serial Block-Face Scanning Electron Microscopy Focussed Ion Beam Scanning Electron Microscopy. in *E. Hanssen (Ed.), Cellular imaging, Biological and medical physics, biomedical engineering.* 117–148 (Springer, 2018). doi:10.1007/978-3-319-68997-5_5.
22. Schindelin, J. *et al.* Fiji: An open-source platform for biological-image analysis. *Nat. Methods* 9, 676–682 (2012).
23. Bankhead, P. *et al.* QuPath: Open source software for digital pathology image analysis. *Sci. Rep.* 7, 1–7 (2017).
24. Revesz, T., Kidd, D., Thompson, A. J., Barnard, R. O. & Mcdonald, W. I. A comparison of the pathology of primary and secondary progressive multiple sclerosis. *Brain* 117, 759–765 (1994).
25. Zrzavy, T. *et al.* Loss of 'homeostatic' microglia and patterns of their activation in multiple sclerosis. *Brain* 140, 1900–1913 (2017).
26. Fransen, N. L. *et al.* Tissue-resident memory T cells invade the brain parenchyma in multiple sclerosis white matter lesions. *Brain* 143, 1714–1730 (2020).
27. Hendrickx, D. A. E., van Eden, C. G., Schuurman, K. G., Hamann, J. & Huitinga, I. Staining of HLA-DR, Iba1 and CD68 in human microglia reveals partially overlapping expression depending on cellular morphology and pathology. *J. Neuroimmunol.* 309, 12–22 (2017).
28. Ronzano, R. *et al.* Microglia-neuron interaction at nodes of Ranvier depends on neuronal activity through potassium release and contributes to remyelination. *Nat. Commun.* 12, (2021).
29. Coman, I. *et al.* Nodal, paranodal and juxtaparanodal axonal proteins during demyelination and remyelination in multiple sclerosis. *Brain* 129, 3186–3195 (2006).
30. Howell, O. W., Rundle, J. L., Garg, A. & Komada, M. Activated microglia mediate axo-glial disruption that contributes to axonal injury in multiple sclerosis. *J. Neuropathol. Exp. Neurol.* 69, 1017–1033 (2015).
31. Waxman, S. *Multiple Sclerosis as A Neuronal Disease*. *Multiple Sclerosis as A Neuronal Disease* (Elsevier Inc., 2005). doi:10.1016/B978-0-12-738761-1.X5000-7.
32. Stikov, N. *et al.* Quantitative analysis of the myelin g-ratio from electron microscopy images of the macaque corpus callosum. *Data Br.* 4, 368–373 (2015).
33. Stassart, R. M., Möbius, W., Nave, K. A. & Edgar, J. M. The Axon-Myelin unit in development and degenerative disease. *Front. Neurosci.* 12, (2018).
34. Albert, M., Antel, J., Brück, W. & Stadelmann, C. Extensive cortical remyelination in patients with chronic multiple sclerosis. *Brain Pathol.* 17, 129–138 (2007).
35. Moscatelli, E. A. & Isaacson, E. Gas liquid chromatographic analysis of sphingosine bases in sphingolipids of human normal and multiple sclerosis cerebral white matter. *Lipids* 4, 550–555 (1969).
36. Marbois, B. N., Faull, K. F., Fluharty, A. L., Raval-Fernandes, S. & Rome, L. H. Analysis of sulfatide from rat cerebellum and multiple sclerosis white matter by negative ion electrospray mass spectrometry. *Biochim. Biophys. Acta - Mol. Cell Biol. Lipids* 1484, 59–70 (2000).
37. Jana, A. & Pahan, K. Sphingolipids in multiple sclerosis. *NeuroMolecular Med.* 12, 351–361 (2010).

38. Singh, I., Pahan, K., Khan, M. & Singh, A. K. Cytokine-mediated induction of ceramide production is redox-sensitive: Implications to proinflammatory cytokine-mediated apoptosis in demyelinating diseases. *J. Biol. Chem.* 273, 20354–20362 (1998).
39. Wang, B. *et al.* Mitochondrial Behavior in Axon Degeneration and Regeneration. *Front. Aging Neurosci.* 13, 1–17 (2021).
40. Youle, R. J. & Van Der Bliek, A. M. Mitochondrial Fission, Fusion, and Stress. *Science (80-. ).* 337, 1062–1065 (2012).
41. Gottlieb, R. A. *et al.* At the heart of mitochondrial quality control: many roads to the top. *Cell. Mol. Life Sci.* 78, 3791–3801 (2021).
42. Rosenkranz, S. C. *et al.* Enhancing mitochondrial activity in neurons protects against neurodegeneration in a mouse model of multiple sclerosis. *Elife* 10, 1–60 (2021).
43. Licht-Mayer, S. *et al.* Enhanced axonal response of mitochondria to demyelination offers neuroprotection: implications for multiple sclerosis. *Acta Neuropathol.* 140, 143–167 (2020).
44. Kozin, M. S., Kulakova, O. G. & Favorova, O. O. Involvement of Mitochondria in Neurodegeneration. *Biochemistry* 83, 1002-1021. (2018).
45. Lassmann, H. & Van Horssen, J. The molecular basis of neurodegeneration in multiple sclerosis. *FEBS Lett.* 585, 3715–3723 (2011).
46. Smolders, J. *et al.* Tissue-resident memory T cells populate the human brain. *Nat. Commun.* 9, 4593 (2018).

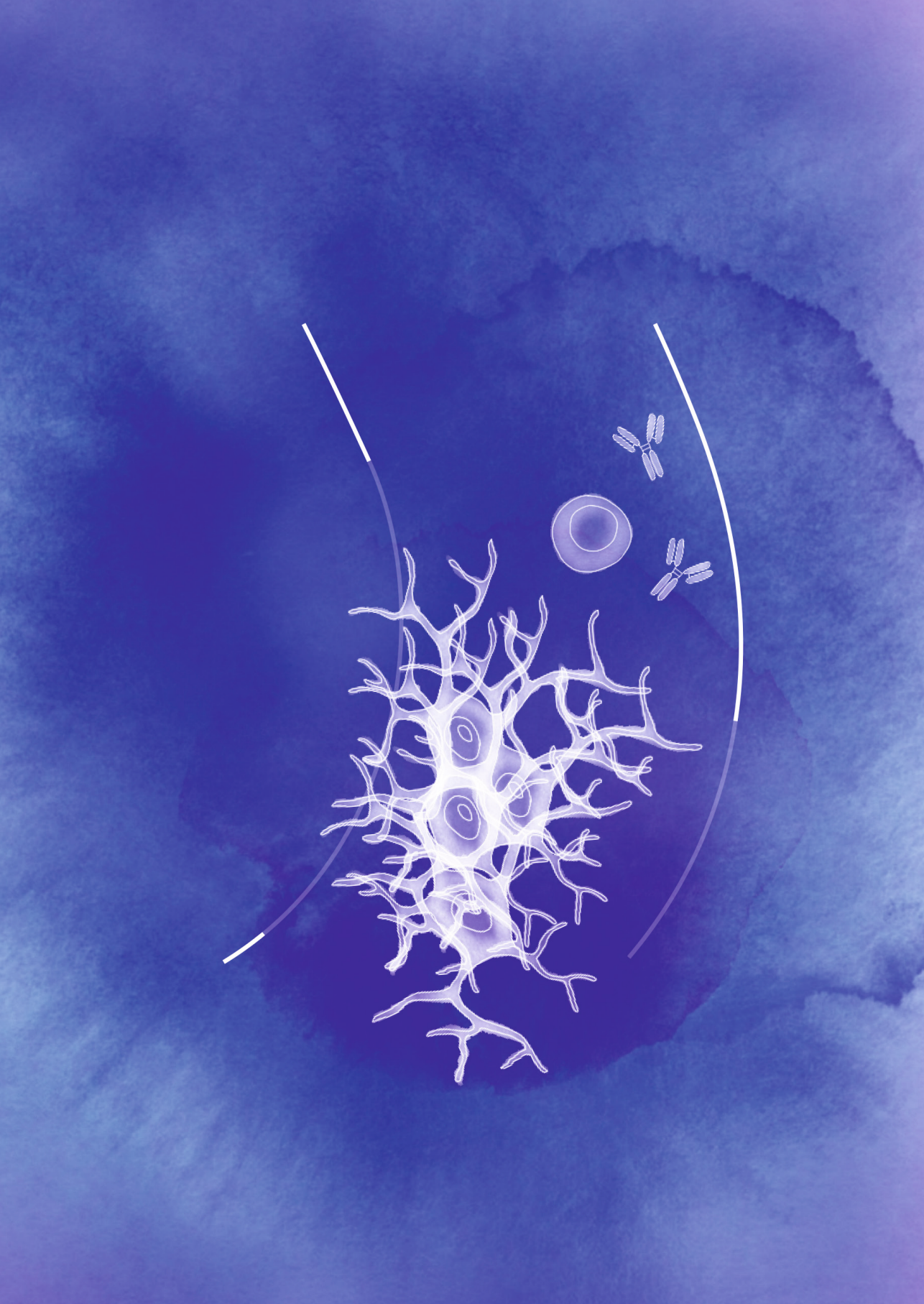

# CHAPTER 4

# Profiling of microglia nodules in multiple sclerosis reveals propensity for lesion formation

Aletta M.R. van den Bosch[1], Marlijn van der Poel[1], Nina L. Fransen[1], Maria C.J. Vincenten[1], Anneleen M. Bobeldijk[1], Aldo Jongejan[2], Hendrik J. Engelenburg[1], Perry D. Moerland[2], Joost Smolders[1,3], Inge Huitinga[1,4x], and Jörg Hamann[1,5x]

[1]Neuroimmunology Research Group, Netherlands Institute for Neuroscience, Amsterdam, The Netherlands; [2]Department of Epidemiology and Data Science, Amsterdam Public Health Research Institute, Amsterdam University Medical Centers, Amsterdam, The Netherlands; [3]MS Center ErasMS, Departments of Neurology and Immunology, Erasmus Medical Center, Rotterdam, The Netherlands; [4]Swammerdam Institute for Life Sciences, University of Amsterdam, Amsterdam, The Netherlands and [5]Amsterdam Infection & Immunity Institute, Amsterdam University Medical Centers, Amsterdam, The Netherlands.

[x] contributed equally

*Adapted from Nature Communications 2024 Feb; 15:1667*

## ABSTRACT

Microglia nodules (HLA-DR$^+$ cell clusters) are associated with brain pathology. We investigated whether these represent the first stage of lesion formation in multiple sclerosis (MS). We found that microglia nodules were associated with more severe MS pathology. Compared to microglia nodules in stroke, those in MS showed enhanced expression of genes previously found to be upregulated in MS lesions. Furthermore, genes associated with lipid metabolism, presence of T and B cells, production of immunoglobulins and cytokines, activation of the complement cascade, and metabolic stress were upregulated in microglia nodules in MS. Compared to stroke, they more frequently had phagocytosed oxidized phospholipids and possessed a more tubular mitochondrial network. In MS, some microglia nodules encapsulated partially demyelinated axons. Taken together, we propose that activation of microglia nodules in MS by cytokines and immunoglobulins, together with phagocytosis of oxidized phospholipids, may lead to a volatile phenotype prone to MS lesion formation.

## INTRODUCTION

Multiple sclerosis (MS) is a chronic neuroinflammatory disease characterized by focal demyelination and axonal damage throughout the brain and spinal cord [1,2]. Microglia are innate phagocytic glia cells of the central nervous system (CNS) that play an essential role in brain homeostasis [3,4]. In MS pathology, they contribute to the HLA-DR$^+$ cell fraction phagocytosing myelin fragments in active and mixed active/inactive (mixed) lesions [1,5]. Despite many studies focusing on the role of microglia in MS, their particular role in lesion initiation is not defined yet.

White matter (WM) in MS that is not lesioned is called the normal appearing white matter (NAWM). Already in 1989, an magnetic resonance imaging (MRI) study showed alterations in the NAWM in MS compared to healthy control WM [6], which later were in part attributed to focal microglial activation in the absence of clear demyelination [7]. Abnormalities detected by MRI in NAWM distant from WM lesions could furthermore not be attributed to axonal pathology [8]. More recently, abnormalities in the NAWM in MS seen on MRI were followed over time and shown to predict the likelihood of developing subsequent MS lesions [9]. Accordingly, we recently identified subtle transcriptional changes in microglia in MS NAWM using bulk RNA sequencing [10]. Top differentially-expressed (DE) genes related to lipid metabolism and phagocytosis that we found were also upregulated in active MS lesions, indicating early demyelination by microglia in NAWM. Since microglia adapt to local changes in the CNS [11–13], subpopulations with distinct cellular states may differentially contribute to MS pathology.

HLA-DR$^+$ ramified microglia can accumulate and cluster in the NAWM forming small clusters of at least four up to 50 cells that are in contact with each other, which was described in relation to MS pathology for the first time in 1993 [14,15]. These so-called microglia nodules are regularly considered to precede MS lesion formation [16–24]. They are found in early as well as advanced MS cases and persist throughout the disease course [25,26]. Moreover, they are associated with axons undergoing Wallerian degeneration [19] and with encapsulation of activated complement deposits [16,17]. Microglia nodules are engaged in phagocytosis [27] and express both pro- and anti-inflammatory cytokines, such as tumor necrosis factor (TNF), interleukin (IL)-1β, and IL-10 [28,29]. Van Horssen and colleagues reported expression of nicotinamide adenine dinucleotide phosphate (NADPH) oxidases by microglia nodules, which promotes the production of radical oxygens that can contribute to axonal damage [29]. In sum, microglia nodules in MS express molecules involved in immune regulation and oxidative stress. However, microglia nodules are not restricted to MS, since these are also found in relation to Wallerian degeneration in brain donors with traumatic brain injury, ischemia,

or stroke [19,24], where microglia nodules line up around complement-opsonized axons similar as in MS [16,17,24]. Therefore, to disclose MS-specific characteristics of microglial nodules and their possible contribution to MS lesion formation, we compared microglia nodules in MS with microglia nodules in stroke and with surrounding non-nodular white matter in MS and stroke. Considering the age and progressive clinical disease course of the donors [30] as well as the frequency of occurrence of microglia nodules, resolution of the microglia nodule is more likely than progression into an MS lesion [18]. We hypothesize that in MS a subset of microglia nodules will initiate MS lesion formation. As microglia nodules in stroke are not involved in lesion formation, differences between microglia nodules in MS and in stroke may reveal mechanisms behind MS lesion formation.

We assessed the pathological and clinical relevance of presence of microglia nodules in the MS autopsy cohort of the Netherlands Brain Bank. Of microglia nodules in MS and stroke tissue, the frequency and size were quantified. Gene expression in microglia nodules and non-nodular white matter in MS and stroke was compared by RNA sequencing of laser micro-dissected tissue, and genes of interest were validated by immunohistochemistry (IHC). Using IHC, we studied the presence of lysosomal oxidized phospholipids, the incidence of adjacent T and B cells, the activation of the complement cascade and formation of the membrane attack complex, the appearance of the mitochondrial network, and the demyelination of axons encapsulated by microglia nodules. Our gene and protein expression data show that microglia nodules in MS are different to those found in stroke. They indicate that part of the microglia nodules in MS show all characteristics of very small and possibly starting MS lesions. Moreover, we identify molecules and pathways that may halt the progression of microglia nodules in MS into inflammatory, demyelinating lesions.

## MATERIALS AND METHODS

### Characterization of MS lesions

Of 167 MS brain donors of the Netherlands Brain Bank MS cohort (NBB-MS, www.brainbank.nl), MS lesions were characterized as described previously by Luchetti and colleagues [5]. The procedure for brain donation and the use of clinical and pathological information for research has been approved by the medical ethics committee of the VU medical center (Amsterdam, The Netherlands). Diagnoses were confirmed by a neuropathologist.

All tissue blocks (on average 23.5 ± 9.7 (standard deviation)) that were dissected during autopsy upon MRI or macroscopical appearance of lesions were stained for HLA-DR/proteolipid protein (PLP) to assess the MS lesion type [5,31]. The

proportions of active, mixed active/inactive (mixed), inactive, and remyelinated lesions were calculated. Active lesions were defined by partial loss of PLP myelin staining and presence of HLA-DR$^+$ cells throughout the lesion. Mixed lesions were defined by an inactive demyelinated center with absence of PLP staining and HLA-DR$^+$ cells present at the border of the lesion. Microglia in active and mixed active/inactive lesions are stratified as ramified (score 0), rounded (score 0.5) or foamy (score 1). The microglia/macrophage activity score (MMAS) of each donor was calculated by dividing the sum of the scores of the microglia/macrophages values by the amount of active and mixed active/inactive lesions. Inactive lesions were defined by an inactive demyelinated center with no HLA-DR$^+$ cells throughout. Remyelinated lesions were defined by partially myelinated axons with similar numbers of HLA-DR$^+$ cells compared to the adjacent NAWM. In addition, we determined lesion load in brainstem tissue blocks as these are dissected at standard locations, which allowed us to compare the same brain region among donors [5]. The load of reactive sites was defined as regions of accumulations of HLA-DR$^+$ microglia cells in normal-appearing brainstem tissue, which are typically larger regions than nodules in which the HLA-DR$^+$ microglia cells do not need to be in contact with each other to be considered as such, and total lesion load was defined as all active, mixed, inactive, and remyelinated but not reactive sites in the brainstem tissue. Additionally, each donor was scored for yes or no presence of microglia nodules in any tissue block dissected.



**Post-mortem brain tissue selection for LDM and IHC**

Frozen and mirror paraffin-embedded tissue from NAWM of MS (n=7) and WM of stroke brain donors (n=7) with HLA-DR$^+$ microglia nodules were matched for age, sex, post-mortem delay, and pH of the cerebrospinal fluid (CSF) (**Table 1**). Normal appearance of tissue was confirmed by intact PLP myelin staining, and microglia nodules were determined as minimally 4 HLA-DR$^+$ accumulating microglia. MS and stroke samples containing foamy microglia, lesions, or reactive sites were excluded. MS brain donors that had experienced any brain infarct during life were excluded. The WM tissue of stroke brain donors did not contain infarcts. Cryo-protected frozen optic nerve samples of MS (n=4) and control donors (n=4) were previously obtained [32].

**Laser dissection microscopy and RNA isolation**

Frozen tissue sections (20 µm) were mounted on PARM MembraneSlides (P.A.L.M. Microlaser Technologies, Bernried, Germany) and dried for 48 hours at room temperature in a sealed box containing silica gel. Sections were fixed in ice-cold dehydrated acetone on ice for 10 min and dried at RT in a slide box with silica gel. Sections were incubated with biotinylated HLA (1:100) and RNase (1:500) in PBS + 0.5% Triton X-100 for 15 min and ABC (1:800) with RNase inhibitor (1:500) in PBS for 15 min.

**Table 1:** Donor demographics of MS and stroke donors

| | **Age** (years) | **Sex** | **PMD** (h:min) | **pH of CSF** | **MS type** | **Disease duration** (years) | **Time to EDSS6** (years) | **Time of stroke to death** (months) |
|---|---|---|---|---|---|---|---|---|
| MS *(n=7)* | 66 (12) | 5M/2F | 8:50 (7:19) | 6.47 (0.10) | 6 SP/1 PP | 38 (12) | 26 (15) | 64 (111) |
| Stroke *(n=7)* | 80 (10) | 4M/3F | 7:18 (4:38) | 6.42 (0.24) | - | - | - | - |
| *p-value* | 0.06 | 0.58 | 0.43 | 0.59 | | | | |

*PMD: post-mortem delay, CSF: cerebrospinal fluid. Data presented as average with standard deviation.*

Immunostaining was visualized with 3'3-diaminobenzidine (1:100; Dako) incubation for 5 min at RT, followed by counterstaining in cresylviolet (0.1% in 70% EtOH) for 10 seconds. A series of 70%–86%–100% ethanol was dripped over the section and sections were transferred to the laser dissection microscope (LDM) (ZEISS) immediately. Of each donor, 90-151 microglia nodules and an equal amount of non-nodular (NA)WM tissue were collected from 8-22 sections, depending on the nodule frequency. Tissue was lysed in 50 µl Trisure (Bioline, London, UK), and RNA was isolated with the RNeasy Micro Kit (Qiagen) using an adapted protocol. Chloroform was added 1:5, and samples were vortexed and incubated on ice for 5 min. After centrifugation at 11,000 rpm for 15 min at 4˚C, the aqueous phase was transferred to a new tube. The remaining sample was incubated with 1 volume of chloroform, vortexed, and centrifuged at 11,000 rpm for 15 min at 4˚C. The aqueous phases were combined. 1 volume of %70 EtOH was added and the sample was transferred to the loading column. The sample was run through the column 3 times by centrifugation for 20 sec at 10,000 rpm at 4˚C. RW1 buffer was added to the column and centrifuged at 10,000 rpm for 20 sec at 4˚C. DNAse1 and RDD buffer were incubated for 15 min RT. The sample was washed with RPE buffer followed by %70 EtOH for 20 sec at 10,000 rpm, and the column was allowed to dry for 5 min at 14,000 rpm. 14 µl of RNase-free $H_2O$ was added to the column, incubated at RT for 2 min, and RNA was collected by centrifugation for 1 min at 14,000 rpm.

**RNA sequencing and gene expression analysis**

PolyA-enriched mRNA sequencing on an Illumina NovaSeq6000 system and sequence alignment were performed by GenomeScan (Leiden, The Netherlands). Putative adapter sequences were removed from the reads when the bases matched a sequence in the TruSeq adapter sequence set using cutadapt (v2.10). Trimmed reads were mapped to the human reference genome GRCh37.75 using

HiSAT2 v-2-1.0 [33]). Gene level counts were obtained using HTSeq (v0.11.0) [34]. Statistical analyses were performed using the edgeR [35] and limma/voom [36] R/Bioconductor packages (R: v4.0.0; Bioconductor: v3.11). Seven highly abundant mitochondrial genes were removed from the dataset. Genes with more than 2 reads in at least 4 of the samples were retained. Count data were transformed to log2-counts per million (logCPM), normalized by applying the trimmed mean of M-values method [37], and precision weighted using voom [38]. One stroke donor (nodule and non-nodular WM sample) and one MS non-nodular NAWM sample were identified as outliers and removed from the dataset **(Supplementary Table 1)**. Differential expression was assessed using an empirical Bayes moderated t-test within limma's linear model framework including the precision weights estimated by voom and the consensus correlation between samples of the same donor (function 'duplicateCorrelation', limma package). The differential expression analysis was performed both with and without a covariate for the estimated microglia content (in percent). The proportion of microglia was determined using cell type deconvolution with dtangle [39] using the set of markers from Darmanis *et al.* [40] and using the script DeconvAnalysis.Rmd by Patrick *et al.* [41] as a template. To test for the possible presence of lymphocytes, we also performed cell type deconvolution using lymphocyte markers as reported by Schirmer *et al.* [42] and Palmer *et al.* [43]. Resulting p values were corrected for multiple testing using the Benjamini-Hochberg false discovery rate. Genes were re-annotated using biomaRt using the Ensembl genome databases (v103). All differentially expressed genes with an adjusted p value of <0.05 were sorted on logFC, and up to 50 top differentially expressed genes were summarized with the p value and logFC adjusted for microglia proportion indicated. Principal component analysis (PCA) was performed on the logCPM values of the 500 most variable genes to distinguish sources of variation. Functional annotation and gene ontology (GO) analysis was performed on genes significantly differentially expressed with adjusted p<0.05 between groups using DAVID [44], with Homo sapiens as background set. As GO terms were utilized to find genes of interest, no multiple testing correction was performed.

**Immunohistochemistry**

For IHC, (NA)WM tissue of MS (n=9) and stroke (n=8) was cut from frozen (20 µm) or paraffin-embedded (8 µm) tissue blocks not containing any lesions or reactive sites. For SMI312 and PLP, normal-appearing optic nerve tissue of MS donors was fixed overnight in 4% paraformaldehyde, protected in 30% sucrose for 24 hours, frozen, and cut at 20 µm [32]. For paraffin-embedded tissue, antigen retrieval was performed as indicated in **Table 2**. Sections were incubated overnight at 4°C with primary antibodies (**Table 2**) diluted in incubation buffer (for paraffin tissue: 0.5% gelatin and 0.5% Triton X-100 in TBS; for frozen tissue: 1% bovine serum albumin and 0.5% Triton X-100 in phosphate-buffered saline,

pH7.6). HLA-DR- and PLP-stained sections were incubated with HRP-labelled anti-mouse antibody (K5007, Dako Real EnVision detection system; Dako, Santa Clara, California, USA) for 1 hour, and immunostaining was visualized with 3'3-diaminobenzidine (DAB) (1:100, Dako) incubation for 10 min, followed by counterstaining with haematoxylin for 30 sec and mounting in Entellan (Merck, Kenilworth, NJ, USA). For CD38/HLA- and HLA/von Willebrand factor (VWF)-stained sections, immunostaining of HLA and VWF respectively was visualized with DAB (1:100, Dako) with 3% nickel, and CD38 and HLA, respectively, were incubated with avidin-biotin complex–alkaline phosphatase kit (Vector, Olean, NY, USA) (1:800) for 1 hour, and staining was visualized with the ImmPACT Vector Red Alkaline Phosphatase Substrate Kit (Vector). For fluorescent stainings, sections were either incubated with a compatible fluorophore (1:400), or the staining was enhanced with a compatible biotinylated secondary antibody (1:400) for 1 hour followed by avidin-biotin complex – HRP kit (1:800) for 45 min, biotinylated tyramide (1:10,000) for 10 min, ABC (1:800) for 45 min at RT, and lastly, streptavidin-conjugated fluorophore (1:800) for 1 hour. All fluorescent stainings were incubated with Hoechst (1:1,000) for 10 min, 0.1% Sudan Black in 70% ethanol for 10 min and mounted in Mowiol.

**Quantification of immunohistochemistry**

HLA-DR$^+$ microglia nodules were visualized with an Axioplan2 microscope (Zeiss, Oberkochen, Germany). The entire tissue section was scanned to manually count nodule numbers in each section and corrected for size of the tissue section. To determine the size of microglia nodules, a picture was made of each nodule and a macro to automatically determine nodule size was developed using Image-Pro software (MediaCybernetics, Bethesda, MD, USA). An outline of each nodule was drawn manually, and an area mask was placed to capture HLA-DR-stained microglia nodules using a greyscale intensity threshold >50 for HLA-DR/PLP stainings and a threshold >110 for HLA-DR stainings. The total area of HLA-DR-stained microglia nodules was automatically calculated and expressed as $\mu m^2$. For CD138, CD3, CD20, CD4, CD8, and PCNA, stainings were visualized using a confocal laser-scanning microscope (SP8; Leica, Wetzlar, Germany) with the software LASX, magnification 40x.

**Table 2:** Antibodies overview

| **Antigen** | **Supplier** (cat#) | **Clone** | **Dilution** | **Antigen retrieval** |
|---|---|---|---|---|
| C1qB | Abcam (ab92508) | EPR2981 | 1:100* | Tris EDTA buffer pH9 |
| C3d | Dako (A0063) | Polyclonal | 1:300 | Citrate buffer pH6 |
| C5b9 | Dako (M077701-8) | aE11 | 1:100 | Citrate buffer pH6 |
| CD138 | BioRad (MCA2459T) | B-A38 | 1:250 | Citrate buffer pH6 |
| CD20 | Dako (M0755) | L26 | 1:100 | Citrate buffer pH6 |
| CD3 | Dako (A0452) | Polyclonal | 1:100 | Citrate buffer pH6 |
| CD38 | Atlas antibodies (HPA022132) | Polyclonal | 1:3000 | Citrate buffer pH6 |
| CD4 | Dako (M7310) | 4B12 | 1:100 | Tris EDTA buffer pH9 |
| CD8 | BD Biosciences (641400) | SK1 | 1:500 | Citrate buffer pH6 |
| DAGLB | Atlas Prestige (HPA069377) | Polyclonal | 1:50* | PBS pH7.6 |
| E06 | Avanti (330002S) | T15 | 1:100 | PBS pH7.6 |
| FABP5 | RabMab (ab255276) | EPR22552-64 | 1:2000 | Tris EDTA buffer pH9 |
| HLA-DR | Dako (M0775) | CR3 | 1:100 | Citrate buffer pH6 |
| IAH1 | Invitrogen (PA5-65270) | Polyclonal | 1:50* | PBS pH7.6 |
| Iba1 | Wako (019-19741) | Polyclonal | 1:500 | Citrate buffer pH6 |
| IGG | Abcam (ab218427) | Polyclonal | 1:100 | Citrate buffer pH6 |
| LAMP1 | Abcam (ab24170) | Polyclonal | 1:200 | Citrate buffer pH6 |
| MBP | Sigma (AB980) | Polyclonal | 1:200 | Citrate buffer pH6 |
| PCNA | Santa Cruz (sc-25280) | PC10 | 1:1000 | Citrate buffer pH6 |
| PLP | Secotec (MCA839G) | plpc1 | 1:3000 | Citrate buffer pH6 |
| SMI312 | Eurogentec (SMI-312R) | SMI-312R | 1:6000 | Citrate buffer pH6 |
| STARD13 | Invitrogen (PA5-63622) | Polyclonal | 1:300* | PBS pH7.6 |
| Tomm20 | RabMab (ab186735) | EPR15581-54 | 1:100* | Citrate buffer pH6 |
| VWF | Atlas antibodies (AMAb90928) | CL1950 | 1:500* | Citraconic anhydride pH6 |

**Staining enhanced*

Each tissue section was scanned for HLA-DR$^+$ or IBA1$^+$ microglia nodules, and pictures were made with each nodule present in the middle to detect immune cells around microglia nodules in a radius of 150-180 µm. Pictures were processed and analyzed using Fiji software [45]. For VWF, CD38, C1qB, C3d, MAC,

FABP5, DAGLB, IAH1, and STARD13, scans were made on the Axio slide scanner, x20 magnification (ZEISS, Oberkochen, Germany). For VWF, the percentage of all nodules in each section in contact with a vessel was quantified. Of each section, all HLA-DR$^+$ microglia nodules were annotated as positive or negative for C1qBb, MAC, FABP5, DAGLB, IAH1, and STARD13, and for CD38 nodules were annotated as positive or negative for CD38$^+$ cells in a radius of 150-180 µm on Qupath (version 0.4.3). The percentage of HLA$^+$ cells in the non-nodular (NA)WM expressing DAGLB, FABP5, IAH1, and STARD13 was quantified using cell profiler in Qupath of on average 5,100 HLA$^+$ cells per donor per staining. Of microglia nodules with a CD138$^+$, CD3$^+$, CD20$^+$, or CD38$^+$ lymphocyte nearby, the percentage of those in direct contact were quantified and of those not in direct contact, the distance from the lymphocyte to the nearest ramification of the microglia nodule was measured. The percentage of non-nodular HLA$^+$ microglia adjacent to microglia nodules (<100 µm distance) expressing DAGLB, FABP5, IAH1, and STARD13 was also quantified using cell profiler in Qupath. In MS, 16.4 ± 22.1 nodules were found per section, and in stroke, 6.1 ± 7.3 nodules were found per section. In MS, 13.5 ± 7.6 HLA$^+$ cells were detected per nodule adjacent to nodules, and in stroke, 14.1 ± 9.0 HLA$^+$ cells were detected per nodule adjacent to nodules.

SMI312–PLP–HLA triple staining, LAMP1–E06–HLA triple staining, Tomm20–HLA double staining, and Tomm20–HLA–SMI312 triple staining were visualized at 63x using stimulated emission depletion (STED) microscopy (STEDYCON; Abberior Instruments, Göttingen, Germany) for z-stacks. 3D-rendered images were analyzed for (partial) demyelination in Fiji. For PLP triple staining, E06 triple staining and Tomm20 double staining, z-stack images were taken of all HLA$^+$ microglia nodules in each section on the STED microscope at magnification 63x with 0.5 µm step size. For E06, using Fiji plugin for ImageJ, all microglia nodules were annotated as positive or negative for LAMP1$^+$ E06$^+$ phagocytosed oxidized phospholipids within the nodule. For Tomm20, the length of the mitochondria network inside microglia was measured for each nodule using Fiji. The mitochondrial network inside the nodule was considered as fragmented if all mitochondria were <2 µm, intermediate if the largest mitochondria was between 2-5 µm, and tubular if the largest mitochondria was >5 µm in size [46], and the axonal mitochondria size and frequency was measured with Imaris (v9.7; Bitplane, Zurich, Switzerland). For the SMI312–PLP–HLA triple staining, the number of nodules in MS and control optic nerve and the number of nodules encapsulating partially demyelinated axons were quantified.

**qPCR of genes involved in immunoglobulin production**

Frozen tissue section (20 µm) was cut from stroke (n=6) and MS (n=6) (NA) WM tissue containing microglia nodules and lysed in 800 µl TRIsure. RNA was

isolated according to manufacturer's instructions (Bioline). Briefly, chloroform (1:5) was added to each TRIsure sample and after centrifugation, the aqueous phase was collected, followed by incubation with 1 µg glycogen (Roche, Basel, Switzerland) for 30 min in ice-cold isopropanol at -20˚C. Precipitated RNA was washed in ice-cold 75% ethanol and diluted in 20 µl deionized water. Synthesis of cDNA was performed according to manufacturer's instructions, using the Quantitect Reverse Transcription kit (Qiagen, Hilden, Germany). 50 ng RNA was mixed with 1 µl gDNA Wipe-out buffer and incubated for 2 min at 42°C, followed by incubation with QuantiTect Buffer, RT Primer Mix, and Quantitect Reverse Transcriptase for 30 min at 42°C and incubation for 3 min at 95°C.

To determine gene expression of immunoglobulin (Ig) genes, quantitative polymerase chain reaction (qPCR) was performed. Control WM tissue and tissue collected from MS lesions and lymph node was used as negative and positive control samples, respectively. Primers were designed at the Integrated DNA Technologies website (eu.ifdna.com). Optimal primers were selected based on dissociation curve and specificity, examined on cDNA derived from control, MS NAWM, and MS lesioned tissue. Gene expression was normalized on the mean of two housekeeping genes, *GAPDH* and *EEF1A1*. For each gene, the relative expression was calculated using the $2^{-\Delta\Delta CT}$ method. Primers used for reverse transcription (RT)-qPCR are provided in **Suppl. Table 2**.



**Statistical analysis**

Data obtained from immunohistochemistry and RT-qPCR was tested for normality by a Shapiro-Wilk normality test, followed by parametric or non-parametric tests for numeric data, quasibinomial generalized linear mixed models for proportional data, or a chi square test for binomial data to define p-values. Statistical analyses were performed in Rstudio (version 1.2.5033; Rstudio, Boston, MA, USA) for R (version 4.2.0), using key packages ggplot2, lme4, car, plyr, ggpubr, Hmisc, and corrplot. P values $<0.05$ were considered significant.

## RESULTS

**Microglia nodules in MS correlate with MS pathology**

In the MS cohort of the NBB, we quantified the number of MS donors with and without microglia nodules. To determine the relevance of microglia nodules for MS pathology and clinical course, we compared the pathological and clinical characteristics of MS donors with and without microglia nodule in all blocks dissected. Out of 167 MS brain donors, 107 donors (64%) had microglia nodules present in at least one tissue block dissected, and 60 donors (36%) did not

have any microglia nodules in any of the tissue blocks dissected. MS donors with microglia nodules present in at least one tissue block, compared to MS donors without microglia nodules, had a significantly higher number of reactive sites (log, with nodules: 0.70 ± 0.75, without nodules: 0.32 ± 0.56, p=6.0e-4) and higher lesion load (log, with nodules: 1.79 ± 0.97, without nodules: 1.15 ± 1.10, p=4.5e-4) in standard locations, a higher proportion of active lesions (with nodules: 0.23 ± 0.22, without nodules: 0.16 ± 0.22, p=0.03) and a lower proportion of inactive lesions (with nodules: 0.30 ± 0.24, without nodules: 0.32 ± 0.26, p=0.03) and remyelinated lesions (with nodules: 0.30 ± 0.28, without nodules: 0.37 ± 0.29, p=0.02) compared to MS donors without microglia nodules present. There was no difference in proportion of mixed active/inactive lesions, MMAS, disease severity measured as time to expanded disease disability scale (EDSS) 6, or disease duration (**Table 3**).

**Table 3:** Donor demographics of NBB-MS cohort with and without nodules

| | **Nodules present (all) N=107** | **No nodules present (all) N=60** | *p-value* |
|---|---|---|---|
| Age (years) | 63.81 (13.73) | 63.55 (12.66) | 0.90 |
| Sex | 77F, 30M | 30F, 30M | **0.01** |
| MS type | 2 RR, 30 PP, 62 SP, 13 NA | 6 RR, 20 PP, 28 SP, 6 NA | - |
| Disease duration | 28.70 (13.39) | 29.60 (12.68) | 0.83 |
| Severity score | 2.38 (0.72) | 2.37 (0.76) | 0.71 |
| Reactive site load (log) | 0.70 (0.75) | 0.32 (0.56) | **1.4e-4** |
| Lesion load (log) | 1.79 (0.97) | 1.15 (1.10) | **5.0e-4** |
| Proportion active | 0.23 (0.22) | 0.16 (0.22) | **0.03** |
| Proportion mixed | 0.30 (0.24) | 0.21 (0.25) | 0.09 |
| Proportion inactive | 0.30 (0.24) | 0.32 (0.26) | **0.03** |
| Proportion remyelinated | 0.30 (0.28) | 0.37 (0.29) | **0.02** |
| MMAS score | 0.35 (0.26) | 0.30 (0.29) | 0.15 |

*Provided is the mean ± standard deviation, BRS: brainstem, F: female, M: male, NA: not available, PMD: post-mortem delay, PP: primary progressive, PR: primary relapsing, RR: relapsing-remitting, SP: secondary progressive, WM: white matter.*

## Microglia nodules in MS are more frequent than in stroke but are not different in size

Nodule frequency and size were quantified in (NA)WM tissue sections of MS (n=7) and stroke donors (n=7). We observed a significantly higher number of

microglia nodules in MS NAWM tissue as compared to stroke WM (MS: 18.1 ± 15.5 per 100 mm$^2$, stroke: 4.8 ± 2.2 per 100 mm$^2$, p=0.03), but the microglia nodules were not different in size (p=0.16, **Fig. 1a-c**). Furthermore, in contrast to stroke WM tissue with microglia nodules, the majority of MS NAWM tissue with microglia nodules showed many HLA-DR$^+$ ramified microglia throughout the whole tissue section.

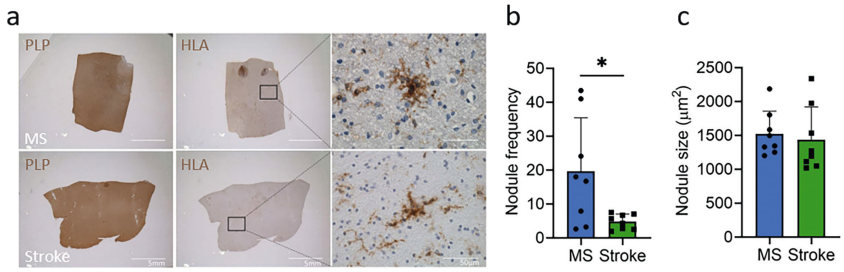


**Figure 1: Microglia nodules in MS are more frequent than in stroke, but are similar in size.** Immunohistochemistry stainings. (a) PLP and HLA of (NA)WM matter in MS and in stroke shows no sign of demyelination and clustering of HLA-DR$^+$ cells into nodules. (b) Microglia nodule frequency was calculated as number of microglia nodules per 100 mm$^2$. The nodule frequency was higher in MS compared to stroke (p=0.03). (c) Microglia nodule size as measured in µm$^2$ was similar in MS and stroke. Bar plots show mean ± standard deviation. Significance was tested with a two-sided students t-test, p value <0.05 is indicated with *.

## Gene expression analysis shows diversity between microglia nodules in MS and stroke

To compare gene expression of microglia nodules in MS with those in stroke and non-nodular (NA)WM, tissue was manually dissected using laser capture microscopy. PCA showed partial clustering of four groups distinguishing MS and stroke tissue in the first dimension and nodular and non-nodular (NA)WM tissue in the second dimension (**Fig. 2a**). Cell type deconvolution analysis of the gene expression data showed that microglia nodules in MS compared to MS non- nodular NAWM were characterized by a significantly higher proportion of microglia cells and endothelial cells and a lower proportion of oligodendrocytes. There were no significant differences in estimated cell type proportions between microglia nodules in MS and microglia nodules in stroke, microglia nodules in stroke and stroke non-nodular WM, or MS non-nodular NAWM and stroke non-nodular WM (**Fig. 2b**). As validated with IHC, microglia nodules were equally often in contact with vessels in MS and in stroke (**Suppl. Fig. 1**). As our main comparison of interest was between microglia nodules in MS and stroke, we focused on the results of the analysis without correction for microglia proportion. Results of the analysis with correction for the proportion of microglia

are shown in the text (indicated with 'after correction') and are also included in **Suppl. Tables 3 and 4**. For each comparison, up to 50 top differentially expressed (DE) genes are shown in **Suppl. Table 3a-d**. Expression of all genes of interest mentioned below is summarized in **Suppl. Table 4**. The highest number of DE genes was observed in microglia nodules in MS vs MS non-nodular NAWM, where 325 DE genes were upregulated. In microglia nodules in MS vs microglia nodules in stroke, 256 DE genes were upregulated, of which 40 DE genes were also upregulated in microglia nodules in MS vs MS non-nodular NAWM and are considered MS nodule-specific genes. The lowest number of DE genes was found in microglia nodules in stroke vs stroke non-nodular WM with 10 upregulated DE genes. In MS non-nodular NAWM vs stroke non-nodular WM, 23 DE genes were upregulated (**Fig. 2c**). The number of downregulated DE genes was low in all comparisons. Microglia nodules compared to non-nodular (NA)WM in MS and in stroke shared only few communally upregulated DE genes (*C1qB*, *RPGR*, and *SLC11A1),* which are associated with involvement in activation of the classical complement pathway and in phagocytosis. After correction for the microglia proportion (hereafter 'correction'), *C1qB* remained significantly differentially expressed for both comparisons, while *SLC11A1* was only significantly upregulated by microglia nodules in stroke compared to stroke non-nodular WM (**Fig. 2c-e**).

**Microglia nodules in MS but not in stroke express MS lesion pathology-associated genes**

Microglia nodules compared to non-nodular NAWM in MS had a significantly higher expression of a multitude of genes previously associated with MS pathology (*CXCL16*, *IL18*, *MX1*, *LPL*, *CD14*, *CD83*, *IL1B*, *CDKN1A*, *GPNMB*, *HLA-DRB5*, *C1QA*, *C1qB*, *SPP1*, *TLR6*, *CHI3L1*, after correction *CXCL16*, *IL18*, *C1QA*, *C1qB* remained significant) [1,10,27,28,47–53]. *C1qB* was also upregulated by microglia nodules in stroke compared to stroke non-nodular WM, also after correction. Microglia nodules in MS, compared to microglia nodules in stroke, also upregulated expression of genes previously associated with MS-lesion pathology (*HLA-DRB5*, *ISG15*, *MX1*, after correction *HLA-DRB5*, *ISG15*) and MS susceptibility (*IFNAR2*, also after correction) [48,54]. In MS non-nodular NAWM compared to stroke non-nodular WM, no genes previously associated with MS pathology were differentially expressed (**Fig. 2d-g**). Thus, microglia nodules in MS and not in stroke show MS lesion-related activation. Markers for phagocytic exhaustion (*CD22*, *NOS1*, *CYBB*, *CD68*, and *CYBA*)[55] were all numerically but not significantly upregulated in microglia nodules in MS compared to stroke (data not shown).

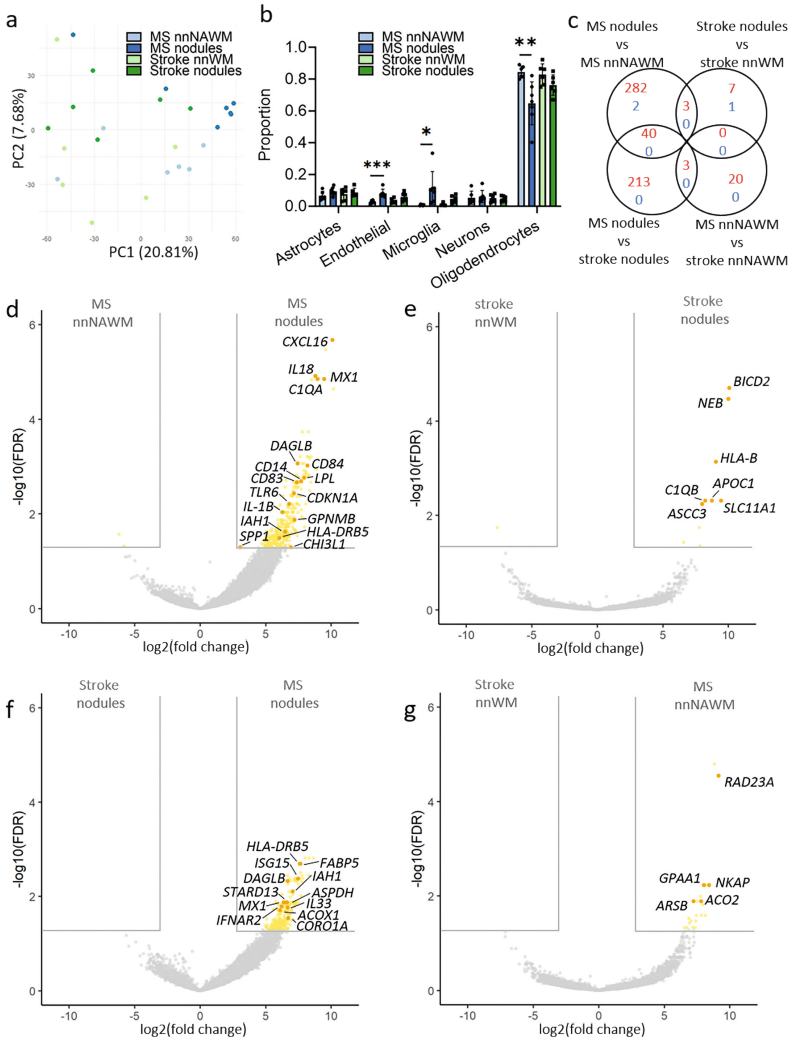


**Figure 2: Microglia nodules in MS and stroke share only few commonalities, and microglia nodules in MS show lesion-associated microglia activation.** (a) PCA plot showing discrimination of MS and stroke samples on the first dimension and discrimination of nodules and non-nodular NAWM in the second component. (b) Proportion of cell types in the groups, shown as mean ± standard deviation. Microglia nodules in MS had a higher proportion of endothelial cells and microglia cells, and a lower proportion of oligodendrocytes. p value <0.05 is indicated with *, <0.01 is indicated with **, <0.001 is indicated with ***. (c) Venn diagram showing the number of DE genes with adjusted p-value <0.05 and logFC > 3 or <-3, either upregulated in red or downregulated in blue between the various groups. Gene expression of (d) MS nodules versus non-nodular NAWM, (e) stroke nodules versus stroke non-nodular WM, (f) MS nodules versus stroke nodules, and (g) MS non-nodular NAWM versus stroke non-nodular WM. DE genes are highlighted in yellow, and top DE genes are highlighted in orange.

**Microglia nodules in MS express genes indicative for lesion formation**
Using the DAVID algorithm for functional annotations, we found DE genes in microglia nodules in MS compared to microglia nodules in stroke and compared to MS non-nodular NAWM that functionally may be indicative for lesion formation (**Suppl. Fig. 2** and **Suppl. Tables 5a-b**). Microglia nodules in MS had upregulated genes that imply involvement in the adaptive and the innate immune response (compared to MS non-nodular NAWM: *HLA-DMB*, *JAK3*, *TLR6*, *IFI27*, none after correction; compared to microglia nodules in stroke: *IDH1*, *PSME3*, *IFNAR2*, *ISG15*, *PARP9*, *IL33*, after correction *IFNAR2*, *ISG15*, *PARP9*), phagocytosis (compared to MS non-nodular NAWM: *CD14*, *IRF8*, *MERTK*, *NCF2*, none after correction), and lipid metabolic processes (compared to MS non-nodular NAWM: *LPL, DAGLB*, *IAH1*, after correction *DAGLB*; compared to microglia nodules in stroke: *PLCD3*, *FABP5*, *ACLY*, *IAH1*, *DAGLB*, *CHI3L1*, *CHI3L2*, *STARD13*, *GPCPD1*, after correction *FABP5*, *IAH1*, *DAGLB*, *STARD13*). Microglia nodules in MS had an increased expression of genes implying T- and B-cell homeostasis and proliferation (compared to MS non-nodular NAWM: *NCKAP1L*, *CASP3*, *JAK3*, *FADD*, *TCIRG1*, after correction *NCKAP1L*; compared to microglia nodules in stroke: *CORO1A*, *NCKAP1L*, *CASP3*, *APBB1IP*, none after correction) and natural killer T (NKT) cell-mediated cytotoxicity (compared to microglia nodules in stroke: *GRB2*, *CASP3*, *BID*, none after correction). In microglia nodules in MS, genes indicating Ig signaling were upregulated as compared to MS non-nodular NAWM: *HLA-DMA*, *HLA-DPB1*, *HLA-DMB*, *HLA-DRB1*, *HLA-DRB5*, none after correction; compared to microglia nodules in stroke: *HLA-DRB5* (also after correction) and of cytokine signaling, specifically interferon (IFN) y and TNF (compared to MS non-nodular NAWM: *IRF8*, *CD84*, *LRRK2*, *FADD*, *LPL*, *TLR2*, *EGR1*, *IL18*, after correction *IL18*; compared to microglia nodules in stroke: *IFNAR2,* also after correction). Furthermore, gene expression of microglia nodules in MS indicates they may be under metabolic stress (compared to MS non-nodular NAWM: *PPRC1*, *SAMM50*, *MTG1*, after correction *MTG1*; compared to microglia nodules in stroke: *ACOX1*, *COA4*, *MTG1*, *PPRC1*, *SAMM50*, after correction *MTG1*) and may be responding to as well as producing reactive oxygen species (ROS) (compared to microglia nodules in stroke: *ASPDH*, *BID*, *CRYZL1*, *IDH1*, *MAOB, SMAD3*, none after correction).

**Microglia nodules in MS reside in an inflammatory environment**
As gene expression analysis revealed the likelihood of nearby lymphocytes, this was assessed using IHC. In MS and not in stroke, $CD20^+$ B cells and $CD138^+$ plasma cells were found in close proximity to microglia nodules. $CD38^+$ plasmablasts were observed more frequently near MS compared to stroke microglia nodules (CD20: MS: 5 of 106 nodules, per donor 5.2% ± 10.4%, stroke: 0 out of 83 nodules, 0% ± %0 per donor; CD138: MS: 13 of 162 nodules, per donor %10.7 ± %6.7, stroke: 0 of 78 nodules, per donor %0 ± %0; CD38: MS: 90

of 202 nodules, per donor %24.5 ± %34.6, stroke: 1 of 65 nodules, per donor %0.9 ± %0.4, p= 6.7e3-, **Fig. 3a-f**). Some microglia nodules with lymphocytes in close proximity were in direct contact with the lymphocytes (CD20: 0%, CD138: 8%, CD38: 38%, CD3: 14%). For microglia nodules not in direct contact with the lymphocytes, the distance was for $CD20^+$ B cells 81.52 ± 53.36 µm, for $CD138^+$ plasma cells 71.48 ± 39.44 µm, for $CD38^+$ plasmablasts 71.48 ± 39.44 µm, and for $CD3^+$ T cells 50.47 ± 35 µm. In line with the presence of B and plasma cells in close proximity to MS but not near microglia nodules in stroke, with IHC we found IgG deposition in some MS cases (4/7 MS donors) in the lumen of some vessels and IgG-producing plasmablasts (2/7 MS donors) near microglia nodules (**Fig. 3g-h)** and never in stroke tissue. Also, we found significantly upregulated expression of the Ig genes *IGKC*, *IGHG1*, *IGHG2*, and *IGKV3-15* in MS nodule NAWM tissue as compared to stroke (**Suppl. Fig. 3**). Together, this indicates that Ig secretion only takes place in tissue containing microglia nodules in MS but not in stroke. In MS, $CD3^+$ T cells were more frequently observed near microglia nodules compared to stroke (MS: 38 of 151 nodules, per donor 26.7% ± %9.1, stroke: 5 of 89 nodules, per donor 5.1% ± %5.1, p = 0.02, **Fig. 3i-j**). In MS, both $CD4^+$ as well as $CD8^+$ T cells were found in close proximity to microglia nodules in MS (CD4: per donor 8.3 ± 6.8 nodules, CD8: per donor 16.5 ± 18.0 nodules, **Fig. 3k-m**). In MS, subsets of microglia nodules and $CD3^+$ T cells expressed the proliferation marker PCNA, suggesting that these T cells have encountered antigenic re-stimulation (**Fig. 3n-o**).

**Classical complement pathway activation in MS leads to MAC formation**

Microglia nodules in MS as well as in stroke have a higher expression of *C1Q* genes compared to non-nodular (NA)WM, which is in line with a previous study showing complement deposition presence in both MS and microglia nodules in stroke [24]. C1q is a complement component expressed by microglia and macrophages that can bind to the Fc tail of Igs [56] and is a critical mediator of microglia activation in MS [57]. As Ig-related genes were only expressed in MS tissue and not in stroke tissue, this may potentially lead to complete activation of the complement cascade causing cell lysis in MS but not in stroke. Therefore, we stained the microglia nodules in MS and in stroke for complement components C1qB, C3d and the membrane attack complex (MAC). In MS and stroke, equal percentages of microglia nodules expressed C1qB (MS: 63 of 163 nodules, per donor 36.6% ± %6.0, stroke: 22 of 68 nodules, per donor %19.0 ± %30.5, p=0.25, **Fig. 4a-c**). In MS, microglia nodules more often were associated with $C3d^+$ axons compared to microglia nodules in stroke (MS: 35 of 150 nodules, per donor 17.2% ± 15.5%, stroke: 4 of 54 nodules, per donor 4.2% ± 7.0%, p=0.008), suggesting an increased activation of the complement pathway in MS (**Fig. 4d-f**).

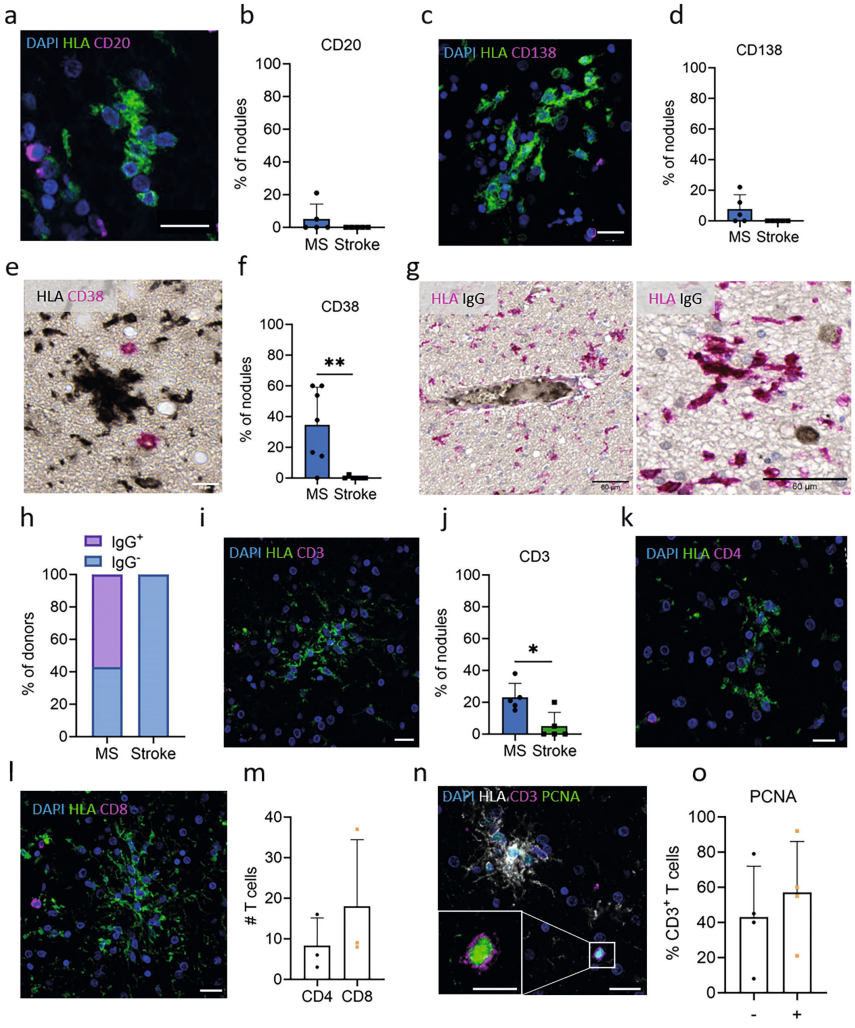


**Figure 3: Microglia nodules in MS reside in a more inflammatory environment compared to stroke nodules.** Immunohistochemistry stainings. (a-b) A CD20$^+$ B cell, (c-d) a CD138$^+$ plasma cell, and (e-f) two CD38$^+$ plasmablasts in MS tissue, which are seen not or less often in stroke. (g-h) Immunohistochemistry of IgG in MS shows IgG staining in the lumen of a blood vessel in close proximity to a nodule and an IgG$^+$ plasmablast in close proximity to a microglia nodule, which was not found in stroke donors. (i-j) A CD3$^+$ T cell in MS tissue, which was less frequent in stroke. (k - m) In MS, both CD4$^+$ and CD8$^+$ T cells are found near microglia nodules in MS. (n-o) Activated PCNA$^+$ CD3$^+$ T cell in close proximity to microglia nodules in MS. Bar plots show mean percentage of nodules ± standard deviation or percentage of donors. Significance for proportional data was tested with a quasibinomial generalized linear model or a student's t-test for continuous numerical data, p value <0.05 is indicated with *. White scale bars indicate 20 µm, black scale bars indicate 60 µm.

Furthermore, microglia nodules in MS were more often associated with C5b-9, which constitutes the MAC, compared to microglia nodules in stroke (MS: 29 of 106 nodules, per donor 31.40% ± 17.37, stroke: 16 of 117 nodules, per donor %7.54 ± %12.96, p=0.03), indicating involvement of microglia nodules in MS in complement mediated tissue degeneration (**Fig. 4g-i**).

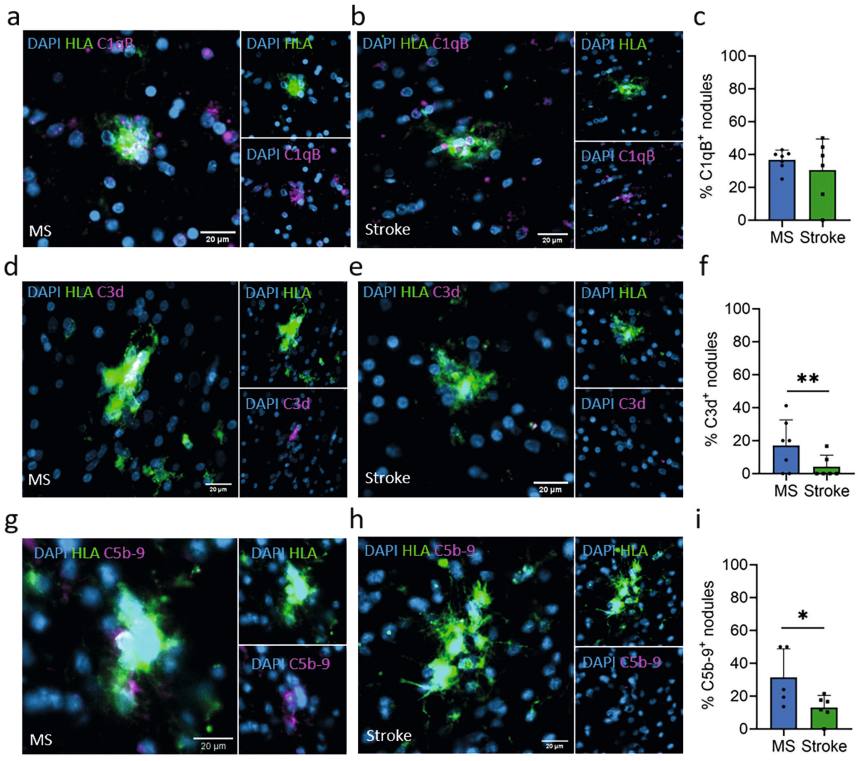


**Figure 4: Microglia nodules in MS are associated with activation of the classical complement pathway and are associated with membrane attack complex formation.** Immunohistochemistry stainings. C1qB$^+$ HLA$^+$ microglia nodule (a) in MS and (b) in stroke. (c) Microglia nodules in MS and in stroke equally often express C1qB. (d) HLA$^+$ microglia nodule associated with a C3d$^+$ axonal fragment in MS and (e) an HLA$^+$ microglia nodule in stroke that is not associated with a C3d$^+$ axonal fragment. (f) In MS, microglia nodules are more often associated with C3d$^+$ axonal fragments than in stroke. Immunohistochemistry of (g) an HLA$^+$ C5b-9$^+$ microglia nodule in MS and (h) an HLA$^+$ microglia nodule in stroke that is not C5b-9$^+$. (i) In MS, microglia nodules are more often C5b-9$^+$ than in stroke. Bar plots show mean value ± standard deviation. Significance was tested with a quasibinomial generalized linear model, p value <0.05 is indicated with *, p value <0.01 is indicated with **.

**Increased lipid metabolism in microglia nodules in MS**

Genes of interest involved in lipid metabolism that were upregulated in microglia nodules in MS compared to microglia nodules in stroke were validated with IHC. $HLA^+$ microglia in the non-nodular (NA)WM and those surrounding microglia nodules (distance <100 *µm,* **Suppl. Fig. 4**) rarely expressed fatty acid-binding protein 5 (FABP5), diaglycerol lipase-beta (DAGLB), StAR-related lipid transfer domain protein 13 (STARD13), or isoamyl acetate hydrolyzing esterase 1 (IAH1). The percentage of $HLA^+$ cells that were also $FABP5^+$, $DAGLB^+$, STARD13 or $IAH1^+$ was similar for MS and stroke (NA)WM. Microglia nodules in MS compared to microglia nodules in stroke significantly more often expressed FABP5 (MS: 81 of 143 nodules, per donor 55.2% ± 8.7%, stroke: 14 of 56 nodules, per donor 22.0% ± 19.6%, $p=3.3^{-6}$), DAGLB (MS: 62 of 79 nodules, per donor 73.8% ± 10.0%, stroke: 12 of 35 nodules, per donor 19.2% ± 22.5%, $p=1.11^{-8}$), and STARD13 (MS: 28 of 57 nodules, per donor 47.5% ± 19.9%, stroke: 7 of 24 nodules, per donor 25.1% ± 20.9%, $p<0.05$). Difference in expression of isoamyl acetate hydrolyzing esterase 1 (IAH1) did not reach significance due to large variation (MS: 21 of 88 nodules, per donor 43.7% ± %31.0, stroke: 7 of 24 nodules, per donor ± %25.1 %20.9, p=0.32, **Fig. 5a-l**).

In MS, the NAWM has more oxidized phospholipids compared to controls [58], which may be one of the triggers for microglia in MS to cluster and form nodules in order to clear up the oxidized phospholipids. Therefore, using IHC and STED microscopy, the percentage of microglia nodules that had phagocytosed oxidized phospholipids were quantified in MS and stroke. In microglia nodules in MS, lysosomal-associated membrane protein 1 $(Lamp1)^+$ lysosomes more often contained oxidized phospholipids (detected using antibody E06) compared to microglia nodules in stroke (MS: 30 of 47 nodules, per donor 68.0% ± %2.8, stroke: 7 of 29 nodules, per donor 29.1% ± 7.0%, $p=3.2^{-12}$), showing that microglia nodules in MS are more involved in phagocytosis of oxidized phospholipids (**Fig. 6a-c**). As microglia nodules in MS are likely involved in lipid metabolism, we set out to investigate if microglia nodules are involved in demyelination with high-resolution IHC. Cryo-protected MS normal-appearing optic nerve tissue [32] provided sufficient resolution to investigate demyelination of individual axons encapsulated by microglia nodules. In MS but not in controls, some axons surrounded by microglia nodules showed partial demyelination, as indicated by loss of PLP staining of a part of the $SMI312^+$ axon (MS: 9 of 20 nodules, per donor 41.0% ± 14.2%, controls: 0 of 24 nodules, 0.0% ± %0.0, $p=^{16-}2.2$, **Fig. 6d-e**).

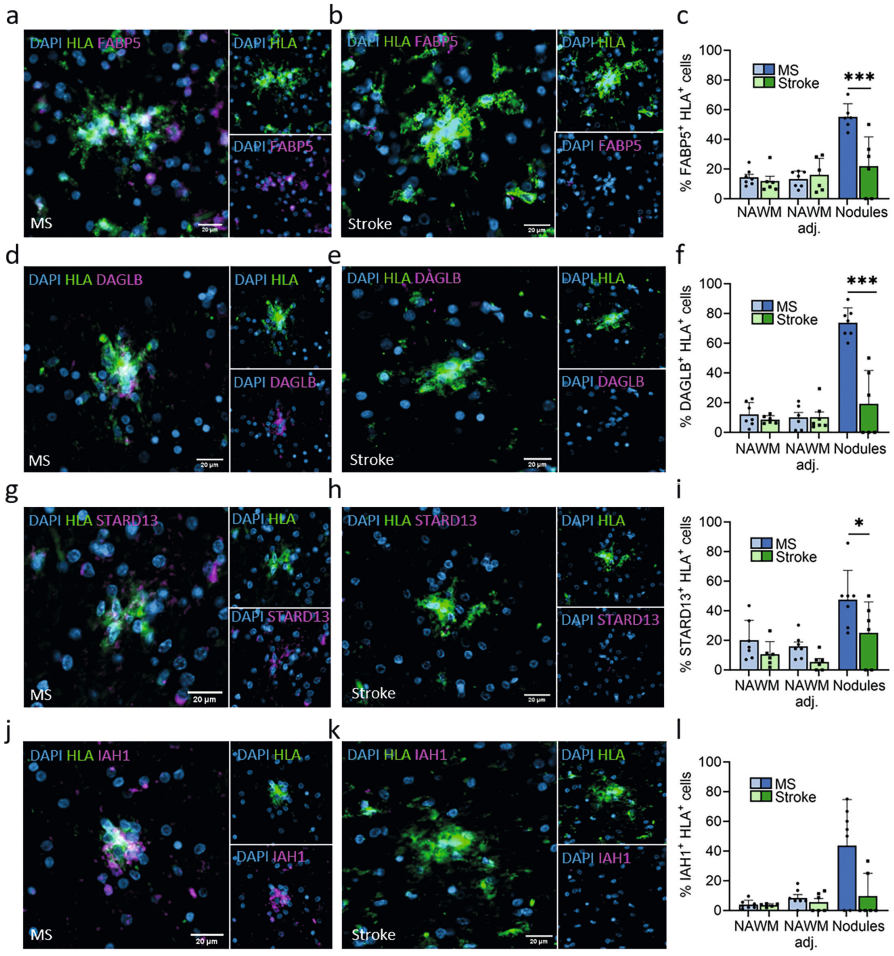


**Figure 5: Microglia nodules in MS are involved in lipid metabolism.** Immunohistochemistry stainings. (a) An HLA$^+$ FABP5$^+$ microglia nodule in MS and (b) an HLA$^+$ FABP5$^-$ microglia nodule in stroke. (c) In MS, microglia nodules more often express FABP5 than in stroke. (d) An HLA$^+$ DAGLB$^+$ microglia nodule in MS and (e) HLA$^+$ DAGLB$^-$ microglia nodule in stroke. (f) In MS, microglia nodules more often express DAGLB compared to microglia nodules in stroke. (g) An HLA$^+$ STARD13$^+$ microglia nodule in MS and (h) an HLA$^+$ STARD13$^-$ microglia nodule in stroke. (i) In MS, microglia nodules more often express STARD13 compared to microglia nodules in stroke. (j) An HLA$^+$ IAH1$^+$ microglia nodule in MS and (k) an HLA$^+$ IAH1$^-$ microglia nodule in stroke. (l) Microglia nodules in MS do not significantly more often express IAH1 compared to those in stroke. Bar plots show mean value ± standard deviation. Significance was tested with a quasibinomial generalized linear model, p value <0.05 is indicated with *, <0.01 is indicated with **, <0.001 is indicated with ***. Bar plots show mean value ± standard deviation.

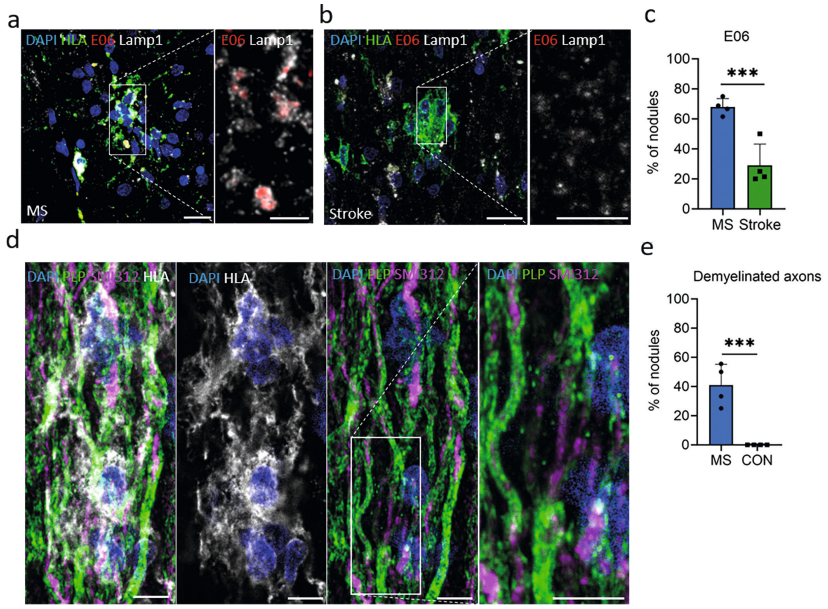


**Figure 6: Microglia nodules in MS are involved in demyelination.** STED microscopy of immunohistochemistry stainings. (a) An HLA$^+$ microglia nodule in MS containing lysosomal (Lamp1) oxidized phospholipids (E06) and (b) an HLA$^+$ microglia nodule in stroke that does not show oxidized phospholipids (E06) in the lysosomes (Lamp1). (c) Microglia nodules in MS have more often phagocytosed oxidized phospholipids compared to microglia nodules in stroke. Bar plot shows mean value ± standard deviation. Significance was tested with a quasibinomial generalized linear model, p value <0.001 is indicated with ***. (d) In MS NAWM in the optic nerve, partially demyelinated axons encapsulated by microglial nodules were found, which was not seen in control optic nerve WM. Scale bars indicate 20 µm.

## Mitochondrial network in microglia nodules in MS is more tubular

DE genes of microglia nodules in MS compared to microglia nodules in stroke were indicative of an altered metabolic state. Using IHC and STED microscopy, we assessed the mitochondrial network of microglia nodules in MS and in stroke, and we quantified the mitochondria frequency and size in axons encapsulated by microglia nodules in MS and in controls. Of each microglia nodule, the translocase of the outer mitochondrial membrane (TOMM20) network was classified as fragmented, intermediate, or tubular. Quantification of the mitochondrial network in microglia nodules in MS and in stroke showed that in MS the mitochondrial network was more often tubular (MS: 51.0% ± %18.5, Stroke: %14.9 ± %13.1, p=0.009) (**Fig. 7a-c**). This tubular network is indicative of a hypermetabolic state of the microglia nodules in MS. In axons encapsulated by microglia nodules, there was no difference in mitochondria frequency nor size.

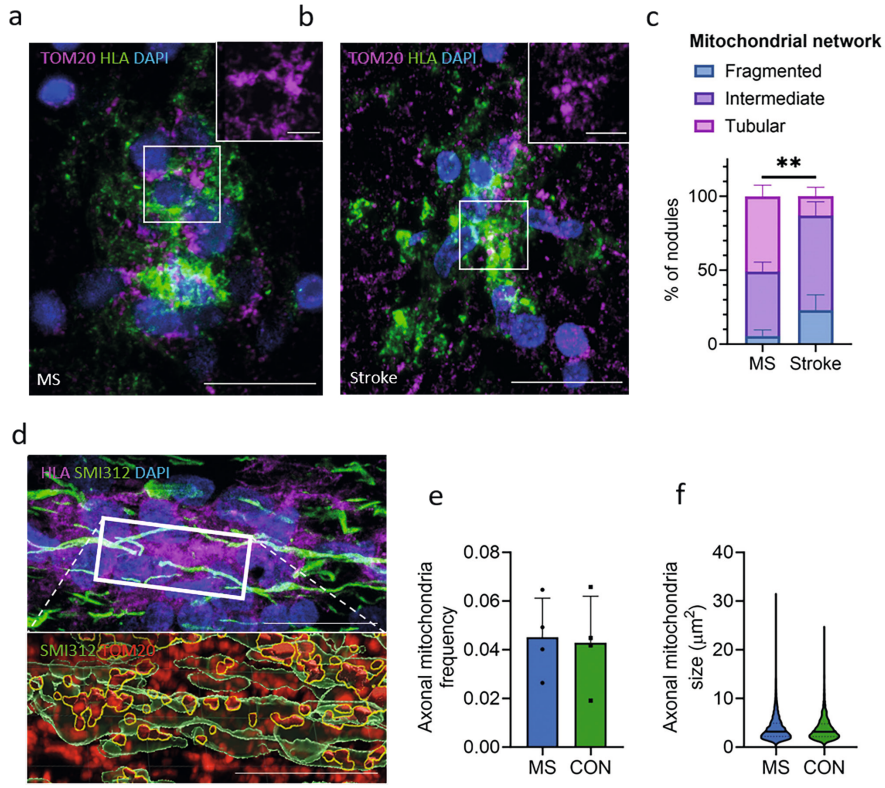


**Figure 7: Microglia nodules in MS show a more tubular mitochondrial network.** STED microscopy of immunohistochemistry staining. (a) An HLA⁺ microglia nodule in MS with a fused and tubular TOM20 mitochondrial network and (b) an HLA⁺ microglia nodule in stroke with a fragmented TOM20 mitochondrial network. (c) Microglia nodules in MS more often showed a tubular and fused mitochondrial network compared to microglia nodules in stroke. Bar plot showing mean percentage per type of mitochondrial network in MS and in stroke. (d) Axonal mitochondria in axons encapsulated by a microglia nodule. In the animated panel (below), axons are reconstructed in green and mitochondria inside axons are highlighted with yellow outlining. There was no difference in (e) frequency and (f) size of axonal mitochondria in axons encapsulated by HLA+ microglia in MS and controls. Significance was tested with a quasibinomial linear model, p value <0.01 is indicated with **. Scale bar indicates 60 µm.

## DISCUSSION

Here, we have studied the potential involvement of microglia nodules in MS-lesion formation by correlating their presence with pathological and clinical characteristics and by comparing microglia nodules in MS to microglia nodules in stroke and to surrounding non-nodular (NA)WM using RNA sequencing of laser-microdissection captured tissue and IHC. The combination of methods provided a highly detailed and comprehensive dissection of the microglia nodule in MS as putative precursors of lesion formation in MS. We show that MS microglia nodules (1) correlate with more severe MS pathology, (2) upregulate expression of genes similar to MS-lesions, (3) upregulate expression of genes associated with adaptive and innate immune responses, lymphocyte activation, phagocytosis, lipid metabolism, and metabolic stress, (4) have nearby lymphocyte presence, (5) contain partially demyelinated axons, (6) are associated with IgG-transcription, complement activation, and MAC formation, and (7) are in a hypermetabolic state associated with increased pro-inflammatory cytokine and ROS gene expression. Our findings indicate that the nodule milieu may be held responsible for early lesion formation.

We here show that microglia nodules in MS are pathologically relevant. MS donors with microglia nodules compared to those without microglia nodules had a higher lesion load and reactive site load. The proportion of active lesions was higher, and the proportion of inactive and remyelinated lesions was lower in MS donors with microglia nodules compared to those without. Interestingly, there was no difference in the proportion of mixed active/inactive lesions. As we hypothesize that active lesions precede mixed active/inactive lesions, this indicates that microglia nodules are possibly associated with new MS lesion formation. Therefore, MS donors without microglia nodules may represent a subgroup in which frequency of new lesion formation has decreased, whereas those with microglia nodules may still develop new MS lesions. Presence of microglia nodules was not associated with clinically more severe MS. Although microglia nodules in MS do not seem to represent previous clinical progression, this does not exclude the possibility that they may represent future clinical progression. Furthermore, clinical progression is associated with more factors than new lesion formation, such as atrophy and ongoing axonal damage [59].

Gene expression was deconvoluted for cell types through integration of a dataset obtained by Absinta *et al.* (2021). Nodule tissue in MS compared to NAWM contained a higher proportion of microglia, a lower proportion of oligodendrocytes, and a higher proportion of endothelial cells. The lower proportion of oligodendrocytes may indicate demyelination of axons encapsulated by nodules. Although IHC showed no difference in percentage

of microglia nodules in contact with vessels in MS compared to stroke, the inflammatory milieu of the vessel in MS may differ from that in stroke. In MS, vessels are preferential lesion formation sites [60], and previously, we have shown that in the NAWM, there is an increase in perivascular tissue-resident memory T cells, which may be influencing the milieu in which microglia nodules in MS reside [61]. Therefore, the cell type composition of nodule tissue in MS suggests that microglia nodules may represent the first stage of MS lesion formation. Future studies focusing on single-cell sequencing and spatial transcriptomics will gain further insight on cell-specific gene expression.

Microglia nodules highly expressed genes that were previously implicated in MS pathology, such as *LPL*, *CXCL16*, *CD14*, *CDKN1A*, and *CHI3L1* [10,51]. Moreover, *CXCL16*, *MX1*, *HLA-DRB5*, *ISG15*, *IFNAR2*, and *IL1B* were previously found upregulated in active lesions or the rim of mixed active/inactive lesions, and *CXCL16* and *CHI3L1*, related to lipid binding, were found upregulated in perilesional areas of active lesions and are indicative for the expansion of lesions [27,28,48]. *CXCL16*, *CHI3L1*, *IFNAR2*, and *HLA-DRB5* have furthermore been suggested as potential prognostic markers in MS [49,52–54]. These genes of interest were not differentially expressed in the non-nodular NAWM in MS compared to the non-nodular WM in stroke. From this, we conclude that microglia nodules in MS show signs of lesion-associated microglia activation and are not part of a diffuse reaction of chronic damage in MS NAWM.

Interestingly, we found MS microglia nodule-specific upregulation of genes associated with lipid metabolism and catabolism (*DAGLB, IAH1, PLCD3, FABP5, ACLY, CHI3L2, STARD13*, and *GPCPD1*) [44]. On the protein level, microglia in the non-nodular (NA)WM rarely expressed FABP5, DAGLB, IAH1, or STARD13, and microglia nodules in MS compared to in stroke were more often FABP5$^+$, DAGLB$^+$, or STARD13$^+$. Of interest, microglia surrounding microglia nodules also rarely expressed FABP5, DAGLB, IAH1, or STARD13. This indicates that upregulation of lipid metabolism is not an intrinsic effect of MS nor a diffuse effect. Therefore, microglia nodules are likely activated by a driver within the microenvironment of the nodule itself. The percentage of IAH1$^+$ microglia nodules was only numerically higher in MS compared to stroke, likely indicating that the increased expression of IAH1 is also driven by other cell types than by microglia alone. We hypothesize that lipid metabolic processes are key in progression of an MS nodule to an inflammatory demyelinating lesion. Previously, we have shown that there are more mitochondria in axons in the NAWM [32] that may precede lipid oxidation in MS [58]. Potentially, this is an important trigger in the formation of microglia nodules. Therefore, microglia nodules in MS and in stroke were stained for lysosomal oxidized phospholipids. Indeed, in MS, a higher percentage of microglia nodules contained phagocytosed oxidized

lipids, indicating that potentially these microglia nodules had formed to clear up damaged myelin. Interestingly, in normal-appearing optic nerve tissue of MS donors, some axons encapsulated by microglia nodules were partially demyelinated, which was not found in control cases. It cannot be excluded that in stroke, axons encapsulated by microglia nodules are partially demyelinated. However, considering the gene expression analysis and IHC of lipid metabolism markers, it is likely that this partial demyelination is MS microglia nodule specific. Considering the differential gene expression and the partially demyelinated axons in the nodules in MS, some nodules seem to be involved in demyelination and the formation of new lesions.

In contrast to what was previously found [24], with gene expression analysis and IHC we show the presence of C1q associated with microglia nodules in both MS and stroke. As complement deposition is necessary for Wallerian degeneration [62], and Wallerian degeneration is a commonality between MS and stroke, microglia nodules in MS and stroke were likely to possess similarities.

Gene expression analysis indicates close proximity of activated lymphocytes that are influencing and being influenced by the microglia nodules in MS and not in stroke (*NCKAP1L, CASP3, JAK3, TCIRG1, CORO1A, GRB2, IRF8, TLR2, IL18)*. With IHC, we found $CD20^+$ B cells, $CD138^+$ plasma cells and $IgG^+$ plasmablasts in close proximity to microglia nodules in MS and not in stroke, and in MS more microglia nodules were associated with activated, proliferating $CD3^+$ T cells and $CD38^+$ plasmablasts. Only a subset of the microglia nodules were in direct contact with lymphocytes, however lymphocytes can be involved in demyelination and acute neurodegeneration through secretion of soluble factors that can activate microglia and do not need direct cell contact [63,64]. Previously, Van Noort *et al*. (2011) have hypothesized that microglia nodules in MS no longer reflect a local neuroprotective and reparative response if there is presence of lymphocytes. Possibly, the presence of activated T cells and Ig-producing B-cell blasts near some microglia nodules together with the phagocytosis of oxidized lipids in MS creates a volatile situation. This might indicate a critical turning point in which the nodule is not able to resolve and progresses into a demyelinating and inflammatory site. Previously, we showed MS NAWM to be enriched for perivascular B cells and T cells [61,65]. These lymphocytes may produce soluble factors contributing to lesion formation as cytokines and Igs [47,63,64]. Therefore, as we show lymphocytes in close proximity to microglia nodules in MS, they may be contributing to the inflammatory environment in which microglia nodules reside.

Moreover, we found $IgG^+$ plasmablasts and IgG deposition in the lumen of blood vessels, possibly $IgG^+$ serum, in MS and not in stroke. We found that tissue containing microglia nodules in MS had significant upregulated Ig

genes (*IGKC*, *IGHG1*, *IGHG2*, and *IGKV3-15*) compared to tissue containing stroke nodules. This corresponds with the characteristic high prevalence of intrathecal unique oligoclonal IgG production in MS and the presence of B cells in MS NAWM [64]. The absence of IgG in stroke donors is unsurprising. A recent study has shown that only few patients with acute ischemic stroke have intrathecal immunoglobulin synthesis (5.7%), of which 33% had a comorbid chronic inflammatory disease, such as MS [66]. Furthermore, most donors had experienced stroke >9 months after death, therefore the chance of still having ongoing IgG production is low in our cohort [67]. Although MS donors with any signs of stroke or ischemia were excluded from the cohort, microvascular pathology was not specifically investigated throughout the CNS, and we can therefore not fully excluded effects of microvascular pathology. Previously, we have shown that microglia in the NAWM are immunosuppressed [68], and that Igs can break this immune tolerance of microglia cells through Fcγ receptors and thereby potentiate inflammation by microglia [69]. Therefore, the presence of Ig-producing cells near microglia nodules in MS in combination with the activation of microglia through pro-inflammatory cytokines secreted by nearby, activated lymphocytes may represent a hazardous situation. Furthermore, complement deposition was found in microglia nodules in both stroke as well as in MS, but only in MS, Igs were found. This may lead to activation of the complement cascade and subsequently to MAC formation and cell death in MS and not in stroke [70]. Previously, it was shown that microglia nodules, both in stroke as well as in MS, encapsulate $C3d^+$ complement deposits associated with the degeneration of axons [17,24,29]. Here, we demonstrate that microglia nodules in MS are more often associated with $C3d^+$ complement deposits compared to microglia nodules in stroke, and microglia nodules in MS were also more often associated with MAC formation. MAC staining was found mainly in the cytoplasm of $HLA^+$ microglia cells, which could indicate osmolysis of the microglia nodule itself or phagocytosis of MAC-targeted cells by the microglia. This may be a key mechanism underlying progression of microglia nodules in MS to Ig-associated, complement-dependent, demyelinating inflammatory lesions. These findings suggest that MS therapies associated with loss of intrathecal oligoclonal bands may also associate with a reduced odds of nodules progressing towards a lesion. Likewise, a higher intrathecal oligoclonal Ig production at the first symptoms of MS is associated with higher odds of new lesion development on MRI and a swifter occurrence of relapses [71–73].

Our data indicate that microglia nodules in MS have a disturbed cell metabolism (*PPRC1*, *SAMM50*, *MTG1*, *ACOX1*, *COA4*) and are responding to as well as producing ROS (*ASPDH*, *BID*, *CRYZL1*, *IDH1*, *MAOB*, *SMAD3*). As axonal mitochondrial dysfunction occurs in many disorders, mitochondria may act as a central sensor for axonal degenerative stimuli. It is hypothesized

that degradative processes are activated when concerted stimuli surpass the mitochondrial homeostatic capacity [74]. Surprisingly, the mitochondria frequency and size in axons encapsulated by microglia nodules were not affected in MS compared to stroke. Possibly, changes to the axonal mitochondria in the axons encapsulated by the microglia nodules are subtle, and electron microscopy may provide more insight in early morphological changes of axonal mitochondria [75]. Correction for the proportion of microglia in the MS nodules negated significance, however this is not very surprising as microglia are main producers of ROS and therefore, the proportion of microglia cells may play a role in the neurodegenerative properties of an MS nodule. Generally, activated microglia cells switch from oxidative phosphorylation to glycolysis and form a fragmented mitochondria network [76]. Notably, microglia nodules in MS generally possess a more tubular and less fragmented mitochondrial network compared to microglia nodules in stroke. We hypothesize that the combined activation of microglia cells by surrounding lymphocytes together with the phagocytosis of oxidized lipids may result in a hypermetabolic and hyperinflammatory state, as previously shown for atherosclerosis [77,78], in which the microglia rely both on glycolysis as well as oxidative phosphorylation. This can result in prolonged longevity and increased production of cytokines and ROS. We further show that microglia nodules in MS compared to stroke have upregulated genes associated with production of cytokines, specifically IFNy and TNF (*IRF8*, *GADD*, *IFNAR2*, *CD84*, *LRRK2*, *FADD*, *LPL*, *TLR2*, *EGR1*, and *IL18*). Future studies need to elucidate a causal relation between the combined stimulation of the microglia cells through pro-inflammatory cytokines and phagocytosis of oxidized phospholipids, the shift in mitochondrial network, and the production of cytokines, as this opens up a potentially interesting therapeutic avenue.

In summary, we propose that some microglia nodules in MS that have the potential to progress into inflammatory and demyelinating MS lesions, whereas those in stroke will not. Therefore, differences between microglia nodules in MS and stroke can provide insight in mechanisms behind MS lesion formation. Here, we demonstrate that microglia nodules in MS upregulate lesion-associated genes and genes indicative for demyelination. We also show that some microglia nodules in MS encapsulate partially demyelinated axons. Moreover, we here describe that a combination of activated T cells, Ig-producing B cells, and oxidized lipids in and around MS microglia nodules may together enable microglia nodules to become hypermetabolic, form MACs, and give rise to 'mini' MS lesions. Together, we conclude that some microglia nodules in MS are likely sites of lesion initiation, and represent an interesting therapeutic target to prevent early demyelination and MS lesion formation.

**Data availability**
The RNA-sequencing dataset is available in the Gene Expression Omnibus (GEO) database, accession number GSE234700. The quantitative IHC dataset is available as supplementary file 'source data'. The code corresponding to the findings of this study are available on request from the corresponding author upon reasonable request.

**Acknowledgements**
We are grateful to the brain donors and their families for their commitment to the Netherlands Brain Bank donor program. We thank Niamh McNamara for her input on the manuscript.

**Funding**
Funding for this research was obtained from MS Research grant 19-1079 and MoveS inspiration Grant 17-975.



**Competing interest**
The authors declare no competing interests.

## REFERENCES


1. Lucchinetti, C. *et al.* Heterogeneity of multiple sclerosis lesions: implications for the pathogenesis of demyelination. *Ann. Neurol.* 47, 707–717 (2000).
2. Lassmann, H. Multiple sclerosis pathology. *Cold Spring Harb. Perspect. Med.* 8, 1–15 (2018).
3. Matcovitch-Natan, O. *et al.* Microglia development follows a stepwise program to regulate brain homeostasis. *Science (80-. ).* 353, aad8670 (2016).
4. Li, Q and Barres, B. Microglia and macrophages in brain homeostasis and disease. *Nat. Rev. Immunol.* 18, 225–242 (2018).
5. Luchetti, S. *et al.* Progressive multiple sclerosis patients show substantial lesion activity that correlates with clinical disease severity and sex: a retrospective autopsy cohort analysis. *Acta Neuropathol.* 135, 511–528 (2018).
6. Miller, D. H., Johnson, G., Tofts, P. S., Macmanus, D. & McDonald, W. I. Precise relaxation time measurements of normal–appearing white matter in inflammatory central nervous system disease. *Magn. Reson. Med.* 11, 331–336 (1989).
7. De Groot, C. J. A. *et al.* Post-mortem MRI-guided sampling of multiple sclerosis brain lesions: Increased yield of active demyelinating and (p)reactive lesions. *Brain* 124, 1635–1645 (2001).
8. Moll, N. M. *et al.* Multiple sclerosis normal-appearing white matter: Pathology-imaging correlations. *Ann. Neurol.* 70, 764–773 (2011).
9. Elliott, C. *et al.* Abnormalities in normal-appearing white matter from which multiple sclerosis lesions arise. *Brain Commun.* 3, (2021).
10. van der Poel, M. *et al.* Transcriptional profiling of human microglia reveals grey–white matter heterogeneity and multiple sclerosis-associated changes. *Nat. Commun.* 10, 1–13 (2019).
11. Hammond, T. R. *et al.* Single-Cell RNA Sequencing of Microglia throughout the Mouse Lifespan and in the Injured Brain Reveals Complex Cell-State Changes. *Immunity* 50, 253-271.e6 (2019).
12. Masuda, T. *et al.* Spatial and temporal heterogeneity of mouse and human microglia at single-cell resolution. *Nature* 566, 388–392 (2019).
13. Paolicelli, R. C. *et al.* Microglia states and nomenclature: A field at its crossroads. *Neuron* 110, 3458–3483 (2022).
14. Sanders, V., Conrad, A. J. & Tourtellotte, W. W. On classification of post-mortem multiple sclerosis plaques for neuroscientists. *J. Neuroimmunol.* 46, 207–216 (1993).
15. Li, H., Newcombe, J., Groome, N. P. & Cuzner, M. L. Characterization and distribution of phagocytic macrophages in multiple sclerosis plaques. *Neuropathol. Appl. Neurobiol.* 19, 214–223 (1993).
16. Prineas, J. W. *et al.* Immunopathology of secondary-progressive multiple sclerosis. *Ann. Neurol.* 50, 646–657 (2001).
17. Barnett, M. H., Parratt, J. D. E., Cho, E. S. & Prineas, J. W. Immunoglobulins and complement in postmortem multiple sclerosis tissue. *Ann. Neurol.* 65, 32–46 (2009).
18. van Noort, J. M. *et al.* Preactive multiple sclerosis lesions offer novel clues for neuroprotective therapeutic strategies. *CNS Neurol. Disord. Drug Targets* 10, 68–81 (2011).
19. Singh, S. *et al.* Microglial nodules in early multiple sclerosis white matter are associated with degenerating axons. *Acta Neuropathol.* 125, 595–608 (2013).

20. Bsibsi, M. *et al.* Alpha-B-crystallin induces an immune-regulatory and antiviral microglial response in preactive multiple sclerosis lesions. *J. Neuropathol. Exp. Neurol.* 72, 970–979 (2013).
21. Sato, F. *et al.* 'Microglial nodules' and 'newly forming lesions' may be a Janus face of early MS lesions; implications from virus-induced demyelination, the Inside-Out model. *BMC Neurol.* 15, 1–6 (2015).
22. Hendrickx, D. A. E., van Eden, C. G., Schuurman, K. G., Hamann, J. & Huitinga, I. Staining of HLA-DR, Iba1 and CD68 in human microglia reveals partially overlapping expression depending on cellular morphology and pathology. *J. Neuroimmunol.* 309, 12–22 (2017).
23. Prineas, J. W. & Parratt, J. D. E. Multiple Sclerosis: Microglia, Monocytes, and Macrophage-Mediated Demyelination. *J. Neuropathol. Exp. Neurol.* 80, 975–996 (2021).
24. Michailidou, I. *et al.* Complement C3 on microglial clusters in multiple sclerosis occur in chronic but not acute disease: Implication for disease pathogenesis. *Glia* 65, 264–277 (2017).
25. Van Der Valk, P. & Amor, S. Preactive lesions in multiple sclerosis. *Curr. Opin. Neurol.* 22, 207–213 (2009).
26. Gay, F. W., Drye, T. J., Dick, G. W. A. & Esiri, M. M. The application of multifactorial cluster analysis in the staging of plaques in early multiple sclerosis: Identification and characterization of the primary demyelinating lesion. *Brain* 120, 1461–1483 (1997).
27. Hendrickx, D. A. E. *et al.* Selective upregulation of scavenger receptors in and around demyelinating areas in multiple sclerosis. *J. Neuropathol. Exp. Neurol.* 72, 106–118 (2013).
28. Burm, S. M. *et al.* Expression of IL-1β in rhesus EAE and MS lesions is mainly induced in the CNS itself. *J. Neuroinflammation* 13, (2016).
29. Horssen, J. Van *et al.* Clusters of activated microglia in normal-appearing white matter show signs of innate immune activation. *J. Neuroinflammation* 9, (2012).
30. Cree, B. A. C. *et al.* Secondary Progressive Multiple Sclerosis: New Insights. *Neurology* 97, 378–388 (2021).
31. Kuhlmann, T. *et al.* An updated histological classification system for multiple sclerosis lesions. *Acta Neuropathol.* 133, 13–24 (2017).
32. Bosch, A. M. R. Van Den *et al.* Ultrastructural Axon–Myelin Unit Alterations in Multiple Sclerosis Correlate with Inflammation. *Ann. Neurol.* 1–15 (2022) doi:10.1002/ana.26585.
33. Kim, D., Paggi, J. M., Park, C., Bennett, C. & Salzberg, S. L. Graph-based genome alignment and genotyping with HISAT2 and HISAT-genotype. *Nat. Biotechnol.* 37, 907–915 (2019).
34. Anders, S., Pyl, P. T. & Huber, W. HTSeq-A Python framework to work with high-throughput sequencing data. *Bioinformatics* 31, 166–169 (2015).
35. Robinson, M. D., McCarthy, D. J. & Smyth, G. K. edgeR: A Bioconductor package for differential expression analysis of digital gene expression data. *Bioinformatics* 26, 139–140 (2009).
36. Ritchie, M. E. *et al.* Limma powers differential expression analyses for RNA-sequencing and microarray studies. *Nucleic Acids Res.* 43, e47 (2015).
37. Robinson, M. D. & Oshlack, A. A scaling normalization method for differential expression analysis of RNA-seq data. *Genome Biol.* 11, 1–9 (2010).
38. Law, C. W., Chen, Y., Shi, W. & Smyth, G. K. Voom: Precision weights unlock linear model analysis tools for RNA-seq read counts. *Genome Biol.* 15, 1–17 (2014).

39. Hunt, G. J., Freytag, S., Bahlo, M. & Gagnon-Bartsch, J. A. Dtangle: Accurate and robust cell type deconvolution. *Bioinformatics* 35, 2093–2099 (2019).
40. Darmanis, S. *et al*. A survey of human brain transcriptome diversity at the single cell level. *Proc. Natl. Acad. Sci. U. S. A.* 112, 7285–7290 (2015).
41. Patrick, E. *et al*. Deconvolving the contributions of cell-type heterogeneity on cortical gene expression. *PLoS Comput. Biol.* 16, 1–17 (2020).
42. Schirmer, L. *et al*. Neuronal vulnerability and multilineage diversity in multiple sclerosis. *Nature* 573, 75–82 (2019).
43. Palmer, C., Diehn, M., Alizadeh, A. A. & Brown, P. O. Cell-type specific gene expression profiles of leukocytes in human peripheral blood. *BMC Genomics* 7, 1–15 (2006).
44. Sherman, B. T. *et al*. DAVID: a web server for functional enrichment analysis and functional annotation of gene lists (2021 update). *Nucleic Acids Res.* 50, 216–221 (2022).
45. Schindelin, J. *et al*. Fiji: An open-source platform for biological-image analysis. *Nat. Methods* 9, 676–682 (2012).
46. Chang, Y. J., Chen, K. W. & Chen, L. Mitochondrial ros1 increases mitochondrial fission and respiration in oral squamous cancer carcinoma. *Cancers (Basel).* 12, 1–15 (2020).
47. Hsiao, C. C. *et al*. Osteopontin associates with brain TRM-cell transcriptome and compartmentalization in donors with and without multiple sclerosis. *iScience* 26, (2023).
48. Hendrickx, D. A. E. *et al*. Gene expression profiling of multiple sclerosis pathology identifies early patterns of demyelination surrounding chronic active lesions. *Front. Immunol.* 8, (2017).
49. Holmøy, T. *et al*. Inflammation Markers in Multiple Sclerosis: CXCL16 Reflects and May Also Predict Disease Activity. *PLoS One* 8, 1–9 (2013).
50. Losy, J. & Niezgoda, A. IL-18 in patients with multiple sclerosis. *Acta Neuropathol. Scand.* 3, 171–173 (2001).
51. Miedema, A. *et al*. Brain macrophages acquire distinct transcriptomes in multiple sclerosis lesions and normal appearing white matter. *Acta Neuropathol. Commun.* 10, 1–18 (2022).
52. Caillier, S. J. *et al*. Uncoupling the Roles of HLA-DRB1 and HLA-DRB5 Genes in Multiple Sclerosis . *J. Immunol.* 181, 5473–5480 (2008).
53. Novakova, L. *et al*. Cerebrospinal fluid biomarkers as a measure of disease activity and treatment efficacy in relapsing-remitting multiple sclerosis. *J. Neurochem.* 141, 296–304 (2017).
54. Leyva, L. *et al*. IFNAR1 and IFNAR2 polymorphisms confer susceptibility to multiple sclerosis but not to interferon-beta treatment response. *J. Neuroimmunol.* 163, 165–171 (2005).
55. Bido, S. *et al*. Microglia-specific overexpression of α-synuclein leads to severe dopaminergic neurodegeneration by phagocytic exhaustion and oxidative toxicity. *Nat. Commun.* 12, 1–15 (2021).
56. Loos, M. The functions of endogenous C1q, a subcomponent of the first component of complement, as a receptor on the membrane of macrophages. *Mol. Immunol.* 19, 1229–1238 (1982).
57. Absinta, M. *et al*. A lymphocyte–microglia–astrocyte axis in chronic active multiple sclerosis. *Nature* 597, 709–714 (2021).
58. Haider, L. *et al*. Oxidative damage in multiple sclerosis lesions. *Brain* 134, 1914–1924 (2011).

59. Andravizou, A. *et al*. Brain atrophy in multiple sclerosis: mechanisms, clinical relevance and treatment options. *Autoimmun. Highlights* 10, (2019).
60. Al-Louzi, O. *et al*. Central Vein Sign Profile of Newly Developing Lesions in Multiple Sclerosis: A 3-Year Longitudinal Study. *Neurol. Neuroimmunol. neuroinflammation* 9, 1–12 (2022).
61. Fransen, N. L. *et al*. Tissue-resident memory T cells invade the brain parenchyma in multiple sclerosis white matter lesions. *Brain* 143, 1714–1730 (2020).
62. Ramaglia, V. *et al*. C3-dependent mechanism of microglial priming relevant to multiple sclerosis. *Proc. Natl. Acad. Sci.* 109, 965–970 (2012).
63. Machado-Santos, J. *et al*. The compartmentalized inflammatory response in the multiple sclerosis brain is composed of tissue-resident CD8+ T lymphocytes and B cells. *Brain* 141, 2066–2082 (2018).
64. Bogers, L. *et al*. Selective emergence of antibody-secreting cells in the multiple sclerosis brain. *eBioMedicine* 89, 104465 (2023).
65. Fransen, N. L. *et al*. Absence of B Cells in Brainstem and White Matter Lesions Associates With Less Severe Disease and Absence of Oligoclonal Bands in MS. *Neurol. Neuroimmunol. neuroinflammation* 8, 1–11 (2021).
66. Laichinger, K. *et al*. No evidence of oligoclonal bands, intrathecal immunoglobulin synthesis and B cell recruitment in acute ischemic stroke. *PLoS One* 18, 1–10 (2023).
67. Bernstein, J. J. & Goldberg, W. J. Injury-related spinal cord astrocytes are immunoglobulin-positive (IgM and/or IgG) at different time periods in the regenerative process. *Brain Res.* 426, 112–118 (1987).
68. Melief, J. *et al*. Microglia in normal appearing white matter of multiple sclerosis are alerted but immunosuppressed. *Glia* 61, 1848–1861 (2013).
69. van der Poel, M., Hoepel, W., Hamann, J., Huitinga, I. & Dunnen, J. den. IgG Immune Complexes Break Immune Tolerance of Human Microglia. *J. Immunol.* 205, 2511–2518 (2020).
70. Toapanta, F. R. & Ross, T. M. Complement-mediated activation of the adaptive immune responses: Role of C3d in linking the innate and adaptive immunity. *Immunol. Res.* 36, 197–210 (2006).
71. Klein, A. *et al*. CSF parameters associated with early MRI activity in patients with MS. *Neurol. Neuroimmunol. NeuroInflammation* 6, 1–11 (2019).
72. Spelman, T. *et al*. Quantifying risk of early relapse in patients with first demyelinating events: Prediction in clinical practice. *Mult. Scler.* 23, 1346–1357 (2017).
73. Kuhle, J. *et al*. Conversion from clinically isolated syndrome to multiple sclerosis: A large multicantre study. *Mult. Scler.* 21, 1013–1024 (2015).
74. Court, F. A. & Coleman, M. P. Mitochondria as a central sensor for axonal degenerative stimuli. *Trends Neurosci.* 35, 364–372 (2012).
75. Mageswaran, S. K. *et al*. Nanoscale details of mitochondrial constriction revealed by cryoelectron tomography. *Biophys. J.* 122, 3768–3782 (2023).
76. Pereira, O. R., Ramos, V. M., Cabral-Costa, J. V. & Kowaltowski, A. J. Changes in mitochondrial morphology modulate LPS-induced loss of calcium homeostasis in BV-2 microglial cells. *J. Bioenerg. Biomembr.* 53, 109–118 (2021).
77. Di gioia, M. *et al*. Endogenous oxidized phospholipids reprogram cellular metabolism and boost hyperinflammation Marco. *Nat. Immunol.* 21, 42–53 (2020).
78. Di Gioia, M. & Zanoni, I. Dooming Phagocyte Responses: Inflammatory Effects of Endogenous Oxidized Phospholipids. *Front. Endocrinol. (Lausanne).* 12, 1–13 (2021).

## SUPPLEMENTAL FILES

**Supplementary table 1**: Outliers removed from RNA sequencing analysis
Available under supplementary information at https://www.nature.com/articles/s41467-024-46068-3

**Supplementary table 2:** Primers used for RT-qPCR on nodule tissue
Available under supplementary information at https://www.nature.com/articles/s41467-024-46068-3

**Supplementary table 3:** Top 50 upregulated DE genes in MS nodules vs MS nnNAWM
Available under supplementary information at https://www.nature.com/articles/s41467-024-46068-3

**Supplementary table 4:** Upregulated DE genes in stroke nodules vs stroke nnNAWM
Available under supplementary information at https://www.nature.com/articles/s41467-024-46068-3

**Supplementary table 5:** Top 50 upregulated DE genes in MS nodules vs stroke nodules
Available under supplementary information at https://www.nature.com/articles/s41467-024-46068-3

**Supplementary table 6:** Upregulated DE genes in MS nnNAWM vs stroke nnNAWM
Available under supplementary information at https://www.nature.com/articles/s41467-024-46068-3

**Supplementary table 7:** DE genes of interest
Available under supplementary information at https://www.nature.com/articles/s41467-024-46068-3

**Supplementary table 8:** Significantly enriched GO classes in MS nodules vs MS nnNAWM
Available under supplementary information at https://www.nature.com/articles/s41467-024-46068-3

**Supplementary table 9:** Significantly enriched GO classes in MS nodules vs stroke nodules
Available under supplementary information at https://www.nature.com/articles/s41467-024-46068-3

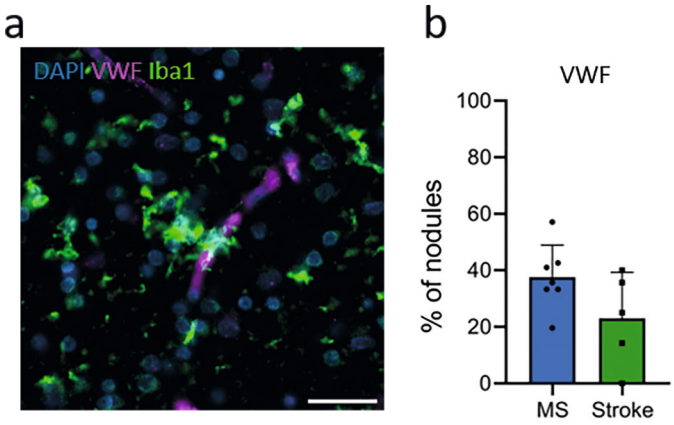


**Supplementary figure 1:** A) Immunohistochemistry staining of iba1⁺ nodule (in green) in MS in contact with a VWF⁺ vessel (in magenta). B) Nodules in MS and in stroke are equally often in contact with vessels, quantified in n=7 MS donors and n=5 stroke donors. Data is shown as mean ± standard deviation. Scalebar = 35 µm. Source data are provided as a Source Data file.

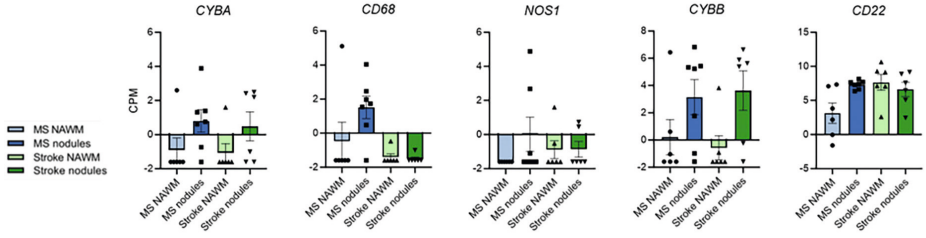


**Supplementary figure 2:** Phagocytic exhaustion markers are not significantly differentially expressed in MS nodules compared to stroke nodules. Analysis performed on n=6 MS NAWM samples, n=7 MS nodule samples, n=6 stroke NAWM samples, n=6 stroke nodule samples. Data is shown as mean ± standard deviation. Source data are provided as a Source Data file.

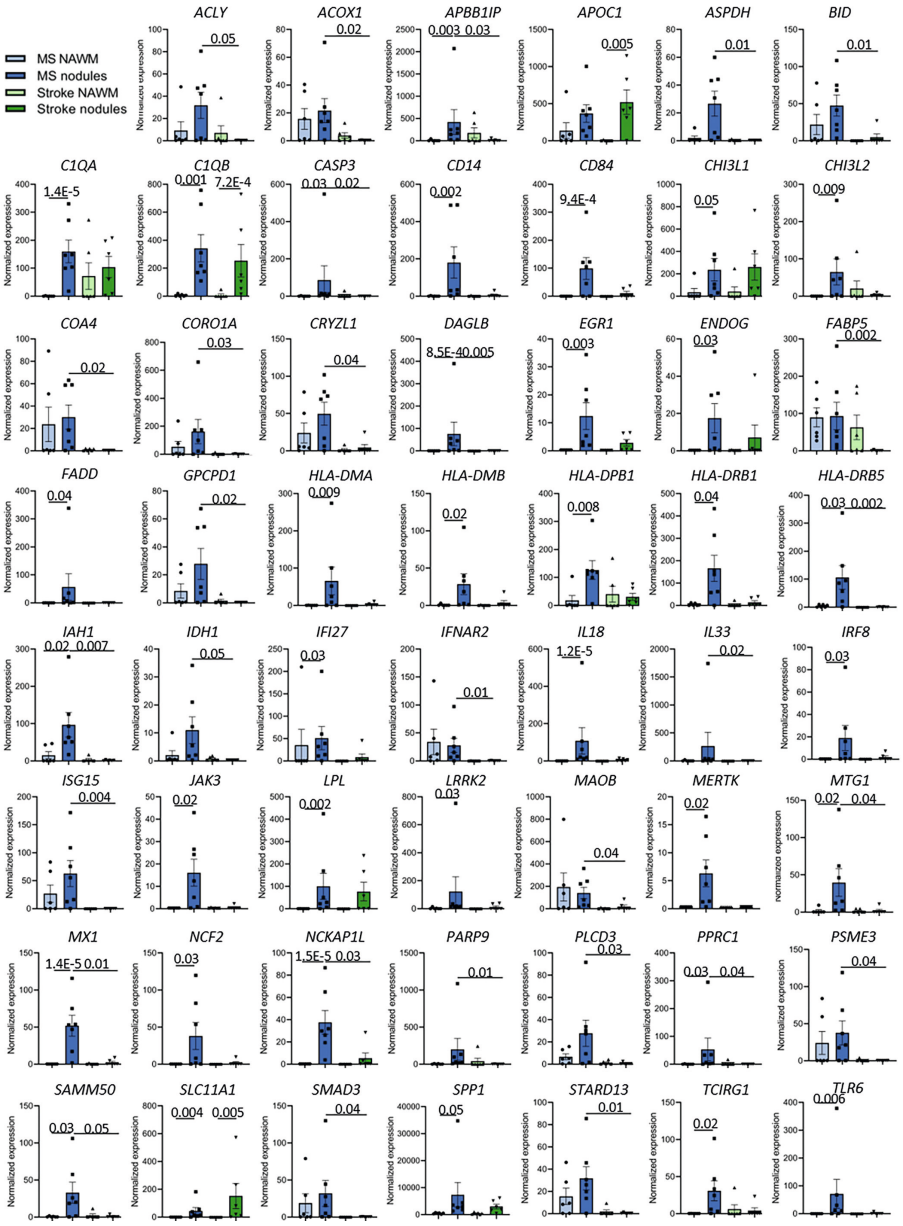


**Supplementary figure 3:** Normalized expression of genes likely involved in functional pathways relevant for MS pathology. Analysis performed on n=6 MS NAWM samples, n=7 MS nodule samples, n=6 stroke NAWM samples, n=6 stroke nodule samples. Data is shown as mean ± standard deviation. Normalized gene expression is calculated as 2log(CPM). p value <0.05 is indicated with *, <0.01 is indicated with **, <0.001 is indicated with ***. Source data are provided as a Source Data file.

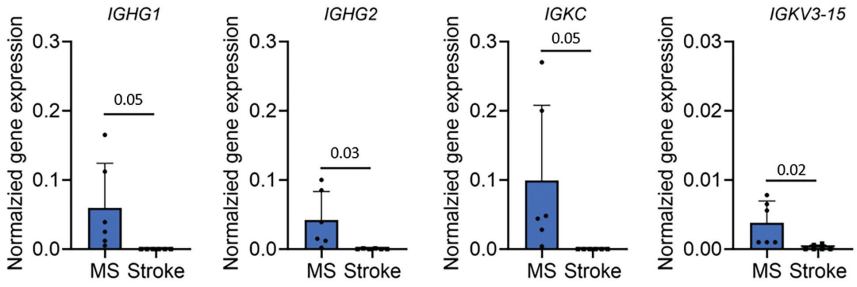


**Supplementary figure 4:** Immunoglobulin gene expression quantified with RT-qPCR of MS (n=6) and stroke (n=6) (NA)WM tissue containing nodules showing higher expression in MS compared to stroke. Data is shown as mean ± standard deviation. Source data are provided as a Source Data file.

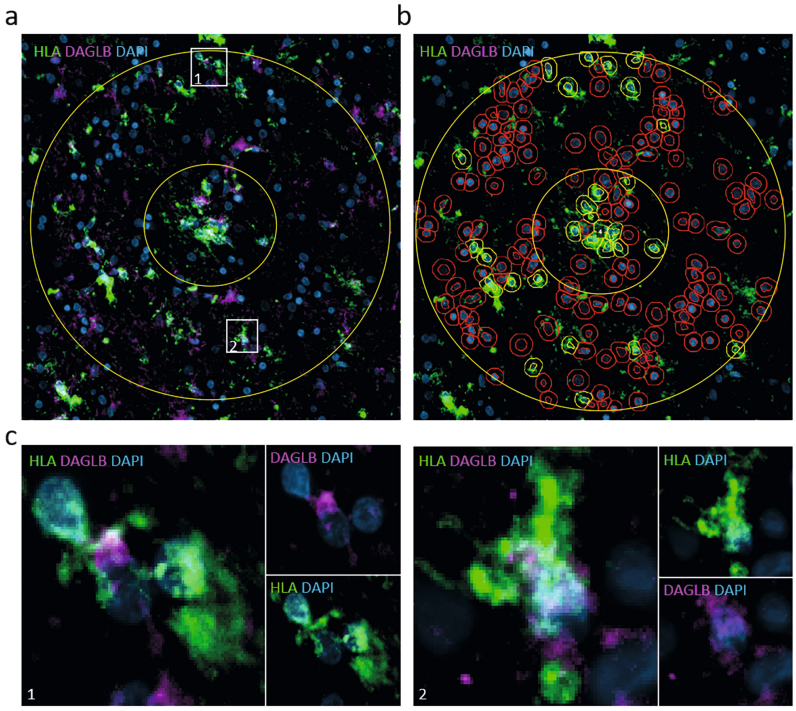


**Supplementary figure 5:** Exemplary figure of quantification of (NA)WM microglia adjacent to microglia nodules for DAGLB, FABP5, IAH1 and STARD13. A) for each nodule, an expansion of 100 µm was created of the annotation. B) Using cell-detection in QuPath, all HLA$^{+}$ cells were annotated with green, all HLA- cells were annotated with red. Each HLA+ cell was annotated as C) negative (left panel) or positive (right panel) for DAGLB.

# Part

# Lesions with foamy microglia are expanding and lesions with ramified microglia are regenerative

2

# CHAPTER 5

# Disentangling the heterogeneity of multiple sclerosis through identification of independent neuropathological dimensions

Alyse de Boer[1], Aletta M.R. van den Bosch[2], Nienke J. Mekkes[1,3], Ekaterina Dagkesamanskaia[1,3], Nina Fransen[2], Eric Hoekstra[1], Joost Smolders[2,4], Jörg Hamann[2,5], Inge Huitinga[2,6,7], Inge R. Holtman[1,7]

[1]Department of Biomedical Sciences of Cells and Systems, Section Molecular Neurobiology, University of Groningen, University Medical Center Groningen, Groningen, The Netherlands; [2]Neuroimmunology Research Group, Netherlands Institute for Neuroscience, Amsterdam, The Netherlands; [3]Machine Learning Lab, Data Science Center in Health, University of Groningen, University Medical Center Groningen, The Netherlands; [4]MS Center ErasMS, Departments of Neurology and Immunology, Erasmus Medical Center, Rotterdam, The Netherlands; [5]Department of Experimental Immunology, Amsterdam Institute for Infection and Immunity, Amsterdam University Medical Centers, University of Amsterdam, Amsterdam, The Netherlands; [6]Swammerdam Institute for Life Sciences, Center for Neuroscience, University of Amsterdam, Amsterdam, The Netherlands; [7]The Netherlands Brain Bank, Netherlands Institute for Neuroscience, Amsterdam, The Netherlands

*Acta Neuropathologica 2024, 147:90*

## ABSTRACT

Multiple sclerosis (MS) is a heterogeneous neurological disorder with regards to clinical presentation and pathophysiology. Here, we investigated the heterogeneity of MS by performing an exploratory factor analysis on quantitative and qualitative neuropathology data collected for 226 MS donors in the Netherlands Brain Bank autopsy cohort. Three promising dimensions were identified and subsequently validated with clinical, neuropathological, and genetic data. Dimension 1 ranged from a predominance of remyelinated and inactive lesions to extensive pathological changes, higher proportions of active and mixed lesions, and foamy microglia morphology. This pattern was positively correlated with more severe disease, the presence of B and T cells, and neuroaxonal damage. Scoring high on dimension 2 was associated with active lesions, reactive sites, and the presence of nodules. These donors had less severe disease, a specific pattern of cortical lesions, and MS risk variants in the human leukocyte antigen region, the latter indicating a connection between disease onset and this neuropathological dimension. Donors scoring high on dimension 3 showed increased lesional pathology with relatively more mixed and inactive lesions and ramified microglia morphology. This pattern was associated with longer disease duration, subpial cortical lesions, less involvement of the adaptive immune system, and less axonal damage. Taken together, the three dimensions may represent (1) demyelination and immune cell activity associated with pathological and clinical progression, (2) microglia (re)activity and possibly lesion initiation, and (3) loss of lesion activity and scar formation. Our findings highlight that a thorough understanding of the interplay between multiple pathological characteristics is crucial to understand the heterogeneity of MS pathology, as well as its association with genetic predictors and disease outcomes. The scores of donors on the dimensions can serve as an important starting point for further disentanglement of MS heterogeneity and translation into observations and interventions in living cohorts with MS.

## INTRODUCTION

Multiple sclerosis (MS) is one of the most common causes of severe neurological disability in early adulthood, resulting from a combination of environmental, lifestyle, and genetic factors [1,2]. This chronic disease is characterised by lesions in the central nervous system, with varying extents of inflammation, demyelination, loss of axons, and gliosis [3]. MS is a highly heterogeneous disease, with contributions from concurrent pathophysiological processes that vary over time and between individuals [4]. As many different regions in the brain and spinal cord can be affected, MS is associated with a broad range of clinical signs and symptoms related to neurological dysfunction. Additionally, there is marked variation in disease course, severity, and response to disease-modifying treatment [5,6]. Historically, MS has been divided into three clinical phenotypes: relapsing-remitting (RR), primary progressive (PP), and secondary progressive (SP) MS [7,8]. This subdivision neither considers the possibility of relapses in progressive MS, nor progression independent of relapse activity in relapsing MS [9]. Therefore, the currently leading view is that this clinical division is rather artificial and that MS should be seen as one heterogeneous disease entity, best described in terms of relapse activity and progression [4,7].



To address the heterogeneity of MS and the challenge this represents for allocating treatment and providing an accurate prognosis, multiple studies have defined MS subtypes based on underlying pathobiological mechanisms, using theory-driven as well as data-driven approaches. For example, analysis of magnetic resonance imaging (MRI) data led to the identification of two patient clusters, which were associated with different levels of clinical disability [10]. Another MRI study defined three subtypes, termed cortex-led, normal-appearing white matter-led, and lesion-led after the site of the earliest MRI abnormalities, which differed in the progression of disease and response to treatment [11]. Furthermore, a study investigating neuropsychological data found five distinct cognitive phenotypes, which were related to clinical, demographic, and MRI features and could be of added value in clinical care [12]. With regards to immunopathology, four patterns of demyelination in early, active MS lesions have been reported [13]. The patterns were heterogeneous between individuals, while lesions within the same brain generally followed the same patterns, even over time [13,14]. This suggests that the four patterns could be used to define MS subgroups that correspond with distinct pathogenetic mechanisms involved in demyelination [13,14]. However, this particular subdivision was not found in more advanced MS as studied at autopsy [15], in which the need for the development of new therapies is even more unmet than in primary stages, and which is the topic of this study.

Here, we aimed to discover dimensions of MS neuropathology, by performing an exploratory factor analysis of mixed data (FAMD) on post-mortem neuropathology data available from a large collection of MS brain donors in the Netherlands Brain Bank (NBB) autopsy cohort. The in-depth characterization of MS brain tissue facilitated a unique input dataset, containing information on the proportion of active, mixed active/inactive (mixed), inactive, and remyelinated white matter lesions, the morphology of microglia present in active and mixed lesions, the lesion load and reactive site load in the brainstem, the cortical lesion rate, and the presence of microglia nodules and perivascular cuffs. To investigate the validity of the FAMD dimensions, additional neuropathological, clinical, and genetic data available for this cohort were assessed. Key parameters that we included were related to disease progression and duration, signs and symptoms and their onset, grey matter lesions, the presence of B and T cells in the brainstem and subcortex, neuroaxonal damage, MS-associated genetic variants, and polygenic risk scores (PRSs).

## MATERIALS AND METHODS

### NBB autopsy procedures and MS lesion characterization

NBB donors provided informed consent for brain autopsy and the use of tissue and data for research purposes. The procedures of the NBB are in compliance with Dutch and European law and have been approved by the Ethics Committee of the VU University Medical Center in Amsterdam, the Netherlands. Both standardized locations in the brainstem and spinal cord as well as macroscopically detectable MS lesions were dissected, as previously described by Luchetti et al. [16]. Since 2001, lesions were additionally dissected under guidance of post-mortem MRI, which increased the yield of active demyelinating lesions and reactive sites [17]. Lesions were classified based on double immunostaining for proteolipid protein and human leukocyte antigen (HLA-DR-DQ) [16]. In total, five qualitatively different white matter lesion types were distinguished: 1) reactive sites, clusters of $HLA^+$ microglia/macrophages without signs of demyelination; 2) active lesions, with partial demyelination and accumulation of $HLA^+$ cells throughout the lesions; 3) mixed lesions, with a demyelinated, hypocellular, and gliotic centre and a rim of $HLA^+$ cells; 4) inactive lesions, a fully demyelinated, hypocellular, and gliotic region with no accumulation of $HLA^+$ cells; and 5) remyelinated lesions, with partial myelination and few $HLA^+$ cells. The $HLA^+$ microglia/macrophages in active and mixed lesions were additionally scored for morphology: 1) thin and ramified; 2) ameboid (rounded) with few ramifications; and 3) foamy. In the remainder, these $HLA^+$ microglia/macrophages will be referred to solely as 'microglia'. Grey matter lesions were dissected as well, and classified according to their location

into: 1) leukocortical, located in both white and grey matter; 2) intracortical; and 3) subpial. Lesions were only considered subpial if the tissue block contained the first layer of the cortex, with the consequence that the number of intracortical lesions is overestimated to some extent. Some (large) cortical lesions may have been sampled and counted multiple times.

Lesion load was previously defined as the total number of active, mixed, inactive, and remyelinated lesions present in standardly dissected brainstem tissue blocks [16,18–22]; similarly, reactive site load was calculated as the total number of reactive sites in these brainstem blocks [16,22]. These values are therefore not affected by sampling bias and considered to be an adequate reflection of the total number of white matter lesions and reactive sites present in a donor, superior to a lesion rate calculated with data from all dissected tissue blocks. Furthermore, the proportions of active, mixed, inactive, and remyelinated lesions relative to the total number of white matter lesions in all dissected tissue blocks were calculated. In addition, the tissue blocks were assessed to determine the presence of cuffs (defined as >1 perivascular ring of leukocytes) and microglia nodules. This was converted into binary scores per donor, indicating the overall presence or absence of cuffing and nodules, respectively. As before, the microglial/macrophage activation score was calculated by assigning scores to the predominant morphology of microglia in active and mixed lesions (ramified = 0, ameboid = 0.5, and foamy = 1) and averaging these scores per donor [16]. With regards to grey matter, the cortical lesion rate was previously defined as the number of cortical lesions per tissue block containing cortex [20]. Note that in contrast to the white matter lesion load, this value can be affected by sampling bias. If one or more cortical lesions were present, the relative proportions of the different grey matter lesion types were determined.



**Identifying dimensions of MS neuropathology**

A centered log ratio (CLR) transformation was applied to the proportional lesion data, to reduce the possibility of correlations arising solely from the constant sum constraint (i.e. for each donor, the values of the proportions sum to 1) [23]. The CLR transformation takes the logarithm of each lesion proportion, relative to the geometric mean of all lesion proportions for a donor; because this requires non-zero data, multiplicative zero replacement was performed beforehand [24]. Both were implemented using the package Compositional (v6.3) with R version 4.1.3 [25]. Initially, analysis was restricted to donors for whom complete proportional white matter lesion data was available (n = 228). To maximize the number of observations in the dataset, missing data in other variables was accepted. For 14 donors, lesion load and reactive site load were missing, most probably because no standard locations were dissected; data on the cortical lesion rate was missing in 25 cases, likely because no blocks with cortical tissue had been

dissected. All missing values were imputed with the function imputeFAMD from the missMDA package (v1.18) [26], based on the predicted optimal number of dimensions returned by estim_ncpFAMD (Kfold cross-validation with standard settings, with the maximum set at 12). The imputed dataset consisted of 228 observations for 13 neuropathology-related variables: transformed white matter lesion proportions, lesion load, reactive site load, cortical lesion rate, and the presence or absence of cuffing and nodules.

Next, a first FAMD (factor analysis of mixed data) was performed using the FactoMineR package (v2.8) [27], which scales continuous and categorical variables in order to balance their impact on the analysis. Of the 12 dimensions comprising the FAMD output, a subset was selected for further investigation based on an objective criterion (eigenvalue > 1.5). Highly contributing outliers were defined as donors that a) contributed substantially to one or more dimensions, i.e. had a contribution larger than the upper cutoff value for the upper whisker of an adjusted boxplot, and b) that were a univariate outlier with regards to the continuous input variables, i.e. had (a) value(s) lower than the lower cutoff value or higher than the upper cutoff value for the whiskers of an adjusted boxplot. Using the adjusted boxplot method ensured that the skewness of the distributions was taken into account when detecting outliers [28]. Donors meeting both conditions a and b were removed from the input dataset, which was followed by further rounds of imputation, FAMD and outlier detection and removal, until no more highly contributing outliers were identified; one round was needed and led to removal of two donors. Altogether, this procedure reduces the impact of individual donors (and variables) on the analysis and thereby results in more robust dimensions that capture shared neuropathological patterns.

**Validation and exploration with additional neuropathology, clinical and genetic data**

To interpret the meaning and validity of the dimensions, relevant external data which was not used as input is of key importance. Here, we assessed whether the dimensions displayed associations with neuropathological, clinical and genetic data for validation purposes, and explored associations with comorbidities and drug use.

**Description of general clinical data**

General clinical information was obtained by retrospective chart analysis for the majority of the donors [16]. Clinical course was extracted from the patient files, categorised by the treating neurologist in clinical practice into relapsing (including both progressive relapsing and relapsing-remitting MS), progressive with a relapsing onset (SP) or progressive without dominant relapsing onset (PP). These phenotypes were reviewed by an independent neurologist. Other

characteristics determined in this manner were age at onset, time from onset to (estimated) Expanded Disability Status Scale (EDSS)-6, and duration of disease.

**Analysis of the frequency and onset of signs and symptoms**

For a complete description of the processing of clinical text data to develop disease trajectories for donors in the NBB autopsy cohort, see Mekkes et al. [29]. Briefly, state-of-the-art natural language processing techniques were used in order to identify the presence of 84 signs and symptoms (attributes) in individual sentences of medical record summaries. This led to a high-quality dataset of clinical disease trajectories, allowing researchers to study the clinical manifestation of signs and symptoms across disorders. For this study, we investigated the frequency and age at onset of the attributes, grouped together into the five overarching domains defined by Mekkes et al. [29]: general, motor, sensory/autonomic, cognitive, and psychiatric. The attribute definitions, ontology structure, and clinical disease trajectories of NBB donors are accessible via https://nnd.app.rug.nl. **Suppl. Fig. 1** (Online Resource 1) shows how often individual attributes were observed in our final cohort (after outlier removal), how many donors experienced the attribute at least once, how often an attribute was observed within the lifetime of these donors, and the ages at which the attribute was observed. To assess the symptom load of donors per domain, the total number of observations (in a donor's lifetime) of all attributes within the domain was divided by the disease duration of the donor. In addition, we determined the median age at onset per domain, by identifying all ages at which the attributes within a domain were first observed and taking the median value.

**Analysis of comorbidities**

Lifetime diagnosis information was available from the study by Mekkes et al. [29]. In short, clinical diagnoses of NBB donors were parsed and manually matched to classes of the Netherlands Neurogenomics Database Human Disease Ontology (NND-HDO, accessible via https://nnd.app.rug.nl or BioPortal (https://bioportal.bioontology.org/ontologies/NND_CD)). In the following, 'category' refers to a higher-level class together with its subclasses, while 'class' is used to indicate only the class itself. For relevant diagnosis categories, we determined how often that category was observed in our final cohort, how many donors had at least one observation of the category, and the years and ages at which the category was observed; the most commonly observed classes in the MS cohort were analysed similarly (**suppl. Fig. 2**, Online Resource 1). If a class was observed multiple times for a donor, only the class observation at the earliest time point was included. To filter out incomplete files and restrict our analysis to comorbidities, donors with no observations of classes other than MS or its subclasses were not considered in our analysis. The relation between comorbidities and the dimensions, year of death, and age at death was investigated for both relevant

categories and common classes by comparing donors with and without at least one observation of the category or class, respectively.

**Analysis of drug use**

Medication data was extracted from the medication summaries in the NBB donor files using a system of text-parsers, and then preprocessed by extracting timepoints, removing non-medication text (including dosages), and manually resolving spelling mistakes and ambiguity. Elements of combination drugs (separated with a slash) were considered individually (e.g. miconazole/hydrocortisone), and common drug names consisting of multiple words (e.g. interferon beta-1a) were manually transformed into one word (connected with dashes). The resulting drug texts were matched to standard Anatomical Therapeutic Chemical (ATC) codes using the MOLGENIS SORTA parser (version 10.1.0) [30,31], modified for drug to ATC matching by Kellmann et al. [32], with the confidence threshold for the similarity score set to 78.5%. For each timepoint, higher ontology level ATC codes were removed if a more specific ATC code (within that same class) was matched as well, to prevent double matching/counting of drug texts. The timepoints were then categorised into 'last hours', 'death year', 'earlier', and 'unknown', and ATC codes were binarized at the level of these categories (i.e. drugs were considered to be observed/not observed per time category). Donor files with ≥ 200 characters and ≥ 25 words in the medication summary that contained observations in both the year of death (i.e. either 'last hours' or 'death year') and another year (i.e. 'earlier' or 'unknown') were considered high quality and were included in our analysis. For all ATC level 1 (L1) classes and a subset of level 2 (L2) classes, we determined how often and at which time category the drug class was observed, and how many donors had at least one observation (**suppl. Fig. 3a**, Online Resource 1). To explore the relation between these drug classes and the dimensions, year of death, and age at death, donors with and without at least one observation of the class were compared, excluding observations in the 'last hours' category. In addition, to address potential confounding of the dimensions by the use of MS-relevant drug therapies, we composed a list with 1) the most commonly observed drugs (over all time categories), 2) the drugs most commonly used by the donors, 3) all drugs within the L1 class 'NERVOUS SYSTEM DRUGS', and 4) all drugs within the L1 class 'ANTINEOPLASTIC AND IMMUNOMODULATING AGENTS'. For each drug on this list (n = 229 unique drugs, of a total of 585 unique drugs observed in the high-quality files), we then determined if it was a disease-modifying or immunosuppressive drug prescribed for MS. **Suppl**. **Fig. 3b** (Online Resource 1) shows an overview of the number of observations and donors using these drugs. Potential confounding was assessed by comparing the scores on the dimensions of donors with and without at least one observation of the disease-modifying

or MS-relevant immunosuppressive drug categories; the association with year of death and age at death was analysed similarly.

**Description of neuropathological data**

Whereas the cortical lesion rate was part of the input dataset, the proportions of grey matter lesion types were used for validation. Similar to the white matter lesion proportions, a CLR transformation was applied before analysing the relation with the dimensions. Furthermore, information on the presence of B cells - either diffusely or as part of (an) infiltrate(s) - in the medulla oblongata was available for 132 donors from a previous study by Fransen et al., which noted that B cell presence at various locations was correlated and could thus be considered a general donor characteristic [18]. We also analysed their data on the presence of B cells in different white matter lesion types in the subcortex when data was available for > 20 donors in our final cohort [18]. The number of $CD3^+$ cells per $mm^2$ in normal-appearing white matter (NAWM) of the pyramidal tract at the level of the medulla oblongata and in subcortical (perilesional) NAWM was previously determined by Fransen et al. [19], and was available for 95 and 53 donors included in this study, respectively. $CD3^+$ cell counts in subcortical white matter lesions derived from the same study were analysed when information was available for > 20 donors [19]. Van den Bosch et al. examined the extent of neuroaxonal damage by measuring neurofilament light chain (NfL) levels in cerebrospinal fluid (CSF), axonal density in the NAWM of the pyramid tract by determining the percentage of Bielschowsky positive area, and acute axonal stress by detecting the presence of amyloid precursor protein (APP) positive axonal fragments or bulbs in subcortical (perilesional) NAWM [21]; this data was available for 99, 55 and 52 of our donors, respectively. Donors with a stroke in the year before death, a clinically silent stroke, or brain atrophy were excluded from the analysis of CSF NfL levels (n = 35 excluded, n = 64 remained), because having a recent or silent stroke or atrophy could confound this data [21].

**Genotyping of the NBB autopsy cohort, quality control (QC) and imputation**

Samples derived from donors in the NBB autopsy cohort were genotyped with the Infinium Global Screening Array (Illumina, v3) by the Human Genomics Facility at Erasmus Medical Centre. The Human Genomics Facility also performed initial processing of the data, using the PLINK toolset [33]. Pre-imputation QC consisted of iterative removal of variants and samples with missing data so that the final call rate exceeded 97.5% (99% after zCall), removal of variants deviating from Hardy-Weinberg equilibrium (HWE) with excess heterozygosity ($P < 1 \times 10^{-5}$), and exclusion of samples with excess heterozygosity (inbreeding coefficient $F_{sample}$ < mean F − 4 × standard deviation (SD)). Genetic duplicates and potential sample swaps were identified and removed. To improve detection

of rare variants, zCall was calibrated and applied [34], followed by QC using the thresholds specified before and removal of duplicate variants. Principal component analysis on ancestry informative markers of samples of the NBB cohort and the 1000 Genomes Project (phase 3, v5 [35]) was used to identify NBB donors with non-European ancestry (deviating > 4 × SD from the mean of the European reference dataset on the first four principal components), which were excluded from further analysis. Correction for first- and second-degree familial relationships within the cohort was performed with KING software [36]. Imputation was done in a two-step procedure using SHAPEIT for phasing and Minimac4 for imputation to the HRC (Haplotype Reference Consortium) r1.1 reference panel [37,38].

**Processing of imputed genetic data and calculation of PRSs (polygenic risk scores)**

Imputed genetic data was processed and analysed using PLINK 2.0 software (v2.00a4LM (3 Mar 2023)) [39]. Variants and samples with a missing call rate > 0.05 were removed. Variants with a nonmajor allele frequency < 0.05, variants with a low or medium quality of imputation (R2 < 0.8) and variants deviating from HWE ($P < 1 \times 10^{-6}$) were filtered out as well. Ultimately, genetic information was available for 194 donors of the final cohort studied here. Since our cohort size precludes an extensive genetic analysis, we decided to focus on two variants: rs3135388, the tagging single nucleotide polymorphism (SNP) of the HLA-DRB1*15:01 allele, which confers a greatly increased susceptibility to develop MS [40,41], and rs10191329, the SNP that was significantly associated with the age-related MS severity score in a recent genome-wide association study (GWAS) [20]. A standard association analysis with the ranked score of genotyped donors on the dimensions was performed with PLINK 2.0 using the command --glm, which fits a linear regression model for each variant. In addition, MS PRSs were constructed using the LDAK-BayesR-SS tool [42]. We implemented QuickPRS to construct a prediction model based on the most recent MS GWAS by Patsopoulos et al. [43]. To assess the relation with autosomal MS-associated variants outside the HLA region, a non-HLA MS PRS was calculated by excluding the extended HLA region on chromosome 6 as defined previously by Patsopoulos et al. [43] (base pairs 24,000,000 to 35,000,000; genome assembly GRCh37/hg19).

**Statistical analysis**

Statistical analyses were performed in Python (v3.8.8). To assess the association between the dimensions and continuous validation variables, non-parametric Spearman correlation was performed with Scipy (v1.10.1). The Spearman correlation coefficient is denoted as 'rho' in figures and text. The association with categorical variables was tested by performing non-parametric Kruskal-Wallis and/or (post-hoc) Mann-Whitney U tests with Scipy. To correct for multiple

testing, the Benjamini-Hochberg - False Discovery Rate (FDR) was implemented using the statsmodels package (v0.14.0); the significance threshold was set to $p \leq 0.1$. FDR correction was performed for all tests between the different dimensions and one variable or a set of closely related variables (i.e. age at MS onset, age at death, years till EDSS-6, and disease duration; symptom load for the different domains; median age at onset per domain; clinical diagnosis categories and classes; drug use for L1 and L2 ATC classes; use of disease-modifying and MS-relevant immunosuppressive drugs; cortical lesion proportions; presence/absence of $CD20^+$ cells, $CD138^+$ cells, and lesions in the brainstem; presence/absence of $CD20^+$ cells in subcortical lesions; presence/absence of $CD138^+$ cells in subcortical lesions; number of $CD3^+$ cells in subcortical NAWM and lesions; the two genetic variants). A regression line was plotted on top of a scatter plot; the slope and intercept were calculated with Scipy, by performing linear least-squares regression on the ranked data. Raw input data and (anonymised) validation data is provided for 228 donors (including the two highly contributing outliers) in Online Resource 2.



## RESULTS

### Dimensionality reduction to disentangle the heterogeneity of MS neuropathology

To identify patterns in MS neuropathology, we established a computational workflow that consists of four stages (**Fig. 1a**). In stage 1, we collected previously generated quantitative and qualitative neuropathological data, predominantly related to the white matter [16]. Stage 2 consisted of processing this data, including transformation, imputation and an initial FAMD (factor analysis of mixed data). We selected the first three dimensions for further analysis and subsequently removed two donors with outlier values who contributed highly to a dimension. In stage 3, FAMD was performed on the definite dataset of 13 variables across 226 donors. Of the final FAMD dimensions, the first three together accounted for almost half of the total variance in the dataset, indicating that closer examination could provide insight into general neuropathological patterns observed in our MS cohort. In stage 4, we used orthogonal data types (clinical [16,29], neuropathological [16,21], immunological [18,19], and genetics) to evaluate and interpret the dimensions.

First, we explored the relation between input variables and the three dimensions identified in stage 3. Each dimension reflected a distinct neuropathological pattern, in which the variables were represented by and contributing to each dimension to varying extents (**Fig. 1b**). In addition, we ranked all donors according to their score on each dimension (in ascending order, from low to

high) to illustrate how the dimensions were related to the values of the input variables (**Fig. 1c**). Critically, donors' scores on one dimension were independent of their scores on the other dimensions (as shown by the scatter plots in **Fig. 1a**). A low score on dimension 1 was associated with a predominance of inactive and remyelinated lesions with few $HLA^+$ microglia/macrophages, a high score with a high lesion load, active and mixed lesions populated by foamy microglia, and the presence of nodules and cuffs (perivascular accumulations of leukocytes). Dimension 2 was positively correlated with the proportion of active lesions, the number of reactive sites, and the presence of nodules. Dimension 3 was positively associated with a higher cortical lesion rate and lesion load, a larger proportion of mixed lesions with ramified microglia and inactive lesions, relatively fewer active lesions with foamy microglia, and an absence of cuffs. Next, we aimed to validate and explore the dimensions. For an overview of the relation between the dimensions and all variables analysed in this study, see **Table 1**.

**Dimensions are associated with year of autopsy and cause of death**

The dimensions were not associated with post-mortem delay, pH or brain weight (**suppl. Fig. 4**, Online Resource 1), implying that they were not driven by these technical covariates. Donors who scored high on dimension 2 or 3 were likely to have died in more recent years (dim. 1: $p = 0.17$, rho = 0.09; 2: $p = 3.5 \times 10^{-5}$, rho = 0.29; 3: $p = 0.006$, rho = 0.19; **suppl. Fig. 5**, Online Resource 1). There was no association with cause of death, except for dimension 2 (dim. 1: $p = 0.12$, 2: $p = 0.05$, 3: $p = 0.51$; **suppl. Fig. 6**, Online Resource 1); donors who died by legal euthanasia scored higher on this dimension than donors who died of unspecified natural causes ($p = 0.02$). This finding could reflect an association between year and cause of death, possibly related to Dutch legislation on euthanasia taking effect in 2002. Accordingly, the median year of autopsy was 2013 for donors who died by euthanasia and 2005.5 for those who died from unspecified natural causes.

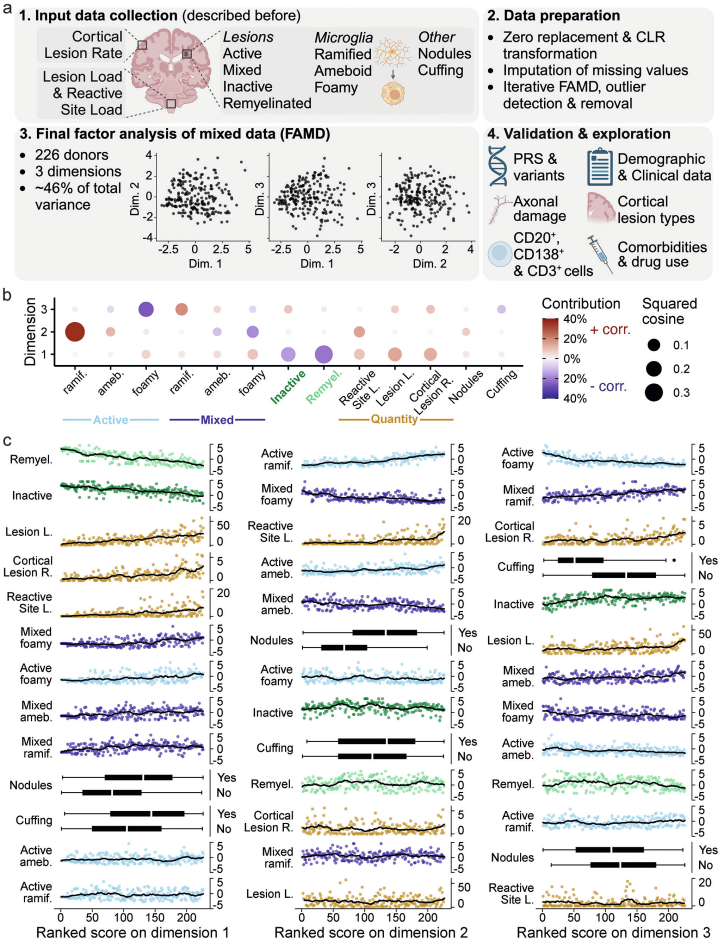


**Figure 1: Overview of the study and the three independent dimensions.** a Graphical outline of this study created with BioRender.com, consisting of 4 stages: 1) collecting previously generated input data, 2) data preparation, 3) exploratory FAMD, and 4) validation and exploration. b Dot plot of FAMD input variables and the first three dimensions. Dot size indicates the squared cosine, reflecting the proportion of variance in a variable explained by a dimension. Dot color indicates whether the correlation between the dimension and the variable is positive (red) or negative (blue); color intensity reflects the relative contribution of the variable to the component. c Scatter plots with fitted line and box plots per dimension depicting the values for the input variables on the Y-axis, for donors ranked according to their score on each dimension on the X-axis. In case of ties, donors were assigned ranks in the order of appearance in the dataset, so that each donor receives a unique rank. The line represents the centered moving average, over a window of 20 observations, with a maximum of 10 missing values. Proportional data is CLR-transformed; unimputed values are shown. Plots are ordered vertically based on the variable's contribution to the dimension. CLR = centered log ratio; FAMD = factor analysis of mixed data; dim. = dimension; PRS = polygenic risk score; ramif. = ramified; ameb. = ameboid; remyel. = remyelinated (lesion); L. = load; R. = rate; corr. = correlation

**Table 1 Overview of the relation between the dimensions and variables analysed in this study.** Note that the correlations are described for one direction, from low to high rank/score on the respective dimension

| | | Dimension 1 | Dimension 2 | Dimension 3 |
|---|---|---|---|---|
| Interpretation | | Immune cell activity & demyelination related to progression | Microglia (re)activity & possibly lesion initiation | Loss of lesion activity & scar formation |
| Eigenvalue (% var.) | | 2.60 (19.98%) | 1.70 (13.06%) | 1.67 (12.83%) |
| Input variables | Lesion quantity | More lesions in brainstem & cortex, more reactive sites | More reactive sites | More lesions in brainstem & cortex |
| | Lesion type | More active & mixed, less inactive & remyelinated | More active, less mixed | More mixed & inactive, less active & remyelinated |
| | Microglia | More foamy | More ramified | More ramified |
| | Cell clusters | More often cuffs & nodules | More often nodules | Less often cuffs |
| Demo-graphic | Sex | ns | ns | ns |
| | Age at death | Younger at death (****) | Older at death (***) | ns |

**Table 1 Overview of the relation between the dimensions and variables analysed in this study.** Note that the correlations are described for one direction, from low to high rank/score on the respective dimension *(continued)*

| | | Dimension 1 | Dimension 2 | Dimension 3 |
|---|---|---|---|---|
| Clinical | MS type | ns | ns | ns |
| | Severity | Shorter time from onset to EDSS-6 (****) & death (****) | Longer time from onset to EDSS-6 (**) & death (****) | Longer time from onset to death (*) |
| | Symptom load per domain | More general (**), motor (*), sens. (*) & cogn. (+) observations | Less general (+), motor (+), sens. (+) & psych. (*) observations | Less sens. (+) & psych. (+) observations |
| | Age at onset | ns | ns | ns |
| | Median age at domain onset | Younger at onset of general (****), motor (****), sens. (****), cogn. (****) & psych. (****) domains | Older at onset of general (**), motor (+), sens. (*), cogn. (**) & psych. (+) domains | Older at onset of cogn. domain (+) |
| | Comorbidities | Less cardiovascular system dis. (**), hypertension (*) & autoimmune dis. (*) | More diabetes mellitus type 2 (*) | ns |
| | Drug use | More disease-modifying drug use (*) | Less use of MS-relevant immunosuppressants (*) | ns |
| Genetics | MS PRS | ns | Higher MS PRS (**) | ns |
| | rs3135388 | ns | Higher risk allele dosage (**) | ns |
| | rs10191329 | ns | ns | ns |
| Cortical lesions | Presence | More often present (****) | ns | More often present (*) |
| | Lesion type | Less intracortical (**) | Less leukocortical (***), more intracortical (*) & subpial (*) | More subpial (*) |

**Table 1 Overview of the relation between the dimensions and variables analysed in this study.** Note that the correlations are described for one direction, from low to high rank/score on the respective dimension *(continued)*

| | | Dimension 1 | Dimension 2 | Dimension 3 |
|---|---|---|---|---|
| Neuro-axonal damage | CSF NfL | Higher levels (+) | ns | Lower levels (*) |
| | Bielschowsky positive area | ns | ns | Higher density (+) |
| | APP+ | ns | ns | ns |
| Immune cells | CD20+ | More in pch (*) & pvs (+), more in active (*) & mixed (*) lesions | ns | Less in active (+) and mixed (+) lesions |
| | CD138+ | More in pch (**) & pvs (*) | ns | Less in pch (*) |
| | Lesion in MOB block | More often with lesion (****) | ns | ns |
| | CD3+ | More in subcortical NAWM (*) & active lesions (+) | ns | Ns |
| Other | Autopsy year | ns | More recent (****) | More recent (**) |
| | CoD | ns | * | ns |
| | pH, pmd & weight | ns | ns | ns |

*var. = variance; EDSS = Expanded Disability Status Scale; sens. = sensory/autonomic; psych. = psychiatric; cogn. = cognitive; dis. = disease; CSF = cerebrospinal fluid; NfL = neurofilament light chain; APP = amyloid precursor protein; pch = parenchyma; pvs = perivascular space; MOB = medulla oblongata; CoD = cause of death; pmd = post-mortem delay; ns p > 0.1; + p ≤ 0.1; * p ≤ 0.05; ** p ≤ 0.01; *** p ≤ 0.001; **** p ≤ 0.0001*

**Dimensions are associated with the clinical manifestations of MS**
To investigate the potential clinical correlates of the neuropathological dimensions, we subsequently focused our analysis on data related to demographics and disease experience. There was no significant correlation with sex (dim. 1: $p = 0.80$; 2: $p = 0.80$; 3: $p = 0.93$) or MS clinical phenotype (dim. 1: $p = 0.30$; 2: $p = 0.88$; 3: $p = 0.30$) (**Fig. 2a,b**), the latter supporting the notion that the historically identified clinical MS phenotypes do not qualitatively differ with regards to the (white matter) pathological features included in our analysis.

Dimension 1 was negatively associated with the years from onset till EDSS-6 ($p = 7.7 \times 10^{-8}$, rho = -0.39), from onset till death (i.e. duration of disease; $p = 5.8 \times 10^{-8}$, rho = -0.39), and age at death ($p = 1.6 \times 10^{-12}$, rho = -0.48); there was no relation with age at MS onset ($p = 0.51$, rho = -0.06) (**Fig. 2c**). In addition, the total number of signs and symptoms adjusted for disease duration (the symptom load) was significantly positively correlated with dimension 1 for the general, motor, sensory/autonomic, and cognitive domains (**suppl. Fig. 7**, Online Resource 1). Corresponding with their earlier death, the median age at symptom onset was generally earlier for donors scoring high on dimension 1 (**suppl. Fig. 8**, Online Resource 1). On the whole, a higher score on dimension 1 associates with a more severe disease course of MS.

In contrast, dimension 2 was associated with milder MS, positively correlating with the years till EDSS-6 ($p = 0.006$, rho = 0.21), till death ($p = 4.3 \times 10^{-5}$, rho = 0.30), and age at death ($p = 2.4 \times 10^{-4}$, rho = 0.26) (**Fig. 2c**). Age at onset was not associated with the dimension ($p = 0.78$, rho = 0.02; **Fig. 2c**). Moreover, for all domains the symptom load was negatively correlated with dimension 2, although not always significantly so (**suppl. Fig. 7**, Online Resource 1). The median age at symptom onset was positively correlated with dimension 2, in line with expectations (**suppl. Fig. 8**, Online Resource 1).

Dimension 3 was not significantly correlated with years till EDSS-6 ($p = 0.74$, rho = 0.03), age at MS onset ($p = 0.31$, rho = -0.09), and age at death ($p = 0.37$, rho = 0.07) (**Fig. 2c**). However, because donors who scored high on dimension 3 tended to develop MS at a slightly younger age and died at a relatively older age, there was a significant positive correlation with disease duration ($p = 0.02$, rho = 0.18; **Fig. 2c**). Interestingly, with regards to the symptom load, the overarching domain might matter: there was a significant negative correlation for the psychiatric and sensory/autonomic domains only (**suppl. Fig. 7**, Online Resource 1). Furthermore, there was a positive association with median age at symptom onset for the cognitive domain (**suppl. Fig. 8**, Online Resource 1).
The identified dimensions correlate with clinical profiles of NBB MS donors, and therefore likely reflect clinically relevant pathological processes. In the

following sections, each dimension will be further examined with regards to comorbidities, drug use, cortical neuropathology, potential immune cell involvement, and genetics.

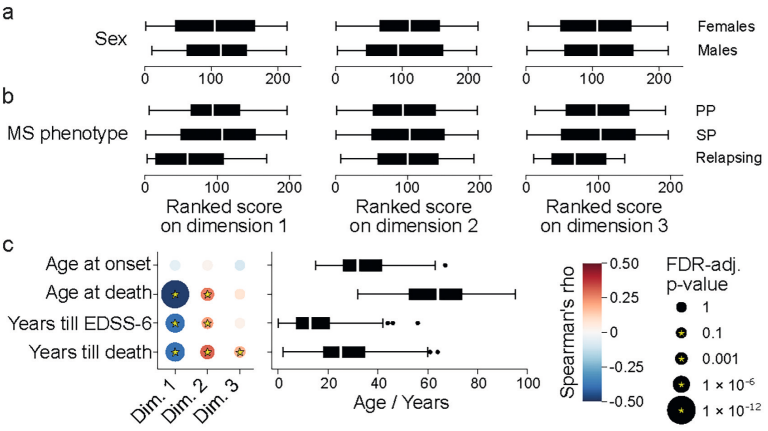


**Figure 2: Association between demographic and clinical variables and dimensions. Note that X-axis scale differs among the different plots.** a Box plots showing the ranked scores of donors, per dimension, per sex. Sex was known for 214 donors (77 males, 137 females). There are no significant differences between sexes (Mann-Whitney U; dim. 1: p = 0.80; 2: p = 0.80; 3: p = 0.93). b Box plots showing the ranked scores of donors, per dimension, per MS clinical phenotype. MS phenotype was determined for 197 donors (12 relapsing, 119 SP, 66 PP). There are no significant differences (Kruskal-Wallis; dim. 1: p = 0.30; 2: p = 0.88; 3: p = 0.30). In plots in a and b, ties were assigned averaged ranks. c Dot plot (left) showing the correlation between the scores on dimensions 1-3 and age at MS onset for 204 donors, age at death for 214 donors, years till EDSS-6 for 191 donors, and years till death (i.e. duration of disease) for 201 donors. Dot colour indicates the strength of the correlation, dot size the p-value, and a yellow star a significant association. Box plots (right) showing the distribution of the demographic and clinical variables. Significance in c was assessed with Spearman correlation and FDR-adjusted for multiple testing. dim. = dimension; PP = primary progressive; SP = secondary progressive; EDSS = Expanded Disability Status Scale; FDR = False Discovery Rate

## Dimensions correlate with certain comorbidities and use of MS-relevant drugs

To assess associations between our dimensions and comorbidity, MS donors with and without other diagnoses (i.e. with or without one or more observations of relevant categories and classes); and who did and did not use a particular class of drugs were compared. MS donors with an autoimmune disease or a cardiovascular system disease or its subclass hypertension scored significantly lower on dimension 1 (**suppl. Fig. 9**, Online Resource 1). Consistently, donors who used cardiovascular system drugs died at an older age and scored lower on dimension 1 (not significant after multiple-testing correction; **suppl. Fig. 10**,

Online Resource 1), corroborating the quality of our datasets. Donors with type 2 diabetes were older and scored significantly higher on dimension 2 (**suppl. Fig. 9**, Online Resource 1). Regarding drug therapies relevant for MS, donors using disease-modifying drugs scored higher on dimension 1, died at a younger age, and died more recently. Donors who used MS-relevant immunosuppressive drugs generally scored lower on dimension 2, died at a younger age, and in less recent years (**suppl. Fig. 11**, Online Resource 1).

**Dimension 1: demyelination with an active immune system**

Microglia morphology was strongly associated with dimension 1, in the form of a positive correlation with the microglial/macrophage activation score (**suppl. Fig. 12**, Online Resource 1); the associated lesion type (active or mixed) seemed to be of less importance. End-stage (remyelinated and inactive) lesions were relatively infrequent in donors with a high score on dimension 1 (**Fig. 3a**).

Donors with (a) cortical lesion(s) scored higher on dimension 1 ($p = 3.8 \times 10^{-6}$). Moreover, donors who scored high on dimension 1 had relatively fewer intracortical lesions ($p = 0.006$, $rho = -0.24$). Although dimension 1 was correspondingly positively correlated with the proportion of leukocortical and subpial lesions, this did not reach statistical significance (leukocortical: $p = 0.26$, $rho = 0.09$; subpial: $p = 0.22$, $rho = 0.10$) (**Fig. 3b** & **suppl. Fig. 13**, Online Resource 1).

Donors with $CD20^+$ and/or $CD138^+$ cells in the parenchyma and/or perivascular space of the brainstem scored higher on dimension 1 ($CD20^+$ parenchyma (pch): $p = 0.01$; $CD20^+$ perivascular space (pvs): $p = 0.06$; $CD138^+$ pch: $p = 0.001$; $CD138^+$ pvs: $p = 0.04$). Furthermore, presence of $CD20^+$ cells in active and mixed subcortical lesions was associated with a higher score on dimension 1 (active: $p = 0.04$; mixed: $p = 0.02$). Presence of $CD20^+$ or $CD138^+$ cells in the meninges was not associated with dimension 1 ($CD20^+$: $p = 0.70$; $CD138^+$: $p = 0.70$), as was presence of $CD138^+$ cells in active and mixed lesions (active: $p = 0.86$; mixed: $p = 0.89$). Donors with a lesion in the brainstem tissue block that was used for investigating B cell presence scored higher on dimension 1 ($p = 5.3 \times 10^{-7}$), as expected (**Fig. 3c**) [18]. There was no significant association with the mean number of $CD3^+$ cells in NAWM (normal-appearing white matter) of the pyramidal tract at the level of the medulla oblongata with dimension 1 ($p = 0.54$, $rho = -0.09$; **suppl. Fig. 14**, Online Resource 1). However, $CD3^+$ cell numbers in subcortical perilesional NAWM were positively correlated with dimension 1 ($p = 0.04$, $rho = 0.39$), as were $CD3^+$ cell numbers in active but not mixed lesions (active: $p = 0.08$, $rho = 0.50$; mixed: $p = 0.54$, $rho = 0.15$) (**Fig. 3d,e**; **suppl. Fig. 15**, Online Resource 1).

Dimension 1 correlated positively with axonal damage (NfL in CSF: p = 0.05, rho = 0.26); consistently, there seemed to be a lower axonal density and more axonal stress in donors with a high score on this dimension, although these associations were not significant (Bielschowsky: p = 0.48, rho = -0.10; $APP^+$: p = 0.43) (**suppl. Fig. 16**, Online Resource 1).

The PRS (polygenic risk score) and two individual variants (rs3135388, highly correlated with the HLA-DRB1*1501 allele [40], and rs10191329, the SNP that was recently associated with disease progression [20]) were not significantly associated with dimension 1 (PRS: p = 0.14, rho = 0.12; rs3135388: p = 0.17; rs10191329: p = 0.31) (**Fig. 3f,g**). However, the progression-associated SNP has a relatively low minor allele frequency and increased risk is mediated exclusively by the homozygous carriers. The five NBB donors homozygous for the risk allele (A) of rs10191329 (1.9 < dosage < 2.1) all scored high on dimension 1 (their median rank was 163, with the maximum possible rank being 194). For a comprehensive overview of dimension 1, see **Fig. 3h**.

**Figure 3: Dimension 1** . a Vertical bar graphs showing on the Y-axis the ramified, ameboid and foamy microglia proportions relative to the total number of active and mixed lesions, white matter lesion proportions relative to the total number of white matter lesions, remyelinated and inactive lesion proportions relative to the total number of end-stage (remyelinated plus inactive) lesions, and active and mixed lesion proportions relative to the total number active plus mixed lesions, from top to bottom respectively, with donors ranked according to their score on the X-axis. The lines represent the centered moving average of the ratio remyelinated to end-stage, and the ratio active to active plus mixed, over a window of 20 observations, with a maximum of 10 missing values. b Box plot (top) showing the ranked scores for 175 donors with and 31 donors without (a) cortical lesion(s). Vertical bar graph (bottom) showing the proportions of cortical lesion types on the Y-axis for donors ranked according to their score on dimension 1. In a and b, ties were assigned ranks in the order of appearance in the dataset. c Box plots showing, from top to bottom, the ranked**)** scores of 132 donors with (83) and without (49) lesions in the MOB tissue block used to determine B cell presence, with (6) and without (126) $CD20^+$ cells in pch, with (21) and without (111) $CD20^+$ cells in pvs, with (69) and without (63) $CD20^+$ cells in men, with (9) and without (123) $CD138^+$ cells in pch, with (14) and without (118) $CD138^+$ cells in pvs, with (62) and without (70) $CD138^+$cells in men; the ranked scores of 26 donors with (10) and without (16) $CD20^+$ cells in subc. active lesions; of 36 donors with (11) and without (25) $CD20^+$ cells in subc. mixed lesions; of 27 donors with (6) and without (21) $CD138^+$ cells in subc. active lesions; and of 36 donors with (4) and without (32) $CD138^+$ cells in subc. mixed lesions. d-e Scatter plots with regression lines, depicting on the Y-axis the rank of the $CD3^+$ cell count in subc. NAWM for 53 donors (d) and in subc. active lesions for 22 donors (e), with donors ranked according to their score on dimension 1 on the X-axis. f Scatter plot with regression line, depicting the rank of the MS PRS (polygenic risk score) on the Y-axis for 194 donors, ranked according to their score on dimension 1 on the X-axis. g Two scatter plots with regression lines showing the ranked score of donors on dimension 1 on the Y-axis, and allele dosage on the X-axis. In c-g, ties were assigned averaged ranks. h Overview of the correlation between relevant input and validation variables and dimension 1, created with BioRender.com.

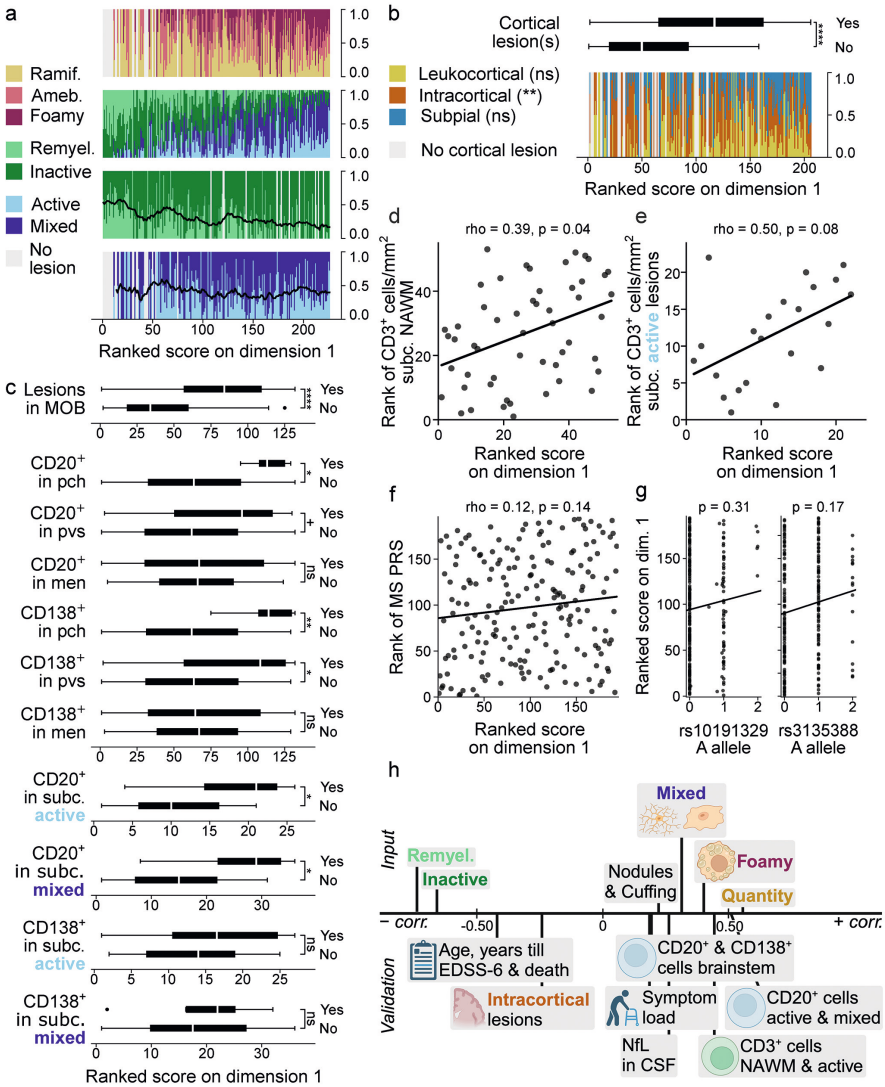


**Figure 3: Dimension 1 (continued)** Position on the axis is a close approximation of the Spearman correlation between the dimension and the variable(s); variables were grouped when appropriate and positioned based on the average of the correlation coefficients. Significance in b-f was assessed with Mann-Whitney U for binary variables and Spearman correlation for continuous variables and FDR-adjusted for multiple testing; for g see text. ns $p > 0.1$; + $p \leq 0.1$; * $p \leq 0.05$; ** $p \leq 0.01$; *** $p \leq 0.001$; **** $p \leq 0.0001$; ramif. = ramified; ameb. = ameboid; remyel. = remyelinated (lesion); MOB = medulla oblongata; pch = parenchyma; pvs = perivascular space; men = meninges; subc. = subcortical; NAWM = normal-appearing white matter; dim. = dimension; EDSS = Expanded Disability Status Scale; CSF = cerebrospinal fluid; NfL = neurofilament light chain; FDR = False Discovery Rate

**Dimension 2: active lesions, ramified microglia and an association with the HLA region**

Dimension 2 is associated with ramified microglia morphology and a corresponding lower microglial/macrophage activation score (**suppl. Fig. 12**, Online Resource 1), as well as a shift from predominantly mixed to more active lesions. The ratio of remyelinated to inactive lesions remains quite stable (**Fig. 4a**). Donors with (a) cortical lesion(s) did not score differently than those without ($p = 0.38$). There was a clear relation with cortical lesion location: scoring high on dimension 2 was associated with relatively fewer leukocortical lesions ($p = 3.1 \times 10^{-4}$, rho = -0.31), and more intracortical and subpial lesions (intracortical: $p = 0.03$, rho = 0.18; subpial: $p = 0.02$, rho = 0.21) (**Fig. 4b** & **suppl. Fig. 13**, Online Resource 1).

There was no association between $CD20^+$ and $CD138^+$ cells in the brainstem and dimension 2 (for $CD20^+$ cells: pch: $p = 0.60$; pvs: $p = 0.12$; meninges (men): $p = 0.75$; for $CD138^+$ cells: pch: $p = 0.82$; pvs: $p = 0.89$; men: $p = 0.29$), and donors with or without a lesion in the brainstem did not score differently on the dimension ($p = 0.19$) (**Fig. 4c**). Presence of $CD20^+$ and $CD138^+$ cells in subcortical active and mixed lesions was also not associated with dimension 2 (for $CD20^+$ cells: active: $p = 0.94$; mixed: $p = 0.38$; for $CD138^+$ cells: active: $p = 0.11$; mixed: $p = 0.86$; suppl. **Fig. 17**, Online Resource 1). Moreover, neither the mean number of $CD3^+$ cells in NAWM nor in subcortical active and mixed lesions was correlated with dimension 2 (brainstem NAWM: $p = 0.54$, rho = -0.12; subcortical NAWM: $p = 0.20$, rho = 0.25; active: $p = 0.20$, rho = 0.35; mixed: $p = 0.69$, rho = 0.07; **suppl**. **Fig. 14 & 15**, Online Resource 1).

Regarding axonal damage, density and stress, there was no correlation with dimension 2 (NfL in CSF: $p = 0.73$, rho = -0.04; Bielschowsky: $p = 0.48$, rho = -0.10; $APP^+$: $p = 0.99$; **suppl. Fig. 16**, Online Resource 1). The PRS and the risk allele (A) of the HLA-DRB1*1501 tag SNP were associated with dimension 2 (PRS: $p = 0.002$, rho = 0.24; rs3135388: $p = 0.002$; **Fig. 4d,e**). After recalculation of the MS PRS without the HLA region, the PRS was no longer significantly correlated with dimension 2 ($p = 0.37$, rho = 0.09; **suppl. Fig. 18**, Online Resource 1). Dimension 2 did not correlate with the progression SNP rs10191329 ($p = 0.53$; **Fig. 4e**), and did not show a particular clustering of the five homozygous carriers of the risk allele. For an overview of dimension 2, see **Fig. 4f.**

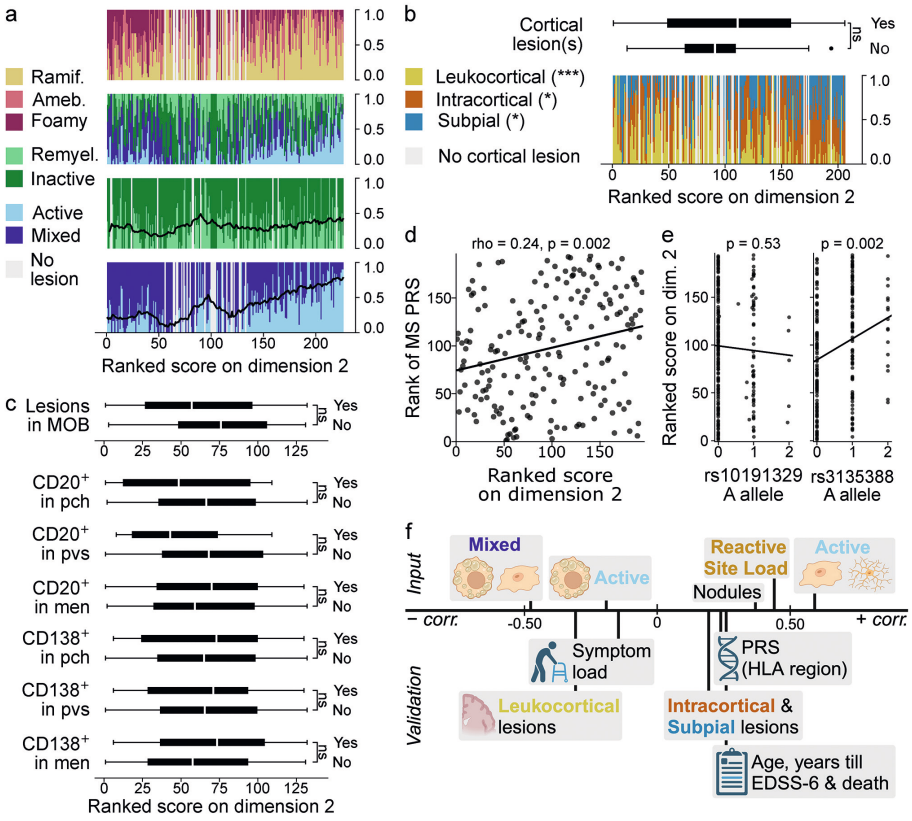


**Figure 4: Dimension 2.** Legends for a-f as for Fig. 3a-c and 3f-h, respectively; the only difference being that ranked scores of donors with and without CD20⁺ and CD138⁺ cells in subcortical lesions are not shown in c but in suppl. Fig. 17 (Online Resource 1). HLA = human leukocyte antigen

## Dimension 3: loss of (white matter) lesion activity and scar formation

Dimension 3 is negatively correlated with the microglial/macrophage activation score (**suppl. Fig. 12**, Online Resource 1). In contrast to dimension 2, this was related to a relative increase of mixed compared to active lesions. Moreover, scoring higher on dimension 3 was associated with a decrease in the ratio of remyelinated to inactive lesions (**Fig. 5a**). Donors with one or more lesions in the cortex generally scored higher on dimension 3 ($p = 0.02$). In addition, higher scoring donors had relatively more subpial lesions ($p = 0.03$, rho = 0.19). There was a non-significant negative correlation with intracortical and leukocortical lesion proportions (leukocortical: $p = 0.11$, rho = -0.14; intracortical: $p = 0.65$, rho = -0.03) (**Fig. 5b** & **suppl. Fig. 13**, Online Resource 1).

Donors with $CD138^+$ cells in the parenchyma but not the perivascular or meningeal regions of the brainstem scored lower on dimension 3 (pch: $p = 0.04$; pvs: $p = 0.95$; men: $p = 0.18$); donors with $CD138^+$ cells in subcortical active and mixed lesions did not score differently (active: $p = 0.89$; mixed: $p = 0.86$). There was no significant association with the presence of $CD20^+$ cells at any of the locations in the brainstem (pch: $p = 0.17$; pvs: $p = 0.29$; men: $p = 0.70$), or with the presence of a lesion in the investigated tissue block ($p = 0.60$). However, the presence of $CD20^+$ cells in subcortical active and mixed lesions was associated with a lower score on dimension 3 (active: $p = 0.08$; mixed: $p = 0.06$) (**Fig. 5c**). Regarding T cells, there was no correlation between $CD3^+$ cells in the NAWM or subcortical lesions and dimension 3 (brainstem NAWM: $p = 0.88$, rho =-0.02; subcortical NAWM: $p = 0.51$, rho = 0.13; active: $p = 0.56$, rho = -0.15; mixed: $p = 0.20$, rho = 0.29; **suppl. Fig. 14** & **15**, Online Resource 1).

Dimension 3 was negatively correlated with axonal damage (NfL in CSF: $p = 0.02$, rho = -0.34) and positively with axonal density (Bielschowsky: $p = 0.06$, rho = 0.31) (**Fig. 5d,e**). Although the association with axonal stress was not significant, donors with $APP^+$ axonal fragments or bulbs generally scored lower on dimension 3 ($p = 0.42$; **suppl. Fig. 16**, Online Resource 1). There was no significant association with the MS PRS ($p = 0.60$, rho = -0.04), the HLA-DRB1*1501 tag SNP ($p = 0.31$) or the progression SNP ($p = 0.31$) (**Fig. 5f,g**). For an overview of dimension 3, see **Fig. 5h**.

## DISCUSSION

Comprehension of pathophysiological processes contributing to MS is necessary to improve prognostic accuracy, therapeutic decision making, and development of disease-modifying therapies. Using a data-driven approach, we identified three biologically and clinically relevant dimensions of MS pathology. Our dimensions correspond to differences on the clinical and genetic level and are associated with grey matter lesional pathology, lymphocyte presence, and neuroaxonal damage. The three dimensions are likely associated with 1) immune cell activity and demyelination, 2) microglia (re)activity and possibly lesion initiation, and 3) loss of lesion activity and scar formation. Our study highlights the importance of taking the heterogeneity within individual lesion types into account and considering (lesional) pathology in the broader context of a donor's tendency towards certain neuropathological patterns, for which we offer a valuable tool in the form of scores on dimensions (Online Resource 3).

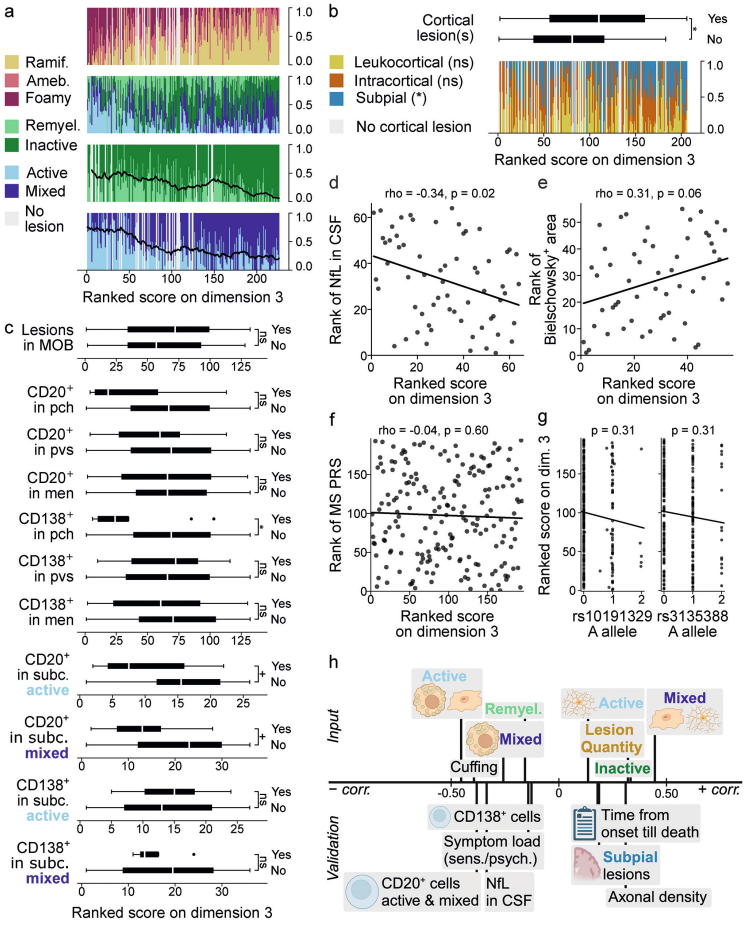


**Figure 5: Dimension 3**. Legends for a-c and f-h as for Fig. 3a-c and 3f-h, respectively. d-e Scatter plots with regression lines, depicting on the Y-axis the rank of CSF NfL levels for 64 donors (d) and the rank of the percentage Bielschowsky+ area for 55 donors (e), with donors ranked according to their score on dimension 3 on the X-axis. sens. = sensory/autonomic, psych. = psychiatric

It is both a strength and a limitation of our approach that our independent dimensions 'overlap' at the level of donors (i.e. each donor is characterised by its scores on all dimensions), because it helps with disentangling the heterogeneity of MS, while potentially complicating the comparison with and translation to findings on the donor level. Furthermore, it is important to recognize that the dimensions only explain part of the variation in the dataset, and the dataset itself is limited to mostly white matter neuropathology, with a focus on microglia. Grey matter pathology (independent of white matter pathology) and cell types such as oligodendrocytes and astrocytes fall outside the scope of the current study, and considering these in the future will further enhance our insight into MS.

Dimension 1 is positively associated with immune cell activity, demyelination, and clinical severity. Donors scoring low on dimension 1 had fewer lesions in white matter and cortex, a higher proportion of end-stage inactive and remyelinated lesions, and experienced a lower symptom load, longer time to EDSS-6, longer disease duration, and older age at death. Accordingly, prior research has associated extensive remyelination with an older age at death and a longer disease duration[44], and a low degree of cortical pathology with a milder disease course [45]. Conversely, donors scoring high on dimension 1 had more extensive pathology, which was associated with more severe disease. With regards to white matter, these donors were characterized by a predominance of active and mixed lesions, foamy microglia morphology, and the presence of nodules and cuffs. A previous post-mortem study of the NBB MS cohort had observed that clinical severity was positively correlated with lesion load and the proportion of mixed lesions [16]. Our study emphasizes the need to consider additional factors such as microglia morphology: having more lesions with foamy microglia (i.e. scoring high on dimension 1, or low on 2) is associated with more severe disease, whereas lesions with ramified microglia may not be as detrimental (i.e. scoring high on dimension 2 or 3). This could be due to axonal stress and acute axonal damage in lesions with foamy but not ramified microglia [21]; indeed, we found that dimension 1 correlated positively with axonal damage. Furthermore, the presence of B cells was associated with dimension 1, and not or negatively with dimension 2 and 3. In line with this, B cell presence has generally been related to clinically and pathologically more severe disease [18,46–48]; in the NBB cohort, B cells have additionally been associated with the proportion of mixed lesions [18]. Perivascular B cells have previously been related to higher levels of T cells and macrophages/microglia [47], fitting with the higher score on dimension 1 of donors with perivascular leukocyte cuffs and the positive correlation with $CD3^+$ cell numbers in subcortical NAWM and active lesions. Moreover, all five homozygous risk allele carriers of the recently identified progression-associated SNP rs10191329, previously shown to be correlated with a shorter time to EDSS-6, higher lesion load, and higher cortical lesion rate in the NBB MS cohort [20], scored high on dimension 1. Taken together, these clinical, neuropathological, and genetic correlates consistently link dimension 1 with disease progression, and indicate that ongoing innate and adaptive immune cell activity and demyelination could be important therapeutic targets in progressive MS. Notably, as Bruton's tyrosine kinase (BTK) is involved in both B cell and microglia activation, BTK inhibition may be a particularly promising therapeutic avenue [49,50].

Dimension 2 is related to microglia (re)activity without demyelination and likely to lesion initiation. This dimension correlated positively with active lesions with ramified (and to a lesser extent ameboid) microglia, reactive sites, and

microglia nodules. Interestingly, the latter two are both accumulations of ramified microglia in NAWM, accentuating the association between dimension 2 and ramified microglia morphology. Nodules are considered the first stage of lesion formation in MS and have previously been associated with active lesions [17,22,51], corresponding with our findings. Importantly, dimension 2 was associated with genetic risk in the HLA region, probably mainly due to an association with the HLA-DRB1*1501 risk allele. The HLA region and the broader MS PRS have previously been associated with the risk of developing MS [41,43,52], but have not been associated with the clinical severity during life [20,52–54]. The negative correlation of dimension 2 with disease severity indicates that the HLA region is more relevant for lesion initiation, rather than expansion and progression of white matter lesions and disability in MS. Our data supports the idea that other factors, such as the vulnerability of white matter to tissue damage and adaptive immune activity, are important mediators of the latter endpoints. Shams et al. recently showed an association between the MS PRS and thalamic atrophy, while Yates et al. found that the HLA-DRB1*1501 risk allele correlated with neuropathology on autopsy, both indicating that genetic factors involved in disease onset also relate to end-organ injury [52,55,56]. Moreover, the PRS has been related to disease activity - specifically, the presence of relapses [52]. Since the pathology underlying clinical attacks are thought to be active lesions [57,58], this seems to agree with our association of the HLA region with the specific neuropathological pattern of dimension 2.

Dimension 3 corresponds to a reduction in lesion activity and propensity for scar formation in relation to a protracted disease course. This dimension was positively associated with a higher lesion load and cortical lesion rate, more mixed compared to active and more inactive compared to remyelinated lesions, and ramified microglia morphology. This pattern correlated with a longer disease duration, without an obvious change in disease severity, and a higher age at onset of symptoms from the cognitive domain. Donors scoring high on dimension 3 had less axonal damage and a higher axonal density. Moreover, they were less likely to have cuffs, parenchymal plasma cells, and lesional B cells, in line with the remark by Fransen et al. that humoral involvement in white matter lesion activity may extinguish over time [18]. The lesional pattern of dimension 3 seems to partially reflect the finding of Frischer et al. [58], that active lesions become less frequent and inactive, remyelinated, and smoldering (mixed) lesions more frequent with increasing disease duration. However, we found a decrease in the ratio of remyelinated to inactive lesions with an increasing score on dimension 3, which might be related to the lower remyelination capacity of mixed compared to active lesions [59].

Each dimension is associated with a distinct pattern of cortical pathology. In this autopsy cohort, mixed lesions have been associated with leukocortical and intracortical lesions (but not subpial lesions) [16]; an MRI study also noted this association between leukocortical and mixed (paramagnetic rim) lesions [60]. In line with this, dimension 2, which demonstrates a shift from a high proportion of mixed lesions towards a predominance of active lesions, negatively correlated with the leukocortical lesion proportion. Interestingly, both dimension 2 and 3 were positively correlated with the proportion of subpial lesions. This may be related to the decrease in the leukocortical lesion proportion for dimension 2, whereas it might reflect a primary increase in subpial lesion burden in donors scoring high on dimension 3, since these also have a higher cortical lesion rate. Demyelination from the meninges in the form of subpial lesions could be mechanistically different from demyelination in relation to perivascular grey and white matter lesions, and dimension 3 might mostly reflect the former. However, meningeal inflammation, subpial lesions, and disease progression are correlated [61], which is in apparent contrast with the longer disease duration and less frequent observations of cuffs, parenchymal plasma cells, and lesional B cells in donors scoring high on dimension 3. More insight in the relation between our dimensions, meningeal inflammation, and subpial lesions will require investigating the presence of meningeal B (and T) cells in regions other than the brainstem, distinguishing between diffuse lymphocyte infiltration and (B cell) follicles, and collecting more data on grey matter pathology.

We did not find an association between the dimensions and age at onset, sex, or clinical MS phenotype. The last supports the contemporary view that MS is one disease in which several types of events can occur (i.e. attacks and progression), rather than distinct clinical entities. Previously, donors with a documented relapsing disease were found to have a lower lesion load with relatively fewer mixed lesions and more remyelinated lesions compared to those with documented progressive disease in the NBB MS cohort [16], and donors with relapsing MS do seem to score somewhat lower on dimension 1 and 3. Clinically, females have a more benign disease course and a higher relapse rate, while males accumulate more disability [62,63]. Neuropathologically, males have a higher proportion of mixed lesions and more often cortical pathology than females [16,58]. Therefore, a difference between the sexes was expected. The current analysis, however, suggests that sex differences may become less apparent when considering neuropathological patterns in the form of dimensions instead of individual lesion types.

Our analyses of the relations between comorbidities and drug use and the neuropathological MS dimensions are correlational in nature, making it difficult to assess causality. Cardiovascular comorbidity and use of drugs to mitigate

cardiovascular risk becomes more prevalent in populations when reaching an older age. This may (partially) explain the lower score on dimension 1 of donors with cardiovascular disease; a similar reasoning can be applied to the higher score on dimension 2 of donors with type 2 diabetes. Some autoimmune diseases are reported to be more common in MS patients, but the effects of comorbid autoimmunity on MS clinical severity and pathology and the underlying mechanisms are still largely unknown [64]. Further investigation on larger numbers of donors is needed before conclusions on the relation between autoimmune comorbidities and MS neuropathology can be drawn.

The dimensions could partially reflect historical changes, for instance related to the autopsy procedure (MRI-guided dissection was introduced in 2001), the availability of disease-modifying therapies, and the cohort itself (in the beginning of the NBB MS cohort, donors generally had more severe forms of MS). Since dimension 2 and 3 were positively correlated with year at autopsy, these two may be particularly affected by historical factors. The lack of an association between dimension 1 and year at autopsy seems to indicate that this dimension does not reflect the contemporary milder disease course of MS observed during the past decade [65]. In line with the development of MS disease-modifying therapies over the last decades, more recent autopsy cases were more frequently treated with disease-modifying therapies, and less often with MS-relevant immunosuppressant therapies such as prednisone pulses. In addition, we observed that donors who used drug therapies relevant for MS died at a younger age. This is in accordance with the higher score on dimension 1 for donors using disease-modifying drugs, and the lower score on dimension 2 for donors using MS-relevant immunosuppressants. Importantly, the direction of these associations makes confounding of our dimensions by MS treatment unlikely, and rather seems to validate them.



In addition to different disease stages, age-related changes, and gradations in disease severity, our genetic analyses support the idea that (some of) the dimensions may partially represent different mechanisms that contribute to disease evolution in individuals with MS. This is in accordance with the view of Kuhlmann et al. [4], who suggest that instead of one disease mechanism underlying MS, there is a combination of mechanisms of injury and repair, with varying importance between patients and over time. Conceptual **Fig. 6** illustrates how the variables in our study - and thereby the dimensions - fit within the broader context of MS.

In conclusion, we identified three dimensions related to initiation and progression of MS. Knowledge of donors' scores on these dimensions - and what this represents - will aid donor selection in future studies that aim to

investigate the distinct underlying mechanisms of MS and thereby disentangle the heterogeneity. Ultimately, achieving stratification of MS patients based on pathobiology in research and clinical settings will require a firm link between these neuropathological mechanisms and biomarkers - including but not limited to genetic and imaging factors.

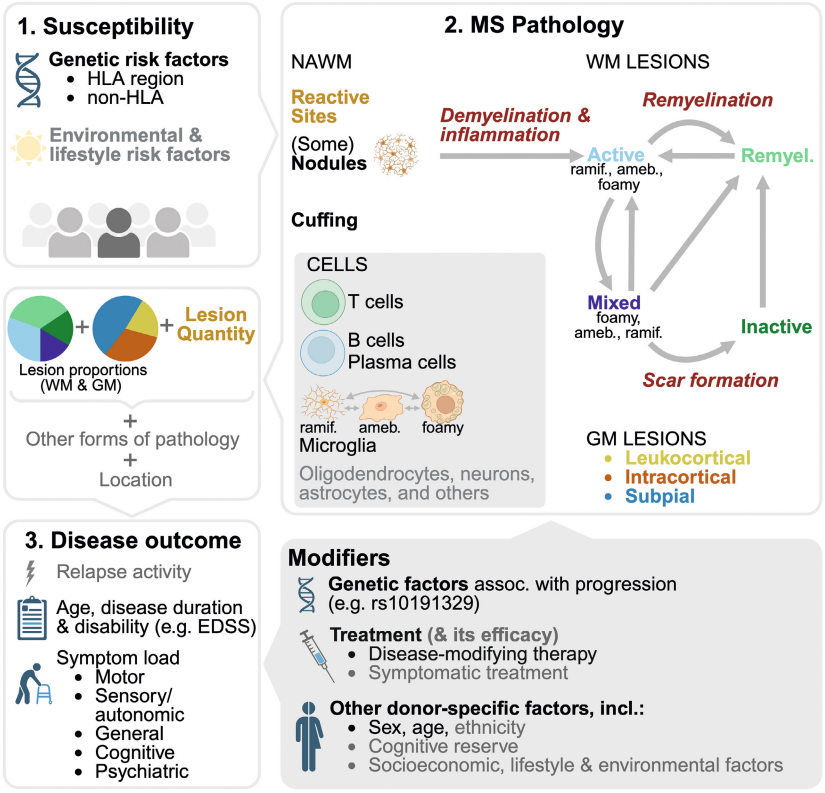


**Figure 6: Overview of our (input and validation) variables in the larger conceptual framework of MS, created with BioRender.com.** 1) MS development is driven by a combination of genetic, environmental and lifestyle factors. Grey text refers to information not included in this study. 2) In white matter (WM), new active lesions form in the normal-appearing white matter (NAWM), possibly developing from a subset of microglia nodules, driven by demyelinating and inflammatory mechanisms. Several mechanisms (in dark red and italics) underlie the rates of WM lesion initiation, evolution and resolution. Immune and brain cells are involved in all steps. WM lesion pathology is correlated with pathology in grey matter (GM); independent (neurodegenerative) mechanisms contributing to GM lesion development are not shown. Lesion type and load, together with lesion location and other forms of pathology, largely determine clinical outcome. 3) Clinically, disease manifests in the form of relapses and disease progression, with the symptoms mainly depending on the brain and spinal cord regions that are affected. Several modifying genetic, therapeutic, and other donor-specific factors can influence MS pathology and/or clinical outcome. HLA = human leukocyte antigen; ramif. = ramified; ameb. = ameboid; EDSS = Expanded Disability Status Scale

**Data availability**

The majority of the datasets used and analysed in the current study are provided as supplementary material (Online Resource 2 & 3); clinical disease trajectories of NBB donors are accessible via the website of the NND (Netherlands Neurogenomics Database; https://nnd.app.rug.nl). Anonymisation was performed by adjusting age at onset and death as well as time from onset to EDSS-6 and death to 5-year intervals, with donors aged <36 years grouped into the '<36' category. Information regarding cause of death categories with <10 donors (i.e. suicide) was not provided. Original data and data involving year of death, clinical diagnosis, and drug use are available upon reasonable request, by contacting the NBB (eNBB@nin.knaw.nl) or its director, I. Huitinga (i.huitinga@nin.knaw.nl). Note that the identifiers for NBB MS donors in Online Resource 2 & 3 correspond to those on the NND website.

**Acknowledgements**

We thank M. Groot, MD for her assistance with the parsing, cleaning and validation of medication data. We thank the Netherlands Neurogenetics Database Advisory Board for their valuable contributions including Prof. Dr. A. Rozemuller, Prof. Dr. B.J.L. Eggen, and Prof. Dr. H.W.G.M. Boddeke. Figures 1a, 3h, 4f, 5h and 6 were created with BioRender.com. Finally, we are grateful to those who donated their brain for research to the Netherlands Brain Bank.

**Funding**

We would like to acknowledge 'Vrienden van het Herseninstituut' for their contributions to this project. This study was supported by the Rosalind Franklin Fellowship from the University Medical Center Groningen and the ERC Starting Grant (no. 101078437), both of which were awarded to Dr. Holtman.

**Conflict of interest**

The authors declare that they have no conflict of interest.

## REFERENCES


1. Thompson, A. J., Baranzini, S. E., Geurts, J., Hemmer, B. & Ciccarelli, O. Multiple sclerosis. *Lancet* 391, 1622–1636 (2018).
2. Wallin, M. T. *et al.* Global, regional, and national burden of multiple sclerosis 1990–2016: a systematic analysis for the Global Burden of Disease Study 2016. *Lancet Neurol.* 18, 269–285 (2019).
3. Kuhlmann, T. *et al.* An updated histological classification system for multiple sclerosis lesions. *Acta Neuropathol.* 133, 13–24 (2017).
4. Kuhlmann, T. *et al.* Multiple sclerosis progression: time for a new mechanism-driven framework. *Lancet Neurol.* 22, 78–88 (2023).
5. Kalincik, T. *et al.* Towards personalized therapy for multiple sclerosis: prediction of individual treatment response. *Brain* 140, 2426–2443 (2017).
6. Oh, J., Vidal-Jordana, A. & Montalban, X. Multiple sclerosis: clinical aspects. *Curr Opin Neurol* 31, 752–759 (2018).
7. Lublin, F. D. *et al.* Defining the clinical course of multiple sclerosis, The 2013 revisions. *Neurology* 83, 278–286 (2014).
8. Lublin, F. D. & Reingold, S. C. Defining the clinical course of multiple sclerosis: Results of an international survey. *Neurology* 46, 907–911 (1996).
9. Cagol, A. *et al.* Association of brain atrophy with disease progression independent of relapse activity in patients with relapsing multiple sclerosis. *JAMA Neurol* 79, 682–692 (2022).
10. Hurtado Rúa, S. M. *et al.* Lesion features on magnetic resonance imaging discriminate multiple sclerosis patients. *Eur J Neurol* 29, 237–246 (2022).
11. Eshaghi, A. *et al.* Identifying multiple sclerosis subtypes using unsupervised machine learning and MRI data. *Nat Commun* 12, 2078 (2021).
12. De Meo, E. *et al.* Identifying the distinct cognitive phenotypes in multiple sclerosis. *JAMA Neurol* 78, 414–425 (2021).
13. Lucchinetti, C. *et al.* Heterogeneity of multiple sclerosis lesions: Implications for the pathogenesis of demyelination. *Ann. Neurol.* 47, 707–717 (2000).
14. Metz, I. *et al.* Pathologic heterogeneity persists in early active multiple sclerosis lesions. *Ann. Neurol.* 75, 728–738 (2014).
15. Breij, E. C. W. *et al.* Homogeneity of active demyelinating lesions in established multiple sclerosis. *Ann. Neurol.* 63, 16–25 (2008).
16. Luchetti, S. *et al.* Progressive multiple sclerosis patients show substantial lesion activity that correlates with clinical disease severity and sex: a retrospective autopsy cohort analysis. *Acta Neuropathol.* 135, 511–528 (2018).
17. De Groot, C. J. A. *et al.* Post-mortem MRI-guided sampling of multiple sclerosis brain lesions: Increased yield of active demyelinating and (p)reactive lesions. *Brain* 124, 1635–1645 (2001).
18. Fransen, N. L. *et al.* Absence of B Cells in Brainstem and White Matter Lesions Associates With Less Severe Disease and Absence of Oligoclonal Bands in MS. *Neurol. Neuroimmunol. NeuroInflammation* 8, 1–11 (2021).
19. Fransen, N. L. *et al.* Tissue-resident memory T cells invade the brain parenchyma in multiple sclerosis white matter lesions. *Brain* 143, 1714–1730 (2020).
20. Harroud, A. *et al.* Locus for severity implicates CNS resilience in progression of multiple sclerosis. *Nat. 2023 6197969* 619, 323–331 (2023).

21. van den Bosch, A. *et al.* Neurofilament Light Chain Levels in Multiple Sclerosis Correlate With Lesions Containing Foamy Macrophages and With Acute Axonal Damage. *Neurol. Neuroimmunol. neuroinflammation* 9, (2022).
22. Bosch, A. M. R. van den *et al.* Profiling of microglia nodules in multiple sclerosis reveals propensity for lesion formation. *Nat. Commun.* 15, 1–16 (2024).
23. Greenacre, M. Compositional data analysis. *Ann Rev Stat Appl* 8, 271–299 (2021).
24. Martín-Fernández, J. A., Barceló-Vidal, C. & Pawlowsky-Glahn, V. Dealing with zeros and missing values in compositional data sets using nonparametric imputation. *Math Geol* 35, 253–278 (2003).
25. Team, R. C. R Foundation for Statistical Computing. *Vienna* (2024) doi:https://www.R-project.org.
26. Josse, J. & Husson, F. missMDA: a package for handling missing values in multivariate data analysis. *J Stat Softw* 70, 1–31 (2016).
27. Lê, S., Josse, J. & Husson, F. FactoMineR: an R package for multivariate analysis. *J Stat Softw* 25, 1–18 (2008).
28. Hubert, M. & Vandervieren, E. An adjusted boxplot for skewed distributions. *Comput Stat Data Anal* 52, 5186–5201 (2008).
29. Mekkes, N. J. *et al.* Identification of clinical disease trajectories in neurodegenerative disorders with natural language processing. *Nat. Med.* 30, 1143–1153 (2024).
30. Pang, C. *et al.* SORTA: a system for ontology-based re-coding and technical annotation of biomedical phenotype data. *Database* 2015, (2015).
31. Van Der Velde, K. J. *et al.* MOLGENIS research: advanced bioinformatics data software for non-bioinformaticians. *Bioinformatics* 35, 1076–1078 (2019).
32. Kellmann, A. J., Lanting, P., Franke, L., Van Enckevort, E. J. & Swertz, M. A. Semi-automatic translation of medicine usage data (in Dutch, free-text) from Lifelines COVID-19 questionnaires to ATC codes. *Database* 2023, (2023).
33. Purcell, S. *et al.* PLINK: a tool set for whole-genome association and population-based linkage analyses. *Am J Hum Genet* 81, 559–575 (2007).
34. Goldstein, J. I. *et al.* zCall: a rare variant caller for array-based genotyping: Genetics and population analysis. *Bioinformatics* 28, 2543–2545 (2012).
35. Auton, A. *et al.* A global reference for human genetic variation. *Nature* 526, 68–74 (2015).
36. Manichaikul, A. *et al.* Robust relationship inference in genome-wide association studies. *Bioinformatics* 26, 2867–2873 (2010).
37. Das, S. *et al.* Next-generation genotype imputation service and methods. *Nat Genet* 48, 1284–1287 (2016).
38. McCarthy, S. *et al.* A reference panel of 64,976 haplotypes for genotype imputation. *Nat Genet* 48, 1279–1283 (2016).
39. Chang, C. C. *et al.* Second-generation PLINK: rising to the challenge of larger and richer datasets. *Gigascience* 4, (2015).
40. De Bakker, P. I. W. *et al.* A high-resolution HLA and SNP haplotype map for disease association studies in the extended human MHC. *Nat. Genet.* 38, 1166–1172 (2006).
41. Hafler, D. A. *et al.* Risk Alleles for Multiple Sclerosis Identified by a Genomewide Study. *N. Engl. J. Med.* 357, 861–862 (2007).
42. Zhang, Q., Privé, F., Vilhjálmsson, B. & Speed, D. Improved genetic prediction of complex traits from individual-level data or summary statistics. *Nat Commun* 12, 4192 (2021).

43. Patsopoulos, N. A. *et al.* Multiple sclerosis genomic map implicates peripheral immune cells and microglia in susceptibility. *Science (80-. ).* 365, 7188 (2019).
44. Patrikios, P. *et al.* Remyelination is extensive in a subset of multiple sclerosis patients. *Brain* 129, 3165–3172 (2006).
45. Calabrese, M. *et al.* Low degree of cortical pathology is associated with benign course of multiple sclerosis. *Mult. Scler. J.* 19, 904–911 (2013).
46. Magliozzi, R. *et al.* Meningeal B-cell follicles in secondary progressive multiple sclerosis associate with early onset of disease and severe cortical pathology. *Brain* 130, 1089–1104 (2007).
47. Moccia, M. *et al.* B Cells in the CNS at Postmortem Are Associated With Worse Outcome and Cell Types in Multiple Sclerosis. *Neurol. Neuroimmunol. NeuroInflammation* 9, 1–12 (2022).
48. Reali, C. *et al.* B cell rich meningeal inflammation associates with increased spinal cord pathology in multiple sclerosis. *Brain Pathol* 30, 779–793 (2020).
49. Saberi, D., Geladaris, A., Dybowski, S. & Weber, M. S. Bruton's tyrosine kinase as a promising therapeutic target for multiple sclerosis. *Expert Opin Ther Targets* 27, 347–359 (2023).
50. Touil, H. *et al.* Cross-talk between B cells, microglia and macrophages, and implications to central nervous system compartmentalized inflammation and progressive multiple sclerosis. *EBioMedicine* 96, 104789 (2023).
51. Horssen, J. Van *et al.* Clusters of activated microglia in normal-appearing white matter show signs of innate immune activation. *J. Neuroinflammation* 9, (2012).
52. Shams, H. *et al.* Polygenic risk score association with multiple sclerosis susceptibility and phenotype in Europeans. *Brain* 146, 645–656 (2023).
53. George, M. F. *et al.* Multiple sclerosis risk loci and disease severity in 7,125 individuals from 10 studies. *Neurol. Genet.* 2, 1–11 (2016).
54. Briggs, F. B. S. *et al.* Genome-wide association study of severity in multiple sclerosis. *Genes Immun* 12, 615–625 (2011).
55. Yates, R. L. *et al.* The influence of HLA-DRB1*15 on the relationship between microglia and neurons in multiple sclerosis normal appearing cortical grey matter. *Brain Pathol.* 32, 1–11 (2022).
56. Yates, R. L., Esiri, M. M., Palace, J., Mittal, A. & Deluca, G. C. The influence of HLA-DRB1*15 on motor cortical pathology in multiple sclerosis. *Neuropathol Appl Neurobiol* 41, 371–384 (2015).
57. Filippi, M. *et al.* Association between pathological and MRI findings in multiple sclerosis. *Lancet Neurol* 11, 349–360 (2012).
58. Frischer, J. M. *et al.* Clinical and Pathological Insights into the Dynamic Nature of the White Matter Multiple Sclerosis Plaque. *Ann Neurol* 78, 710–721 (2015).
59. Heß, K. *et al.* Lesion stage-dependent causes for impaired remyelination in MS. *Acta Neuropathol.* 140, 359–375 (2020).
60. Beck, E. S. *et al.* Cortical lesion hotspots and association of subpial lesions with disability in multiple sclerosis. *Mult. Scler.* 28, 1351–1363 (2022).
61. Magliozzi, R., Howell, O. W., Calabrese, M. & Reynolds, R. Meningeal inflammation as a driver of cortical grey matter pathology and clinical progression in multiple sclerosis. *Nat Rev Neurol* 19, 461–476 (2023).
62. Crielaard, L. *et al.* Factors associated with and long-term outcome of benign multiple sclerosis: A nationwide cohort study. *J. Neurol. Neurosurg. Psychiatry* 90, 761–767 (2019).

63. Magyari, M. & Koch-Henriksen, N. Quantitative effect of sex on disease activity and disability accumulation in multiple sclerosis. *J Neurol Neurosurg Psychiatry* 93, 716–722 (2022).
64. Nociti, V. & Romozzi, M. Multiple sclerosis and autoimmune comorbidities. *J Pers Med* 12, 1828 (2022).
65. Sorensen, P. S. *et al*. The apparently milder course of multiple sclerosis: changes in the diagnostic criteria, therapy and natural history. *Brain* 143, 2637–2652 (2020).

## SUPPLEMENTARY INFORMATION

**Online Resource 1:** .pdf file with Suppl. Figures 1 – 18
Available under supplementary information at https://link.springer.com/article/10.1007/s00401-024-02742-w#Sec24

**Online Resource 2:** .xlsx file with raw input and anonymised validation data
Available under supplementary information at https://link.springer.com/article/10.1007/s00401-024-02742-w#Sec24

**Online Resource 3:** .xlsx file with (ranked & unranked) scores of NBB MS donors on the dimensions
Available under supplementary information at https://link.springer.com/article/10.1007/s00401-024-02742-w#Sec24

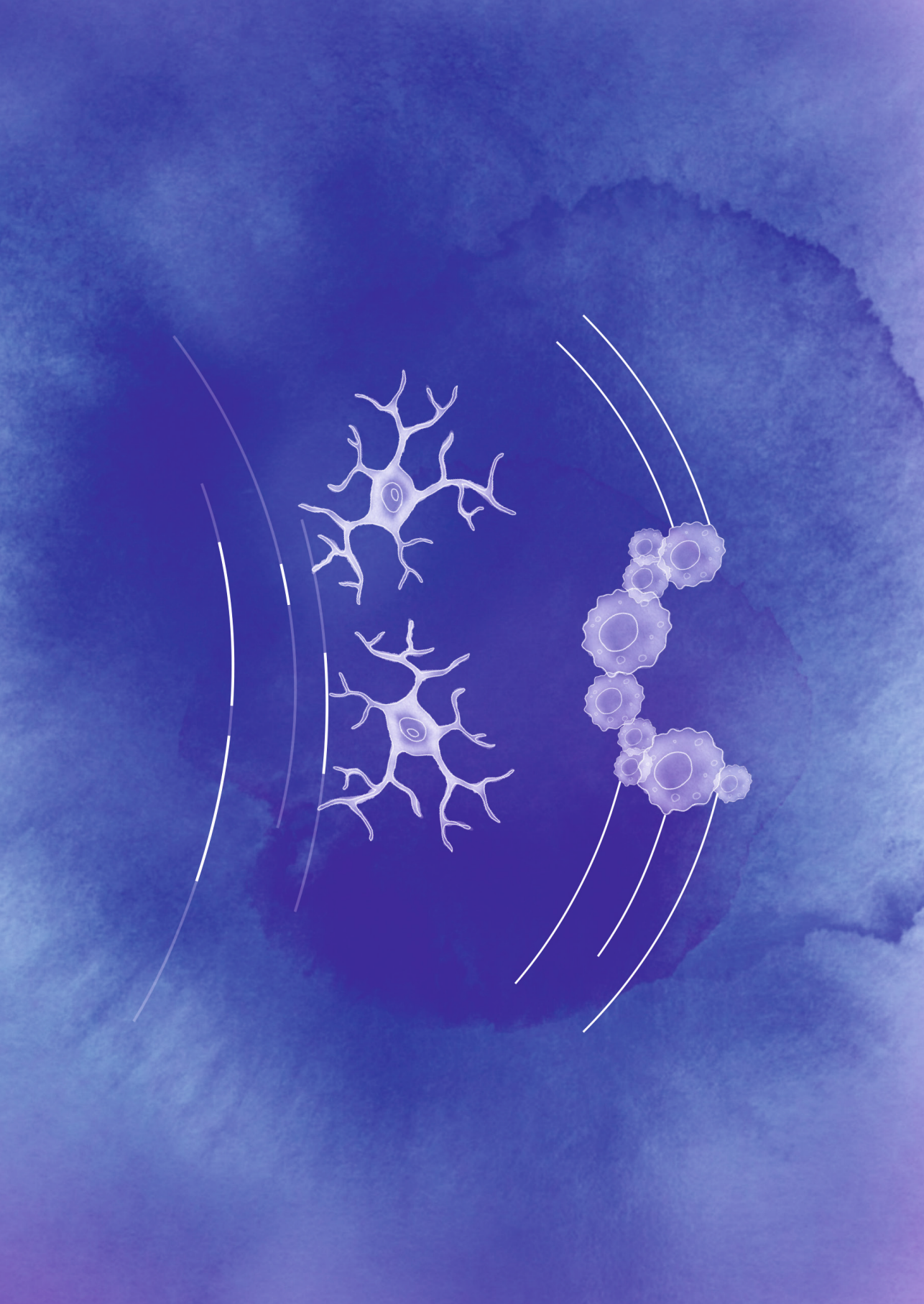

# CHAPTER 6

# Neurofilament light chain levels in multiple sclerosis correlate with lesions containing foamy macrophages and with acute axonal damage

Aletta M.R. van den Bosch[1]†, Nina L. Fransen[1]†, Matthew R.J. Mason[1], Annemieke Rozemuller[2], Charlotte E. Teunissen[3], Joost Smolders[1,4] and Inge Huitinga[1,5]

[1]Neuroimmunology Research Group, Netherlands Institute for Neuroscience, Amsterdam, The Netherlands; [2]Dept. Pathology, Amsterdam UMC, Amsterdam, The Netherlands; [3] Neurochemistry lab, Dept. Clinical Chemistry, Amsterdam Neuroscience, Amsterdam UMC, Vrije Universiteit, Amsterdam, The Netherlands; [4] Dept. of Neurology and Immunology, MS center ErasMS, ErasmusMC, Rotterdam, The Netherlands; [5]Swammerdam Institute for Life Sciences, University of Amsterdam, Amsterdam, The Netherlands

† These authors contributed equally to this work.

*Neurology Neuroimmunology & Neuroinflammation 2022 Mar 3;9(3):e1154*

## ABSTRACT

To investigate whether white matter lesion activity, acute axonal damage, and axonal density in MS associate with CSF neurofilament light chain (NfL) levels. Of 101 brain donors with MS (n = 92 progressive MS, n = 9 relapsing-remitting MS), ventricular CSF was collected, and NfL levels were measured. White matter lesions were classified as active, mixed, inactive, or remyelinated, and microglia/macrophage morphology in active and mixed lesions was classified as ramified, ameboid, or foamy. In addition, axonal density and acute axonal damage were assessed using Bielschowsky and amyloid precursor protein (APP) (immune) histochemistry. CSF NfL measurements of donors with recent (<1 year) or clinically silent stroke were excluded. CSF NfL levels correlated negatively with disease duration (p = 6.9e-3, r = 0.31). In donors without atrophy, CSF NfL levels correlated positively with the proportion of active and mixed lesions containing foamy microglia/macrophages (p = 9.85e-10 and p = 1.75e-3, respectively), but not with those containing ramified microglia. CSF NfL correlated negatively with proportions of inactive (p = 5.66e-3) and remyelinated lesions (p = 0.03). In the normal appearing pyramid tract, axonal density negatively correlated with CSF NfL levels (Bielschowsky, p = 0.02, r = -0.31), and the presence of acute axonal damage in lesions was related to higher NfL levels (APP, p = 1.17e-6). The amount of acute axonal damage was higher in active lesions with foamy microglia/macrophages and in the rim of mixed lesions with foamy microglia/macrophages when compared with active lesions containing ramified microglia/macrophages (p = 4.6e-3 and p = 0.02, respectively), the center and border of mixed lesions containing ramified microglia/macrophages (center: p = 4.6e-3, border, p = 4.6e-3, and n.s., p = 4.6e-3, respectively), the center of mixed lesions containing foamy microglia/macrophages (p = 4.6e-3 and p = 0.02, respectively), inactive lesions (p = 4.6e-3 and p = 4.6e-3, respectively), and remyelinated lesions (p = 0.03 and p = 0.04, respectively). Our results demonstrated that active and mixed white matter MS lesions with foamy microglia show high acute axonal damage and correlate with elevated CSF NfL levels. Our data support the use of this biomarker to monitor inflammatory demyelinating lesion activity with axonal damage in MS.

## INTRODUCTION

Multiple sclerosis (MS) is a chronic inflammatory disease of the central nervous system (CNS) with focal demyelinating lesions throughout the CNS.[1,2] Pathologically, MS is characterized by different types of lesions that can be staged by the presence and morphology of microglia/macrophages in relation to demyelination.[3,4] Furthermore, some patients show diffuse atrophy with axonal loss throughout the CNS.[3,5] We and others found that at time of death, there is substantial inflammatory lesion activity,[6] and 57% of all lesions in the MS autopsy cohort of the Netherlands Brain Bank (NBB) are either active or mixed.[3] The level of inflammatory lesion activity is correlated to a more severe disease course,[3] and in this study we assess if axonal damage coincides with the inflammatory lesion activity in the same MS autopsy cohort.

Neurofilaments are neuron-specific structural scaffolding protein components of the cytoskeleton that are essential for axonal growth and maintenance.[7] During axonal damage, neurofilaments are released into the cerebrospinal fluid (CSF). Therefore neurofilaments are a potential molecular fluid biomarker for the extent of axonal damage.[8] Indeed, levels of neurofilament light (NfL) in the CSF or blood plasma/serum have been used as general indicators or predictors of neuronal damage in various neurological disorders and events, among which MS, Alzheimer's Disease and traumatic brain injury.[8–16] In MS, NfL can serve as a prognostic biomarker in both relapsing remitting and progressive MS, and for monitoring clinical relapses and treatment response.[13] Previous studies have focused on understanding the value of NfL measurements in MS by combining conventional MRI measurements and clinical data with NfL in the blood and/or CSF.[17–21] NfL levels correlate with clinical relapses and radiological biomarkers of inflammatory disease activity, as it reflects the amount of gadolinium-enhancing lesions, [18,20] the amount of paramagnetic rim MRI lesions in the absence of gadolinium-enhancing lesions, [22] as well as disease progression in terms of the T2 lesion load,[12,20] T2 lesion volume[18,20] and presence of atrophy of the brain and spinal cord.[18,21,23]

These observations raise the question whether neuropathological hallmarks of inflammatory lesion activity, neuroaxonal damage or neurodegeneration correlate with axonal damage as reflected by CSF NfL levels in MS. Here, we assessed the relationship between CSF NfL levels and disease severity, axonal loss in the normal appearing white matter (NAWM), and white matter lesion characteristics including microglia/macrophage activation score (MMAS) and acute axonal damage as measured with amyloid precursor protein (APP) in lesions in a well characterized MS autopsy cohort of 101 cases of the NBB.

## MATERIALS AND METHODS

### Donors

For inclusion in this study, we screened N=182 MS brain donors that came to autopsy at the Netherlands Brain Bank (NBB) between 1991 and 2015.[3] MS pathology was confirmed by a certified neuropathologist and donors with clinical or pathological features of encephalomyelitis were excluded. Donors were also excluded if there were clinical signs of dementia or if a neuropathologist diagnosed pathological dementia based on senile pathology of α-synuclein presence, Tau+ tangles and β-amyloid plaques (Braak > 2, Thal fase >2). Cases of whom no CSF was available for analysis were excluded. The included study cohort consisted of 101 MS donors (*n* = 92 progressive MS, *n* = 9 relapsing-remitting MS). Clinical disability status was scored following the Kurtze's Expanded Disability Status Scale (EDSS), and the time from first symptoms to EDSS-6 and EDSS-8 was determined, together with the age at onset and the total duration of disease from onset of first symptoms. Disease severity score was calculated as 5 – log (years to EDSS6 + 1). Donors were scored for minor senile pathology (Braak ≤ 2, Thal fase ≤ 2), previous history of stroke in their clinical and post-mortem neuropathological files and for the presence of atrophy as based on the post-mortem macroscopic examination. Donor demographics are summarized in **Table 1**. The exclusion criteria and studied characteristics that were related to NfL levels of the various subgroups is visualized in the flowchart in **Fig. 1**.

### Tissue dissection and sample collection

Donors provided informed consent for brain autopsy and for the use of material and clinical data for research purposes in compliance with national ethical guidelines. The NBB autopsy procedures were approved by the Ethical Committee of the VU University Medical Center in Amsterdam, the Netherlands. CSF of all donors was collected from the ventricles and stored at -80°C. Of *n* = 43 MS donors blood was collected from the heart, centrifuged at 3.000 rpm for 15 minutes, and the plasma was aliquoted and stored at -80°C. Regarding the higher number of donors with available CSF samples compared to plasma samples, we focused our current analysis on CSF samples. Blocks were dissected as previously described[3] from standardized locations from the brain stem and the spinal cord, as well as any MS plaques visible macroscopically or on MRI guidance from 1-cm-tick coronal brain slices cut throughout the brain. For the NAWM cohort (Fig. 1), of all donors the brain stem sample containing the pyramid tract was analyzed, as this area is standardly dissected and therefore comparable between donors, and because the axons are oriented in the same direction when cut longitudinal facilitating comparable quantifications. Donors

were excluded if there was a lesion present in the pyramid tract or if the pyramid tract was missing, resulting in a NAWM cohort of *n* = 57.

**Table 1: MS donor characteristics of the various subgroups studied.**

| | **All donors** | | **Donors without recent (<1 year) or clinically silent stroke** | | | |
|---|---|---|---|---|---|---|
| | **All** | **NAWM pyramid tract present** | **All** | **Without atrophy** | **With atrophy** | **NAWM pyramid tract present** |
| | *N=101* | *N=57* | *N=75* | *N=57* | *N=18* | *N=44* |
| Age (years, SD) | 64,5 (12,90) | 69,10 (11,28) | 63,39 (12,57) | 62,33 (12,30) | 66,72 (13,20) | 66,76 (11,53) |
| Sex (F%) | 64,36 | 59,09 | 64,00 | 59,65 | 77,78 | 60,61 |
| PMD (hours, SD) | 8,01 (2,70) | 7,81 (3,18) | 7,80 (2,72) | 7,91 (2,83) | 7,46 (2,41) | 7,83 (3,43) |
| Brain weight (grams, SD) | 1182,4 (135,86) | 1198,53 (136,48) | 1168,89 (134,53) | 1202,09 (122,88) * | 1063,78 (116,84) * | 1190,93 (127,37) |
| pH of CSF (SD) | 6,47 (0,25) | 6,48 (0,27) | 6,46 (0,25) | 6,49 (0,25) | 6,37 (0,24) | 6,49 (0,30) |
| Storage time (years, SD) | 13,64 (6,23) | 14,51 (6,05) | 13,65 (6,41) | 13,21 (6,11) | 15,06 (7,31) | 14,60 (5,80) |
| Age at onset (years) | 33,56 (10,52) | 35,39 (11,57) | 33,54 (11,07) | 32,89 (10,79) | 35,5 (11,98) | 35,03 (11,85) |
| Years to EDSS6 | 17,52 (12,12) | 18,39 (11,57) | 16,85 (11,92) | 17,72 (12,90) | 13,94 (7,36) | 16,72 (11,13) |
| Microglia/ macrophage score (SD) | 0,31 (0,27) | 0,26 (0,28) | 0,30 (0,27) | 0,33 (0,28) | 0,23 (0,22) | 0,25 (0,27) |
| Lesion load BRS (SD) | 6,66 (7,75) | 4,12 (4,89) | 6,86 (8,05) | 6,31 (7,70) | 8,56 (9,08) | 4,19 (4,92) |

**Brain weight is significantly lower in donors with atrophy compared to donors without atrophy (p=3.34e-5, Generalized Linear Model). Abbreviations: NAWM = normal appearing white matter, SD = standard deviation, F = female, PMD = post mortem delay, CSF = cerebrospinal fluid, EDSS6: (Kurtze's) Expanded Disability Status Scale*

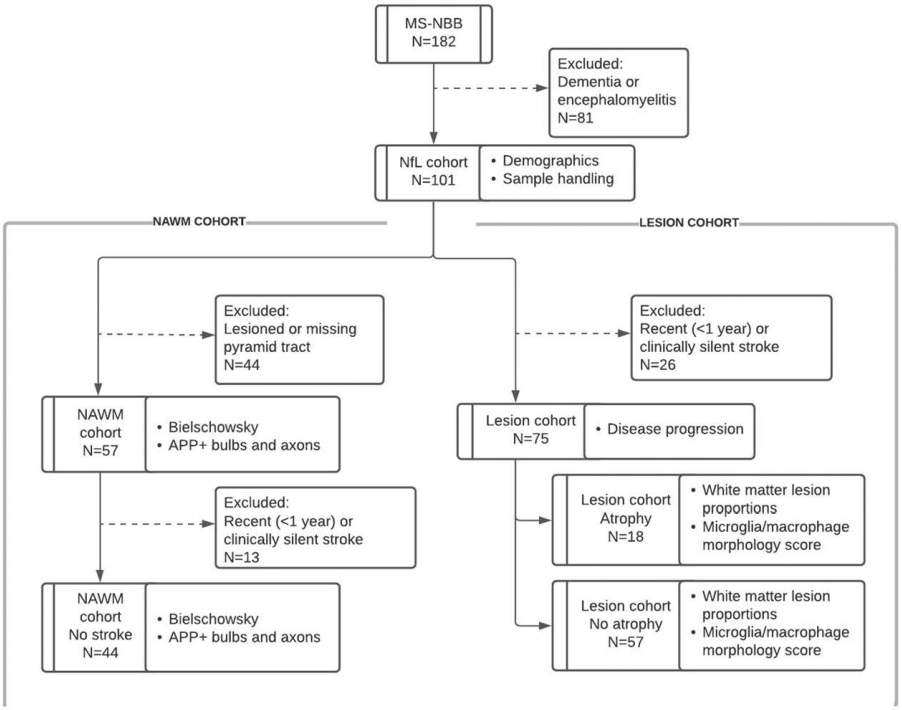


**Figure 1: Flowchart of inclusion criteria and tests performed on the subgroups in the NAWM cohort and the lesion cohort.** NAWM: normal appearing white matter.

## Neurofilament measurements

CSF ($n$ = 101) and paired plasma samples ($n$ = 43) were run simultaneously using a single molecule array (Simoa) assay to measure the NfL levels on a HD-X instrument (Quanterix, Billerica, MA, USA) using the manufacturer's instructions[21,22]. The Simoa assay is a highly sensitive sandwich based enzyme-linked immune sorbent assay (ELISA). The immunocomplex beads fir into one femtomolar-sized chamber, resulting in highly concentrated reaction volume and signal per well. This technology allows an up to 1000-fold increase in sensitivity, with multiple studies reporting strong correlations of CNS-proteins between CSF and blood samples[24]. Post-mortem CSF and plasma samples were standardly diluted 1:100 and 1:4 respectively, and further diluted conform the assay's dynamic range of 0,686 – 500 pg/mL, with a dilution linearity (Mean %L between LLOQ and ULOQ) within the acceptable range of 85-115%.

**Lesion characterization**

Characterization of MS lesions had been carried out previously by Luchetti *et al*. for each donor on all available archived material (3819 lesions in total) following the system of Van der Valk *et al*. (2000) and Kuhlmann *et al*. (2017). Double immunohistochemistry for proteolipid protein (PLP) (MCA839G, AD Serotec, Oxford, UK, with DAB) and human leukocyte antigen (HLA-DR-DQ) (M0775, CR3/43, DAKO, Denmark, with DAB + nickel) [3 w]ere [performed]. Reactive sites and white matter lesion types were discriminated based on demyelination and HLA-DR+ microglia/macrophages. In reactive sites there is no demyelination and there is accumulation of microglia/macrophages. In active lesions there is partial demyelination and accumulation of microglia/macrophages throughout. In mixed lesions there is a fully demyelinated, gliotic center with a border of accumulated microglia/macrophages. The microglia/macrophages in active and mixed lesions are scored 0 if the majority is ramified, 0.5 if the majority is ameboid or 1 if the majority is foamy. In inactive lesions there is complete demyelination of the lesion and there is no presence of microglia/macrophages. In remyelinated lesions there is partial myelination and there are sparse microglia/macrophages throughout[3,26,27].

**Calculation of lesion load and proportions of lesions**

All white matter lesion parameters were calculated per donor previously by Luchetti *et al*. (2018). In the brainstem, a standardly dissected area, of each donor the lesion load has been calculated as the sum of all white matter lesions present, and the reactive load has been calculated as the numbers of reactive sites identified.[3] The MMAS of each donor has been calculated by dividing the sum of de score of the microglia/macrophages values (0, 0.5, 1) in active and mixed lesions by the amount of active and mixed lesions. Proportions of active, mixed and inactive lesions throughout the CNS were calculated per donor as the sum of number of the specific type of lesions divided by the number of all lesions (active, mixed, inactive and remyelinated lesions), discriminating between ramified, ameboid or foamy microglia/macrophages in active and mixed lesions. The proportion of remyelinated lesions was calculated per donor as the number of remyelinated lesions divided by the sum of inactive and remyelinated lesions.[3]

**Quantification of axonal density and APP presence**

To quantify axon density, Bielschowsky silver staining was performed on 8 $\mu$m paraffin-embedded pyramid tract of the NAWM cohort ($n$ = 57). Deparaffinization and rehydration was performed in a series of xylene and alcohol. Incubation with pre-heated 20% silver nitrate solution in H2O at 40°C was performed for 20 minutes. Tissue was placed in H2O, and 32% ammonium hydroxide solution droplets were added before incubation with silver nitrate solution and incubated at 40°C for 20 minutes. Incubation with 1% ammonium

solution was performed for 1 minute. Developer solution (50% nitric acid (65%) + 0.8% formaldehyde (40%) + 0.2% citric acid in depH2O) was added to the ammonium silver nitrate solution and incubated for 10 minutes. 5% sodium thiosulfate solution was incubated for 5 minutes and dehydration was performed in alcohol series and xylene. Images were taken on an Axioskop (Zeiss) at 10x magnification an automated random selection of ROI's comprising >40% of the area was made, and the percentage of area covered by axons at 40x magnification was analyzed with the Image Pro Cell Count Grid software (Media Cubernetics).

For APP [28,29] 8$\mu$m paraffin-embedded NAWM sub-cortical white matter lesion ($n$ = 50) sections were deparaffinized in a series of xylene and alcohol. Antigen retrieval was performed by microwaving citrate buffer pH6.0 for 10 minutes at 800W before blocking with SUMI (0.25% gelatin + 0.5% Triton-X + 10% NHS in TBS). Primary antibodies (APP: MAB348 Millipore, 1:1000) were diluted in SUMI and incubated overnight. After blocking for endogenous peroxidase (0.03% H2O2 in SUMI), biotinylated secondary antibody 1:400 in SUMI was incubated for 1 hour and avidin-biotin-complex (1:800 in TBS) was incubated for 45 minutes, then visualized with DAB (50% diaminobenzidine + 0.03% H2O2 in TBS) and counterstained with hematoxylin. In the NAWM, donors were scored for presence of APP+ bulbs or axons. In the different white matter lesion types the number of APP+ bulbs and axon fragments relative to the area were counted, with the center and border of mixed lesions separately, and in the perilesional white matter of the same tissue block. The counts were normalized to the APP+ events in the perilesional white matter and to the area of the lesion.

**Statistical analysis**

NfL measurements of the CSF and plasma, as well as lesion and reactive site load of the brainstem were natural log-transformed to normalize the data for further analysis. Correlations between continuous variables were tested with Pearson Correlation Coefficient. Differences between dichotomous variables and NfL concentrations were tested with Wilcoxon Rank sum test. Differences between dichotomous variables and proportion measures were tested with Binomial Generalized Linear Models (GLMs). Correlations between proportion measures and continuous variables were tested with Quasibinomial GLMs. Associations between dichotomous variables were tested with Fisher's Test. If multiple groups were tested at once, a Kruskal-Wallis rank sum test was used in combination with pairwise Wilcoxon Rank Sum Tests with corrections for multiple testing. All statistics were performed in RStudio Desktop (version 1.2.5033, Rstudio, Inc., Boston, MA, USA), using key packages ggplot2, devtools, car and lsmeans.

## RESULTS

### Donor demographics and sample handling

Correlations of CSF NfL levels with donor demographics and sample handling are summarized in **Table 2**. CSF NfL levels were not correlated with age, sex, pH of the CSF, weight of the brain, post-mortem delay or storage time. Compared to donors without stroke, NfL levels were significantly higher in donors with recent stroke (<1 year before death) (Pairwise Wilcoxon Rank Sum Tests with corrections for multiple testing, $P$ = 2.4e-3) and with clinically silent stroke ($P$ = 3.5e-4), and there were no differences found in donors with stroke 1-5 years or >5 years before death. As recent and clinically silent stroke elevate CSF NfL levels, this may confound the data. Therefore, for subsequent MS pathology-specific analysis, MS donors with recent (<1 year) and clinically silent stroke were excluded from further analyses (Fig. 1, $n$ = 26 excluded, $n$ = 75 remained). Minor senile pathology (Braak score 1-2 and/or Thal phase 1-2) did not correlate with NfL levels. Lastly, atrophy was validated by the lower brain weight of donors with atrophy than without atrophy (Wilcoxon Rank sum test $P$ = 7.4e-5).

Correlations of CSF NfL with disease progression measures are summarized in **Table 2**. CSF NfL levels of MS donors at time of death did not correlate with age at onset of MS or severity score as calculated with time to EDSS 6, but did correlate negatively with the duration of disease, being higher in patients who had a shorter disease duration (Pearson's Correlation Test, $P$ = 6.9e-3, $r$ = -0.29), also after correction for age ($P$ = 0.04, $r$ = -0.24).



### Axonal damage in the normal appearing white matter

Of 44 MS donors, in the dissected medulla oblongate the pyramid tract was missing or a lesion was present in the pyramid tract. In the remaining 57 donors, axonal density, quantified as the percentage of Bielschowsky positive area (high axonal density: **Fig. 2A**, low axonal density: **Fig. 2B**) in the NAWM, negatively correlated with NfL (Fig. 2C, Pearson's Correlation Test, $P$ = 0.02, $r$ = -0.31). In donors without recent or clinically silent stroke ($n$ = 44), axonal density in the NAWM was not correlated to CSF NfL levels (data not shown).

In the NAWM ($n$ = 57), presence of APP+ axons and bulbs was scored (no APP present: Fig 2D, APP+ axons and bulbs present: Fig. 2E). CSF NfL levels were significantly higher in donors with presence of APP+ axons or bulbs compared to those without ($P$ = *1.17e-6)*. In donors without recent or clinically silent stroke ($n$ = 44), donors with presence of APP+ axons or bulbs also had significantly higher CSF NfL levels compared to donors with without APP+ axons or bulbs present (data not shown, $P$ = 2.3e-4).

**Table 2:** Correlations of clinical and pathological donor characteristics with CSF NFL levels of all MS donors.

| | | | **CSF NfL** mean (SD) pg/mL (log) | **P** | **r** |
|---|---|---|---|---|---|
| Age | | | - | 0.85 | -0.02 |
| Sex | M | | 7.57 (1.25) | 0.35 | - |
| | F | | 7.75 (1.23) | - | - |
| pH of CSF | | | - | 0.25 | -0.12 |
| Brain weight | | | - | 0.31 | 0.10 |
| PMD | | | - | 0.38 | 0.09 |
| Storage time | | | - | 0.36 | 0.09 |
| Plasma NFL (pg/mL (log)) | | | - | **1.9e-4** | 0.54 |
| Minor senile pathology | No | | 7.71 (1.37) | 0.78 | - |
| | Yes | | 7.66 (1.09) | - | - |
| Stroke (years from death) | No | | 7.25 (0.98) | - | - |
| | Yes | <1 | 9.42 (1.40) | **2.4e-3** | - |
| | | 1-5 | 7.47 (0.87) | 0.46 | - |
| | | >5 | 7.68 (1.33) | 0.72 | - |
| | | Clinically silent | 8.50 (1.13) | **3.5e-4** | - |
| Atrophy | No | | 7.73 (1.27) | 0.31 | - |
| | Yes | | 7.49 (1.02) | - | - |
| Age at onset (years)* | | | 33.53 (11.07) | 0.33 | 0.12 |
| Severity score* | | | 3.85 (0.31) | 0.16 | 0.16 |
| Disease duration (years)* | | | 30.31 (12.80) | **6.9e-3** | -0.31 |

*All associations were tested with either Pearson Correlation Coefficient. Wilcoxon Rank sum test was used if two groups were compared, and Pairwise Wilcoxon Rank Sum Test corrected for multiple testing for stroke at different time points. Abbreviations: SD = standard deviation, M = male, F = female, PMD = post mortem delay, CSF = cerebrospinal fluid. * Donors without recent (<1 year) or clinically silent stroke*

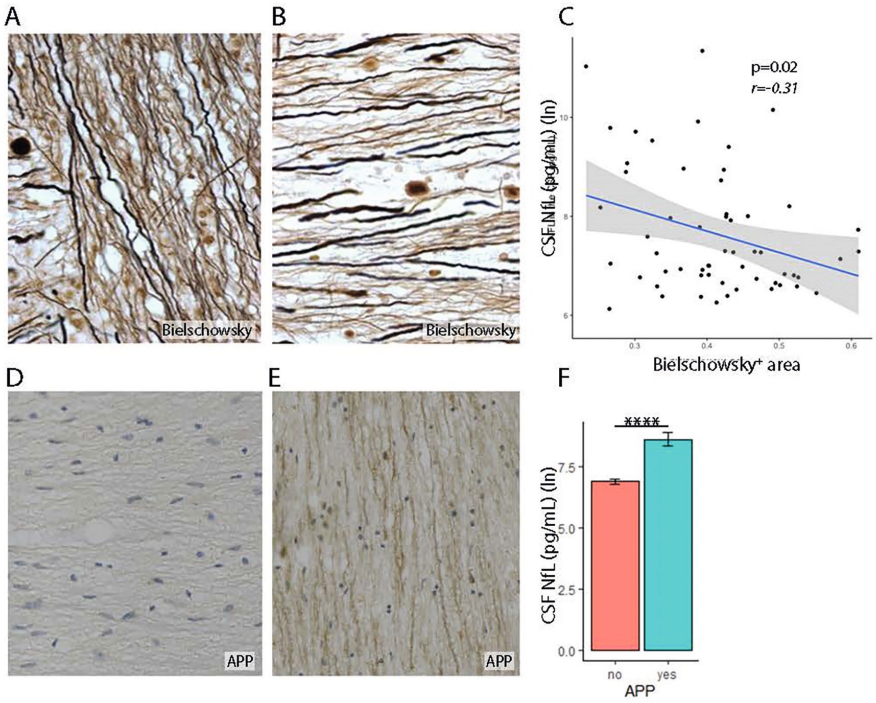


**Figure 2: NfL levels are negatively correlated with axonal density and are increased with presence of acute axonal damage in the normal appearing white matter.** For axonal density, a Pearson's Correlation Test was performed, and the regression line is visualized with the gray area indicating the 95% confidence interval. For APP+ a Wilcoxon Rank Sum test with correction of multiple testing was performed. Images are taken at 40x magnification. **(A)** Representative image of a high number of Bielschowsky+ axons and (**B)** low number of Bielschowsky+ axons. **(C)** Axonal density, as measured by Bielschowsky+ axons, was negatively correlated with CSF NfL (p=0.02, r=0.31). **(D)** Representative image of NAWM without APP+ axons or bulbs, **(E)** representative image of NAWM with APP+ axons and bulbs. **(F)** The CSF NfL levels of donors with APP+ axons or bulbs were significantly higher that of those without APP+ axons or bulbs (*P* = 1.17e-6).

## White matter inflammation and lesion activity

As brain atrophy on MRI is related to NfL levels [9], we have analyzed correlations of CSF NfL in MS donors with macroscopic brain atrophy and without atrophy separately. Donor demographics were not different between donors with atrophy and without atrophy, as visualized in **Table 1**. CSF NfL levels of MS donors without atrophy were similar to donors with atrophy (Wilcoxon Rank sum test, **Table 2**). Donors with and without atrophy have comparable lesion measures (**Table 3**).

**Fig. 3** shows ramified microglia/macrophages with MMAS score 0 (**Fig. 3A**) and foamy microglia/macrophages with MMAS score 1 (**Fig. 3B**), and shows microscopic images of an active lesion containing ramified (**Fig. 3C**) and foamy (**Fig. 3D**) microglia/macrophages, a mixed lesion containing ramified (**Fig. 3E**) and foamy (**Fig. 3F**) microglia/macrophages, an inactive lesion (**Fig. 3G**) and a remyelinated lesion (**Fig. 3H**). As shown in **Table 3**, correlations of CSF NfL with lesion measures found in all donors become stronger when donors with atrophy are removed. In donors without atrophy, CSF NfL levels correlated with several lesion type proportions.

In donors without atrophy, the MMAS positively correlated with CSF NfL (GLM, $P = 1.2e\text{-}6$, **Fig. 3I**). CSF NfL levels correlated with the proportion of all active lesions (GLM, $P = 6.35e\text{-}3$) and this correlation was considerably stronger for active lesions containing foamy microglia/macrophages (GLM, $P = 9.85e\text{-}10$, **Fig. 3K**). CSF NfL levels did not correlate with the proportion of all mixed lesions but was significantly correlated to the proportion of mixed lesions containing foamy microglia/macrophages (GLM, $P = 1.75e\text{-}3$, **Fig. 3M**). CSF NfL levels did not correlate significantly with the proportion of active or mixed lesions containing ramified microglia/macrophages (**Fig. 3J & 3L**). Reciprocally, CSF NfL levels negatively correlated with the proportion of inactive lesions (GLM, $P = 1.75e\text{-}3$, **Fig. 3N**) and remyelinated lesions (GLM, $P = 0.03$, **Fig. 3O**). Lastly, CSF NfL did not correlate with the lesion load or the proportion of reactive sites in the brain stem. In donors with atrophy, only a weak correlation was found of CSF NfL levels with the proportion of active lesions containing foamy microglia/macrophages (GLM, $P = 0.03$), and no correlation was found with other lesion proportions.

**Table 3:** Correlations of lesion proportions and NfL levels in the CSF in MS donors without recent or clinically silent stroke, differentiated between donors with and without atrophy

| | | Donors without recent or clinically silent stroke | | | | | | | |
|---|---|---|---|---|---|---|---|---|---|
| **Lesion type** | ***Subtype*** | **All (n=75)** | | | **With atrophy (n=18)** | | **Without atrophy (n=57)** | | **With vs without atrophy** |
| | | Total #lesions | Average load / Proportion / score (SD) | P | Average load / Proportion / score (SD) | P | Average load / Proportion / score(SD) | P | P |
| Lesion load (BRS) | | 659 | 1.51 (1.14) | 0.36 | 1.65 (1.27) | 0.37 | 1.46 (1.10) | 0.68 | 0.55 |
| Reactive load (BRS) | | 149 | 0.55 (0.74) | 0.85 | 0.73 (0.87) | 0.20 | 0.49 (0.68) | 0.47 | 0.24 |
| Active | | 874 | 0.21 (0.23) | **0.01** | 0.18 (0.22) | 0.64 | 0.22 (0.23) | **6,35e-3** | 0.51 |
| | *Ramified* | *299* | 0.08 (0.15) | 0.33 | 0.09 (0.16) | 0.73 | 0.08 (0.15) | 0.31 | 0.70 |
| | *Foamy* | *356* | 0.07 (0.13) | **6.25e-10** | 0.03 (0.06) | **0.03** | 0.08 (0.14) | **9.85e-10** | 0.14 |
| Mixed | | 985 | 0.27 (0.27) | 0.50 | 0.22 (0.29) | 0.15 | 0.28 (0.27) | 0.14 | 0.40 |
| | *Ramified* | *416* | 0.13 (0.17) | 0.43 | 0.07 (0.08) | 0.41 | 0.14 (0.19) | 0.41 | 0.08 |
| | *Foamy* | *194* | 0.04 (0.06) | **0.02** | 0.02 (0.05) | 0.13 | 0.04 (0.07) | **1,75e-3** | 0.14 |
| Inactive | | 901 | 0.32 (0.27) | **0.04** | 0.34 (0.30) | 0.85 | 0.32 (0.26) | **5,66e-3** | 0.78 |
| Remyelinated | | 548 | 0.20 (0.22) | 0.16 | 0.19 (0.21) | 0.14 | 0.20 (0.22) | **0.03** | 0.39 |
| MMAS score | | 1859 | 0.31 (0.27) | **7.47e-7** | 0.23 (0.22) | 0.28 | 0.33 (0.28) | **1.2e-6** | 0.07 |

*Associations of lesion load and reactive load are tested with Pearson Correlation, and the rest were tested with quasibinomial Generalized Linear Models*
*Abbreviations: SD = standard deviation, BRS = brain stem, vs = versus.*

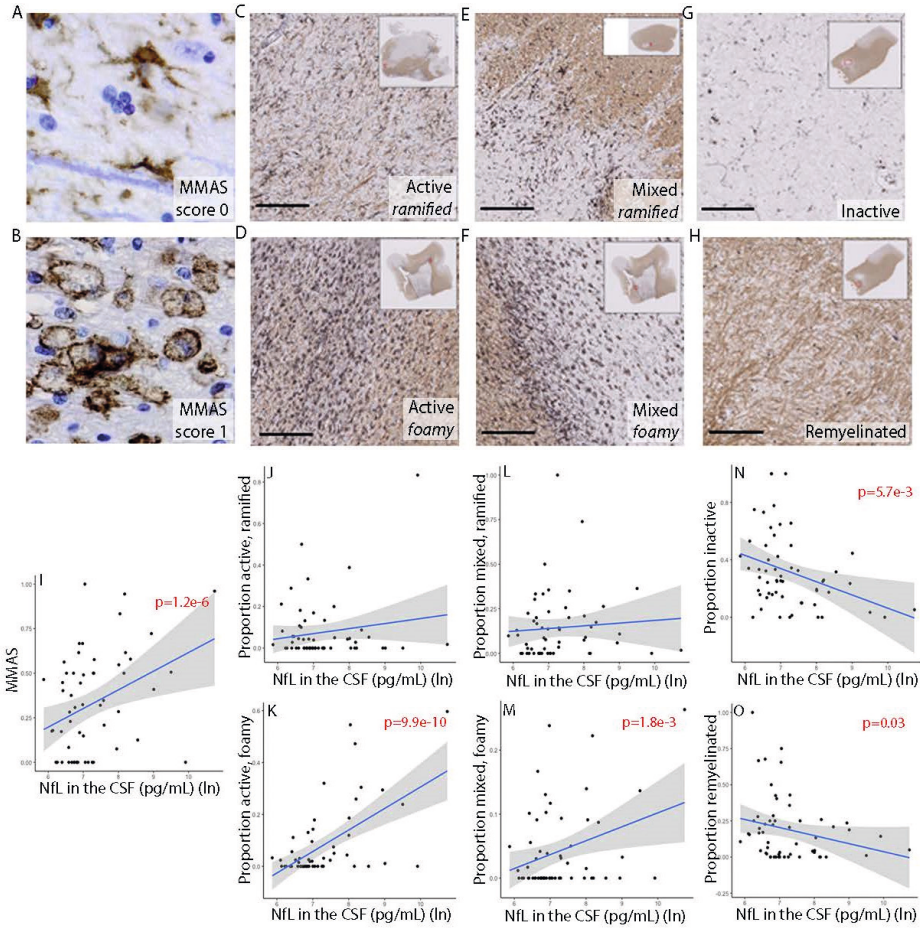


**Figure 3: CSF NfL levels correlate with pathological hallmarks of inflammatory lesion activity.** Correlations for different lesion measures were tested with a general linear model and correlation between NfL levels in the CSF and plasma was tested with a Pearson's Correlation Test , and the regression line is visualized with the gray area indicating 95% confidence interval. Representative immunohistochemical stainings show **(A)** ramified microglia/macrophages with microglia/macrophage activation score (MMAS) 0 and **(B)** foamy microglia/macrophages with MMAS 1. Representative immunohistochemical stainings stained for PLP in brown and HLA-DR+ microglia in black with a scalebar of 200µm of active lesions with **(C)** ramified microglia/macrophages, **(D)** foamy microglia/macrophages, mixed lesions with **(E)** ramified microglia/macrophages and **(F)** foamy microglia/macrophages, **(G)** inactive lesions and **(H)** remyelinated lesions. In donors without atrophy, CSF NfL levels positively correlated with **(I)** MMAS (p=1.2e-6), and proportions of **(K)** active lesions (p=9.9e-10) with foamy microglia/macrophages, **(M)** mixed lesions with foamy microglia/macrophages (p=1.8e-3), and CSF NfL levels negatively correlated with the proportions of **(N)** inactive lesions (p=5.7e-3) and **(O)** remyelinated lesions (p=0.03).

**Plasma NfL levels and white matter inflammation and lesion activity**

Regarding the more frequent use of plasma samples compared to CSF samples for NfL analyses in clinical monitoring of MS activity, we have explored the relation of plasma NfL with neuropathological substrates in the small MS cohort with available plasma samples (N=43). Unfortunately the sample size of donors without recent (<1 year) or clinically silent stroke with plasma samples was low (n=26). Plasma and CSF NfL levels correlated significantly (Fig. 3P, Pearson's Correlation Test, $P$ = 1.9e-4, r =0.54). Correlations between plasma NfL levels and lesion load, reactive site load, lesion proportions and the MMAS score are summarized in Supplementary table 1. In donors without atrophy (n=22) the correlation between plasma NfL and the MMAS score and the proportion of active lesions with foamy microglia/macrophages showed generally similar trends as CSF NfL (Supplementary figure 1).

**Acute axonal damage in subcortical white matter lesions**

To confirm the association of foamy macrophages with increased axonal damage, as reflected by higher CSF NfL levels, we performed APP stainings in different lesion types. As visualized in **Fig. 4**, in active lesions containing foamy microglia/macrophages the amount of APP+ bulbs and axon fragments, normalized to the amount of APP+ bulbs and axon fragments in the perilesional white matter and the area of the lesion, is significantly higher compared to active lesions containing ramified microglia/macrophages (pairwise Wilcoxon Rank Sum Tests with corrections for multiple testing, $P$ = 4.6e-3), active lesions containing ameboid microglia/macrophages, the border and the center of mixed lesions containing ramified microglia/macrophages ($P$ = 4.6e-3 & $P$ = 4.6e-3 resp), the center of mixed lesions containing foamy microglia/macrophages ($P$ = 4.6e-3), inactive lesions ($P$ = 4.6e-3) and remyelinated lesions ($P$ = 0.03). The amount of APP+ bulbs and axon fragments is significantly higher in the border of mixed lesions containing foamy microglia/macrophages compared to active lesions containing ramified microglia/macrophages ($P$ = 0.02), the center of mixed lesions with ramified microglia/macrophages ($P$ = 4.6e-3), the center of mixed lesions with foamy microglia ($P$ = 0.02), inactive lesions ($P$ = 4.6e-3) and remyelinated lesions ($P$ = 0.04).

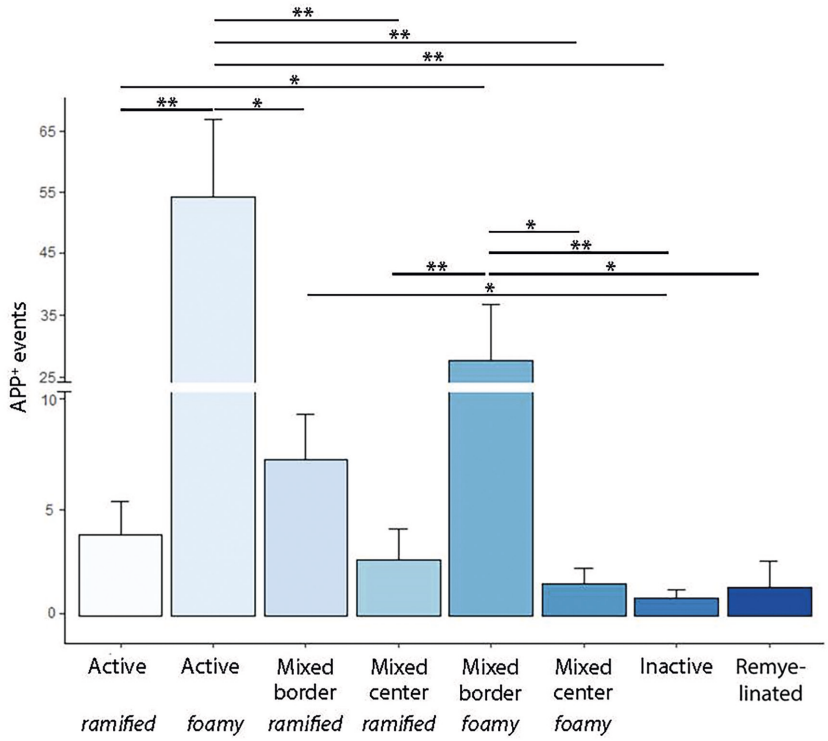


**Figure 4: Acute axonal damage most prevalent in active lesions with foamy microglia/macrophages and the border of mixed lesions with foamy microglia/macrophages.** A Kruskal-Wallis test followed by pairwise Wilcoxon Rank sum tests with correction for multiple testing was performed. In active lesions containing foamy microglia/macrophages, the amount of APP+ bulbs and axon fragments is significantly higher compared to active lesions containing ramified microglia/macrophages (p=4.6e-3), the border and the center of mixed lesions containing ramified microglia/macrophages (p=4.6e-3 & p=4.6e-3 resp.), the center of mixed lesions containing foamy microglia/macrophages (p=4.6e-3), inactive lesions (p=4.6e-3) and remyelinated lesions (p=0.03). The amount of APP+ bulbs and axon fragments is significantly higher in the border of mixed lesions containing foamy microglia/macrophages compared to active lesions containing ramified microglia/macrophages (p=0.02), the center of mixed lesions with ramified and foamy microglia/macrophages (p=4.6e-3, p=0.02, resp.), inactive lesions (p=4.6e-3) and remyelinated lesions (p=0.04). The amount of APP+ bulbs and axon fragments in the border of mixed lesions containing ramified microglia/macrophages is significantly higher compared to inactive lesions (p=0.04)

## DISCUSSION

Here we present a quantitative neuropathological analysis of an extensive MS autopsy cohort of 101 brain donors and 3819 lesions showing that acute axonal damage relating to active inflammatory lesion activity and reduced axonal density associate with increased CSF NfL levels. Our key findings are that 1) CSF NfL levels were negatively correlated with disease duration. 2) CSF NfL levels were positively correlated with increased axonal loss and with acute axonal damage in the normal appearing white matter. 3) CSF NfL levels were positively correlated with proportions of active and mixed lesions containing foamy microglia/macrophages, and negatively correlated with inactive and remyelinating lesion proportions. 4) Active lesions with foamy microglia/macrophages and the border of mixed lesions with foamy microglia/macrophages have a higher amount of APP+ bulbs and axonal fragments compared active and mixed lesions containing ramified microglia, inactive lesions and remyelinated lesions. These findings show that specifically MS lesions containing lipid laden foamy microglia/macrophages are associated with acute axonal damage, and that proportion of such lesions positively correlate with CSF NfL levels. Furthermore, CSF Nfl levels correlate with fast progression of MS. Together, this validates CSF NfL as a quantifiable biomarker for inflammatory white matter lesion activity driven axonal damage and disease progression in MS.



In our cohort, CSF NfL levels were not confounded by donor demographics nor by post-mortem delay or storage time. In line with clinical studies, we found post mortem CSF NfL levels positively correlated with post mortem plasma NfL levels, with the same order of magnitude.[19–21] In contrast to some previous studies, but in line with the clinical cohorts of Kuhle *et al.* (2019), Uher *et al.* (2020) and Bridel *et al.* (2019), we did not observe an effect of age on CSF NfL levels in MS[12,14,18,19,21] Most likely, increases in CSF NfL due to acute axonal damage and demyelinating activity are superimposed on the increases due to ageing in our autopsy cohort.[12] Similar to previous clinical studies, there were no sex-related differences in post-mortem CSF NfL levels.[14,15,19,21] The pH of the CSF, the brain weight and the storage time did not correlate with CSF NfL levels further validating our post mortem sampling method.

We confirmed a history of a recent stroke and a clinically silent stroke as confounding factors when studying MS-specific pathologies in relation to CSF NfL, and these donors were therefore excluded from MS-specific analyses.[30–33] Brain atrophy in MS can also be a source of increases in NfL,[23] but in our study it did not have an effect on CSF NfL levels. Most likely, this is due to the spatial and temporal variations in atrophy that are not taken into account with the yes/

no score used in this study. However, CSF NfL changes due to atrophy, the irreversible neurodegenerative component of MS[34], superimposed on the effect of lesion characteristics on CSF NfL. Therefore, the relation between MS lesion characteristics and CSF NfL levels were analyzed separately in donors with and without atrophy in our study.

CSF and plasma NfL levels have previously been correlated with progression of MS-related disability during life.[11,19,21] Here we show that CSF NfL levels were negatively correlated with the disease duration reflecting a more severe course, but not the age at onset or the disease severity score as calculated with time to EDSS6. This suggests that donors with a shorter disease duration had experienced more neurodegeneration in the year before death compared to donors with a longer disease duration. CSF NfL levels reflect recent acute MS-related axonal damage[15,30], likely reflecting lesion activity causing axonal damage within a period of approximately the previous year and are therefore not likely retrospectively reflecting the speed of disease progression before reaching EDSS6.

In the NAWM, CSF NfL negatively correlated with Bielschowsky+ axons and therefore positively correlated with increased axonal loss. CSF NfL levels were significantly higher in donors with APP+ axons or bulbs in the NAWM compared to donors without APP+ axons or bulbs ($P$ = 1.17e-6). This is most likely due to both Wallerian degeneration and neuro-axonal damage.[35,36]

Previously was shown that APP+ axons and bulbs are more frequently present in the border of mixed lesions than in the center[22,37]. Here, we corroborate these findings, and additionally show in active lesions and the border of mixed lesions with foamy macrophages significantly more APP+ acute axonal damage compared to active lesions and the border of mixed lesions with ramified microglia/macrophages. Therefore, the strong positive correlation between CSF NfL levels and the proportion of active and mixed lesions with foamy microglia/macrophages is most likely due to the increased acute axonal damage in these lesions. The correlation of CSF NfL levels and proportions of (mixed) active MS lesions is in line with radiological studies showing correlations between NfL with MRI biomarkers of inflammatory disease activity in terms of the amount of gadolinium-enhancing lesions and paramagnetic rim MRI lesions. Interestingly, our data suggest that foamy and ramified microglia may have different implications in terms of neuro-axonal damage, likely relating to functional differences between lipid laden foamy versus ramified microglia/macrophages[38].

Our study suggests several important issues about the use of CSF NfL as a biomarker for acute axonal damage in MS relating to lesion activity. Firstly, we show that recent or clinically silent stroke and atrophy influence the relation between NfL CSF levels and MS lesion activity and acute axonal damage. Thus, these are comorbid conditions to use CSF NfL to monitor lesion activity and related axonal damage in MS patients. Sequential NfL measurements within individual patients should solve this problem. Secondly, CSF samples were available of more brain donors than plasma samples and therefore we studied NfL levels in CSF. However, we show that CSF NfL levels and plasma NfL correlate and that plasma NfL levels show a similar trend as CSF NfL levels towards a positive correlation with the MMAS score and the proportion of active lesions with foamy microglia/macrophages. Future studies should attempt to establish the relation of plasma NfL with neuropathological substrates in MS, as measurements of plasma NfL would be easier to apply clinically than of CSF NfL. Lastly, due to a smaller group of donors with atrophy compared to donors without atrophy, it is possible that differences between these two groups are due to a loss of statistical power in the group with atrophy. However, as the relations between CSF NfL and lesion measures of all donors together are less significant than the relations between CSF NfL and lesion measures of only donors without atrophy, this suggests that these groups are fundamentally different.



In summary, in an MS autopsy cohort of 101 cases we show that CSF NfL levels negatively correlate with disease duration and positively correlate neuropathologically with proportions of active and mixed lesions containing foamy microglia/macrophages and acute axonal damage, validating NfL as marker of disease activity.

**Data availability**

The data presented in this study are available on request from the corresponding author.

**Acknowledgements**

The authors are grateful to the brain donors with multiple sclerosis who donated their brain for research and to the team of the Netherlands Brain Bank for their excellent service.

**Funding**

MS Research grant 17-975 and MoveS inspiration Grant 19-1079.

**Disclosure**

The authors report no disclosures relevant to the manuscript.

## REFERENCES


1. Lassmann, H. Multiple sclerosis pathology. *Cold Spring Harb. Perspect. Med.* 8, 1–15 (2018).
2. Lassmann, H., Raine, C. S., Antel, J. & Prineas, J. W. Immunopathology of multiple sclerosis: Report on an international meeting held at the Institute of Neurology of the University of Vienna. *J. Neuroimmunol.* 86, 213–217 (1998).
3. Luchetti, S. *et al.* Progressive multiple sclerosis patients show substantial lesion activity that correlates with clinical disease severity and sex: a retrospective autopsy cohort analysis. *Acta Neuropathol.* 135, 511–528 (2018).
4. Stadelmann, C., Wegner, C. & Bruek, W. Inflammation, demyelination, and degeneration - Recent insights from MS pathology. *Mol. Basis Dis.* 1812, 275–282 (2011).
5. Frischer, J. M. *et al.* Clinical and Pathological Insights into the Dynamic Nature of the White Matter Multiple Sclerosis Plaque. *Ann Neurol* 78, 710–721 (2015).
6. Lucchinetti, C. *et al.* Heterogeneity of multiple sclerosis lesions: implications for the pathogenesis of demyelination. *Ann. Neurol.* 47, 707–717 (2000).
7. Yuan, A., Rao, M. V., Veeranna & Nixon, R. A. Neurofilaments at a glance. *J. Cell Sci.* 125, 3257–3263 (2012).
8. Ferreira-atuesta, C., Reyes, S., Giovanonni, G. & Gnanapavan, S. The Evolution of Neurofilament Light Chain in Multiple Sclerosis. *Front. Neurosci.* 15, 1–13 (2021).
9. Khalil, M. *et al.* Neurofilaments as biomarkers in neurological disorders. *Nat. Rev. Neurol.* 14, 577–589 (2018).
10. Ziemssen, T., Akgün, K. & Brück, W. Biomarkers in multiple sclerosis. *J. Neuroinflammation* 9, 1–11 (2019).
11. Varhaug, K. N., Torkildsen, Ø., Myhr, K. M. & Vedeler, C. A. Neurofilament light chain as a biomarker in multiple sclerosis. *Front. Neurol.* 10, 1–6 (2019).
12. Uher, T. *et al.* Neurofilament levels are associated with blood – brain barrier integrity , lymphocyte extravasation , and risk factors following the first demyelinating event in multiple sclerosis. 1–12 doi:10.1177/1352458520912379.
13. Kapoor, R. *et al.* Serum neurofilament light as a biomarker in progressive multiple sclerosis. *Neurology* 95, 436–444 (2020).
14. Bridel, C. *et al.* Diagnostic Value of Cerebrospinal Fluid Neurofilament Light Protein in Neurology: A Systematic Review and Meta-analysis. *JAMA Neurol.* 76, 1035–1048 (2019).
15. Shahim, P. *et al.* Serum neurofilament light protein predicts clinical outcome in traumatic brain injury. *Sci. Rep.* 6, 1–9 (2016).
16. Zetterberg, H. *et al.* Association of Cerebrospinal Fluid Neurofilament Light Concentration With Alzheimer Disease Progression. *JAMA Neurol.* 73, 60–67 (2016).
17. Gafson, A. R. *et al.* Neurofilaments: neurobiological foundations for biomarker applications. *Brain* 143, 1975–1998 (2020).
18. Kuhle, J. *et al.* Blood neurofilament light chain as a biomarker of MS disease activity and treatment response. *Neurology* 92, E1007–E1015 (2019).
19. Piehl, F. *et al.* Plasma neurofilament light chain levels in patients with MS switching from injectable therapies to fingolimod. *Mult. Scler. J.* 1–9 (2017) doi:10.1177/https.
20. Barro, C. *et al.* Serum neurofilament as a predictor of disease worsening and brain and spinal cord atrophy in multiple sclerosis. *Brain* 141, 2382–2391 (2018).

21. Disanto, G. *et al.* Serum Neurofilament light: A biomarker of neuronal damage in multiple sclerosis. *Ann. Neurol.* 81, 857–870 (2017).
22. Maggi, P. *et al.* Chronic White Matter Inflammation and Serum Neurofilament Levels in Multiple Sclerosis. *Neurology* 0, 10.1212/WNL.0000000000012326 (2021).
23. Kuhle, J. *et al.* Serum neurofilament is associated with progression of brain atrophy and disability in early MS. *Neurology* 88, 826–831 (2017).
24. Kuhle, J. *et al.* Comparison of three analytical platforms for quantification of the neurofilament light chain in blood samples: ELISA, electrochemiluminescence immunoassay and Simoa. *Clin. Chem. Lab. Med.* 54, 1655–1661 (2016).
25. Bridel, C., Verberk, I. M. W., Heijst, J. J. A., Killestein, J. & Teunissen, C. E. Variations in consecutive serum neurofilament light levels in healthy controls and multiple sclerosis patients. *Mult. Scler. Relat. Disord.* 47, 102666 (2020).
26. Kuhlmann, T. *et al.* An updated histological classification system for multiple sclerosis lesions. *Acta Neuropathol.* 133, 13–24 (2017).
27. Van Der Valk, P. & De Groot, C. J. A. Staging of multiple sclerosis (MS) lesions: Pathology of the time frame of MS. *Neuropathol. Appl. Neurobiol.* 26, 2–10 (2000).
28. Lindner, M., Fokuhl, J., Linsmeier, F., Trebst, C. & Stangel, M. Chronic toxic demyelination in the central nervous system leads to axonal damage despite remyelination. *Neurosci. Lett.* 453, 120–125 (2009).
29. Nystad, A. E., Torkildsen, Ø. & Wergeland, S. Effects of vitamin D on axonal damage during de- and remyelination in the cuprizone model. *J. Neuroimmunol.* 321, 61–65 (2018).
30. Gattringer, T. *et al.* Serum neurofilament light is sensitive to active cerebral small vessel disease. *Neurology* 89, 2108–2114 (2017).
31. Lewis, S. B., Wolper, R. A., Miralia, L., Yang, C. & Shaw, G. Detection of phosphorylated NF-H in the cerebrospinal fluid and blood of aneurysmal subarachnoid hemorrhage patients. *J. Cereb. Blood Flow Metab.* 28, 1261–1271 (2008).
32. Zanier, E. R. *et al.* Neurofilament light chain levels in ventricular cerebrospinal fluid following acute aneurysmal sybarachnoid hemorrhage. 8, 157–159 (2011).
33. Uphaus, T. *et al.* NfL (Neurofilament Light Chain) Levels as a Predictive Marker for Long-Term Outcome After Ischemic Stroke. *Stroke* 50, 3077–3084 (2019).
34. Andravizou, A. *et al.* Brain atrophy in multiple sclerosis: mechanisms, clinical relevance and treatment options. *Autoimmun. Highlights* 10, (2019).
35. Allen, I. V., McQuaid, S., Mirakhur, M. & Nevin, G. Pathological abnormalities in the normal-appearing white matter in multiple sclerosis. *Neurol. Sci.* 22, 141–144 (2001).
36. Singh, S. *et al.* Relationship of acute axonal damage, Wallerian degeneration, and clinical disability in multiple sclerosis. *J. Neuroinflammation* 14, 1–15 (2017).
37. Ferguson, B., Matyszak, M. K., Esiri, M. M. & Perry, V. H. Axonal damage in acute multiple sclerosis lesions. *Brain* 120, 393–399 (1997).
38. Zia, S. *et al.* Microglia Diversity in Health and Multiple Sclerosis. *Front. Immunol.* 11, 1–14 (2020).

## SUPPLEMENTARY FILES

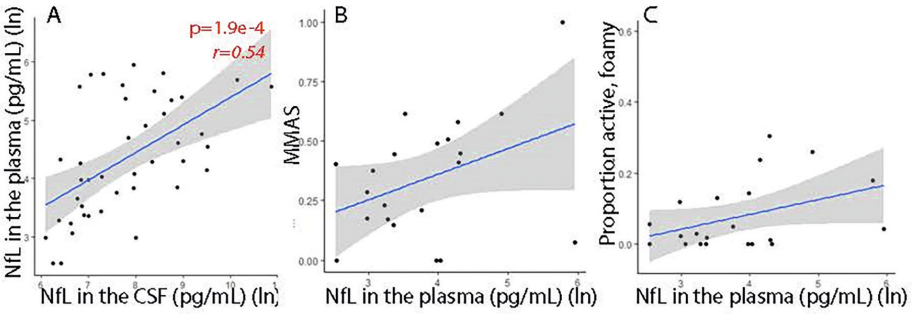


**Supplementary figure 1: Plasma NfL levels correlate with CSF NfL levels. (A)** Plasma NfL levels and CSF NfL levels are positively correlated (p=1.9e-4). Plasma NfL levels are not significantly correlated to **(B)** the MMAS score or **(C)** the proportion of active lesions with foamy microglia/macrophages (p=0.07), but show generally similar trends as CSF NfL levels.

**Supplementary table 1:** Correlations of lesion proportions and NfL levels in the plasma in MS donors without recent or clinically silent stroke, differentiated between donors with and without atrophy

| | | Donors without recent or clinically silent stroke | | | | | | | |
|---|---|---|---|---|---|---|---|---|---|
| **Lesion type** | ***Subtype*** | **All (n=27)** | | | **With atrophy (n=5)** | | **Without atrophy (n=22)** | | **With vs without atrophy** |
| | | Total #lesions | Average load / Proportion / score (SD) | P | Average load / Proportion / score (SD) | P | Average load / Proportion / score(SD) | P | P |
| Lesion load (BRS) | | 358 | 0.94 (0.96) | 0.38 | 1.01 (0.90) | 0.60 | 1.00 (1.00) | 0.79 | **0.04** |
| Reactive load (BRS) | | 86 | 0.34 (0.44) | | 0.41 (0.47) | | 0.39 (0.50) | | 0.22 |
| Active | | 427 | 0.22 (0.18) | 0.19 | 0.22 (0.18) | 0.58 | 0.22 (0.17) | 0.24 | 0.75 |
| | *Ramified* | *180* | 0.09 (0.12) | **5.5e-3** | 0.10 (0.14) | 0.30 | 0.09 (0.12) | **2.5e-3** | 0.89 |
| | *Foamy* | *127* | 0.06 (0.08) | 0.13 | 0.07 (0.08) | 0.98 | 0.08 (0.09) | 0.07 | 0.65 |
| Mixed | | 537 | 0.29 (0.23) | 0.41 | 0.32 (0.21) | 0.41 | 0.31 (0.23) | 0.94 | 0.38 |
| | *Ramified* | *267* | 0.15 (0.14) | 0.37 | 0.19 (0.12) | 0.99 | 0.18 (0.16) | 0.72 | 0.09 |
| | *Foamy* | *98* | 0.04 (0.06) | 0.24 | 0.04 (0.05) | 0.24 | 0.04 (0.05) | 0.66 | 0.22 |
| Inactive | | 460 | 0.37 (0.25) | 0.14 | 0.34 (0.22) | 0.87 | 0.36 (0.23) | 0.18 | 0.44 |
| Remyelinated | | 297 | 0.19 (0.18) | 0.87 | 0.17 (0.13) | 0.26 | 0.19 (0.15) | 0.32 | 0.96 |
| MMAS score | | 964 | 0.33 (0.24) | 0.18 | 0.31 (0.23) | 0.56 | 0.33 (0.25) | 0.22 | 0.85 |

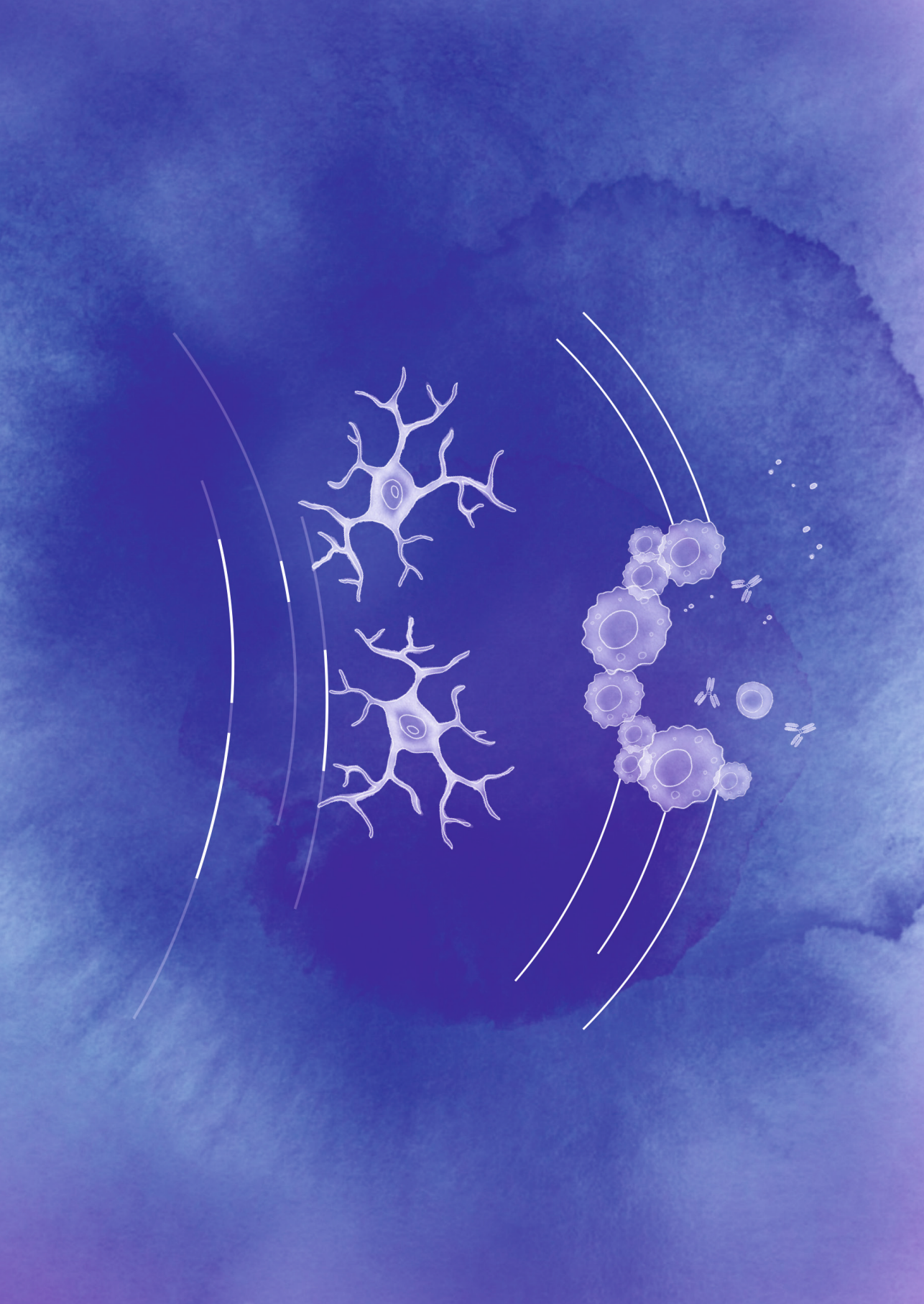

# CHAPTER 7

# Spatial profiling of multiple sclerosis lesion expansion and repair

Aletta M.R. van den Bosch[1]*, Jia H. Khoo[2]*, Zhigang Lu[2], Han Liang[2], Dennis Wever[1], Li Pu[2], Bart J.L. Eggen[3], Joost Smolders[1,4], Jörg Hamann[1,5], Zhouchun Shang[2#], Jan Mulder[6#], Inge Huitinga[1,7#]

* and # contributed equally

[1]Neuroimmunology Research Group, Netherlands Institute for Neuroscience, Amsterdam, The Netherlands; [2]BGI Research, Riga, Latvia; [3]Department of Neuroscience, Section Medical Physiology, University Medical Center Groningen, Groningen, The Netherlands; [4]MS Center ErasMS, Department of Neurology and Immunology, Erasmus Medical Center, Rotterdam, The Netherlands; [5]Department of Experimental Immunology, Amsterdam institute for Immunology and Infectious Diseases, Amsterdam University Medical Center, Amsterdam, The Netherlands; [6]Department of Neuroscience, Karolinska Institute, Stockholm, Sweden; [7]Swammerdam Institute for Life Sciences, University of Amsterdam, Amsterdam, The Netherlands

*In preparation*

## ABSTRACT

Multiple sclerosis (MS) is characterized by demyelinating lesions in the central nervous system . MS lesions are heterogeneous, having varying states of microglia that may have different roles in MS lesion expansion, remyelination, and scar formation [1–3]. Here, we performed spatial transcriptomics with single-cell resolution on post-mortem human brain tissue to compare mixed active/inactive (mixed) lesions with either foamy microglia or ramified microglia within the same MS donors. We identified distinct cellular and molecular mechanisms driving smoldering lesion activity and failure of remyelination relating to microglia phenotype. Mixed lesions with foamy microglia were characterized by enhanced immune activation and higher lymphocyte density, immunoglobulin production, complement-mediated microglial activity, iron dysregulation, and demyelination. Conversely, ramified microglia were linked to regeneration and remyelination, displaying gene expression profiles indicative of myelin stability and neuro-axonal protection, fostering an environment conducive to repair. Our findings highlight the utility of microglial morphology as a marker for identifying smoldering mixed lesions in post-mortem human tissue, and we shed light on the cellular and molecular mechanisms driving lesion expansion and repair in MS, providing targets to develop therapeutic approaches to prevent disease progression.

## INTRODUCTION

Multiple sclerosis (MS) is the most common neuro-inflammatory disorder among young adults, affecting more than 2.8 million people worldwide [4]. Clinically, MS is characterized by recurrent episodes of to a large extent reversible neurological dysfunction alongside a progressive accumulation of chronic neurological disability [5]. MS pathology is characterized by focal demyelinating lesions throughout the central nervous system (CNS) [6]. The complex and heterogenic pathology of MS is reflected in the poor predictability of the course and progression of the disease [7]. Disease progression is at least partly driven by lesions with smoldering lesion activity that fail to remyelinate. The processes underlying lesion expansion and failed remyelination are insufficiently understood, thereby impeding the development of effective therapeutic strategies.

In MS, microglia homeostasis is disrupted [8]. Chronic inflammatory microglia activity drives demyelination and disturbs axonal and synaptic functions [9]. In contrast, microglia also facilitate endogenous myelin repair mechanisms through potent phagocytic and tissue-remodeling capabilities [10]. Both active demyelination as well as remyelination occur throughout the course of the disease, though the extent of both processes varies among MS patients [3,7,11]. MS lesion types can be characterized based on the degree of de- or re-myelination, and on the degree of accumulation of activated microglia in different activation states [3]. Mixed active/inactive (mixed) lesions are characterized by a completely demyelinated core and a border with an accumulation of activated microglia. These lesions are highly versatile, as they combine continuous demyelinating activity with the potential to remyelinate, or become inactive sclerotic scars [3]. Our previous research has shown that mixed lesions with foamy microglia are associated with increased levels of acute axonal damage and stress compared to mixed lesions with ramified microglia that was associated with clinically more severe MS [12], highlighting a role for microglia state in lesion dynamics.

The morphological diversity and state of microglia has been largely overlooked within the field. Most research on disease progression in MS investigates mixed lesions with foamy microglia. However, understanding the cause and consequences of various microglial states and their biological relevance for lesion progression or repair may be key for identifying new therapeutic targets for MS. To identify the cellular and molecular profiles of mixed lesions with ramified microglia compared to mixed lesions with foamy microglia, we performed spatial transcriptomics with single-cell resolution and immunohistochemistry analyses of post-mortem MS brain tissue. To control for individual variation, both lesion types as well as normal-appearing white matter (NAWM) were included from

each donor. This approach allowed us to unravel the intricate interplay between microglial state and dynamics and the molecular interaction with local cell environments. Understanding of the molecular and cellular pathophysiological processes in smoldering lesion activity associated with impaired remyelination is essential for the development of novel therapeutic strategies.

## METHODS

### Donors

Postmortem subcortical white matter tissue of n = 8 MS donors (6 females, 2 males) and n = 3 healthy control donors (1 female, 2 males) was provided by the Netherlands Brain Bank (Amsterdam, The Netherlands, www.brainbank.nl). All donors provided informed consent for brain autopsy and the use of their tissue and clinical data for research purposes in compliance with national ethics guidelines. For all MS donors, MS pathology was confirmed by a certified neuropathologist. Donor demographics are shown in **table 1.** The cohort was balanced for sex, age, post-mortem delay and the pH of the CSF. For control donors, fresh-frozen subcortical WM was collected (n = 3). For MS donors, fresh-frozen subcortical white matter lesions were collected (n = 8). If available the formalin-fixed paraffin embedded (FFPE) mirror block was additionally collected (n = 4). MS lesions were characterized as previously described [3,7,48]. Mixed lesions have a hypo-cellular and fully demyelinated core. At the border zone of the lesion, there is an accumulation of HLA-DR$^{+}$ microglia. For each donor, one mixed lesion with ramified microglia and one mixed lesion with foamy microglia was included.

### Tissue preparation and spatial sequencing

Stereo-seq libraries were prepared as previously described by Chen et al. (2022). In brief, Stereo-seq samples were prepared by flash freezing post-mortem human brain tissue at -80°C. 10 µm cryosections were collected and adhered to the Stereo-seq chip and incubated at 37°C for 3 minutes. The tissue sections were fixed in methanol at -20°C for 30 minutes. The chip was permeabilized with 100 µL 0.1 % pepsin at 37°C for 12 to 18 minutes and washed with 0.1× SSC buffer containing 0.05 U/µL RNase inhibitor. RNA captured by the DNA nanoball on the chip was reverse transcribed at 42°C for 180 min.

**Table 1:** Donor demographics spatial sequencing cohort of MS and control samples

| NBB | Group | MS type | Sex | Age | PMD | pH | Onset (years) | EDSS6 (years) | DOD (years) | Cause of death |
|---|---|---|---|---|---|---|---|---|---|---|
| 04-055 | MS | SP | F | 43 | 10:45 | - | 22 | 16 | 21 | Subdural haematoma, pneumonia |
| 11-080 | MS | SP | F | 56 | 08:25 | 6.16 | 22 | 2 | 34 | Respiratory insufficiency by pneumonia |
| 12-027 | MS | PP | F | 54 | 09:20 | 6.27 | 23 | 8 | 31 | Heart failure |
| 15-064* | MS | SP | M | 50 | 10:50 | 6.55 | 29 | 17 | 21 | Euthanasia |
| 15-082 | MS | SP | F | 47 | 08:35 | 5.78 | 18 | 3 | 29 | Aspiration Pneumonia |
| 18-085* | MS | PP | F | 67 | 11:25 | 6.80 | 38 | 7 | 29 | Pneumonia |
| 19-011* | MS | PP | M | 63 | 10:00 | 6.52 | 34 | 17 | 30 | Aspiration pneumonia, sepsis |
| 20-060* | MS | SP | F | 60 | 05:05 | 6.80 | 38 | 21 | 23 | Euthanasia |
| 19-116 | CON | *NA* | M | 79 | 06:20 | 6.65 | *NA* | *NA* | *NA* | Metastatic prostate cancer, dehydration |
| 20-096 | CON | *NA* | M | 57 | 04:55 | 6.51 | *NA* | *NA* | *NA* | Liver cirrhosis, urosepsis |
| 21-040 | CON | *NA* | F | 80 | 08:45 | 6.88 | *NA* | *NA* | *NA* | Electrolyte imbalance |

**Donors with mirror formalin-fixed paraffin-embedded block available for validation. NBB: Netherlands Brain Bank autopsy number, CON: control, DOD: duration of disease, EDSS6: years to EDSS6, F: female, M: male, NA: not applicable, Onset: age at onset, PMD: post-mortem delay, PP: primary progressive, SP: secondary progressive.*

**Stereo-seq data processing**
Raw sequencing data were processed using the Stereo-seq Analysis Workflow (SAW) v5.1.4 [49]. Briefly, CID sequences from read 1 were mapped to the Chip T mask file allowing 1 mismatch. Unqualified MID reads were discarded, and short reads (less than 30 bases after trimming) filtered. The resulting clean reads were mapped to the hg38 reference genome to generate a gene-spot expression matrix, for which counts can be aggregated to different square-bin sizes using a customized script in R.

Raw counts at bin 50 level were processed using the *sctransform* function in Seurat v5.0.1 [50] by regressing out mitochondrial expression, *RunUMAP* with dims=1:20 and *FindClusters* with a resolution of 0.5. This was performed for each individual Stereo-seq chip including all bin units. Cluster markers were calculated using the FindAllMarkers function in Seurat with default method and used to check differential expression between clusters.

**Cell-segmentation and cell type annotation**
Cell segmentation was performed based on the ssDNA image using the Deep Learning Model V3 algorithm as implemented in Stereopy. The GMM method was applied for cell correction afterwards. Segmented cells were filtered to have minimal gene and MID counts of 10 and mitochondrial expression < 20%. For cell type annotation, we only kept cells in the outlined zones (see below methods) and used the single-cell RNA-seq data from Absinta *et al*. [13] as a reference for cell type annotation. Briefly, we removed chronic inactive and neuron data from the scRNA-seq dataset and constructed a reference using the Reference function in spacexr v2.2.1 (previously named RCTD; [51]). Major cell types (astrocytes, immune, lymphocytes, oligodendrocytes, oligodendrocyte precursor cells, and vascular cells) were deconvoluted to the Stereo-seq spatial data using the run.RCTD command in "doublet" mode. The cell type of a cellbin spot was assigned with the largest weight. For annotation of subtypes, we subdivided the single-cell and spatial datasets and ran RCTD separately for each cell type using the same settings. Cell density in each zone in the Stereo-seq data was calculated using cell number and zone area, which was calculated roughly as number of bin50 units x 25 x 25 $\mu m^2$.

**Differential gene expression in zones of interest**
To calculate differential gene expression between outlined zones, we merged the data from all donors and used Seurat to normalize the counts and ran FindMarkers with default parameter. Genes adjusted p-value < 0.05 were regarded as differentially expressed genes (DEGs).

**Characterization of perivascular and parenchymal lymphocytes**
A parenchymal lymphocyte is characterized by the lack of vascular cells and less than 3 neighbouring lymphocytes in a 50 µm radius. The adjacency matrix within 50 µm radius was calculated using the getAdj_manual function from the DR.SC package (v3.3 [52]). To calculate differential expression between perivascular and parenchymal types, we used the FindMarker function from Seurat using the default Wilcoxon method. We also aggregated the counts per type per donor and fed the pseudo-bulk counts to DESeq2 v1.40.2 [53] and calculated corresponding log2FoldChange and padj values, which were used for gene set enrichment analysis (GSEA) using the gseGO function from ClusterProfiler v4.8.3 [54]. We set the ontology to "BP", minGSSize to 10, and maxGSSize to 500.

**Cell-cell interaction using CellChat**
Cell-cell interactions within a specific zone were predicted using CellChat v2.1.2 [55] at subtype levels. We used the integrated CellChatDB for ligand-receptor interactions in human and performed computeCommuProb using the following parameters: *trim = 0.1, distance.use = TRUE, interaction.range = 250, scale.distance = 0.1, contact.dependent = TRUE, contact.range = 100*. Communication pathways were kept for those with minimal 10 cells. Communication networks were visualized using circle plots or heatmaps within CellChat. Ligand-receptor pairs contributing to the pathways were retrieved using the netAnalysis_contribution command.

**Immunohistochemistry**
For immunohistochemistry, 8 µm sections of FFPE tissue were deparaffinized and rehydrated in a xylene and ethanol series. Antigen retrieval was performed using citrate buffer or EDTA buffer (**extended data file 1**). Fresh-frozen sections were cryosectioned at 10 µm and fixated. Sections were incubated with 1% $H_2O_2$ in phosphate buffered saline (PBS) + 0.5% TritonX for 20 minutes. Non-specific antibody binding was blocked with blocking buffer (PBS + 10% normal horse serum + 1% bovine serum albumin + 0.5% TritonX) for 1 hour. Primary antibodies were incubated overnight at 4°C, at dilutions indicated in **extended data file 1**. For 3,3'-diaminobenzidine (DAB) stainings, appropriate secondary antibodies 1:400 in blocking buffer were incubated for 1 hour, and avidin-biotin complex 1:800 in PBS was incubated for 45 minutes. DAB envision kit 1:100 was incubated to visualize the staining and sections were counterstained with haematoxylin before dehydration and coverslipped with Entellan For immunofluorescent stainings, sections were either incubated with the appropriate secondary antibodies conjugated to fluorophores 1:800 for 1 hour, or incubated with appropriate biotinylated secondary antibodies 1:400, avidin-biotin complex 1:800 for 45 minutes, biotinylated tyramide 1:10,000 for 10 minutes and streptavidin conjugated fluorophore 1:800 for 1 hour. Nuclei

were stained with DAPI 1:1,000 before incubation with Sudan black 0.1% for 10 minutes, and were coverslipped with Mowiol.

**Immunohistochemistry analysis**
For quantification of cell-type density, stainings of HLA-PLP, Iba1, CD3, CD20, CD79A, CD138, VWF, GFAP and SOX10 were scanned (Axio slide scanner, x20 magnification) and images were analyzed with Qupath [56]. Based on the HLA-PLP staining the core, border zone, peri-lesional zone and NAWM were annotated. Annotations were transferred onto the Iba1, CD3, CD20, CD79A, CD138, VWF, GFAP and SOX10 scan, and the size was measured per annotation. Cell detection was performed on the nuclei staining, and positive cells were found with object classification. For each annotation, the number of microglia (Iba1), lymphocytes (CD3 + CD20), plasmablasts (CD79A + CD138), vascular cells (VWF), astrocytes (GFAP) and oligodendrocytes (SOX10) per $mm^2$ were quantified with a cell profiler. The density of $IGG^+CD79A^+$ B-cells, $FTH^+HLA^+$ microglia, $B2M^+SOX10^+$ oligodendrocytes, $ABCA2^+SOX10^+$ oligodendrocytes, and $QKI^+SOX10^+$ oligodendrocytes was quantified by training a random trees classifier.

**Statistical analysis**
Differences in proportions or density were tested with a quasi-Poisson general linear mixed model, with an offset of the total detected cells or area. Correlations were tested with Pearson's correlation coefficient. All p-values were corrected for multiple testing with FDR. P-values were considered significant if <0.10, or if <0.05 for single-cell level zone comparison.

## RESULTS

**Identification of the molecular signature of distinct cell niches**
We first investigated if we could identify distinct expression profiles of cellular environments associated with pathological processes. Using a binning (25 $\mu m^2$) approach to capture local cell environments and unsupervised Seurat clustering, several tissue zones could be identified. In each donor the NAWM, border zone, and core of mixed lesions with ramified and foamy microglia can be distinguished **(Fig. 1A).** An overview of all clusters per donor is provided in the **extended data file 2.** Bin-clusters mainly found in NAWM had high counts for oligodendrocyte and myelin-related genes (*MBP, PLP1, MOBP, MAG, APLP1, MOG*). The core of mixed lesions was enriched for genes associated with astrogliosis (*GFAP, S100B, VIM, AQP4*). In all donors, clusters associated with the core and the border zone of mixed lesions were found with enriched levels of immunoglobulin (Ig) gene transcripts (*IGHGP, IGKC, IGHG3, IGHG1, IGHG4,*

*IGHG2, IGLC3, IGLC2, IGKV3015, IGLC7, IGHM, IGLL5, JCHAIN, IGLV1-51, IGHGP, CD79A*), which for some donors was more pronounced in the core and border zone of mixed lesions with foamy microglia than those with ramified microglia. For a set of donors, bin-clusters specific for the border zone of mixed lesion with foamy microglia could be identified. These cluster have elevated levels of gene transcripts associated with microglia inflamed in MS (MIMS) or disease associated microglia (DAMS) [13,14] (*FTH1, HLA-B, APOE, SPP1, HLA-B, CD74, FTL, C1QB, HLA-DRA, C3, HLA-DRB1, GPNMB, C1QA, TREM2)*. In addition, these tissue zones were also often enriched with gene transcripts associated with astrogliosis. Donors with clusters associated with Ig-genes in NAWM also had clusters associated with MIMS or DAMS and astrogliosis in NAWM. For another set of donors, bin-clusters associated with MIMS or DAMS were more sparsely distributed throughout the border zone, peri-lesional zone and NAWM. These results confirm many of the reported molecular and cellular changes associated with the myelination state, microglia states, and immunoglobulin levels [15–17]. The high resolution and preservation of spatial information of our assays revealed donor and lesion state heterogeneity resembling the spectrum of disease stages in MS [18].

**Cell type composition of mixed lesion zones containing ramified or foamy microglia**

To determine the cell-types and cell-states within tissue zones we investigated the cell type composition of the core, border zone, peri-lesional zone and NAWM of mixed lesions with ramified microglia compared to their corresponding zones of lesions with foamy microglia or to the WM in from control donors. Manual segmentation tissue zones was performed based on expression of HLA-related genes, density and morphology of $HLA^+$ cells, expression of *MBP* and *PLP,* and RNA density **(Fig 1B)**. Single-cell segmentation was performed based on ssDNA as visualized in **Fig. 1C**. Major cell-types (astrocytes, immune cells, lymphocytes, oligodendrocytes, oligodendrocyte precursor cells (OPCs) and vascular cells) were identified using the single-cell RNA-sequencing dataset of Absinta *et al.* [13] **(Fig. 1D)** and with immunohistochemistry of CD3 for T cells, CD79A for B cells, VWF for endothelial cells, Iba1 for microglia, GFAP for astrocytes and SOX10 for oligodendrocytes **(Fig. 1E).** Quantification of cell-type proportion and density is provided in **Fig. 1F**.

Comparison of NAWM from donors with MS to WM of control donors, revealed a higher proportion of lymphocytes ($p=0.009$), vascular cells ($p<0.0001$), astrocytes ($p<0.0001$), and immune cells ($p=0.035$), and a lower proportion of oligodendrocytes ($p<0.0001$) in NAWM of donors with MS. Within individual MS donors, the proportion of OPCs in mixed lesions with ramified or foamy microglia was comparable to the proportion of OPCs in NAWM (lesion cores: $p=0.896$ &

p=0.896, lesion border zones: p=0.903 & p=0.896, peri-lesional zones: p=0.986 & p=0.986, respectively). In mixed lesions with ramified microglia and those with foamy microglia a loss of oligodendrocytes was found in the core zones, (deconvolution p<0.0001 & p<0.0001, IHC p<0.001 & p<0.001, respectively), border zones (deconvolution p=0.052 & p<0.001, IHC p=0.010 & p=0.009, respectively), and peri-lesional zones compared to NAWM (deconvolution p<0.001 & p=0.002, IHC p=0.233 & p=0.077, respectively). In core zones of mixed lesions with ramified microglia and those with foamy microglia an enrichment of astrocytes was identified compared to NAWM (deconvolution p<0.001 & p<0.001, IHC p=0.386 & p=0.760, respectively). In border zones of mixed lesions with ramified microglia and those with foamy microglia an enrichment of immune cells was found compared to NAWM (deconvolution p=0.809 & p=0.050, IHC p=0.007 & p=0.003, respectively), and a higher density of immune cells was identified in the border of mixes lesions with foamy microglia compared to the border of those with ramified microglia (p=0.085). This cellular composition aligns with previously reported characteristics of NAWM and mixed lesions [13], and validates the segmentation and deconvolution method. The preservation of OPCs suggests that a differentiation block contributes to remyelination failure in MS [15].

In the core zone of mixed lesions with ramified microglia and in the core of those with foamy microglia, higher proportion of lymphocytes was identified compared to NAWM (deconvolution p=0.046 & p=0.008, IHC p=0.116 & p=0.059, respectively). The lymphocyte proportion was enriched in the border zone of mixed lesions with foamy microglia compared to NAWM (deconvolution p=0.095, IHC p=0.161), but not in the border zone of mixed lesions with ramified microglia, which highlights a possible role for lymphocytes in lesion progression.

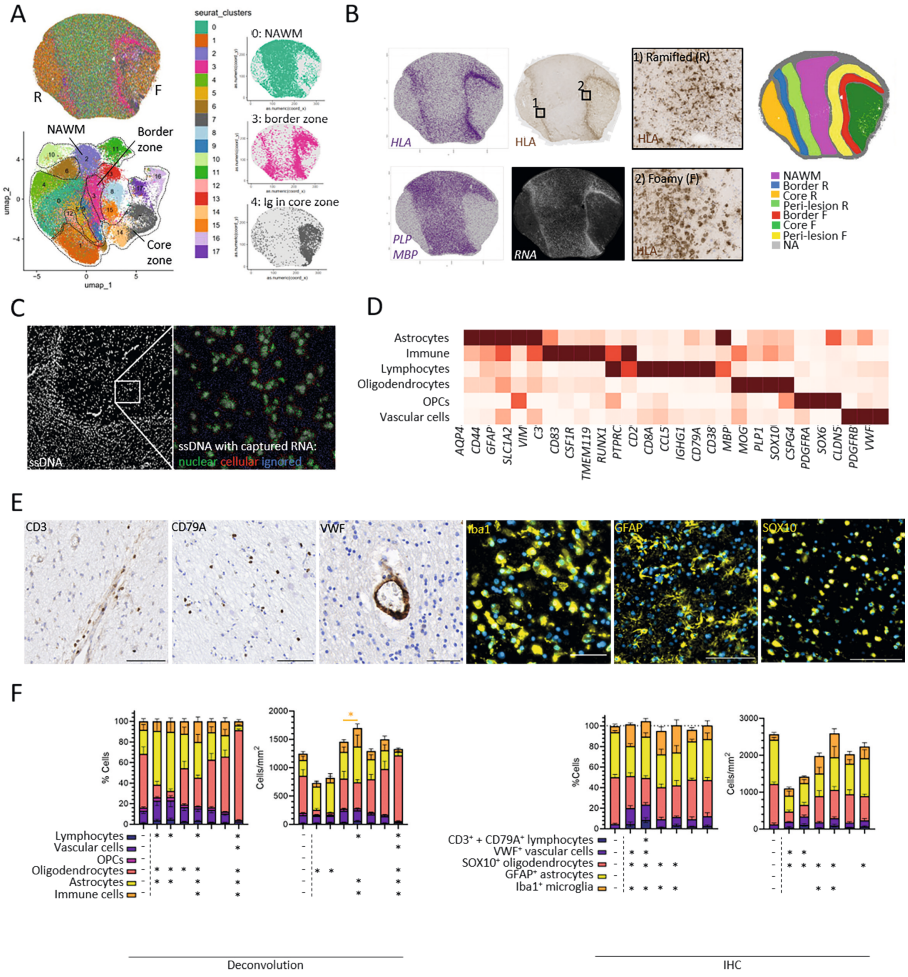


**Figure 1: Cellular composition of mixed lesions with ramified and foamy microglia.** A) Unsupervised Seurat clustering of bins (25 µm) identified distinct clusters in NAWM, core, and border zones of mixed lesions, and distinguished between mixed lesions with ramified or foamy microglia. B) Zones of interest were manually segmented based on counts of HLA-related genes and myelin-related genes *MBP* and *PLP*, RNA density, and density and morphology of HLA⁺ cells. C) RNA captured at spots overlapping or surrounding ssDNA were binned into cell bins. D) Cell bins were deconvoluted for major cell types astrocytes, immune cells, lymphocytes, oligodendrocytes, OPCs, and vascular cells. E) IHC of CD3 (scale bar 100 µm), CD79A (scale bar 100 µm), VWF (scale bar 50 µm), Iba1 (scale bar 50 µm), GFAP (scale bar 100 µm), and SOX10 (scale bar 100 µm). F) Proportions and density of major cell types identified through deconvolution of cell bins or IHC quantified per zone of interest. Significance was tested with a quasipoisson generalized linear model to compare the raw counts with offset for area or total number of cells, correcting for multiple testing with FDR. Significant differences indicated for NAWM compared to all zones of interest, and for the cores, borders or peri-lesion zones of mixed lesions with ramified *vs* those with foamy microglia. *: p<0.10.

**Perivascular lymphocytes are more reactive than parenchymal lymphocytes**

To compare perivascular lymphocytes to parenchymal lymphocytes, we performed pre-ranked gene-set enrichment analysis (GSEA). On average, 211.3 (± 151.8) T cells and 128.6 (± 93.4) B cells were identified per donor. We annotated T and B cells that were in close proximity (<50µm) to a cell annotated by the vascular cluster or clustered together (>3) as perivascular cuffs [19], and considered them perivascular lymphocytes (77.1% and 79.9%, respectively). The other lymphocytes were considered parenchymal T and B cells (22.9% and 20.1%, respectively) **(Fig. 2A)**. The distribution of perivascular and parenchymal lymphocytes is in line with previous reported analysis of MS tissue [19]. Gene ontology analysis was performed to predict functional changes based on molecular profiles. All enriched GO-terms are provided in **extended data file 3**, and those considered most relevant to lesion formation are visualized in **Fig. 2B**. Compared to perivascular lymphocytes, parenchymal lymphocytes had higher gene counts for functions associated with opsonization. Compared to parenchymal lymphocytes, perivascular lymphocytes had higher gene counts for functions associated with T cell activation, and with generation and maintenance of tissue-resident memory T cells and T helper cells. In line with this, a lower proportion of parenchymal T cells stains for TNF compared to perivascular T cells, which correlated with a reduced *in vitro* TNF-production by lesional T-cells compared to NAWM T cells, likely due to a higher abundancy of parenchymal T cells in lesions [20]. Additionally, compared to parenchymal lymphocytes, perivascular lymphocytes were enriched for functions indicative of B cell activation, immunoglobulin production, and somatic diversification and recombination of immunoglobulins. Production of soluble mediators by activated perivascular lymphocytes has been postulated to be a driver of lesion expansion [21]. Altogether, this suggests that mainly perivascular lymphocyte cytokine and immunoglobulin production contribute to lesion expansion in MS.

**AIMS are associated with mixed lesions with foamy microglia**

To identify possible cellular mechanisms of lesion expansion, oligodendrocyte, astrocyte, immune cell, and OPC clusters were further deconvoluted revealing states utilizing the high contrast in the Absinta snRNAseq dataset [13]. Distribution of identified cells in a certain state in WM, NAWM, cores, border zones, and peri-lesional zones of mixed lesions with ramified or foamy microglia was determined **(Fig. 3A)**. An enrichment of reactive astrocytes and of astrocytes inflamed in MS (AIMS) was identified in NAWM compared to WM ($p=0.043$, $p=0.052$, respectively). Within MS donors, compared to NAWM an enrichment of AIMS was identified in the border of mixed lesions with foamy microglia ($p=0.065$) but not in the border of those with ramified microglia, which may indicate activation of microglia inflamed in MS (MIMS) in mixed lesions with foamy microglia [13].

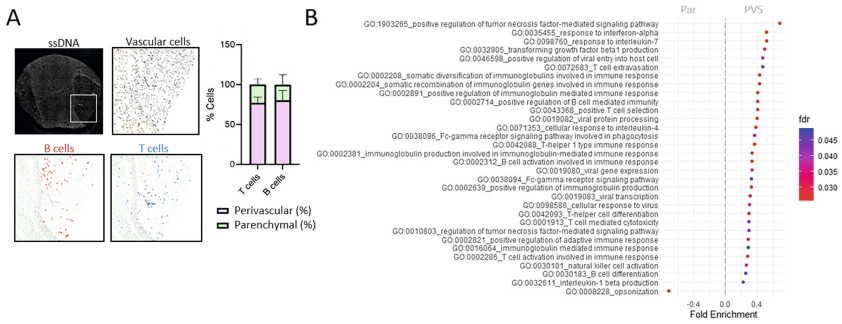


**Figure 2: Perivascular lymphocytes are more reactive than parenchymal lymphocytes.** A) Cell-bins identified as vascular cells, T cells or B cells were used to quantify the number of perivascular and parenchymal lymphocytes. The majority of T and B cells were perivascular, as they were in close proximity (<50 µm) to a cell annotated by the vascular cluster or clustered together (>3) as perivascular cuffs. B) Pre-ranked GSEA of perivascular (PVS) lymphocytes compared to parenchymal (Par) lymphocytes.

## Inflammatory MIMS-iron are associated with lesion expansion

The immune cluster was further deconvoluted to identify immune cell states associated with lesion expansion. Compared to WM, an enrichment of macrophages (p=0.031) and MIMS-iron (p=0.056) was identified in NAWM. Compared to NAWM, the density of MIMS-foamy and of MIMS-iron was higher in the border zone of mixed lesions with foamy microglia (p=0.062, p=0.056, respectively), but not in the border zone of mixed lesions with ramified microglia. Accordingly, the density of MIMS-iron was higher in the border zone of mixed lesions with foamy microglia compared to the border zone of mixed lesions with ramified microglia (p=0.080) **(Fig. 3A).** Projection of MIMS, MIMS-iron and MIMS-foamy onto the cell-bins visualizes the regional specificity of these cell states **(Fig. 3B)**. With IHC, higher density of MIMS-iron in the border zone of mixed lesions with foamy microglia compared to the border zone of those lesions with ramified microglia was validated (p=0.066) **(Fig. 3C)**. Iron-rim positive lesions detected by MRI are associated with a higher clinical severity. In these iron-rim positive lesions, microglia have accumulated iron [22]. Our findings indicate that mixed lesions with foamy microglia have more iron accumulation than mixed lesions with ramified microglia, and may therefore be more damaging.

## Senescent and stressed OPCs are associated with failed remyelination

To identify possible mechanisms of failed remyelination, the OPC cluster was further deconvoluted into homeostatic, stressed, immune-like, senescent, and pre-oligo OPCs, and in MS the density of cell states was correlated to proportion of remyelinated lesions. The density of all OPC cell states was comparable for

the WM, NAWM, cores, border zones, and peri-lesional zones of control tissue and mixed lesions with ramified or foamy microglia, and is therefore not zone specific **(Fig. 3A)**. However, the density of senescent and stressed OPCs was negatively correlated to the proportion all lesions identified at autopsy that were remyelinated **(Fig. 3D)**. Our data indicates that donor-specific impaired OPC differentiation and maturation caused by cellular senescence and oxidative stress [23,24] may underly the high variation of remyelinated lesions among people with MS [25].

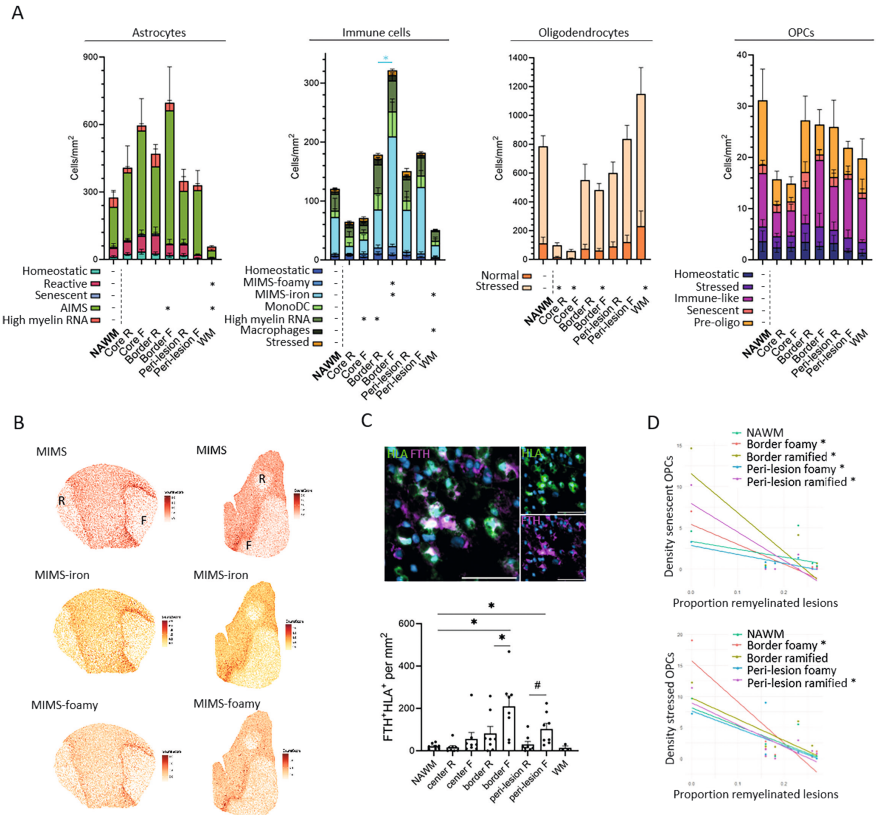


**Figure 3: Cell states are associated with lesion expansion and failed remyelination**. A) Further deconvolution of the astrocyte, immune, oligodendrocyte, and OPC clusters into cell states. B) MIMS clusters projected onto cell bins. C) IHC of HLA and FTH (scale bar 50 µm). There are more $HLA^+FTH^+$ microglia/$mm^2$ in the border zone of mixed lesions with foamy microglia than in the border zone of mixed lesions with ramified microglia. D) The density of senescent OPCs and stressed OPCs is negatively correlated to the proportion of remyelinated lesions. Significance of count data was tested with a quasipoisson generalized linear model to compare the raw counts with offset for area or total number of cells, correcting for multiple testing with FDR. Significant differences indicated for NAWM compared to all zones of interest, and for the cores, borders or peri-lesion zones of mixed lesions with ramified *vs* those with foamy microglia. Correlations were tested with Pearson's correlation test, corrected with FDR. *: $p<0.10$.

**Table 2:** Number of receptor-ligand pair interactions in the border and peri-lesion zone of mixed lesions with ramified or foamy microglia

| Receptor-ligand pair | Interpretation | Donors | Border | | Peri-lesion | |
|---|---|---|---|---|---|---|
| | | | *R* | *F* | *R* | *F* |
| APP-CD47 | Failed cell repair after oxidative damage[30] | 7/7 | 98 | 204 | 91 | 98 |
| PSAP-GPR37 | Lysosomal degradation of sphingolipids[31] | 5/7 | 52 | 127 | 42 | 52 |
| Cholesterol-cholesterol-LIPA-RORA | Inflammatory processes and differentiation of Th17 cells[32] | 4/7 | 19 | 62 | 19 | 21 |
| APOE-TREM2-TYROBP | Lipid metabolism and phagocytosis[33] | 2/7 | 22 | 56 | 22 | 20 |
| PSAP-GPR37L1 | Lipid metabolism and phagocytosis[31] | 5/7 | 10 | 76 | 10 | 19 |
| APP-TREM2-TYROBP | Lipid metabolism and phagocytosis[33] | 2/7 | 18 | 43 | 18 | 26 |
| PTN-NCL | Lymphocyte survival and recruitment[34,35] | 3/7 | 2 | 31 | 2 | 9 |
| CD99-CD99 | Lymphocyte survival and recruitment[34,35] | 5/7 | 4 | 16 | 4 | 9 |
| SEMA4D-PLXNB1 | Repulsion of axonal growth cones[36] | 3/7 | 2 | 6 | 2 | 4 |
| C3-ITGAX-ITGB2 | Complement mediated activation of microglia[37] | 1/7 | 0 | 0 | 0 | 10 |
| SPP1-CD44 | Inhibition of T cell activity[38] | 5/7 | 117 | 129 | 117 | 65 |

*R: ramified, F: foamy*



**Receptor ligand pair interactions associated with lesion expansion**

Interacting cells were identified through upregulation of ligand-receptor pairs of adjacent cells using Cell-Chat. Ligand–receptor pairs per donor for each zone is provided in **extended data file 4**. Most interactions were found in the border zone of mixed lesions with foamy microglia. Stressed oligodendrocytes are the main signaling source, and stressed oligodendrocytes, MIMS-iron and immune-OPCs are the the main signaling targets **(extended Fig. 1)**. The number of interactions of receptor–ligand pairs relevant to lesion expansion are summarized in **table 2.** Increased receptor–ligand interactions indicative of oxidative damage, demyelination, and lymphocyte activation were identified in the border zone of mixed lesions with foamy microglia compared to the border zone of those with ramified microglia. Less receptor-ligand interactions indicative of T cell inhibition were identified in the peri-lesional zone of mixed

lesions with foamy microglia compared to the peri-lesional zone of those with ramified microglia. Together, this further highlights the destructive interplay of lymphocytes activation and oxidative stress driving pathological demyelination.

**Gene profile of lesion expansion, regeneration, and remyelination**

To identify molecular mechanisms of lesion expansion and repair, we performed single-cell level zone comparison. Top 200 differentially expressed (DE) genes of control WM *vs* NAWM, the border zone of mixed lesions with foamy *vs* the border zone of those with ramified microglia, and of the peri-lesional zone of mixed lesions with foamy microglia *vs* the peri-lesional zone of those with ramified microglia are provided in the **extended data file 5.** In NAWM compared to healthy control WM, 2386 genes had higher counts and 1300 genes had lower counts. In line with previous research [26–28], gene counts were indicative of complement activation, microglia activation, cytokine production, lipid metabolism, phagocytosis, Ig production, and iron dysregulation **(Fig. 4A)**. Next, gene counts of cell-bins were compared between in the border zone or the peri-lesional zone of mixed lesions with ramified microglia to those of mixed lesions with foamy microglia. Cell-bins in mixed lesions with foamy microglia had higher counts of genes known to be upregulated in the border zone and peri-lesional zones of mixed lesions associated with phagocytosis, lipid metabolism, iron dysregulation, immune-oligodendrocytes, astrogliosis, immune activation, and Ig production [13,29] in the border zone **(Fig. 4B)** and peri-lesional zone (**Fig. 4C)**. DE genes were plotted onto the uniform manifold approximation and projection (uMap) of the single-cell dataset of Absinta *et al.* [13] **(extended Fig. 2)**. DE genes with lower counts in NAWM compared to the WM mainly associated with oligodendrocytes, astrocytes, and immune cells. Those with higher counts mainly associated with astrocytes and immune cells. DE genes with lower counts in the border zone of mixed lesions with foamy microglia compared to the border zone of those with ramified microglia mainly associated with oligodendrocytes and OPCs, and those with higher counts mainly associated with astrocytes, immune cells and to a low extent with lymphocytes. DE genes with lower counts in the peri-lesional zone of mixed lesions with foamy microglia compared to the peri-lesional zone with ramified microglia were often genes with low cell-type specificity. Those with higher counts mainly associated with oligodendrocytes, astrocytes, immune cells and vascular cells.

To identify enriched gene sets, GSEA was performed on all DE genes with higher or lower counts in the border and peri-lesional region of mixed lesions with foamy microglia compared to those with ramified microglia. All gene sets are provided in **extended data file 6**, and those most relevant visualized in **Fig. 4D-E.** Enriched gene sets in the border zone of mixed lesions with

foamy microglia compared to the border zone of mixed lesions with ramified microglia were associated with reactive oxygen species production and response, ferroptosis, antigen processing and presentation via MHC class II, immunoglobulin production, T cell activation, complement activation, phagocytosis, lipid metabolism, cellular senescence and neurodegeneration. Contrastingly, gene sets enriched in the border zone of mixed lesions with ramified microglia compared to the border zone of mixed lesions with foamy microglia were associated with myelination and axonal growth (**Fig. 4D)**. While many genes with higher counts in the border zone of mixed lesions with foamy similarly also had higher counts in the peri-lesional zone of lesion with foamy microglia (1141 unique to the border zone, 391 unique to the peri-lesional zone, 1377 co-expressed), only few genes had higher counts in both the border zone as well as in the peri-lesional zone of mixed lesions with ramified microglia (512 unique to the border zone, 40 unique to the peri-lesional zone, 22 co-expressed). Correspondingly, similar gene sets were enriched in the peri-lesional zone as in the border zone of mixed lesions with foamy microglia, and not in those with ramified microglia **(Fig. 4E)**, which implies that mixed lesions with foamy microglia are expanding.

Gene modules of genes of interest from mixed lesions with foamy microglia associated with lesion expansion (*APOC1, APOE, APP, B2M, C1QA, C1QB, C1QC, C3, CD44, CD68, CD74, CD99, CHI3L1, CHIRL2, CHIT1, CLU, FABP5, FCGR1A, FCGR2A, FCGR2B, FTH1, FTL, GPNMB, HLA-A, HLA-DQB1, HLA-DRB1, IAH1, IFNGR1, IHA1, IGHG1, IGHG3, IGHM, IGLC2, IGLC3, IGLL5, JCHAIN, LIPA, MSR1, NCAM1, OLR1, DERPINA3, SPP1, UBB*) or from mixed lesions with ramified microglia associated with repair and myelination (*APOD, CTNNB1, QKI, SBF2, BOK, CTTN, SHTN1, BCAS1, SHANK2, CDH4, SKI, NEAT1, DDR1*) were projected onto the cell-bins (**Fig. 4F**, for all donors see extended **Fig. 3**). Counts of the gene module associated with neuro-destruction, inflammation and demyelination was mainly localized with the border zone and peri-lesional zone of mixed lesions with foamy microglia. Visually, these genes seem to expand from the border zone into the peri-lesional zone in a gradient. In contrast, counts of the gene module associated with (re)myelination and axonal outgrowth was visually lower expressed in the border zone of mixed lesions with foamy microglia compared to other zones of interest. This may indicate that in mixed lesions with foamy microglia, axons are less receptive of remyelination [30].

We next visualized specific genes of interest projected onto the cell-bins, and show distinct patterns for *GPNMB, FTH1, APOE, IGHG3* and *C1QB* in the lesion with foamy microglia, while *ABCA2* was more prevalent in the lesion with ramified microglia (**Fig. 4G).** Accordingly, we validated our findings at protein level, through IHC of IgG, ABCA2, QKI, and B2M. We show that in

the core and border zone of mixed lesions with foamy microglia, there was a higher density of $IgG^+CD79A^+$ B cells compared to NAWM (p=0.066 & p=0.066, respectively). This was not found in the core and border zone of mixed lesions with ramified microglia (p=0.580 & p=0.710, respectively). Accordingly, the number of $IgG^+CD79A^+$ B cells was higher in the border zone of mixed lesions with foamy microglia compared to the border zone of those with ramified microglia (p=0.082) and there was a trend in the core (p=0.108). The increased level of IgG production by $CD79A^+$ B-cells in the border zone and core of mixed lesions with foamy microglia compared to those with ramified microglia may play a role in sustained neuro-inflammation (**Fig. 4H-I)**. These finding expand earlier work showing IgG-related gene transcription in the rim of mixed lesions [18] and the association of lesional and meningeal $CD20^+$ B cells with CSF oligoclonal IgG production [31]. Igs can break microglial immune-tolerance [32] and activate the complement cascade, contributing to sustained inflammation and lesion expansion [33]. Our findings also indicated upregulation of complement-related genes and complement-mediated activity in the border zone and peri-lesional zone of mixed lesions with foamy microglia, suggesting a role of immune-complex formation and related complement activation in smoldering lesion expansion. In the border zone of mixed lesions with foamy microglia, there was a higher density of $B2M^+SOX10^+$ oligodendrocytes compared to NAWM and compared to the border zone of mixed lesions with ramified microglia (p=0.016 & p=0.049, respectively) (**Fig. 4H-I)**, indicating a higher number of immune-oligodendrocytes. In neurodegenerative diseases, OPCs and oligodendrocytes can present MHC-I and MHC-II antigens, which can be induced by IFNγ. In MS, these immune OPCs and immune oligodendrocytes are active immunomodulators and cytotoxic targets, thereby contributing to a perpetuated autoimmune response and ongoing oligodendrocyte destruction and consequently myelin degradation [34–36]. Furthermore, we found a lower density of $QKI^+SOX10^+$ oligodendrocytes, which are necessary for mature myelin maintenance [37], in the border zone of mixed lesions with foamy microglia compared to those with ramified microglia (p=0.044), and lower density of $ABCA2^+SOX10^+$ oligodendrocytes in the border zone of mixed lesions with foamy microglia compared to those with ramified microglia (p=0.061), indicating dysregulated sphingolipid metabolism [38] (**Fig. 4H-I)**. Together, our data highlights the role of oligodendrocytes in perpetuated demyelinating activity and loss of myelin stability and integrity in the border zone of mixed lesions with foamy microglia.

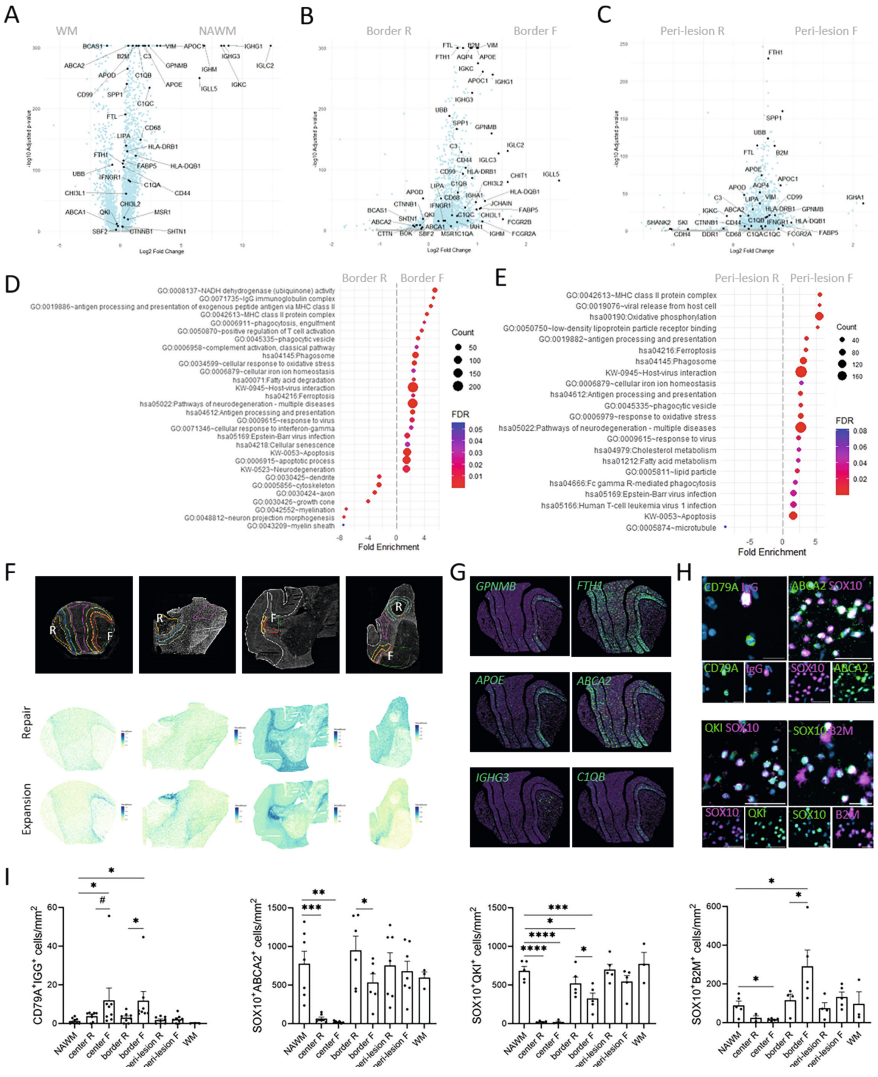


**Figure 4: Gene expression patterns associated with lesion expansion and repair.** A) Volcano plot of control WM compared to NAWM, B) the border zone of mixed lesions with foamy microglia compared to NAWM, B) the border zone of mixed lesions with foamy microglia compared to the border zone of those with ramified microglia, and C) of the peri-lesion zone of mixed lesions with foamy microglia compared to the peri-lesion zone of those with ramified microglia. Genes of interest previously associated with demyelinating lesion activity, MS pathology, remyelination and axonal growth indicated. D) GSEA of the border zone of mixed lesions with foamy microglia compared to the border zone of mixed lesions with ramified microglia. E) GSEA of the peri-lesion zone of mixed lesions with foamy microglia compared to the peri-lesion zone of mixed lesions with ramified microglia. F) Gene modules associated with lesion expansion or lesion repair are projected on cell bins. G) Genes of interest projected on cell bins. H) IHC double stainings of CD79A + IgG (scale bar 25 µm), SOX10 + ABCA2 (scale bar 50 µm), SOX10 + QKI (scale bar 50 µm), and SOX10 + B2M (scale bar 50 µm). I)There are more $CD79A^+IgG^+$ cells/$mm^2$ in the border

zone and core of mixed lesions with foamy microglia than in the border zone and core of mixed lesions with ramified microglia, less $SOX10^+ABCA2^+$ oligodendrocytes/$mm^2$ and less $SOX10^+QKI^+$ oligodendrocytes/$mm^2$ in the border zone of mixed lesions with foamy microglia than in the border zone of mixed lesions with ramified microglia, and more $SOX10^+B2M^+$ oligodendrocytes/$mm^2$ in the border zone of mixed lesions with foamy microglia compared to the border zone of mixed lesions with ramified microglia. Significance was tested with a quasipoosson generalized linear model to compare the raw counts with offset, correcting for multiple testing with FDR. #: $p<0.11$, *: $p<0.10$, **: $p<0.01$, ***: $p<0.001$, **** $p<0.0001$.

## DISCUSSION

Microglia are highly dynamic cells integral to critical CNS functions, including myelinogenesis, phagocytic debris clearing, myelin and synaptic remodeling, and immune surveillance. These cells undergo intricate morphological, transcriptional, and functional changes in response to environmental stimuli and due to phagocytosis [10,39]. In MS, microglia play a crucial role in lesion dynamics. Mixed lesions can expand, become inactive, or undergo remyelination, however the molecular and cellular mfechanisms underlying these processes remain poorly understood. In this study, we performed spatial transcriptomics with single-cell resolution on post-mortem human MS tissue, to investigate the cellular composition, gene expression profiles, and intercellular communication in mixed lesions with ramified microglia and of those with foamy microglia within the same MS donors and compared this to control donors. Our findings indicate that mixed lesions with ramified microglia are more likely to transit into inactive or remyelinated lesions. In contrast, mixed lesions with foamy microglia tend to undergo continuous smoldering lesion activity and degeneration.

We have found that in mixed lesions with foamy microglia, smoldering activity is driven by perivascular B and T cells, producing Igs and pro-inflammatory cytokines. Igs can opsonize myelin [17], activate the complement cascade [33], and disrupt microglial immune-tolerance [32], which sustains microglial activation and demyelination. Pro-inflammatory cytokines further induce immune-oligodendrocytes, which become cytotoxic targets [35,36], leading to their destruction and subsequent iron release. Microglia clear up this iron, but its uptake inhibits lysosomal acidification [40], impacting on the metabolism of phagocytosed myelin. Iron-laden microglia produce high levels of reactive oxygen species (ROS), causing oxidative damage to DNA, lipids and proteins [27]. Oxidized lipids perpetuate inflammation [41]. Additionally, ROS-induced oxidative stress and inflammation can induce stressed or senescent OPCs that have a differentiation block [42], leading to failed remyelination. Iron chelators, such as deferoxamine, might serve as promising therapeutic targets to suppress iron-mediated lesion expansion [43].

Conversely, in mixed lesions with ramified microglia, axonal protection and myelin stability combined with lower complement and inflammatory responses, appear to safeguard surrounding tissue from lesion expansion. Notably, in the rat brain, QKI identifies actively myelinating oligodendrocytes [44]. The preservation of QKI$^+$ oligodendrocytes in mixed lesions with ramified microglia suggests enhanced remyelinating potential. Additionally, ABCA2 is involved in low-density lipoprotein trafficking, and is crucial for regulation of the sphingolipid metabolism, and therefore myelin integrity [38,45]. Higher preservation of ABCA2$^+$ oligodendrocytes in mixed lesions with ramified microglia therefore contributes to myelin stability and resistance to ongoing demyelination.

These zone- and donor-specific mechanisms of degeneration and repair failure offer insights in mechanisms underlying lesion dynamics. Understanding the distinct roles of microglial states in lesion dynamics is crucial for developing targeted interventions to modify the disease course in MS

**Limitations**

Tissue permeabilization is necessary for RNA to bind to the probes, especially with lipid-rich white matter tissue. This may have caused some diffusion of the RNA. Although most RNA captured from around the nuclear area of the cell, possibly some RNA has diffused away from the cell-bins, reducing the counts per cell. Additionally, as we determined cell-bins based on the nucleus and spatial expansion, ramifications of the cell are not taken into account, which could also reduce the counts per cell. As spatial transcriptomics does not allow for an accurate delineation of the Virchow-Robin space, it is possible that some parenchymal lymphocytes near vessels were classified as perivascular lymphocytes. However, as the percentage of perivascular over parenchymal lymphocytes is similar to previous work [46], the effect this may have on the GSEA results should be negligible. Lastly, beyond the Kuhlmann classification system [47], the biological landscape of MS lesions is likely far more intricate and multifaceted. Lesions selected for this study were comparable on the histopathological level, but confounding factors are unknown (e.g. age of the lesion and speed of lesion expansion), and our findings are heterogenous between donors. This highlights the heterogenous nature of MS and resembles the spectrum of disease stages.

**Data availability**

Data will be publicly available at the website of the Human Protein Atlas. Raw data will be available upon reasonable request. Supporting files are available upon request.

**Acknowledgements**
We are grateful to the brain donors and their families for their commitment to the Netherlands Brain Bank donor program.

**Funding**
Funding for this research was obtained from MS Research grants 19-1079 and 17-975 (MoveS inspiration Grant) received by Inge Huitinga.

**Competing interests**
Authors declare no competing interests.

## REFERENCES


1. *The Multiple Sclerosis International Federation. Atlas of MS, 3rd edition* (2020).
2. Heß, K. *et al.* Lesion stage-dependent causes for impaired remyelination in MS. *Acta Neuropathol* 140, 359–375 (2020).
3. Kuhlmann, T. *et al.* An updated histological classification system for multiple sclerosis lesions. *Acta Neuropathol.* 133, 13–24 (2017).
4. Walton, C. *et al.* Rising prevalence of multiple sclerosis worldwide: Insights from the Atlas of MS, third edition. *Mult. Scler. J.* 26, 1816–1821 (2020).
5. Thompson, A. J., Baranzini, S. E., Geurts, J., Hemmer, B. & Ciccarelli, O. Multiple sclerosis. *Lancet* 391, 1622–1636 (2018).
6. Lassmann, H. Multiple sclerosis pathology. *Cold Spring Harb. Perspect. Med.* 8, 1–15 (2018).
7. Luchetti, S. *et al.* Progressive multiple sclerosis patients show substantial lesion activity that correlates with clinical disease severity and sex: a retrospective autopsy cohort analysis. *Acta Neuropathol.* 135, 511–528 (2018).
8. Zrzavy, T. *et al.* Loss of 'homeostatic' microglia and patterns of their activation in multiple sclerosis. *Brain* 140, 1900–1913 (2017).
9. Bosch, A. M. R. Van Den *et al.* Ultrastructural Axon–Myelin Unit Alterations in Multiple Sclerosis Correlate with Inflammation. *Ann. Neurol.* 93, 1–15 (2022).
10. Distéfano-Gagné, F., Bitarafan, S., Lacroix, S. & Gosselin, D. Roles and regulation of microglia activity in multiple sclerosis: insights from animal models. *Nat. Rev. Neurosci.* 24, 397–415 (2023).
11. Patani, R., Balaratnam, M., Vora, A. & Reynolds, R. Remyelination can be extensive in multiple sclerosis despite a long disease course. *Neuropathol. Appl. Neurobiol.* 33, 277–287 (2007).
12. van den Bosch, A. *et al.* Neurofilament Light Chain Levels in Multiple Sclerosis Correlate With Lesions Containing Foamy Macrophages and With Acute Axonal Damage. *Neurol. Neuroimmunol. neuroinflammation* 9, (2022).
13. Absinta, M. *et al.* A lymphocyte–microglia–astrocyte axis in chronic active multiple sclerosis. *Nature* 597, 709–714 (2021).
14. Safaiyan, S. *et al.* White matter aging drives microglial diversity. *Neuron* 109, 1100-1117.e10 (2021).
15. Heß, K. *et al.* Lesion stage-dependent causes for impaired remyelination in MS. *Acta Neuropathol.* 140, 359–375 (2020).
16. Ramaglia, V. *et al.* Multiplexed imaging of immune cells in staged multiple sclerosis lesions by mass cytometry. *Elife* 8, 1–29 (2019).
17. Hendrickx, D. A. E. *et al.* Selective upregulation of scavenger receptors in and around demyelinating areas in multiple sclerosis. *J. Neuropathol. Exp. Neurol.* 72, 106–118 (2013).
18. Bogers, L. *et al.* Selective emergence of antibody-secreting cells in the multiple sclerosis brain. *eBioMedicine* 89, 104465 (2023).
19. Fransen, N. L. N. L. *et al.* Tissue-resident memory T cells invade the brain parenchyma in multiple sclerosis white matter lesions. *Brain* 143, 1714–1730 (2020).
20. Hsiao, C. C. *et al.* Osteopontin associates with brain TRM-cell transcriptome and compartmentalization in donors with and without multiple sclerosis. *iScience* 26, (2023).

21. Machado-Santos, J. *et al.* The compartmentalized inflammatory response in the multiple sclerosis brain is composed of tissue-resident CD8+ T lymphocytes and B cells. *Brain* 141, 2066–2082 (2018).
22. Maggi, P. *et al.* Chronic White Matter Inflammation and Serum Neurofilament Levels in Multiple Sclerosis. *Neurology* 0, 10.1212/WNL.0000000000012326 (2021).
23. Koutsoudaki, P. N., Papadopoulos, D., Passias, P. G., Koutsoudaki, P. & Gorgoulis, V. G. Cellular senescence and failure of myelin repair in multiple sclerosis. *Mech. Ageing Dev.* 192, 111366 (2020).
24. Spaas, J. *et al.* Oxidative stress and impaired oligodendrocyte precursor cell differentiation in neurological disorders. *Cell. Mol. Life Sci.* 78, 4615–4637 (2021).
25. Patrikios, P. *et al.* Remyelination is extensive in a subset of multiple sclerosis patients. *Brain* 129, 3165–3172 (2006).
26. Dziedzic, T. *et al.* Wallerian degeneration: A major component of early axonal pathology in multiple sclerosis. *Brain Pathol.* 20, 976–985 (2010).
27. Hametner, S. *et al.* Iron and neurodegeneration in the multiple sclerosis brain. *Ann. Neurol.* 74, 848–861 (2013).
28. Melief, J. *et al.* Transcriptome analysis of normal-appearing white matter reveals cortisol- and disease-associated gene expression profiles in multiple sclerosis. *Acta Neuropathol. Commun.* 7, 60 (2019).
29. Hendrickx, D. A. E. *et al.* Gene expression profiling of multiple sclerosis pathology identifies early patterns of demyelination surrounding chronic active lesions. *Front. Immunol.* 8, (2017).
30. Duncan, G. J., Simkins, T. J. & Emery, B. Neuron-Oligodendrocyte Interactions in the Structure and Integrity of Axons. *Front. Cell Dev. Biol.* 9, (2021).
31. Fransen, N. L. *et al.* Absence of B Cells in Brainstem and White Matter Lesions Associates With Less Severe Disease and Absence of Oligoclonal Bands in MS. *Neurol. Neuroimmunol. NeuroInflammation* 8, 1–11 (2021).
32. van der Poel, M., Hoepel, W., Hamann, J., Huitinga, I. & Dunnen, J. den. IgG Immune Complexes Break Immune Tolerance of Human Microglia. *J. Immunol.* 205, 2511–2518 (2020).
33. Toapanta, F. R. & Ross, T. M. Complement-mediated activation of the adaptive immune responses: Role of C3d in linking the innate and adaptive immunity. *Immunol. Res.* 36, 197–210 (2006).
34. Falcão, A. M. *et al.* Disease-specific oligodendrocyte lineage cells arise in multiple sclerosis. *Nat. Med.* 24, 1837–1844 (2019).
35. Kirby, L. *et al.* Oligodendrocyte precursor cells present antigen and are cytotoxic targets in inflammatory demyelination. *Nat. Commun.* 10, 1–20 (2019).
36. Pandey, S. *et al.* Disease-associated oligodendrocyte responses across neurodegenerative diseases. *Cell Rep.* 40, (2022).
37. Zhou, X. *et al.* Mature myelin maintenance requires Qki to coactivate PPARβ-RXRα-mediated lipid metabolism. *J. Clin. Invest.* 130, 2220–2236 (2020).
38. Sakai, H. *et al.* ABCA2 deficiency results in abnormal sphingolipid metabolism in mouse brain. *J. Biol. Chem.* 282, 19692–19699 (2007).
39. Paolicelli, R. C. *et al.* Microglia states and nomenclature: A field at its crossroads. *Neuron* 110, 3458–3483 (2022).
40. Kao, J. K. *et al.* Chronic iron overload results in impaired bacterial killing of THP-1 derived macrophage through the inhibition of lysosomal acidification. *PLoS One* 11, 1–16 (2016).

41. Di Gioia, M. & Zanoni, I. Dooming Phagocyte Responses: Inflammatory Effects of Endogenous Oxidized Phospholipids. *Front. Endocrinol. (Lausanne).* 12, 1–13 (2021).
42. Kuhlmann, T. *et al.* Differentiation block of oligodendroglial progenitor cells as a cause for remyelination failure in chronic multiple sclerosis. *Brain* 131, 1749–1758 (2008).
43. Li, Z. *et al.* Iron Neurotoxicity and Protection by Deferoxamine in Intracerebral Hemorrhage. *Front. Mol. Neurosci.* 15, 1–6 (2022).
44. Wu, H. Y., Dawson, M. R. L., Reynolds, R. & Hardy, R. J. Expression of QKI proteins and MAP1B identifies actively myelinating oligodendrocytes in adult rat brain. *Mol. Cell. Neurosci.* 17, 292–302 (2001).
45. Wheeler, D., Bandaru, V. V. R., Calabresi, P. A., Nath, A. & Haughey, N. J. A defect of sphingolipid metabolism modifies the properties of normal appearing white matter in multiple sclerosis. *Brain* 131, 3092–3102 (2008).
46. Fransen, N. L. *et al.* Tissue-resident memory T cells invade the brain parenchyma in multiple sclerosis white matter lesions. *Brain* 143, 1714–1730 (2020).
47. Kuhlmann, T. *et al.* An updated histological classification system for multiple sclerosis lesions. *Acta Neuropathol* 133, 13–24 (2017).
48. Van Der Valk, P. & De Groot, C. J. A. Staging of multiple sclerosis (MS) lesions: Pathology of the time frame of MS. *Neuropathol. Appl. Neurobiol.* 26, 2–10 (2000).
49. Gong, C. *et al.* SAW: an efficient and accurate data analysis workflow for Stereo-seq spatial transcriptomics. *Gigabyte* 2024, 1–12 (2024).
50. Hao, Y. *et al.* Dictionary learning for integrative, multimodal and scalable single-cell analysis. *Nat. Biotechnol. 2023 422* 42, 293–304 (2023).
51. Cable, D. M. *et al.* Robust decomposition of cell type mixtures in spatial transcriptomics. *Nat. Biotechnol. 2021 404* 40, 517–526 (2021).
52. Liu, W. *et al.* Joint dimension reduction and clustering analysis of single-cell RNA-seq and spatial transcriptomics data. *Nucleic Acids Res.* 50, e72–e72 (2022).
53. Love, M. I., Huber, W. & Anders, S. Moderated estimation of fold change and dispersion for RNA-seq data with DESeq2. *Genome Biol.* 15, 1–21 (2014).
54. Wu, T. *et al.* clusterProfiler 4.0: A universal enrichment tool for interpreting omics data. *Innov.* 2, 100141 (2021).
55. Jin, S., Plikus, M. V. & Nie, Q. CellChat for systematic analysis of cell-cell communication from single-cell and spatially resolved transcriptomics. *bioRxiv* 2023.11.05.565674 (2023) doi:10.1101/2023.11.05.565674.
56. Bankhead, P. *et al.* QuPath: Open source software for digital pathology image analysis. *Sci. Rep.* 7, 1–7 (2017).

# EXTENDED DATA FIGURES

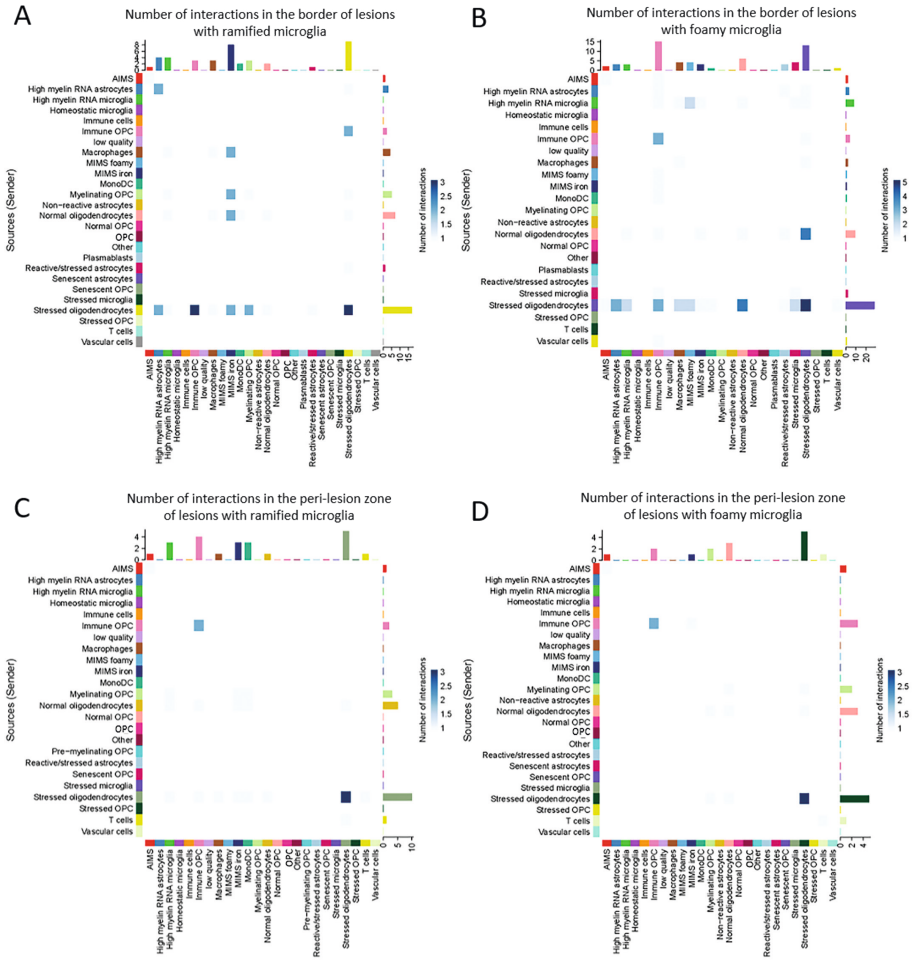


**Extended Fig. 1: Intercellular communication of cell types identified with CellChat**. A) Interactions in the border of mixed lesions with ramified microglia. B) Interactions in the border of mixed lesions with foamy microglia. C) Interactions in the peri-lesional zone of lesions with ramified microglia. D) Interactions in the peri-lesional zone of lesions with foamy microglia.

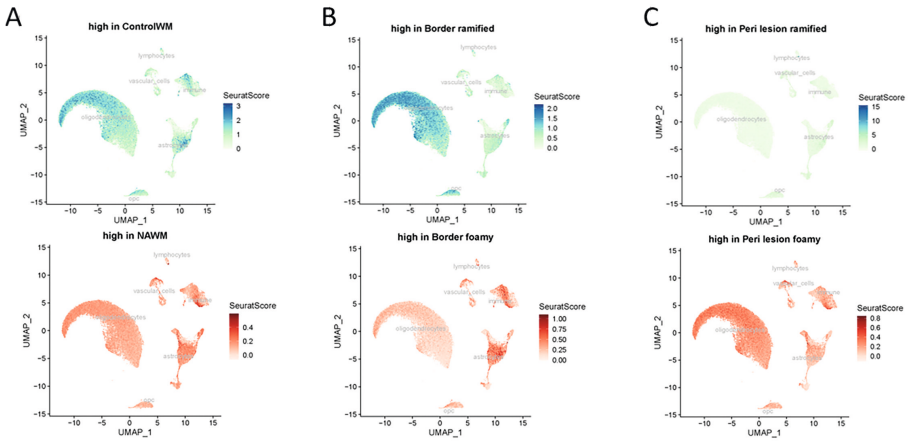


**Extended Fig. 2: Differentially expressed genes plotted onto the single-cell uMap of Absinta *et al.*, indicating major cell types affected**. A) De genes in NAWM compared to control WM. Genes with higher counts in the control WM (top panel) and with higher counts in the NAWM (lower panel). B) The border of mixed lesions with foamy microglia compared to the border of those with ramified microglia. Genes with higher counts in the border of mixed lesions with ramified microglia (top panel) and with higher counts in the border of those with foamy microglia (lower panel). C) The peri-lesional zone of mixed lesions with foamy microglia compared to the peri-lesional zone of those with ramified microglia. Genes with higher counts in the peri-lesional zone of mixed lesion with ramified microglia (top panel) and with higher counts in the peri-lesional zone of mixed lesions with foamy microglia (lower panel).

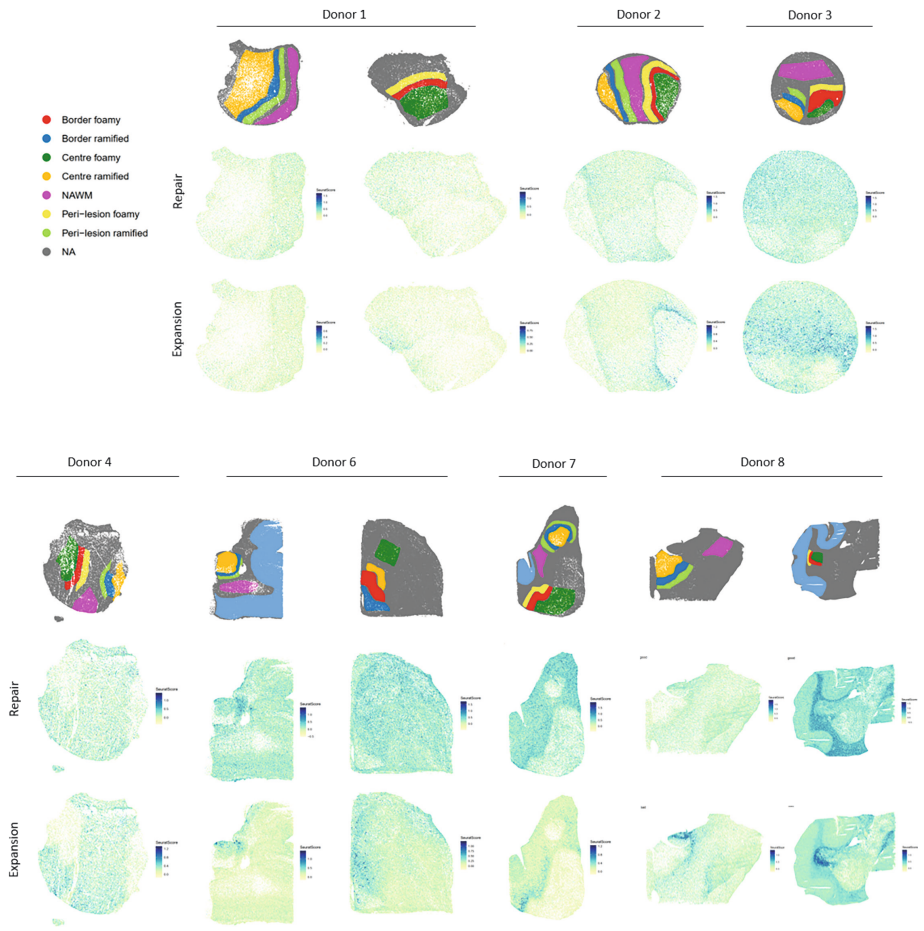


**Extended Fig. 3: Gene modules associated with repair or with expansion of lesions plotted onto the chip.** For each chip, zones of interest are indicated. Genes associated with repair were *APOD, CTNNB1, QKI, SBF2, BOK, CTTN, SHTN1, BCAS1, APOD, SHANK2, CDH4, SKI, NEAT1, DDR1*, those associated with expansion were *APOC1, APOE, APP, B2M, C1QA, C1QB, C1QC, C3, CD44, CD68, CD74, CD99, CHI3L1, CHIRL2, CHIT1, CLU, FABP5, FCGR1A, FCGR2A, FCGR2B, FTH1, FTL, GPNMB, HLA-A, HLA-DQB1, HLA-DRB1, IAH1, IFNGR1, IHA1, IGHG1, IGHG3, IGHM, IGLC2, IGLC3, IGLL5, JCHAIN, LIPA, MSR1, NCAM1, OLR1, DERPINA3, SPP1, UBB.*

# Part

# Genetic susceptibility for clinical severity is associated with more severe pathology

3

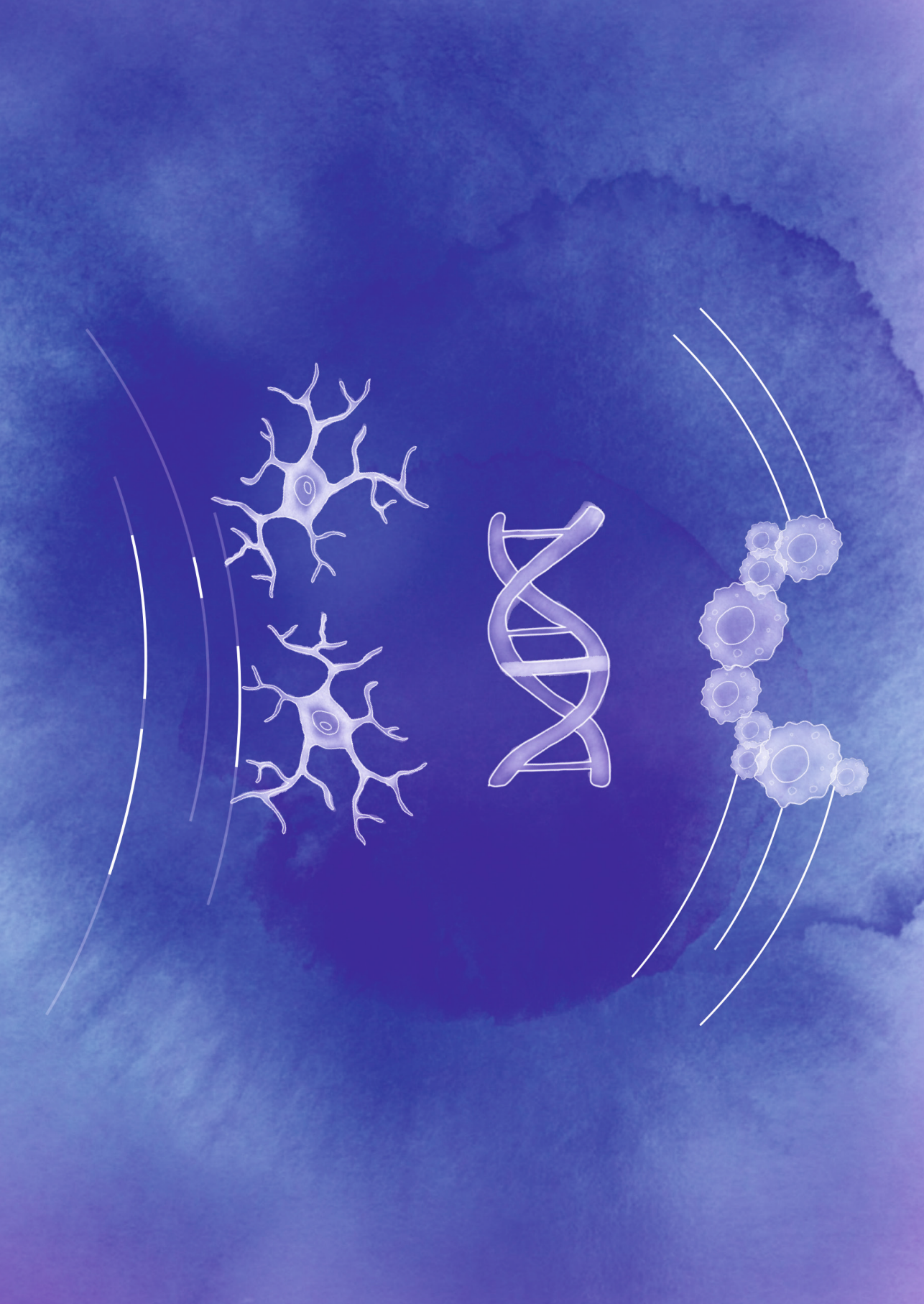

# CHAPTER 8

# Multiple sclerosis severity-associated genetic locus exacerbates neuropathology

Aletta M.R. van den Bosch[1], Hendrik J. Engelenburg[1], Dennis Wever[1], Adil Harroud[2,3], Jörg Hamann[1,4], Inge Huitinga[1,5] and Joost Smolders[1,6]

[1]Neuroimmunology Research Group, Netherlands Institute for Neuroscience, Amsterdam, The Netherlands; [2]UCSF Weill Institute for Neurosciences, Department of Neurology, University of California, San Francisco, CA, USA; [3]The Neuro (Montreal Neurological Institute and Hospital), Department of Neurology and Neurosurgery, McGill University, Montreal, Quebec, Canada; [4]Department of Experimental Immunology, Amsterdam Institute for Immunology and Infectious Diseases, Amsterdam University Medical Center, Amsterdam, The Netherlands; [5]Swammerdam institute for Life Sciences, Center for Neuroscience, University of Amsterdam, Amsterdam, The Netherlands; [6]MS Center ErasMS, Departments of Neurology and Immunology, Erasmus MC, University Medical Center Rotterdam, Rotterdam, The Netherlands

*Adapted from Nature 2023 Jul;619(7969):232-331*

## ABSTRACT

Multiple sclerosis (MS) is an autoimmune disease of the central nervous system (CNS) that results in significant neurodegeneration in the majority of those affected and is a common cause of chronic neurological disability in young adults. Here, to provide insight into the potential mechanisms involved in progression, we conducted a genome-wide association study of the age-related MS severity score in 12,584 cases and replicated our findings in a further 9,805 cases. We identified a significant association with rs10191329 in the *DYSF–ZNF638* locus, the risk allele of which is associated with a shortening in the median time to requiring a walking aid of a median of 3.7 years in homozygous carriers and with increased brainstem and cortical pathology in brain tissue. We also identified suggestive association with rs149097173 in the *DNM3–PIGC* locus and significant heritability enrichment in CNS tissues. Mendelian randomization analyses suggested a potential protective role for higher educational attainment. In contrast to immune-driven susceptibility, these findings suggest a key role for CNS resilience and potentially neurocognitive reserve in determining outcome in MS.

MS affects more than 2.8 million individuals worldwide, profoundly reducing quality of life for the majority of affected individuals [1,2]. Clinically, the disease is characterized by recurrent episodes of largely reversible neurological dysfunction, known as relapses, followed by a steady and unrelenting accumulation of chronic neurological disability, referred to as progression [1]. Case-control genome-wide association studies (GWAS) have identified more than 200 variants associated with susceptibility to the disease. Yet they do not associate with disease severity [3], which suggests that an independent genetic architecture determines the clinical course of the disease, as has been seen in other autoimmune [3] and neurological conditions [4].

To shed light on the genetic basis of MS progression, a large in-depth characterization of the genetic architecture underlying severity of MS was performed. This study combined cross-sectional and longitudinal analyses of MS-specific disability outcomes in 12,584 people of European ancestry with MS [5]. An association signal with a higher age-related MS-severity score at rs10191329 (DYSF–ZNF638 locus) reached genome-wide significance ($p = 9.7 \times 10^{-9}$), which was confirmed in the replication population and retained genome-wide significance in fixed-effects meta-analysis ($p = 3.6 \times 10^{-9}$). The direction of effect was consistent across all replication centers without evidence of heterogeneity (Q-statistic = 1.5, P = 0.99; I2 = 0%). In individuals who had been assessed longitudinally, analysis of serial EDSS across all visits revealed that the homozygous DYSF–ZNF638 risk allele carriers displayed faster disability progression ($p = 0.002$). Adjusted Cox proportional hazards analyses showed that the risk allele rs10191329A at the DYSF–ZNF638 locus was associated with faster 24-week confirmed disability worsening, (hazard ratio = 1.1 per unit increase in allele dosage, 95% confidence interval 1.02–1.18, $p = 7.9 \times 10^{-3}$), a metric used as the primary outcome in progressive MS therapeutic trials [6]. In homozygous carriers, the lead variant also conferred a 3.7-year shorter median time to using a walking aid (EDSS 6.0; hazard ratio = 1.22, 95% confidence interval 1.09–1.38, P = $9.3 \times 10^{-4}$), a clinically relevant MS disability milestone that typically tracks with the progressive phase of the disease and fixed neurological disability [7]. Furthermore, MS severity is associated with variation in genes that are preferentially expressed within the central nervous system (CNS). Prioritized MS severity genes (*DYSF, ZNF638*) even displayed cell type specificity for oligodendrocyte lineage cells. In conclusion, this recent study provided evidence for a role of genetic variation in MS progression, identifying a genetic locus associated with disability accrual in MS [5].

Here, we aim to further explore the association between the severity locus rs10191329 and MS pathology. We examined the variant's association with disease-relevant markers of tissue injury in an independent MS autopsy cohort

comprising 4,652 tissue blocks from 290 individuals. Following informed consent, brain donors with pathologically confirmed MS recruited to the Netherlands Brain Bank since 1990 were clinically and pathologically characterized (**Table 1**). Autopsy procedures were approved by the Ethical Committee of the VU University Medical Center in Amsterdam, the Netherlands. As previously described [8], blocks were dissected at standardized CNS locations (including the brainstem), with additional blocks targeted to MS lesions using macroscopic and post-mortem MRI assessment. Sections were double-labelled for proteolipid protein (PLP) and human leukocyte antigen (HLA) using immunohistochemistry and lesions were subsequently characterized in each dissected tissue block. For each individual, a brainstem lesion count was quantified using one section per standardized block. Areas of cortical grey matter demyelination were identified and classified by location (subpial, intracortical, leukocortical). These lesion locations were selected based on their recognized importance to MS pathophysiology [8,9]. DNA was extracted from whole blood or frozen cerebellar tissue, or when neither were available from formalin-fixed paraffin-embedded cerebellar tissue. Genotyping for rs10191329 was performed using the KASP genotyping platform (LGC Genomics). Pathological characterization was undertaken blind to genotype status. Differences in brainstem lesion load and rate of cortical lesions between genotype groups were examined using quasi-Poisson regression adjusted for sex, age at onset and initial disease course. To account for a variable number of supratentorial blocks sampled between individuals, cortical lesions were considered as a rate by adding the number of tissue blocks with visible cortex as an offset. Individuals with missing dependent variables or covariates were excluded. P values less than 0.025 were considered significant (adjusting for 2 pathological variables).

Consistent with estimates from the longitudinal analysis [5], homozygous risk allele carriers showed on average a four-year shorter median time to EDSS 6.0, although the differences were not significant in this smaller cohort (**Table 1**). Pathologically, homozygous carriers displayed a 1.83-fold higher number of lesions in the brainstem (95% confidence interval 1.09–3.06, P = 0.023; Methods), as well as a 1.76-fold higher rate of cortical lesions across sampled supratentorial tissue (95% confidence interval 1.15–2.69, P = 0.001; **Fig. 1**), confirming that the risk allele at the DYSF–ZNF638 locus is associated with more extensive injury at key brain locations. It is well established that focal lesions such as those in the brainstem result in axonal loss, and that cortical demyelination, which occurs independently of white matter lesions, is associated with selective neuronal loss [10]; both of these degenerative features are prominent determinants of progression [10,11].

Here, we demonstrate the association of rs10191329 with a more extensive MS-specific brainstem and cortical pathology which likely results in axonal and neuronal degeneration, and drive progression [10,11]. The specific pathways regulating this accelerated worsening still need to be uncovered. Our data provide a biological validation for a role of genetic variation in MS progression as suggested by its association with disability scores . MS has undergone a therapeutic revolution in the past few decades, with the emergence of ever more effective immune therapies that reduce and even halt relapses. Despite this, treatment of progression remains an unmet need. We have validated a genetic locus associated with faster disability progression in MS. A better understanding of the mechanisms underlying this association will provide new directions for functional characterization and drug development targeted on the neurodegenerative component of the disease.

**Table 1:** Donor demographics and clinical disease duration of MS donors the risk SNP rs10191329.

| Variable | n | rs10191329 C/C | n | rs10191329 C/A | n | rs10191329 A/A | p-value[c] | SMD |
|---|---|---|---|---|---|---|---|---|
| Female, no. (%) | 155 | 97 (62.6%) | 68 | 43 (63.2%) | 6 | 6 (100%) | 0.188 | 0.728 |
| Disease course, no. (%) | 153 | | 63 | | 6 | | 0.354 | 0.373 |
| relapsing onset | | 103 (67.3%) | | 37 (58.7%) | | 5 (83.3%) | | |
| primary progressive | | 50 (32.7%) | | 26 (42.3%) | | 1 (16.7%) | | |
| Years to EDSS 6.0, median [IQR][a] | 131 | 14.0 [7.0, 22.0] | 52 | 13.0 [8.0, 20.3] | 5 | 10.0 [4.0, 13.0] | 0.450 | 0.499 |
| Age at onset, mean (SD) | 144 | 34.0 (11.1) | 63 | 35.4 (11.0) | 6 | 35.3 (7.9) | 0.707 | 0.087 |
| Age at death, mean (SD) | 155 | 62.8 (12.8) | 68 | 64.6 (13.6) | 6 | 56.7 (12.0) | 0.293 | 0.418 |
| Disease duration, mean (SD) | 155 | 31.2 (16.7) | 68 | 31.9 (14.8) | 6 | 21.3 (10.8) | 0.304 | 0.521 |
| Total tissue blocks, median [IQR][b] | 204 | 18.0 [0.0, 26.0] | 80 | 21.0 [1.8, 27.0] | 6 | 40.0 [31.5, 41.8] | 0.001 | 1.252 |
| Targeted tissue blocks, median [IQR][b] | 146 | 13.0 [8.0, 19.0] | 65 | 14.0 [8.0, 19.0] | 6 | 28.0 [20.3, 29.8] | 0.006 | 1.120 |

*[a]Information on time to EDSS 6.0 was only available for individuals who reached this milestone during the clinical observation period; [b]The number of tissue blocks was significantly different between genotype groups, driven by a higher number of non-standardized blocks targeted to MS lesions in homozygous risk allele carriers (post-hoc Dunn test adjusted P = 0.004), in support of a higher lesion burden in this group; [c]Fisher's exact test; one-way ANOVA (Kruskal-Wallis test for nonnormal continuous variables, reported as median [IQR]). P-values are two-sided. IQR, interquartile range; SD, standard deviation; SMD, standardized mean difference.*

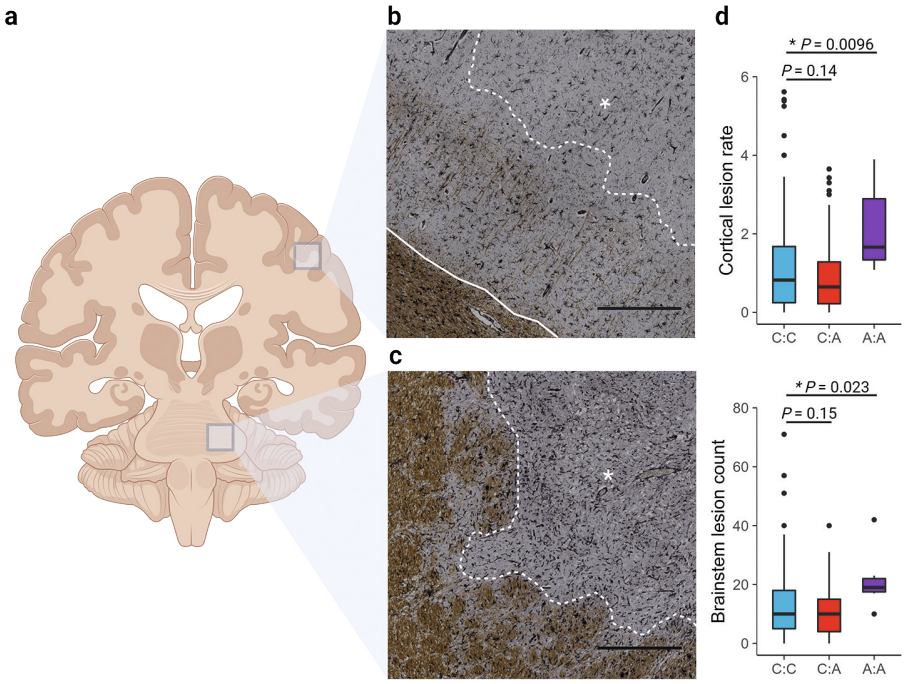


**Figure 1: Cortical lesion rate and brainstem lesion count are higher in homozygous rs10191329 risk allele carriers.** A) Schematic representation of tissue sampling locations. Demyelinating lesions were quantified on a brainstem section dissected in a consistent manner across individuals. Cortical lesions were identified on supratentorial tissue blocks targeted to macroscopic or MRI-visible MS lesions. B) Brain tissue section immunostained for the proteolipid protein marker of myelin (brown). A subpial cortical lesion characterized by the loss of myelin is marked by an asterisk and delineated by the dotted white line. The solid white line separates normal-appearing grey matter (sparse brown) from white matter (dense brown). C) A lesion spanning grey and white matter in the brainstem of the same donor, marked by an asterisk and delineated from normal-appearing tissue by the dotted white line. The donor was homozygous for the A allele of rs10191329. D) The displayed cortical lesion rate was calculated by dividing the number of lesions by the number of tissue blocks containing cortex. Box plots show median, first, and third quartiles; whiskers represent the smallest and largest values within 1.5-times the interquartile range; outliers are depicte das dots. Two-sided *P* values were obtained from generalized linear models comparing lesion count in the cortex (offset by the relevant number of tissue blocks: $n$ = 174 donors) and brainstem ($n$ = 181 donors) across genotype groups adjusting for covariates; significant differences are marked with an asterisk. Scale bars, 0.5mm. Image of brain in A created with BioRender.com. Figure from Harroud *et al.*, 2023, Nature, doi: 10.1038/s41586-023-06250-x

**Acknowledgements**
We thank the IMSGC and MultipleMS consortium for giving us the opportunity to contribute to their important work. We thank the late R. Q. Hintzen for his contributions to human genetic research.

**Funding**
Funding for this research was obtained from MS Research grants 17-975 (MoveS inspiration Grant) and 19-1079.

**Conflict of interest**
Authors report no conflict of interest.

## REFERENCES


1. Thompson, A. J., Baranzini, S. E., Geurts, J., Hemmer, B. & Ciccarelli, O. Multiple sclerosis. Lancet 391, 1622–1636 (2018).
2. Walton, C. et al. Rising prevalence of multiple sclerosis worldwide: Insights from the Atlas of MS, third edition. Mult. Scler. J. 26, 1816–1821 (2020).
3. George, M. F. et al. Multiple sclerosis risk loci and disease severity in 7,125 individuals from 10 studies. Neurol. Genet. 2, 1–11 (2016).
4. Liu, G. et al. Genome-wide survival study identifies a novel synaptic locus and polygenic score for cognitive progression in Parkinson's disease. Nat. Genet. 53, 787–793 (2021).
5. Harroud, A. et al. Locus for severity implicates CNS resilience in progression of multiple sclerosis. Nature 619, (2023).
6. Hauser, S. L. & Cree, B. Treatment of Multiple Sclerosis: A Review Stephen. Am. J. Med. 133, 1380–1390 (2021).
7. Tremlett, H., Yousefi, M., Devonshire, V., Rieckmann, P. & Zhao, Y. Impact of multiple sclerosis relapses on progression diminishes with time. Neurology 73, 1616–1623 (2009).
8. Luchetti, S. et al. Progressive multiple sclerosis patients show substantial lesion activity that correlates with clinical disease severity and sex: a retrospective autopsy cohort analysis. Acta Neuropathol. 135, 511–528 (2018).
9. Geurts, J. J. G. & Barkhof, F. Grey matter pathology in multiple sclerosis. Rev. Neurol. Argentina 1, 161 (2009).
10. Schirmer, L. et al. Neuronal vulnerability and multilineage diversity in multiple sclerosis. Nature 573, 75–82 (2019).
11. Absinta, M., Lassmann, H. & Trapp, B. D. Mechanisms underlying progression in multiple sclerosis. Curr. Opin. Neurol. 33, 277–285 (2020).

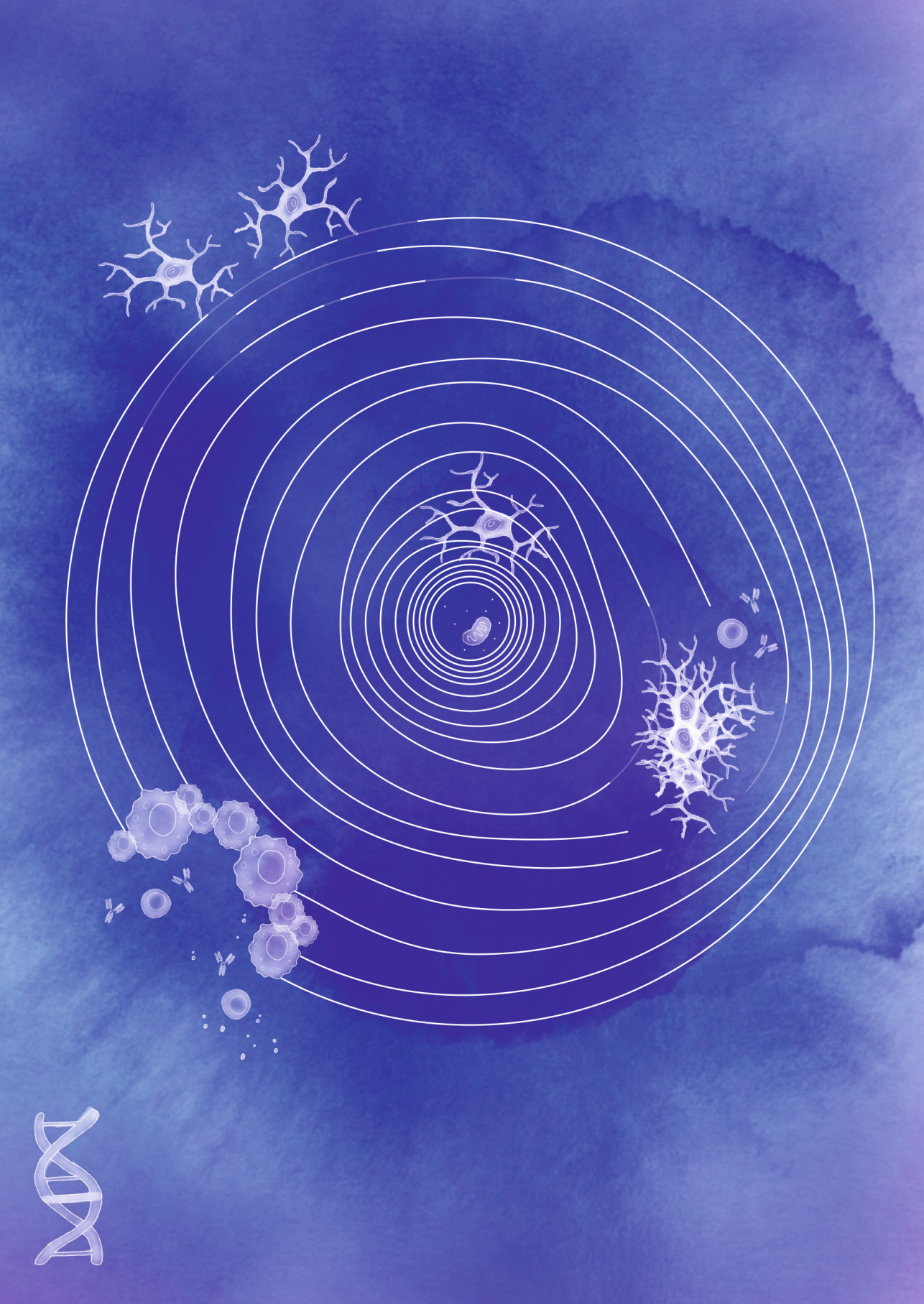

# CHAPTER 9

# The progression-associated genetic variant in the DYSF–ZNF638 locus associates with increased neuronal loss and inflammation in multiple sclerosis

Hendrik J. Engelenburg[1], Aletta M.R. van den Bosch[1], Alida Chen[1], Cheng-Chih Hsiao[1], Marie-José Melief[2], Inge Huitinga[1,3], Jörg Hamann[1,4], and Joost Smolders[1,2]

[1]Neuroimmunology Research Group, Netherlands Institute for Neuroscience, Amsterdam, The Netherlands; [2]MS Center ErasMS, Departments of Neurology and Immunology, Erasmus Medical Center, Rotterdam, The Netherlands; [3]Swammerdam Institute for Life Sciences, University of Amsterdam, Amsterdam, The Netherlands; [4]Department of Experimental Immunology, Amsterdam Infection & Immunity Institute, Amsterdam University Medical Center, Amsterdam, The Netherlands

*Submitted*

## ABSTRACT

A recent genome-wide association study identified homozygous carriership of risk variant rs10191329 to associate with faster disability accrual in multiple sclerosis (MS). We investigated the impact of homozygous risk carriership on MS pathology in the Netherlands Brain Bank MS cohort (n=290) and explored its impact on neuro-axonal damage, lymphocyte accumulation, and protein expression of the flanking genes dysferlin (DYSF) and zinc finger protein 638 (ZNF638) in homozygous risk carriers (n=6) compared to homozygous non-risk carriers (n=12). Homozygous risk carriership associated with more amyloid precursor protein (APP)$^+$ bulbs/axons, reflecting increased acute axonal stress, in normal-appearing white matter (NAWM) and white matter lesions, as well as with reduced neuronal density in cortical normal-appearing grey matter (NAGM). Further, Homozygous risk carriers showed a higher proportion of active and mixed active/inactive lesions with foamy microglia, which associate with higher cerebrospinal fluid neurofilament light chain levels. DYSF and ZNF638 were expressed by neurons and oligodendrocytes. In homozygous risk carriers, NAWM was characterized by a higher proportion of ZNF638$^+$ oligodendrocytes, and NAGM showed more DYSF$^+$ cells. Unexpectedly, nuclear RNA sequencing did not show changes in DYSF or ZNF638 expression in oligodendrocytes and neurons but rather an upregulation of mitochondrial genes in homozygous risk carriers, specifically those associated with Leber's hereditary optic neuropathy (LHON), which associated with a severe MS disease course. Increased susceptibility to neurodegeneration and demyelination could drive the association between MS severity-associated rs10191329 carriership and increased presence of foamy myeloid cells. Our data indicate that further unravelling of the role of DYSF and ZNF638 as well as LHON-associated mitochondrial pathways in MS pathology may disclose new therapeutic targets to attenuate MS progression.

## INTRODUCTION

Multiple sclerosis (MS) is an inflammatory disease of the central nervous system (CNS). Clinically, MS is characterized by neurodegenerative attacks resulting in temporary neurological disability and/or progression of sustained disability.[1] Pathologically, people with MS have focal, demyelinating lesions throughout the CNS.[2] Some lesions display neuroinflammatory components, reflected by activated microglia/macrophages and presence of (resident) lymphocytes.[2–5] MS lesions can also display neurodegenerative components,[6] such as neuro-axonal loss and acute axonal stress, the extent of which is associated with the presence of myelin laden foamy microglia.[7]

To date, over 200 single-nucleotide polymorphisms (SNPs) have been associated with increased susceptibility for MS. Most of these associated loci are related to immunological pathways.[8] In line with this, immune-modulating and -depleting therapies are efficacious in preventing early attacks of MS. However, especially in advanced disease, there is an unmet need for therapies capable of halting and reversing progression of the disease due to limited knowledge of underlying neurodegenerative processes driving disability progression.[9]

Recently, a first genetic locus was reported that affects disability progression. A genome-wide association study (GWAS) of 12,584 people with MS has identified homozygous carriership of risk variant rs10191329 (A:A) in the *DYSF–ZNF638* locus to associate with a 3.7-year shorter median time to require a walking aid. Accordingly, homozygous risk carriers in the MS cohort of the Netherlands Brain Bank (NBB), had a more extensive pathological disease load as characterized by an increased brainstem lesion load and cortical lesion rate.[10] This provided a first validation that rs10191329 is biologically relevant, as its effects are reflected in MS pathology. Importantly, a better understanding of the biological implications of this SNP on MS pathology could reveal essential underlying mechanisms of therapy-resistant disease progression in MS. Here, we analyzed the NBB MS cohort using immunohistochemistry and gene expression analysis to further explore the pathological characteristics that coincide with rs10191329 aiming to unravel biological mechanisms of disease progression.



## METHODS

### Characterization of MS lesions and genotyping

Following informed consent, brain donors with pathologically confirmed MS that were recruited to the NBB since 1990 were included in this study (**Table 1**). Autopsy procedures were approved by the Ethics Committee of the VU

medical center in Amsterdam, the Netherlands. Of all donors, detailed clinical summaries were available.

**Table 1:** Donor demographics, clinical characteristics, and pathological characteristics of SNP rs10191329 in the Netherlands Brain Bank MS cohort

| | C:C | A:C | A:A | *p*-value |
|---|---|---|---|---|
| **Donor demographics** (C:C n = 155, A:C n = 68, A:A n = 6) | | | | |
| Age (years) | 62.83 (12.75) | 64.63 (13.62) | 56.67 (12.03) | 0.22 |
| Sex (F/M) | 97/58 | 43/25 | 6/0 | 0.15 |
| PMD (hours) | 8:38 (2:45) | 7:45 (2:08) | 9:36 (1:03) | 0.25 |
| pH of CSF | 6.47 (0.29) | 6.52 (0.35) | 6.50 (0.48) | 0.92 |
| Weight of brain (g) | 1183.76 (8.05) | 1193.65 (130.14) | 1138.60 (119.72) | 0.94 |
| **Clinical characteristics** (C:C n = 155, A:C n = 68, A:A n = 5) | | | | |
| MS type (R/PP/SP) | 10/47/95 | 4/20/38 | 0/1/5 | 0.45 |
| Duration of disease (years) | 30.44 (16.53) | 31.86 (14.94) | 21.33 (10.76) | 0.17 |
| Age at onset (years) | 28.54 (19.57) | 31.36 (19.68) | 35.33 (7.87) | 0.81 |
| Years from onset to EDSS6 | 15.38 (11.62) | 16.61 (12.70) | 9.20 (5.63) | 0.18 |
| Years from EDSS6 to EDSS8 | 6.78 (5.26) | 8.38 (6.64) | 5.00 (2.45) | 0.42 |
| **Pathological characteristics** (C:C n = 146, A:C n = 64, A:A n = 6) | | | | |
| Reactive site load | 2.14 (3.30) | 3.12 (6.92) | 2.17 (2.71) | 0.97 |
| Lesion load | 13.29 (11.55) | 10.29 (8.42) | 21.67 (10.84) | 0.01 |
| Proportion active | 0.20 (0.21) | 0.20 (0.22) | 0.26 (0.20) | 0.63 |
| Proportion mixed | 0.29 (0.24) | 0.28 (0.26) | 0.40 (0.22) | 0.20 |
| Proportion active & mixed with ramified microglia | 0.23 (0.23) | 0.21 (0.18) | 0.17 (0.12) | 0.01 |
| Proportion active & mixed with foamy microglia | 0.12 (0.18) | 0.13 (0.20) | 0.29 (0.25) | 0.04 |
| Proportion inactive | 0.32 (0.28) | 0.32 (0.27) | 0.26 (0.18) | 0.46 |
| Proportion remyelinated | 0.32 (0.24) | 0.32 (0.27) | 0.20 (0.18) | 0.29 |
| Cortical lesion rate | 12.17 (16.80) | 9.11 (12.71) | 49.67 (40.69) | 0.003 |

*F, female; M, male; PP, primary progressive; R, relapsing; SP, secondary progressive. Significance tested between homozygous non-risk carriers (C:C) and heterozygous risk carriers (A:C) versus homozygous risk carriers (A:A). Proportions were tested for significance using a quasi-binomial regression, categorical data using a chi-square test, other data using a quasi-Poisson regression.*

As previously described,[11] blocks were dissected at standardized CNS locations (including the brainstem), with additional blocks targeted to MS lesions using macroscopic and post-mortem magnetic resonance imaging (MRI) assessment. Sections were stained for proteolipid protein (PLP) and human leukocyte antigen (HLA) for lesion characterization.[12] Each MS lesion has been characterized blind to genotype status. In the white matter (WM), reactive sites, active lesions, mixed active/inactive (mixed) lesions, inactive lesions, and remyelinated lesions were characterized. Reactive sites were defined by an accumulation of HLA-DR$^+$ cells without loss of PLP staining. Active lesions were defined by partial loss of PLP staining and accumulation of HLA-DR$^+$ cells throughout the lesion. Mixed lesions were defined by a hypocellular and fully demyelinated core and a hypercellular border of HLA-DR$^+$ cells. Inactive lesions were defined as hypocellular and fully demyelinated areas with no HLA-DR$^+$ cells throughout. Remyelinated lesions were defined by partially myelinated axons with similar numbers of HLA-DR$^+$ cells compared to the adjacent normal-appearing WM (NAWM). For active and mixed lesions, the microglia were stratified as ramified, ameboid, or foamy. Cortical lesions grey matter (GM) were defined as fully demyelinated areas, stratifying for subpial, intracortical, or leukocortical lesions. Of each donor, the reactive site load and the lesion load were calculated in the standardized CNS locations, the proportions of active, mixed lesions, inactive lesions, and remyelinated lesions were calculated, the proportion of active and mixed lesions with foamy or ramified microglia was calculated, and the cortical lesion rate was calculated as described previously.[2]

Nested case-control cohort: For further investigation, all 6 homozygous risk carriers (A:A) and 12 homozygous non-risk carriers (C:C) were matched for age, sex, post-mortem delay, and pH of the CSF for a nested case-control cohort (**Table 2**). We collected, if available, FFPE tissue blocks from (1) the brainstem containing the pyramidal tract longitudinally (A:A, $n = 6$; C:C, $n = 12$), (2) mixed lesions (A:A, $n = 5$; C:C, $n = 9$), and (3) NAWM and NAGM from the medial frontal gyrus (A:A, $n = 6$; C:C, $n = 9$) as well as (4) fresh-frozen tissue from NAWM and NAGM from the superior temporal gyrus (A:A, $n = 6$; C:C, $n = 9$).

**Table 2:** Donor demographics, clinical characteristics, and pathological characteristics of the nested case-control design study

| | C:C (n = 12) | A:A (n = 6) | *p*-value |
|---|---|---|---|
| **Donor demographics** | | | |
| Age (years) | 62.33 (15.26) | 56.67 (12.03) | 0.41 |
| Sex (F/M) | 12/0 | 6/0 | 1.00 |
| PMD (hours) | 9:35 (3:36) | 9:36 (1:03) | 0.99 |
| pH of CSF | 6.32 (0.31) | 6.50 (0.48) | 0.42 |
| Weight of brain (g) | 1193.33 (115.19) | 1131.33 (108.55) | 0.29 |
| **Clinical characteristics** | | | |
| MS type (PP/SP) | 5/7 | 1/5 | 0.60 |
| Duration of disease (years) | 27.17 (9.80) | 17.80 (7.16) | 0.05 |
| Age at onset (years) | 35.17 (14.68) | 34.80 (8.67) | 0.95 |
| Years from onset to EDSS6 | 12.83 (10.93) | 8.25 (6.02) | 0.42 |
| Years from EDSS6 to EDSS8 | 10.67 (7.84) | 5.67 (2.52) | 0.27 |
| **Pathological characteristics** | | | |
| Lesion load | 17.58 (10.00) | 21.67 (10.84) | 0.46 |
| Reactive site load | 5.00 (4.31) | 2.17 (2.71) | 0.11 |
| Proportion active lesions | 0.30 (0.21) | 0.26 (0.20) | 0.70 |
| Proportion mixed lesions | 0.34 (0.21) | 0.40 (0.22) | 0.56 |
| Proportion active & mixed lesions with ramified microglia | 0.32 (0.16) | 0.17 (0.12) | 0.06 |
| Proportion active & mixed lesions with foamy microglia | 0.13 (0.12) | 0.29 (0.25) | 0.05 |
| Proportion inactive lesions | 0.23 (0.15) | 0.26 (0.18) | 0.76 |
| Proportion remyelinated lesions | 0.36 (0.20) | 0.20 (0.18) | 0.23 |
| Cortical lesion rate | 1.42 (0.81) | 2.14 (1.16) | 0.21 |

*Proportions were tested for significance using a quasi-binomial regression, categorical data using a chi-square test, other data using a quasi-Poisson regression. F, female; M, male; PP, primary progressive; SP, secondary progressive.*

**Genotyping**
Of 290 MS brain donors from the NBB, DNA was extracted from whole blood or frozen cerebellar tissue using the DNeasy Blood & Tissue Kit (QIAGEN). When neither was available, DNA was extracted from formalin-fixed, paraffin-embedded (FFPE) cerebellar tissue. Genotyping for rs10191329 was performed using the KASP genotyping platform (LGC Genomics).

**Quantitative immunohistochemistry**
Neuronal damage and degeneration, immune components, and the flanking regions of rs10191329 were assessed through immunohistochemistry (IHC) on 8-µm FFPE sections or on 8-µm fresh-frozen sections. After rehydration, antigen retrieval was accomplished with microwave treatment at 700 W. Endogenous peroxidase activity and non-specific binding were blocked by incubating sections with 3% $H_2O_2$ in PBS for 15 minutes. Sections were incubated with a primary antibody overnight in blocking buffer at 4°C (details on primary antibodies and concentrations are provided in **Suppl. Table 1**). For 3,3'-diaminobenzidine (DAB) visualized stainings, the appropriate biotinylated, secondary antibody was applied, followed by conjugation with avidin-biotin-horseradish peroxidase (HRP) complex (Vector Elite ABC kit; Vector Laboratories), before visualization with DAB and counterstaining with hematoxylin. For immunofluorescence (IF) double stainings, sections were incubated with secondary antibodies conjugated with Cy3. The NeuN antibody was directly labelled with Alexa Fluor 488. Alternatively, for SOX10 staining, sections are incubated with biotinylated, secondary antibodies and enhanced by tyramide signal amplification (Sigma-Aldrich) and fluorescently labelled using streptavidin conjugated with Alexa Fluor 488. Finally, all sections were incubated with Hoechst 33342 (Thermo Fisher Scientific).Brightfield of IF tiled images of stained sections were taken using the Axioscan Z1 (Zeiss) using a 20x objective. Additionally, for IF sections, confocal imaging was performed using a STED microscope (STEDYCON; Abberior Instruments) at 40x magnification. In the brainstem, pyramidal tracts were outlined based on anatomical location. Lesions were outlined based on HLA-PLP stains. For axonal density, a thresholder was performed on SMI312 staining to detect positive signal. For acute axonal damage, $APP^+$ bulbs/axons were manually counted in lesions and in the NAWM of the pyramidal tract. In mixed lesions, $APP^+$ bulbs/axons were normalized to the number of $APP^+$ bulbs/axons in the surrounding NAWM. $NeuN^+$ cells were counted in the NAGM of the medial frontal gyrus. When no NAGM was available, fresh frozen sections from the superior temporal gyrus were used. The number of $CD3^+$ and $CD79A^+$ cells were quantified in lesions and in the NAWM of the pyramidal tract. DYSF and ZNF638 were quantified in lesions and in the NAWM and NAGM of the medial frontal gyrus. A positive cell thresholder was used for quantification of NeuN, CD3, CD79A, DYSF, and ZNF638 stainings. Thresholds were set based

on visual inspection. For SOX10, NeuN, ZNF638, and DYSF, positive cells were detected using a random trees-based classifier. All images were analyzed using QuPath 0.4.0.[13]

**NfL ELISA**

NfL was measured in CSF of the patients using the NF-light ELISA CE kit for CSF from Uman Diagnostics (Umea, Sweden, 10-7001). The ELISA was performed according the data sheet. Concentrations were calculated using the standard curve range 50-5,000 pg/ml. Donors with a lot of atrophy, as described by a neuropathologist, or a cerebrovascular accident within a year prior to autopsy were excluded.

**Tissue RNAseq analysis**

Active lesions and adjacent NAWM were collected from $n = 96$ frozen tissue blocks (unpublished data). RNA was extracted using the RNeasy Micro kit (Qiagen, Hilden, Germany), according to the manufacturer's instructions. Bulk RNA sequencing was performed on a NovaSeq6000 platform by GenomeScan (Leiden, the Netherlands).

**Nuclei isolation and RNAseq**

Nuclei were isolated from frozen normal appearing super temporal gyrus tissue from the case-control cohort (A:A, n=5; C:C, n=8), according to a previously described protocol.[14] First, 1mL ice-cold NF1 buffer (10 mM Tris-HCl pH 8.0, 1 mM EDTA, 5 mM MgCl2, 0.1 M sucrose, and 0.5% Triton X-100, 1x proteinase inhibitor) was added to 100 mg of brain tissue and homogenized. Afterwards, the homogenate was incubated in a total volume of 5 mL NF1 buffer for 30 minutes on ice and strained afterwards. Then, the homogenate was diluted in NF1 buffer to a total of 20 mL and a sucrose cushion (1 M sucrose solution with 10 mM Tris-HCl pH8.0, 3 mM MgCl2, and 1 mM DTT) was underlaid. The homogenate was centrifuged at 3,166g for 45 minutes at 4°C without braking, and all supernatant was carefully removed. The nuclei pellet was resuspended in 1 mL NF1 buffer and diluted to a total volume of 10 mL and centrifuged at 1,600g for 5 minutes at 4°C. Then the pellet was resuspended in 10 mL FANS buffer (DPBS, 1% BSA, 1 mM EDTA) and centrifuged 1,600g for 5 minutes at 4°C. The pellet was then incubated in FcR blocking reagent for 30 minutes at 4°C and subsequently incubated with Hoechst 33342, rabbit-anti-human-olig2-AF647 and mouse-anti-human-NeuN-AF488 for 30 minutes. Single-positive $NeuN^+$ or $Olig2^+$ nuclei were sorted on a BD FACSAria II cell sorter (BD Biosciences). Total RNA was isolated with the RNeasy MicroKit according to the manufacturers' instructions. All RNA samples were depleted for rRNA, and the DV200 was measured as a quality control on a fragment analyzer (Advanced Analytical, Heidelberg, Germany). Samples were then library prepped using the Takara

SMARTer Stranded Total RNA-Seq Kit v3 - Pico Input Mammalian Library Prep Kit and was sequenced with a depth of 60 million reads by GenomeScan (Leiden, the Netherlands) on an Illumina NovaSeq6000 platform. Visualization of flow cytometry was performed using FlowJo (v10.10.0).

**Confocal imaging of nuclei**

Nuclei of one pilot-sample were isolated as described above, spun down and diluted in mowiol. This was mounted on a glass slide and imaged using a Leica TCS SP8 confocal microscope and Application Suite X (Leica) (**Suppl. Fig. 3B**). Images were processed using ImageJ (v. 1.54f).

**Statistical analysis**

Differences in clinical characteristics were assessed using linear regression, adjusted for sex, age at onset, and initial disease course. Pathological characteristics were tested for differences using a quasi-binomial regression, corrected for sex, age at onset, and initial disease course.

SMI312-positive area, density DYSF$^+$ cells, and density ZNF638$^+$ cells was tested using a quasi-binomial regression. APP$^+$ bulbs/axons, NeuN$^+$ cells, SOX10$^+$ cells, CD3$^+$ cells, and CD79A$^+$ cells per mm$^2$ were tested for significance using quasi-Poisson or negative binomial regression, offset by the area measured. All statistics were performed in R (v4.3.1) using key packages ggplot2, tidyverse, lme4, glmmTMB, and emmeans. *p*-values <0.05 were considered significant.

To correct for NfL increases in normal aging, we calculated z-scores for NfL using the following formula (personal communication)[15]: CSF NfL z-score = [log2(NfL-value) – (6.661 + (age × 0.045))] / 0.736. [15] Differences between risk and non-risk carriers were tested using a two-sided t-test. The correlation between proportion of lesions containing foamy macrophages in a donor and NfL z-scores were tested using a Pearson correlation.

Adapter sequences were trimmed with Trimmomatic (v0.39), and alignment was performed against the human reference genome GRCh38.105 using the default parameters of HISAT2 (v2.2.1). Quality control was performed using FastQC (v0.11.9) and dupRadar (v1.12.1). Counts were obtained using HTseq (v1.99.2) with the 'Homo_sapiens.GRCh38.105.gtf' file. Resulting counts were analysed in R (v4.1.0) with Bioconductor (v3.13). Genes with more than two count-per-million reads (CPM) in at least six samples were kept. Count data were then normalized using the trimmed mean of M-values (TMM) method[16] (edgeR package, v3.34.1) and transformed to log2-counts per million (logCPM). Differential gene expression of *DYSF* and *ZNF638* was determined using a t-test.

Reads were first clipped for adapters using fastp (v0.23.4), and subsequently mapped using STAR2 (v0.23.4) using the following settings: --outFilterMismatchNmax 2 --outFilterScoreMinOverLread 0 --outFilterMatchNminOverLread 0 --outFilterMatchNmin 60. Separate fastq-files from the same sample were merged after mapping using samtools (v1.20). Quality control was performed using FastQC (v0.12.1). Counts were obtained using featureCounts (v2.0.6) with the 'gencode.v45.primary_assambly.annotation.gtf' file. Resulting counts were analyzed in R (v4.3.1). One sample (Olig2 – A:A) was removed as outlier, due to having the lowest library size and no olig2 expression. The eventual median library size was 3,2 million counts. Genes with more than two count-per-million reads (CPM) in at least two samples were kept. Count data were transformed to log2-counts per million (logCPM), normalized using the trimmed mean of M-values (TMM) method[16] (edgeR package, v3.42.4) and precision weighted using voom (limma package, v3.56.2). The remaining genes were reannotated with the biomaRt package (v2.58.2), using Ensembl (v112). PCA was performed on the logCPM values of the 500 most variable genes to distinguish sources of variation using the PCAtools package (v 2.14.0). For both the olig2$^{+}$ and NeuN$^{+}$ nuclei, the first principal component was strongly correlated with the log10-transformed nuclei number counts and percentage of respectively oligodendrocytes and neurons based on deconvolution (**Suppl. Fig. 3C**). Therefore, principal component plots were made after correction for this covariate and donor variation, using the function removeBatchEffect (limma package). Proportional abundance of cell types was estimated using the marker genes from a single cell study[17] with the dtangle (v2.0.9) deconvolution method.

Differential expression was assessed using an empirical Bayes moderated t-test within limma's linear model framework including estimated proportion of oligodendrocytes or neurons and log10-transformed nucleus number counts as covariates [Y = 0 + experimental condition + estimated cell-type proportion + log10 (cell number)]. Resulting p values were corrected for multiple testing using the Benjamini-Hochberg false discovery rate (FDR). Genes with FDR<0.05 were considered significantly differentially expressed. Results were visualized with the ggplot2 package (v3.5.1). Competitive gene set enrichment analysis was performed with CAMERA with preset value of 0.01 for the inter-gene correlation using the Hallmark, C1, C2, C3, C5, C6, and C7 gene set collections retrieved from the Molecular Signatures Database (MSigDB, version 2023.2; https://www.gsea-msigdb.org/gsea/msigdb/index.jsp).

## RESULTS

### Homozygous risk variant associates with foamy microglia morphology

In line with the earlier reported minor allele frequency of 0.17,[10] we identified n = 6 homozygous risk carriers of rs10191329 (A:A) within the NBB MS autopsy cohort (2.1%, n = 290). Clinical and pathological characteristics were compared between homozygous risk carriers and homozygous non-risk and heterozygous brain donors of the MS cohort of the NBB (**Table 1**). Point estimates were suggestive of homozygous risk carriers skewing consistently towards on average 6.16-year younger age of death ($p = 0.22$), 9.11-year shorter disease duration ($p = 0.17$), 6.18-year shorter period from onset of symptoms to reach expanded disability status scale (EDSS)6 ($p = 0.18$), and 1.78-year shorter period from EDSS6 to EDSS8 ($p = 0.42$). Homozygous risk carriers skew toward 1.30-times higher proportion of active ($p = 0.63$) and 1.40-time higher proportion of mixed lesions ($p = 0.20$) compared to homozygous non-risk carriers. The average proportion of inactive ($p = 0.46$) and remyelinated ($p = 0.29$) lesions were comparable between groups. Most prominently, there was 2.42-times higher abundance of active and mixed lesions with foamy microglia/macrophages in homozygous risk carriers ($p = 0.04$) and a 1.35-times lower proportion of lesions with a ramified microglia/macrophage morphology ($p = 0.01$). In accordance with a more severe clinical disease and a more extensive pathology earlier associated with rs10191329, these results indicate that there is more extensive phagocytosis by myeloid cells in carriers with a homozygous risk genotype.

### Increased neuro-axonal damage and lymphocyte infiltration in homozygous risk carriers

To further characterize the impact of rs10191329 on MS-associated neuro-axonal damage and on lymphocyte infiltration in the NAWM, we compared the n = 6 homozygous risk carriers with n = 12 matched homozygous non-risk carriers for rs10191329 (**Fig. 1A**). Although axonal density, as measured with neurofilament (SMI312), was comparable ($p = 0.50$), NAWM of the pyramidal tract of homozygous risk carriers showed a higher frequency of amyloid precursor protein $(APP)^+$ bulbs/axons reflecting acute axonal stress compared to homozygous non-risk carriers ($p < 0.001$). The density of $CD3^+$ T cells and $CD79A^+$ B cells were similar in homozygous risk carriers and homozygous non-risk carriers ($p = 0.75$ and $p = 0.21$, respectively). In the NAWM of the medial-frontal gyrus, the density of $SOX10^+$ oligodendrocytes was comparable between homozygous risk carriers and homozygous non-risk carriers ($p = 0.79$). Next, we compared the extent of acute axonal damage and infiltration of lymphocytes in mixed lesions (**Fig. 1B**). Similar to the NAWM, mixed active/inactive lesions displayed more $APP^+$ bulbs/axons normalized to the NAWM in homozygous risk carriers compared to homozygous non-risk carriers ($p = 0.01$). Accordingly,

although non-significant, A:A risk carriers showed a higher level of neurofilament light chain (NfL) Z-scores in CSF samples (Suppl. Fig. 1A; $p = 0.339$), which did however show a strong positive correlation with abundance proportion of foamy (active and mixed active/inactive) lesions (**Suppl. Fig. 1B**; $R^2 = 0.68$, $p = 0.043$). There was a substantial variation in mixed-lesional lymphocyte presence in homozygous risk carriers, showing a higher abundance of $CD3^+$ T cells ($p = 0.03$) but not clearly of $CD79A^+$ B cells ($p = 0.07$) compared to homozygous non-risk carriers. In the NAGM (**Fig. 1C**), homozygous risk carriers had a lower neuronal density as measured with NeuN compared to homozygous non-risk carriers ($p = 0.04$). There was no difference in the density of oligodendrocytes as measured with SOX10 ($p = 0.40$). Taken together, homozygous risk carriers had a higher propensity of neuro-axonal damage in the NAWM, mixed lesions and the NAGM. This finding is in line with the higher lesion rate and higher abundance of foamy myeloid cells in lesions.

## Flanking regions of rs10191329 associate with oligodendrocyte presence in MS

Rs10191329 is a methylation quantitative trait locus (QTL) in the promotor region of *DYSF,* and showed a correlation with other expression and splicing QTLs for *ZNF638*.[10,18] Thus, we explored the association of these flanking regions with MS pathology. Expression of *DYSF* and *ZNF638* was lower in active lesions compared to NAWM from the same tissue block ($p < 0.001$ and $p = 0.02$, respectively; **Fig. 2A**). Through deconvolution cell composition per sequenced sample was determined. The proportion of oligodendrocytes correlated positively with the expression of *DYSF* ($R = 0.8$, $p < 0.001$) and *ZNF638* ($R = 0.71$, $p < 0.001$; **Fig. 2B**).

**Figure 1. Homozygous risk carriers of rs10191329 have more severe neuro-axonal pathology and increased lymphocyte infiltration. (p235).** Panels show quantifications stratified for matched homozygous risk compared to homozygous non-risk carriers. **(A)** Left to right show distribution in NAWM of axonal density as measured by surface area of SMI312 ($mm^2/mm^2$), acute axonal stress as measured by $APP^+$ bulbs/axons ($n/mm^2$), lymphocyte density of $CD3^+$ T cells and $CD79A^+$ B cells ($cells/mm^2$), and density of $SOX10^+$ oligodendrocytes ($cells/mm^2$). Scale bars indicate 50 µm. **(B)** Left to right show distribution in mixed lesions of acute axonal stress as measured by $APP^+$ bulbs/axons normalized to the NAWM ($n/mm^2$), density of $CD3^+$ T cells and $CD79A^+$ B cells ($cells/mm^2$). Scale bars indicate 50 µm. **(C)** Left to right show distribution in NAGM of neuronal density ($NeuN^+$ $cells/mm^2$), and $SOX10^+$ oligodendrocytes ($cells/mm^2$). Scale bars indicate 100 µm and 50 µm, respectively. SMI312 stainings were tested for significance with a quasi-binomial regression. Quantifications in mixed active/inactive lesions were tested for significance using a mixed generalized model with a quasi-Poisson distribution. Other quantifications were tested for significance with a quasi-Poisson regression. *p*-values are shown in the plots.

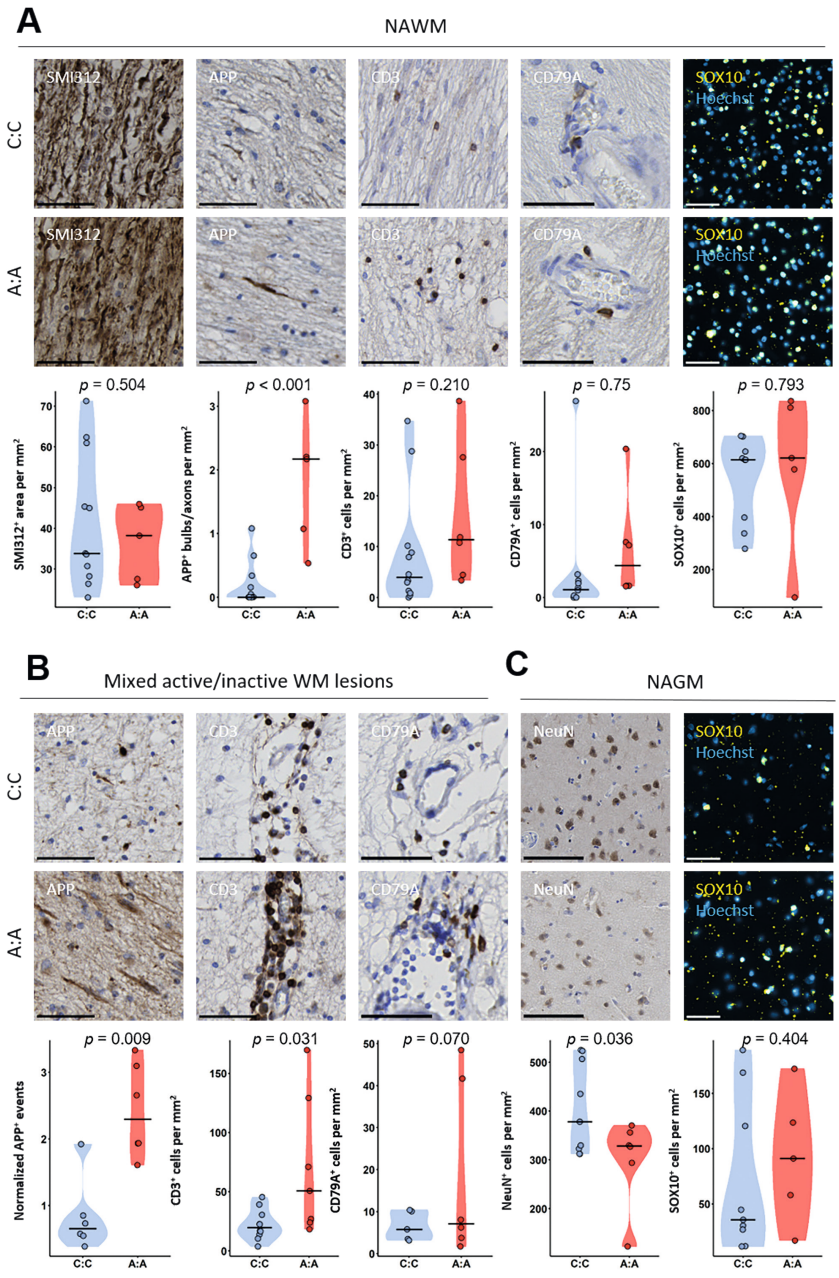
A
NAWM
C:C
A:A
SMI312
APP
CD3
CD79A
SOX10
Hoechst
p = 0.504
p < 0.001
p = 0.210
p = 0.75
p = 0.793
SMI312+ area per mm2
APP+ bulbs/axons per mm2
CD3+ cells per mm2
CD79A+ cells per mm2
SOX10+ cells per mm2
B
Mixed active/inactive WM lesions
C
NAGM
NeuN
p = 0.009
p = 0.031
p = 0.070
p = 0.036
p = 0.404
Normalized APP+ events
CD3+ cells per mm2
CD79A+ cells per mm2
NeuN+ cells per mm2
SOX10+ cells per mm2

Accordingly, previously conducted single-nucleus RNA sequencing by Jäkel *et al.* also shows most expression of *ZNF638* and *DYSF* in oligodendrocytes and, to a lesser extent, in neurons (**Suppl. Fig. 2**).[19] With immunohistochemistry in the NAWM, we indeed found SOX10$^{+}$ oligodendrocytes cells positive for DYSF or ZNF638 (**Fig. 2C**). Additionally, in the NAGM, DYSF and ZNF638 also colocalized with NeuN (Fig. 2D). This confirms the expression of DYSF and ZNF638 as detected in single-nucleus RNA sequencing.

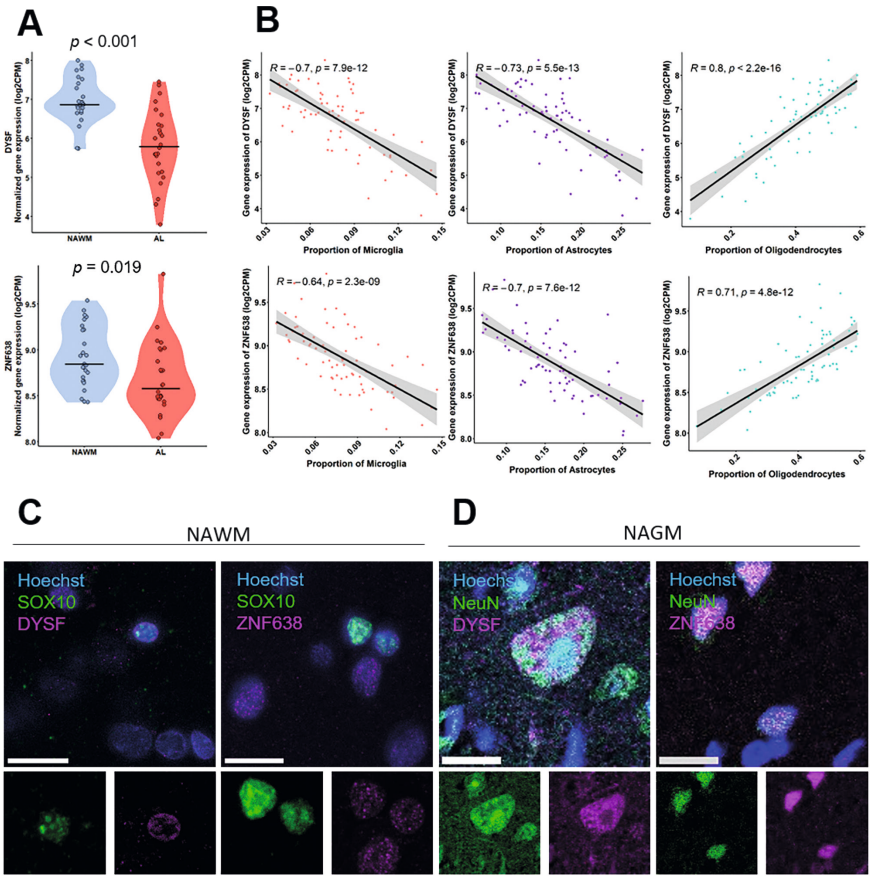


**Figure 2. Expression of ZNF638 and DYSF in lesions and normal-appearing tissue. (A)** *DYSF* and *ZNF638* gene expression in active lesions compared to NAWM. **(B)** Correlations between cell type presence assessed by cell type deconvolution and gene expression of *DYSF* and *ZNF638* associates *DYSF* and *ZNF638* with oligodendrocytes. Immunofluorescence image of DYSF and ZNF638 double labelled **(C)** with SOX10, a pan-lineage oligodendrocyte marker, in the NAWM and (**D)** with NeuN, a neuronal cell marker, in the NAGM. Scale bars indicate 15 µm. Changes in gene expression between NAWM and active lesions were tested using t-tests. The relationships between gene expression and cell type deconvolution were tested using a Pearson correlation.

**Increased expression of flanking genes DYSF and ZNF683 in rs1019329 risk carriers**

Subsequently, we investigated whether there was a difference between homozygous risk carriers and non-risk carriers in expression of flanking regions. In the NAWM, there was no difference in the density of cells expressing DYSF ($p = 0.34$). In homozygous risk carriers compared to homozygous non-risk carriers, we observed a higher density of cells expressing ZNF638 ($p = 0.04$; **Fig. 3A**) and accordingly a higher percentage of SOX10$^+$ oligodendrocytes expressing ZNF638 ($p = 0.02$; **Fig. 3B**). In mixed lesions, the density of DYSF$^+$ cells and of ZNF638$^+$ cells were comparable between homozygous risk carriers and homozygous non-risk carriers ($p = 0.85$, $p = 0.49$, respectively; **Fig. 3C**). Contrastingly to the NAWM, in the NAGM, the density of cells expressing DYSF was higher in homozygous risk carriers compared to homozygous non-risk carriers ($p = 0.01$), and the density of cells expressing ZNF638 was comparable between the groups ($p = 0.28$; **Fig. 3D**). The increased expression of DYSF was not associated with an increased percentage of NeuN$^+$ neuronal cells nor SOX10$^+$ oligodendrocytes expressing DYSF ($p = 0.88$, $p = 0.45$, respectively; **Fig. 3E**). In cortical GM lesions, the density of DYSF$^+$ cells and of ZNF638$^+$ cells was comparable between homozygous risk carriers and homozygous non-risk carriers ($p = 0.811$, $p = 0.633$, respectively; **Fig. 3F**). The altered abundance of flanking genes implicates ZNF638 and DYSF as potential molecular mediators.

**Brain nuclear gene expression implicates mitochondrial changes in homozygous risk carriers**

To further investigate potential driving factors of the more severe disease course, we isolated and sequenced Olig2$^+$ and NeuN$^+$ nuclei from normal-appearing superior temporal gyrus of homozygous rs10191329 risk and non-risk carriers (**Fig. 4A/B, Suppl. Fig. 3A-C**). Principal component analysis shows that the most variation was explained by cell type (**Fig. 4C**). First, we explored the gene expression of the flanking genes of rs10191329 in NeuN$^+$ neuronal and Olig2$^+$ oligodendrocytic nuclei, and found no apparent differences in *DYSF* and *ZNF638* between risk and non-risk carriers (**Fig. 4D**). In a PCA on both nuclear subsets separately, most variation was explained by genotype for rs10191329 (**Fig. 4E/G, Suppl. Fig. 3D/E**), however with little significant differential gene expression between risk and non-risk carriers. Significant differently abundant genes in Olig2$^+$ nuclei are *TOGARAM2*, *RMRP* (downregulated in A:A carriers), and *MT-ND4* (upregulated in A:A carriers; **Suppl. Data 1**). Pathway enrichment analysis showed a significant enrichment for mitochondrial genes in both Olig2$^+$ (FDR < 0.001) and NeuN$^+$ nuclei (FDR < 0.001), and specifically genes related to Leber's hereditary optic neuropathy (LHON) in A:A risk carriers (Olig2: FDR = 0.019; NeuN: FDR = 0.093; **Fig. 4F/H, Suppl. Fig. 3F/G, Suppl. Data 1**).

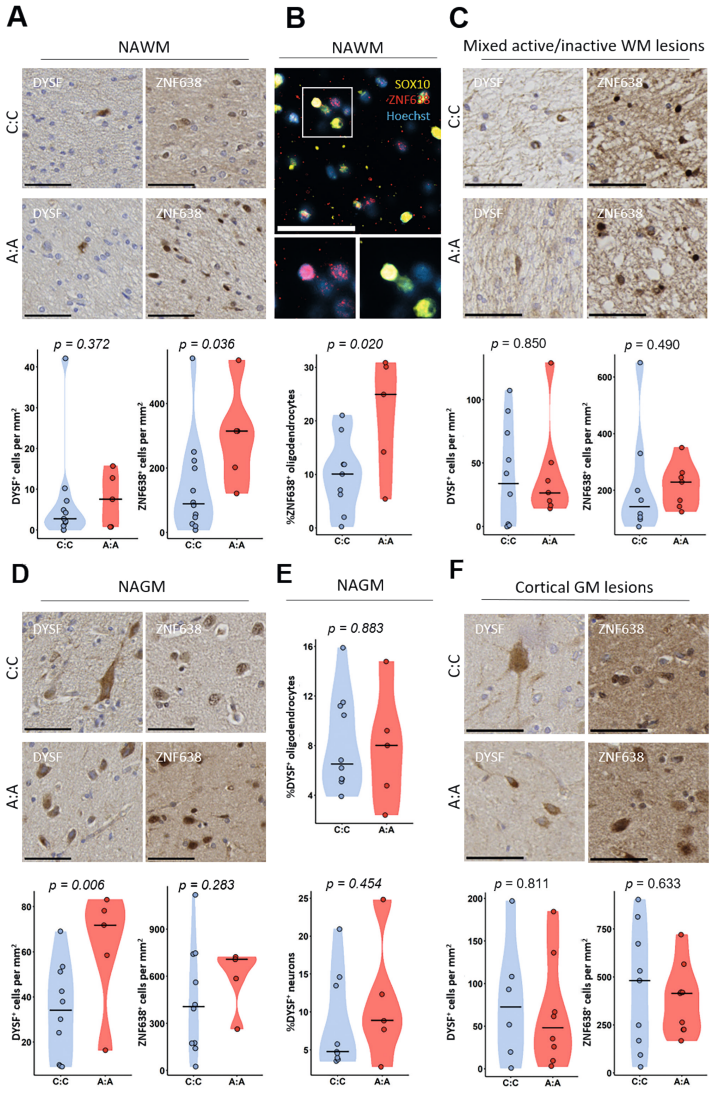


**Figure 3. Expression of DYSF and ZNF638 by oligodendrocytes and neurons.** Panels show quantifications stratified for matched homozygous risk compared to homozygous non-risk carriers. **(A)** Left to right show distribution in NAWM of DYSF$^+$ and ZNF638$^+$ cell density (cells/mm$^2$) and **(B)** percentage ZNF638$^+$ of SOX10$^+$ oligodendrocytes. Arrowhead indicates a ZNF638$^+$SOX10$^+$ cell. **(C)** Left to right show distribution in mixed lesions of DYSF$^+$ and ZNF638$^+$ cell density (cells/mm$^2$). **(D)** Left to right show distribution in NAWM of DYSF$^+$ and ZNF638$^+$ cell density (cells/mm$^2$). **(E)** Percentage of DYSF$^+$ cells among SOX10$^+$ oligodendrocytes or NeuN$^+$ neurons. **(F)** Left to right of distribution in cortical lesions of DYSF$^+$ and ZNF638$^+$ cell density (cells/mm$^2$). Immunohistochemistry quantifications were tested for significance using a quasi-binomial generalized linear model. Scale bars = 50 µm. *p*-values are shown in the plots.

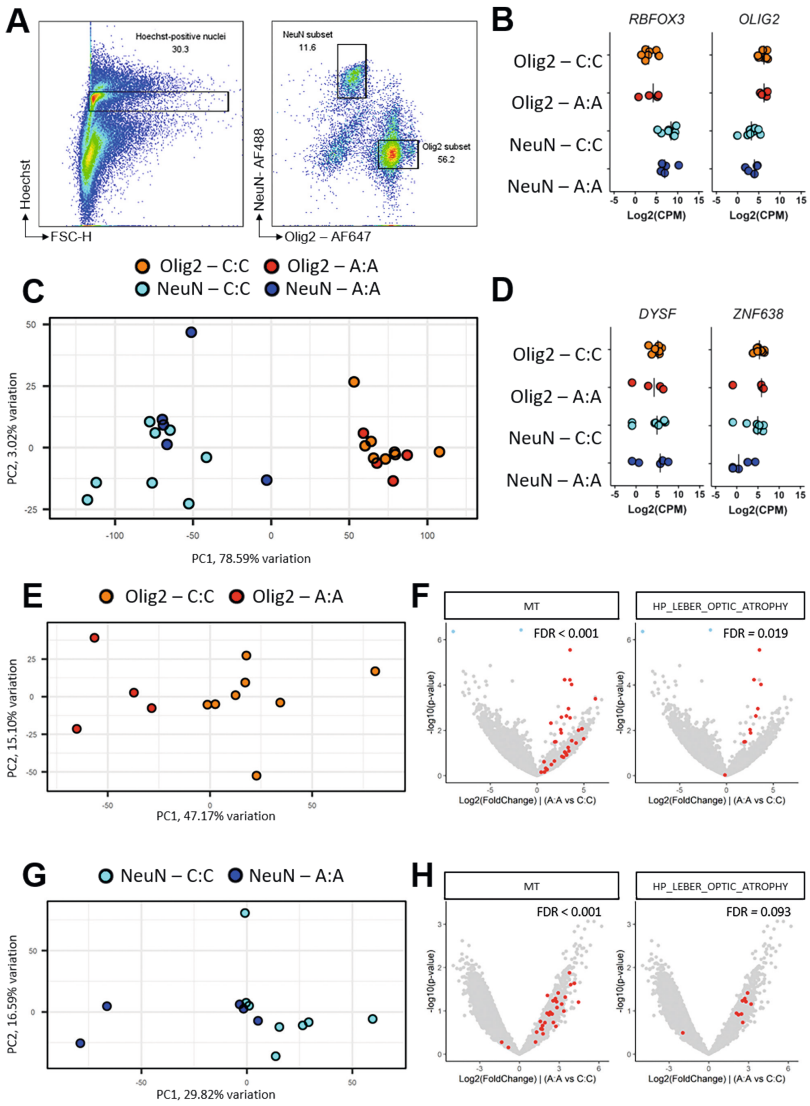


**Figure 4. Whole transcriptome profiling of NeuN⁺ and Olig2⁺ nuclei of homozygous risk and non-risk carriers of rs10191329.** Bulk RNAseq was performed on isolated nuclei from normal appearing superior temporal gyrus of n = 5 A:A risk and n = 8 C:C non-risk carriers. **(A)** Representative dot plot showing flow cytometry gating strategy used for isolating nuclear subsets. **(B)** Expression of genes (*RBFOX3*/NeuN and *OLIG2*), on which was gated during isolation. **(C)** PCA plot of all samples, where the first principal component correlates with cell type. **(D)** Gene expression of flanking genes (*DYSF and ZNF638)* of rs10191329. **(E)** PCA plot of Olig2⁺ nuclei, where the first principal component correlates with rs10191329 genotype. **(F)** Volcano plot of Olig2⁺ nuclei of A:A vs C:C carriers, showing gene set enrichment analysis (GSEA) for mitochondrial genes and genes related to LHON. Points in red are part of the respective gene set. Other significant genes are shown in blue. **(G)** PCA plot of NeuN⁺ nuclei, where the first principal component correlates

with rs10191329 genotype. **(H)** Volcano plot of NeuN$^+$ nuclei of A:A vs C:C carriers, showing GSEA for mitochondrial genes and genes related to Leber's hereditary optic neuropathy. Points in red are part of the respective gene set. PCA was performed on counts-per-million that were corrected for number of nuclei input and estimated proportional cell type abundance using deconvolution. GSEA was performed using 'CAMERA' from the limma R package. CPM = counts-per-million; PC = principal component.

## DISCUSSION

Here, we explored the impact of rs10191329 as a SNP associated with MS progression in a cohort with n = 6 homozygous risk allele donors. Our key findings are that (1) there is more immune activation in homozygous risk allele carriers as indicated by an increased frequency of foamy macrophages and an increased number of T cells in mixed active/inactive lesions; (2) propensity for neurodegeneration is more prominent in homozygous risk allele carriers as characterized by lower neuronal density and more acute axonal stress, and by CSF NfL levels correlating with foamy macrophage presence; (3) flanking region *DYSF* and *ZNF638* gene expression positively correlate with oligodendrocyte presence in MS WM lesions; (4) in homozygous risk carriers, there is a higher

density of ZNF638$^+$ cells and a higher percentage of oligodendrocytes expressing ZNF638 in the NAWM and a higher density of DYSF$^+$ cells in the NAGM. Yet, nuclear RNA sequencing did not show any changes in *DYSF* or *ZNF638* expression, but rather (5) show an upregulation of mitochondrial genes in homozygous risk carriers, specifically those associated with LHON. These data suggest that an increased susceptibility to tissue damage could drive the association between the MS severity-associated SNP rs10191329 and increased myeloid cell activation, and identifies both DYSF and ZNF638 as well as upregulated mitochondrial pathways shared with LHON as potential molecular mediators.

Previously, increased abundance of foamy microglia/macrophages has been associated with increased axonal damage and acute axonal stress in MS lesions in brain donors as measured with CSF neurofilament light chain levels and disease duration from onset to autopsy [7]. Replication of this observation in homozygous risk allele carriers confirms the importance of rs10191329 as a variant related to progression risk. Moreover, the increase in axonal damage and decreased neuronal density in itself illustrates the skewing towards a more severe disease course in homozygous risk allele carriers. It is known that clearance of myelin by anti-inflammatory microglia/macrophages is a prerequisite for remyelination.[20] However, excessive myelin uptake, as is the

case in foamy microglia, can be pro-inflammatory.[3,21] As we found a higher lesion load and no difference in proportion of remyelinated lesions in combination with a positive correlation of CSF NfL levels with a higher proportion of foamy microglia/macrophages, a more pro-inflammatory phenotype of these brain-resident foamy phagocytes in homozygous risk carriers is likely. In addition, there was an increased amount of $CD3^+$ T cells in mixed active/inactive lesions of homozygous risk allele carriers possibly indicating an increased recruitment of T cells in the inflammatory environment of these mixed active/inactive lesions.[3] Taken together, rs10191329 associates with a higher propensity of tissue damage and speculatively with increased secondary immune activation.

A better understanding of the mechanism underlying this association is vital to better understand and treat disability progression in MS. Regarding the flanking genes, we have confirmed the gene and protein expression of DYSF and ZNF638 in neurons and oligodendrocytes. We also report an increase of these proteins in normal-appearing tissue of homozygous risk allele carriers. Increased DYSF expression in NAGM could not be attributed to a specific cell type, whereas increased expression of ZNF638 in NAWM of homozygous risk is associated with an increase in $ZNF638^+$ oligodendrocytes. These observations suggest that both molecules could be relevant to better understand the impact of rs10191329 on MS severity. The association of these molecules with neurons and oligodendrocytes primarily suggests an impact on susceptibility of these cell types to MS-inflicted tissue damage, although immune-regulatory properties have also been attributed to oligodendrocytes [22]. We have not explored whether rs10191329 can have effects more distal than its flanking genes. However, this is not very likely because rs10191329 has, as of yet, not been identified as a trans QTL.

*DYSF* is well known for its expression in muscle cells, where a deficiency may cause muscular dystrophy.[23] As a general function, DYSF is a universal mediator of plasma membrane repair in response to membrane damage.[24–26] In MS, $DYSF^+$ endothelial cells contribute to a disturbed blood-brain barrier which is not associated with lymphocyte aggregation.[27] Here, we do not note an alteration of DYSF expression in NAWM, but only general increased expression in the NAGM without specificity for neurons. Thus, an increase in $DYSF^+$ cells as seen in homozygous risk allele carriers might reflect the increased cellular damage. As a parallel, DYSF aggregates are seen in association with neuritic plaques in Alzheimer disease,[28] and these aggregates are hypothesized to form due to the inability of neurons to repair membrane damage. The MS progression risk variant might alter DYSF functionality in a similar fashion in context of MS. However, this is unlikely as rs10191329 is a suspected methylation QTL of the DYSF promotor and should not impact function. Still, we do not find these

changes in *DYSF* on transcript level of NeuN$^+$ nuclei. This makes it less probable that rs10191329 is a direct regulator of *DYSF*, and changes at protein level may indeed reflect post-translational regulation, potentially due to cell damage.

The other flanking gene, *ZNF638*, is a transcription factor implicated in transcriptional silencing in association with the human silencing hub (HUSH) complex.[29,30] Up to now, this has been functionally described in retroviruses and adeno-associated viruses. This could be an important mechanism of action of the progression risk SNP, especially in light of the involvement of Epstein-Barr virus (EBV) in MS pathogenesis.[31,32] That we do not see our observed increase in protein level of ZNF638 at the transcript level make our findings less certain. Still, it has to be noted that there are a couple of factors obscuring the RNAseq data. First, oligodendrocyte nuclei were sampled from both NAWM and NAGM, whereas an effect was only to be seen in NAWM at protein level. Furthermore, nuclear RNA mostly reflects transient and ongoing transcription and only reflects a small proportion of all RNA within a cell.[33] If we reason from an increase in protein level of ZNF638 in the NAWM, our results could either indicate: (1) a higher need for viral silencing due to a higher viral load, although this would not be a logical consequence of a SNP or (2) a failure to silence viral DNA implicated in MS, possibly due to alternative splicing. In light of the increased abundance of ZNF638$^+$ oligodendrocytes in homozygous risk carriers, the functionality of the SNP might be driven by alterations in oligodendrocytes, and the mechanism of action needs further investigation. ZNF638 is also implicated in the differentiation of adipocytes through upregulation of peroxisome proliferator-activated receptor γ (PPARγ).[34] Regularly, PPARγ is associated with controlling lipid metabolism of macrophages.[35] PPARγ is expressed in most CNS cell types, though it is not detectable in oligodendrocytes.[36] Interestingly, agonists of PPARγ are associated with an anti-inflammatory response and remyelination.[37,38] Whether ZNF638 has a similar role in neurons as in adipocytes is currently not clear. If ZNF638 would fail to upregulate such pathways in oligodendrocytes and neurons of homozygous risk allele carriers, this could potentially contribute to dysregulation of lipid metabolism and increased inflammation, contributing to a more severe disease course.

Bulk nuclear RNA sequencing suggests mitochondrial gene expression as differentiating between risk and non-risk donors. Frequently in RNAseq studies, high levels of mitochondrial RNA are associated with sample quality or stressed cells. Due to the randomized and balanced way in which nuclei and RNA isolations as well as sequencing were performed, and that quality metrics, such as DV200, were comparable between groups, this likely reflects a biological effect. Since we performed nuclear RNAseq, this means that in A:A donors there is more translocation of mtRNA to the nucleus. Indeed, it has been described

in endothelial cells of human diabetic donors that mtRNAs translocate to the nucleus in a cell stress- and disease-dependent manner.[39] When mitochondrial genes are simply upregulated due to a higher abundance of mitochondria, this could indicate a higher energy demand. In turn, more activity of complex I and III can generate increased reactive oxygen species (ROS) production which is damaging to cells and tissues.[40] The increase in mitochondrial genes could even be beneficial, since the isolated nuclei were still intact, signaling through survivorship bias that these cells might have been able keep up with energy demand and thus persisted.

Mitochondrial changes have been described to associate with MS pathology.[41] For instance, changes in axonal mitochondrial frequency positively correlates with the amount of active and phagocytic microglia in the optic nerve of people with MS.[42] Furthermore, in acute human MS lesions there are signs of focal axonal degeneration, often associated with mitochondrial pathology.[41] In an MS mouse model, experimental autoimmune encephalomyelitis (EAE), this was reversible by neutralization of reactive oxygen and nitrogen species.[43] More evidence from the EAE model shows that (1) at onset of neurological symptoms, respiratory chain complex I activity is compromised in the spinal cord, and (2) mitochondrial dysfunction coincides with the presence of $CD45^{+}$ perivascular macrophages.[44] In line with our other findings, the increased presence of mitochondrial genes describes a more severe MS disease course in homozygous risk carriers of rs10191329.

Of special interest is the finding that mitochondrial genes related to LHON are upregulated in homozygous risk carriers. LHON is a mitochondrial genetic disease characterized by focal degeneration of the retinal ganglion cell layer and the optic nerve.[45] In LHON, causative genetic variants cause mitochondrial dysfunction.[46,47] The selectivity for optic nerve degeneration is hypothesized to exist because the retinal ganglion cells have the highest demand for mitochondrially-produced energy. [48] Clinically, case series of people with both MS and LHON have been published. Although the co-occurrence of these two distinct diseases has been described to likely be due to chance, MS tends to develop more severely in people with both MS and LHON, implying a mechanistic interaction between the two pathologies.[49] Since mitochondrial RNA is increased in cells affected by LHON,[50] this gene-association could indicate a similar mitochondrial dysfunction in MS, where an unmet energy demand could cause a more rapid decline in people with MS. Overall, this supports the theory that homozygous carriers of the progression risk allele would be more vulnerable to neurodegeneration coinciding with either the inability to provide enough energy to neurons or an abundance of ROS production. Whether these mitochondrial aberrancies might be a cause or effect remains to be determined.

There are some limitations to this study. For instance, due to the low minor allele frequency of 0.17 and the scarce available tissue, this study generally lacks power to investigate all components of MS pathology extensively. Furthermore, the isolation of nuclei yielded low abundance of RNA, resulting in limited library sizes. Overall, the characterization as performed by the Netherlands brain bank[2] and the availability of genotyped high-quality brain tissue make this dataset unique and provide a first insight into the influence of rs10191329 on the pathophysiology of MS.

In conclusion, we show that the impact of rs10191329 on MS severity associates with an increased susceptibility to tissue damage and increased myeloid cell activation and disclose both DYSF and ZNF638, as well as LHON-shared mitochondrial pathways, as potentially molecular mediators. Furthermore, we see increased expression of mitochondrial genes in homozygous risk carriers, potentially indicating more cell stress. In sum, we have further biologically validated the findings of the recently discovered MS-severity variant rs10191329 by showing changes associated with homozygous carriership of the risk allele. These findings may open new avenues for ameliorating neurodegeneration in MS progression.

**Data availability**

Nucleus RNA-seq data have been deposited at GEO and are publicly available as of the date of publication. Tissue RNAseq data will be published at a later stage. Microscopy data reported in this paper will be shared by the lead contact upon request. This paper does not report original code.

**Acknowledgements**

We are grateful to the brain donors and their families for their commitment to the Netherlands Brain Bank donor program. We are grateful to dr. Aldo Jongejan for sharing his knowledge on RNAseq analysis and to dr. Adil Harroud for his considerations on this study.

**Funding**

Funding for this research was obtained from the Monique Blom-de Wagt Foundation (23-1208), MoveS inspiration Grant (17-975), and MS Research (19-1079).

**Competing interest**

The authors declare no competing interests.

## REFERENCES


1. Lublin, F. D. *et al.* Defining the clinical course of multiple sclerosis. *Neurology* 83, 278–286 (2014).
2. Luchetti, S. *et al.* Progressive multiple sclerosis patients show substantial lesion activity that correlates with clinical disease severity and sex: a retrospective autopsy cohort analysis. *Acta Neuropathol.* 135, 511–528 (2018).
3. Boven, L. A. *et al.* Myelin-laden macrophages are anti-inflammatory, consistent with foam cells in multiple sclerosis. *Brain* 129, 517–526 (2006).
4. Smolders, J. *et al.* Tissue-resident memory T cells populate the human brain. *Nat. Commun.* 9, 4593 (2018).
5. Hsiao, C. C. *et al.* Osteopontin associates with brain TRM-cell transcriptome and compartmentalization in donors with and without multiple sclerosis. *iScience* 26, (2023).
6. Frischer, J. M. *et al.* The relation between inflammation and neurodegeneration in multiple sclerosis brains. *Brain* 132, 1175–1189 (2009).
7. van den Bosch, A. *et al.* Neurofilament Light Chain Levels in Multiple Sclerosis Correlate With Lesions Containing Foamy Macrophages and With Acute Axonal Damage. *Neurol. Neuroimmunol. neuroinflammation* 9, (2022).
8. Nourbakhsh, B. & Mowry, E. M. Multiple sclerosis risk factors and pathogenesis. *Contin. Lifelong Learn. Neurol.* 25, 596–610 (2019).
9. Kuhlmann, T. *et al.* Multiple sclerosis progression: time for a new mechanism-driven framework. *Lancet Neurol.* 22, 78–88 (2023).
10. Harroud, A. *et al.* Locus for severity implicates CNS resilience in progression of multiple sclerosis. *Nat. 2023 6197969* 619, 323–331 (2023).
11. Fransen, N. L. *et al.* Tissue-resident memory T cells invade the brain parenchyma in multiple sclerosis white matter lesions. *Brain* 143, 1714–1730 (2020).
12. Kuhlmann, T. *et al.* An updated histological classification system for multiple sclerosis lesions. *Acta Neuropathol.* 133, 13–24 (2017).
13. Bankhead, P. *et al.* QuPath: Open source software for digital pathology image analysis. *Sci. Rep.* 7, 1–7 (2017).
14. Nott, A., Schlachetzki, J. C. M., Fixsen, B. R. & Glass, C. K. Nuclei isolation of multiple brain cell types for omics interrogation. *Nat. Protoc. 2021 163* 16, 1629–1646 (2021).
15. Vermunt, L. *et al.* Age- and disease-specific reference values for neurofilament light presented in an online interactive support interface. *Ann. Clin. Transl. Neurol.* 9, 1832–1837 (2022).
16. Robinson, M. D. & Oshlack, A. A scaling normalization method for differential expression analysis of RNA-seq data. *Genome Biol.* 11, 1–9 (2010).
17. Darmanis, S. *et al.* A survey of human brain transcriptome diversity at the single cell level. *Proc. Natl. Acad. Sci. U. S. A.* 112, 7285–7290 (2015).
18. Ng, B. *et al.* An xQTL map integrates the genetic architecture of the human brain's transcriptome and epigenome. *Nat. Neurosci. 2017 2010* 20, 1418–1426 (2017).
19. Jäkel, S. *et al.* Altered human oligodendrocyte heterogeneity in multiple sclerosis. *Nat. 2019 5667745* 566, 543–547 (2019).
20. Kotter, M. R., Li, W. W., Zhao, C. & Franklin, R. J. M. Myelin impairs CNS remyelination by inhibiting oligodendrocyte precursor cell differentiation. *J. Neurosci.* 26, 328–332 (2006).

21. Grajchen, E., Hendriks, J. J. A. & Bogie, J. F. J. The physiology of foamy phagocytes in multiple sclerosis. *Acta Neuropathol. Commun.* 6, 124 (2018).
22. Falcão, A. M. *et al.* Disease-specific oligodendrocyte lineage cells arise in multiple sclerosis. *Nat. Med.* 24, 1837–1844 (2019).
23. Selcen, D., Stilling, G. & Engel, A. G. The earliest pathologic alterations in dysferlinopathy. *Neurology* 56, 1472–1481 (2001).
24. Redpath, G. M. I. *et al.* Calpain cleavage within dysferlin exon 40a releases a synaptotagmin-like module for membrane repair. *Mol. Biol. Cell* 25, 3037–3048 (2014).
25. Dias, C. & Nylandsted, J. Plasma membrane integrity in health and disease: significance and therapeutic potential. *Cell Discov.* 7, (2021).
26. Glover, L. & Brown, R. H. Dysferlin in membrane trafficking and patch repair. *Traffic* 8, 785–794 (2007).
27. Hochmeister, S. *et al.* Dysferlin Is a New Marker for Leaky Brain Blood Vessels in Multiple Sclerosis. *J. Neuropathol. Exp. Neurol.* 65, 855–865 (2006).
28. Galvin, J. E., Palamand, D., Strider, J., Milone, M. & Pestronk, A. The muscle protein dysferlin accumulates in the Alzheimer brain. *Acta Neuropathol.* 112, 665–671 (2006).
29. Zhu, Y., Wang, G. Z., Cingöz, O. & Goff, S. P. NP220 mediates silencing of unintegrated retroviral DNA. *Nat. 2018 5647735* 564, 278–282 (2018).
30. Das, A. *et al.* Epigenetic Silencing of Recombinant Adeno-associated Virus Genomes by NP220 and the HUSH Complex. *J. Virol.* 96, (2022).
31. Bjornevik, K. *et al.* Longitudinal analysis reveals high prevalence of Epstein-Barr virus associated with multiple sclerosis. *Science (80-. ).* 375, 296–301 (2022).
32. Lanz, T. V. *et al.* Clonally expanded B cells in multiple sclerosis bind EBV EBNA1 and GlialCAM. *Nat. 2022 6037900* 603, 321–327 (2022).
33. Barthelson, R. A., Lambert, G. M., Vanier, C., Lynch, R. M. & Galbraith, D. W. Comparison of the contributions of the nuclear and cytoplasmic compartments to global gene expression in human cells. *BMC Genomics* 8, 340 (2007).
34. Meruvu, S., Hugendubler, L. & Mueller, E. Regulation of Adipocyte Differentiation by the Zinc Finger Protein ZNF638. *J. Biol. Chem.* 286, 26516–26523 (2011).
35. Chawla, A. *et al.* PPAR-γ dependent and independent effects on macrophage-gene expression in lipid metabolism and inflammation. *Nat. Med. 2001 71* 7, 48–52 (2001).
36. Villapol, S. Roles of Peroxisome Proliferator-Activated Receptor Gamma on Brain and Peripheral Inflammation. *Cell. Mol. Neurobiol. 2017 381* 38, 121–132 (2017).
37. Villapol, S. Roles of Peroxisome Proliferator-Activated Receptor Gamma on Brain and Peripheral Inflammation. *Cell. Mol. Neurobiol.* 38, 121–132 (2017).
38. Ai, R. S. *et al.* Baicalin Promotes CNS Remyelination via PPARγ Signal Pathway. *Neurol. Neuroimmunol. neuroinflammation* 9, (2022).
39. Sriram, K. *et al.* Regulation of nuclear transcription by mitochondrial RNA in endothelial cells. *Elife* 13, (2024).
40. Nunnari, J. & Suomalainen, A. Mitochondria: In Sickness and in Health. *Cell* 148, 1145–1159 (2012).
41. Witte, M. E., Mahad, D. J., Lassmann, H. & van Horssen, J. Mitochondrial dysfunction contributes to neurodegeneration in multiple sclerosis. *Trends Mol. Med.* 20, 179–187 (2014).
42. Bosch, A. M. R. Van Den *et al.* Ultrastructural Axon–Myelin Unit Alterations in Multiple Sclerosis Correlate with Inflammation. *Ann. Neurol.* 93, 1–15 (2022).

43. Nikić, I. *et al.* A reversible form of axon damage in experimental autoimmune encephalomyelitis and multiple sclerosis. *Nat. Med.* 17, 495–499 (2011).
44. Sadeghian, M. *et al.* Mitochondrial dysfunction is an important cause of neurological deficits in an inflammatory model of multiple sclerosis. *Sci. Rep.* 6, 1–14 (2016).
45. Man, P. Y. W., Turnbull, D. M. & Chinnery, P. F. Leber hereditary optic neuropathy. *J. Med. Genet.* 39, 162 (2002).
46. Carelli, V., La Morgia, C. & Yu-Wai-Man, P. Mitochondrial optic neuropathies. *Handb. Clin. Neurol.* 194, 23–42 (2023).
47. Fraser, J. A., Biousse, V. & Newman, N. J. The neuro-ophthalmology of mitochondrial disease. *Surv. Ophthalmol.* 55, 299–334 (2010).
48. Howell, N. Leber hereditary optic neuropathy: Respiratory chain dysfunction and degeneration of the optic nerve. *Vision Res.* 38, 1495–1504 (1998).
49. Pfeffer, G., Burke, A., Yu-Wai-Man, P., Compston, D. A. S. & Chinnery, P. F. Clinical features of MS associated with Leber hereditary optic neuropathy mtDNA mutations. *Neurology* 81, 2073–2081 (2013).
50. Wu, Y. R. *et al.* Bioactivity and gene expression profiles of hiPSC-generated retinal ganglion cells in MT-ND4 mutated Leber's hereditary optic neuropathy. *Exp. Cell Res.* 363, 299–309 (2018).
51. Jäkel, S. *et al.* Altered human oligodendrocyte heterogeneity in multiple sclerosis. *Nature* 566, 543–547 (2019).

## SUPPLEMENTARY FILES

**Supplementary Table 1:** Antibody overview

| Protein | Company (catalog #) | Host | Clone | Dilution | Fixation | Antigen retrieval |
|---|---|---|---|---|---|---|
| SMI312 | Biolegend (837901) | Mouse | SMI312 | 1:2,000 | FFPE | CB, pH6.0 |
| APP | Millipore (MAB348) | Mouse | A4 | 1:2,000 | FFPE | CB, pH6.0 |
| NeuN | Sigma (MAB377) | Mouse | A60 | 1:100 | FFPE | PBS, pH7.6 |
| CD3 | DAKO (A045201) | Rabbit | Polyclonal | 1:100 (FFPE)<br>1:250 (Frozen) | FFPE<br>4% PFA | CB, pH6.0<br>- |
| CD79A | DAKO (M705001-2) | Mouse | Polyclonal | 1:200 | FFPE | CB, pH6.0 |
| DYSF | Leica (HAMLET-CE) | Mouse | HAM1/7B6 | 1:50 | FFPE | CA, pH7.6 |
| ZNF638 | Sigma (HPA036784) | Rabbit | Polyclonal | 1:100 | FFPE | CA, pH7.6 |
| SOX10 | R&D (AF2864) | Goat | Polyclonal | 1:200 | FFPE | CA, pH7.6 |
| NeuN | Sigma (MAB377X) | Mouse | A60 | 1:500 | FFPE | CA, pH7.6 |

*CB: citrate buffer; CA: citraconic anhydride; FFPE, formalin-fixed, paraffin-embedded; PBS, phosphate-buffered saline; PFA: paraformaldehyde*

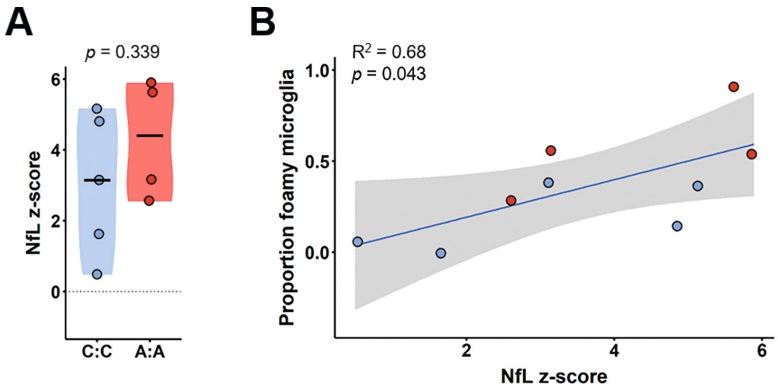


**Supplementary Figure 1: NfL correlates with foamy macrophages pathology. (A)** NfL z-scores not significantly different between risk (A:A) and non-risk (C:C) carriers of rs10191329. Statistics were performed using a two-sided t-test. **(B)** NfL z-scores are significantly correlated with the proportion of (active and mixed active/inactive) lesions with foamymicrogia/macrophage morphology. Statistics were performed using a Pearson correlation. Z-scores were calculated using the formula: CSF NfL z-score = [log2(NfLvalue)-(6.661 + (age x 0.045))]/0.736.

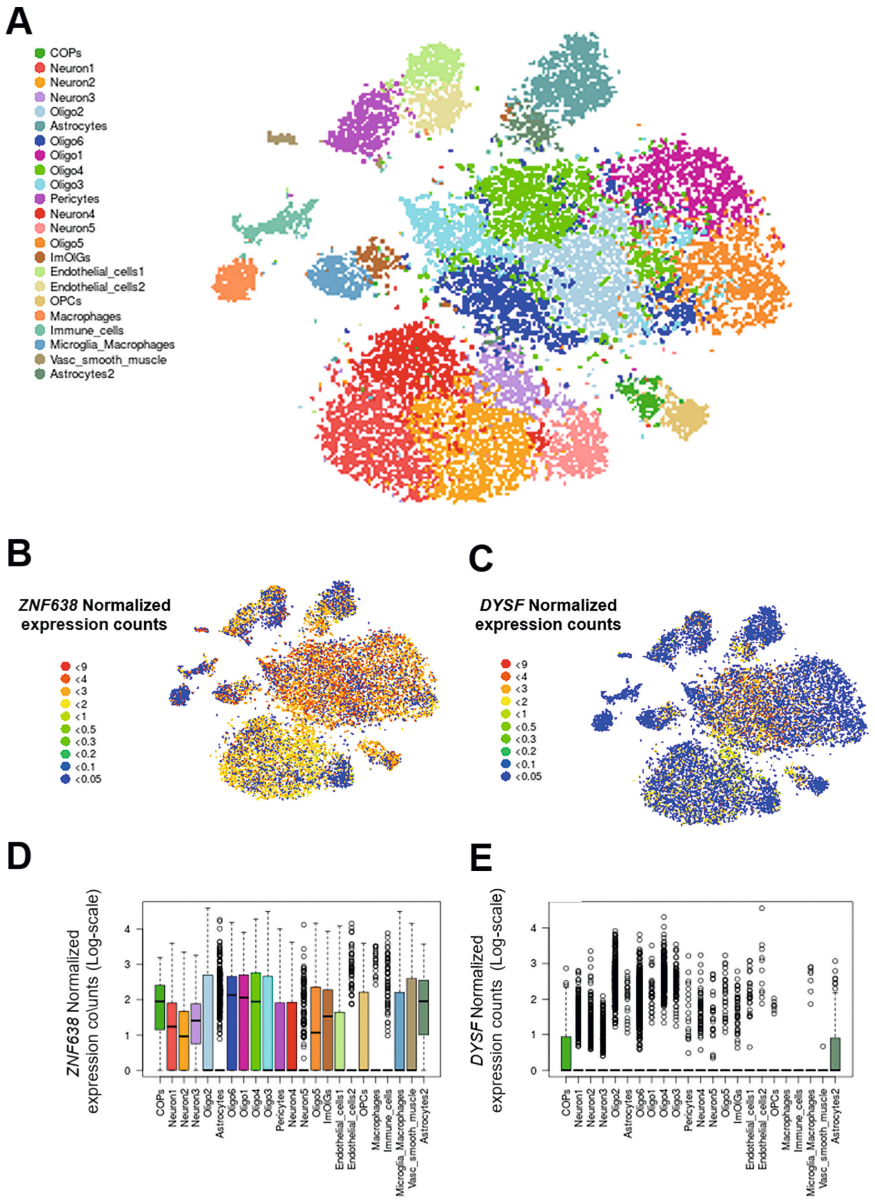


**Supplementary Figure 2: *ZNF638* and *DYSF* expression is most abundant in neurons and oligodendrocytes.** All data acquired from Jäkel *et al.*, Nature 2019 [51]. **(A)** Single nuclei tSNE plots colored for cell type. **(B)** *ZNF638* normalized expression counts. **(C)** *DYSF* normalized expression counts. Single nuclei expression boxplots of **(D)** *ZNF638* normalized expression counts and **(E)** *DYSF* normalized expression counts in different cell type clusters. Data was accessed and plotted via OligoInternode (https://ki.se/en/mbb/oligointernode).

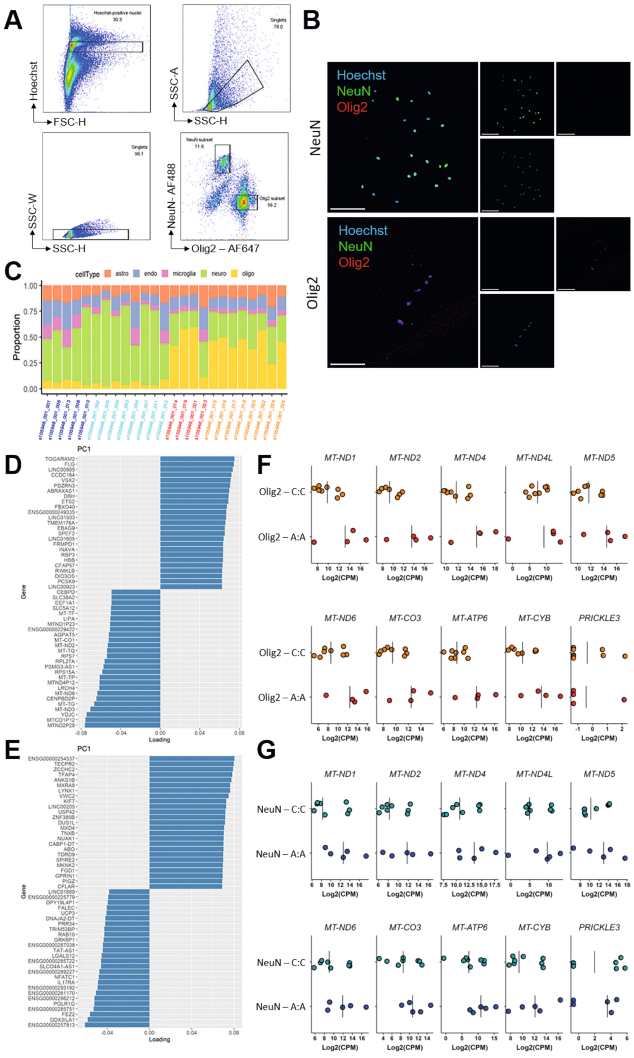


**Supplementary Figure 3. Mitochondrial genes upregulated in A:A risk carriers.** Bulk RNAseq was performed on isolated nuclei from normal appearing superior temporal gyrus of n = 5 A:A risk and n = 8 C:C carriers. **(A)** Representative dot plot showing flow cytometry gating strategy used for isolating nuclear subsets, including singlet gating. **(B)** Fluorescent images of sorted nuclei. **(C)** Estimated proportional cell type abundance as determined by deconvolution using the dtangle algorithm with the dataset of Darmanis *et al.*39 as a reference. Color of the sample name indicate grouping (Blue = NeuN-A:A; Cyan = NeuN-C:C; Red = Olig2-A:A; Orange = Olig2-C:C). **(D)** Loadings of the first principal component of the PCA on Olig2+ nuclei. **(E)** Plots of CPMs from Olig2+ nuclei of genes in the LHON geneset. **(F)** Loadings of the first principal component of the PCA on NeuN+ nuclei. **(E)** Plots of CPMs from NeuN+ nuclei of genes in the LHON geneset. CPM = Counts-permillion; PC = principal component.

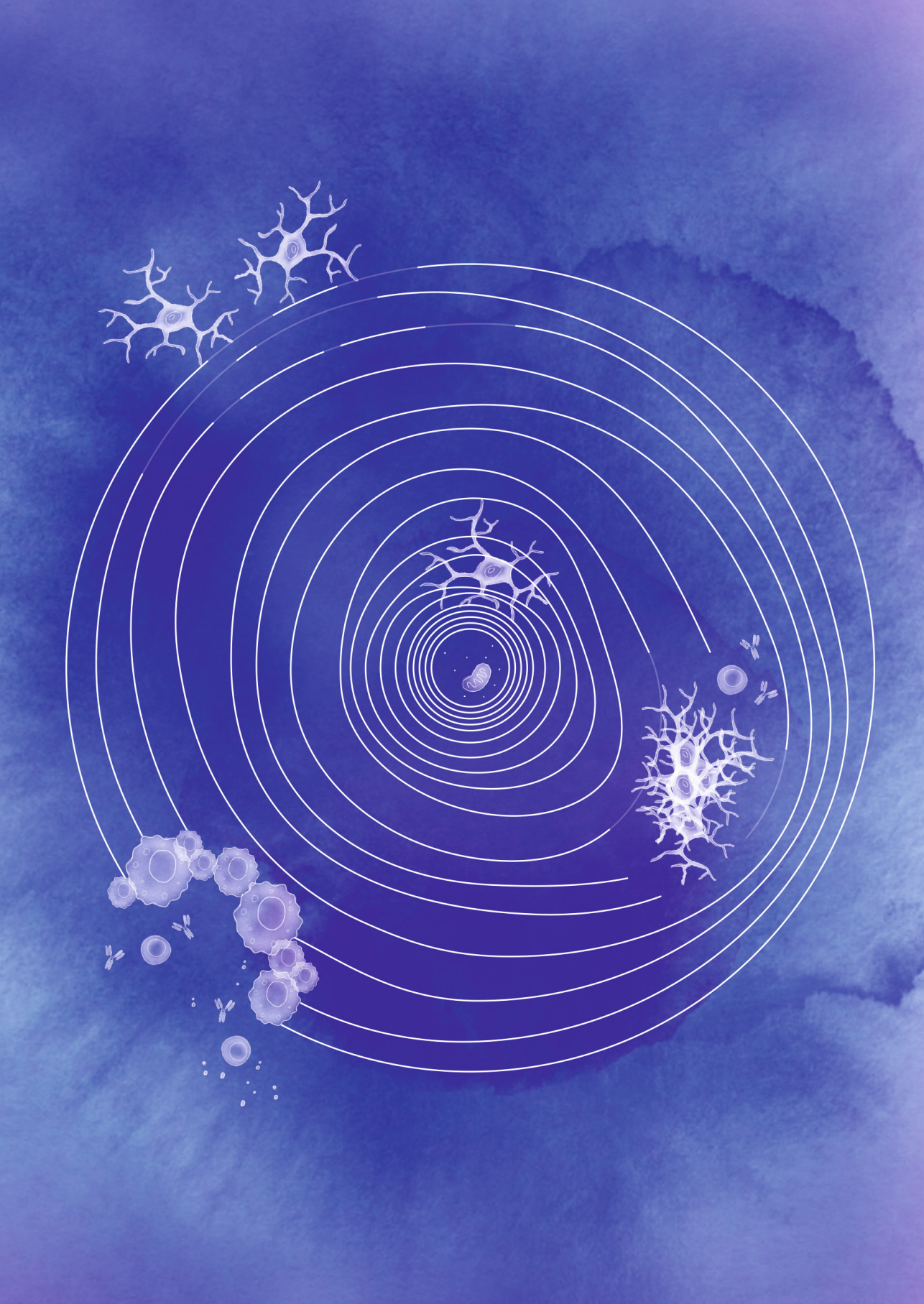

# CHAPTER 10

# General discussion

Multiple sclerosis (MS) is a chronic inflammatory disorder in which focal demyelination occurs throughout the central nervous system (CNS) [1]. Bi-directional communication between microglia and neurons plays an important role in MS pathology. Microglia are essential in regulating neuro-axonal health, and neurons and their axons can regulate microglia homeostasis. Altered neuro-axonal communication with microglia can therefore cause activation of microglia, and consequentially trigger or exacerbate neurodegeneration. Understanding how changes in neuro-axonal communication with microglia are contributing to pathological progression in MS may elucidate therapeutic targets to prevent initiation and expansion of MS lesions, and to promote regeneration. The proposed view of MS lesion formation, expansion and repair summarizing the findings of this thesis is displayed in **Figure 1**.

## INITIATION OF LESION FORMATION

The observation of changes in MS normal-appearing white matter (NAWM) as putative origin of MS lesions formation is not novel. In 1989, an MRI study showed alterations in the NAWM compared to healthy control white matter (WM) [2], which later were in part attributed to focal microglial activation in the absence of clear demyelination [3]. Importantly, abnormalities detected by MRI in NAWM distant from WM lesions could not be attributed to axonal pathology [4], indicating that microglial activation occurs prior to axonal damage. More recently, abnormalities in the NAWM in MS seen on MRI were followed over time and shown to predict the likelihood of developing subsequent MS lesions [5]. Accordingly, there are subtle transcriptional changes in microglia in MS NAWM compared to control WM [6]. Top differentially expressed genes related to lipid metabolism and phagocytosis were also upregulated in active MS lesions indicating early demyelination by microglia in NAWM. Since microglia adapt to local changes in the CNS [7–9], subpopulations with distinct cellular states may differentially contribute to MS pathology. The mechanisms by which these changes can lead to progressive multifocal changes as observed in MS has been uncertain. In this thesis, some of these mechanisms have been unveiled, including changes in check-point molecule expression, myelin structure, axonal mitochondria distribution, and microglia clustering in the context of adaptive immune activation.

### Decreased expression of check-point molecule CD200 and its receptor CD200R in the MS NAGM

Microglia in MS are chronically activated, and show partial loss of homeostasis in peri-lesion regions and NAWM [6,10]. We investigated the protein expression of CD200, which is mainly expressed by neurons and to a lesser extent by

oligodendrocytes. CD200 is a check-point molecule: binding of CD200 to its receptor, CD200R, on microglia keeps microglia in a homeostatic state [11,12]. Previously, it was shown that CD200 expression was lower in MS NAWM compared to control WM [11,12]. In experimental autoimmune encephalomyelitis (EAE), a mouse model for MS, CD200 expression is already down-regulated prior to any clinical symptoms [13]. In **Chapter 2** we show that in the normal-appearing grey matter (NAGM), CD200 expression is lower in layer 1 and layer 2 of the NAGM in MS compared to control grey matter (GM). The expression of CD200 was negatively correlated with cortical lesion rate. We hypothesize that the altered expression of CD200 may cause an altered activation state of microglia due to the loss of inhibition, and could lower the threshold for microglia to become activated and initiate demyelination. This indicates that the CD200-CD200R axis may play a pivotal role in susceptibility of GM lesion formation in MS.

Interestingly, the number of cells expressing CD200R was lower in MS NAGM compared to healthy GM. However, the low expression of CD200R by microglia makes interpretation difficult. In our study it remains unclear if there are less microglia in the MS NAGM cortex or if the microglia cells have lost their CD200R expression. CD200R blockage *in vitro* leads to increased secretion of inflammatory cytokines by macrophages and increased neuronal death in co-culture with hippocampal neurons. *In vivo*, blocking the CD200R leads to an spontaneous activation of microglia and aggravated clinical course of EAE, accompanied by increased infiltrates of T cells [14,15]. If cells in the MS NAGM have reduced CD200R expression, this may be related to the increased inflammation in the GM of people with MS, as seen in previous studies [6,16,17].

**Myelin decompaction precedes demyelination in MS NAWM**

Changes to the structure of myelin may be a second mechanism contributing to MS lesion formation susceptibility. Myelin derived from MS NAWM tissue is phagocytosed more efficiently than myelin derived from controls, which implies that there are already changes to myelin preceding demyelination [18]. With Nile red fluorescence spectroscopy, even in absence of histological myelin thinning or loss, a different polarity of the myelin in the NAWM in MS can be observed compared to healthy control myelin, indicating physiochemical alterations of the myelin sheath [19]. This may be due to an altered lipid metabolism in the MS NAWM, which leads to an increase in phospholipids and decrease in sphingolipids, that has been modelled to result in an increased repulsive force between myelin sheaths [20]. In **chapter 3**, we show, in line with previous research [21], that the nodes of Ranvier were disorganized. The elongation of the paranodal region could indicate that the myelin is wrapped less tightly around the axon. Indeed, we show that the G-ratio is smaller in MS compared to healthy controls,

indicating that the myelin diameter relative to the axon diameter is thicker in MS compared to controls. This relatively thicker myelin diameter was attributed to a less compact wrapping of the myelin in MS leading to gaps between the myelin lamellae.

Interestingly, the length of the paranode and the myelin decompaction were positively correlated to the number of activated and phagocytic microglia and to the number of T cells. *In vitro*, pro-inflammatory cytokines can cause elongation of paranodes [21]. Furthermore, pro-inflammatory cytokines *in vitro* can cause lipid metabolic defects leading to decreased sphingolipids and increased phospholipids [22], as seen in MS NAWM. Therefore, we conclude that the loss of homeostasis of microglia and the increased number of T cells in the NAWM in MS may trigger the ultrastructural alterations to the axon-myelin unit in MS. Alternatively, biochemically altering myelin structure in mice can elicit a demyelinating inflammatory immune response [23]. Together, altered myelin structure may be a trigger to initiate demyelination.

**Increased axonal mitochondria may oxidize myelin and initiate demyelination**

The observed myelin alterations may impact axonal energy demand. Decompaction of the myelin in the NAWM in MS implies that the axon is less well isolated, which may impact the action potential velocity. Additionally, the juxtaparanode has elongated in the NAWM in MS and has become overlapping with the paranode. The overlap of the juxtaparanode with the paranode may indicate that the potassium channels are unmasked, which can also cause alterations to the action potential velocity of the axon [24]. Mitochondria are highly dynamic organelles of the cell that are responsible for energy production. Although most axonal mitochondria are stationary, they will rapidly redistribute to sites of pathological stress and mitigate this stress through mitochondrial fission and fusion [25,26]. The density, shape, and size of axonal mitochondria are an indirect indicator of the axonal energy required to potentiate action potentials. In **chapter 3**, we show an increased number of axonal mitochondria in MS NAWM. It remains elusive if the increased number of mitochondria indeed indicates a higher axonal energy demand, or if it indicates a blockage of the transport of mitochondria.

The size of axonal mitochondria were comparable in MS NAWM and control WM. When mitochondria fragmentation occurs, increasing the number of mitochondria, while the surface area remains the same, the calcium buffering capacity increases. Unfortunately, although calcium buffering is considered neuroprotective, it also leads to an increase of free radicals, which when in pathological amounts can cause tissue damage and oxidize lipids, such as myelin

[27–30]. In MS NAWM, the level of oxidized phospholipids is higher compared to control WM [31]. We hypothesize that in regions where pathological levels of free radicals are produced, the myelin will become oxidized, and this will trigger demyelination.

**Some microglia nodules form 'mini lesions'**

Microglia nodules were described in relation to MS pathology for the first time in 1993 [32,33] and are regularly considered to precede MS lesion formation [34–42]. They are associated with axons undergoing Wallerian degeneration [37] and with encapsulation of activated complement deposits [34,35]. Microglia nodules are engaged in phagocytosis [43] and express both pro- and anti-inflammatory cytokines, such as tumour necrosis factor (TNF), interleukin (IL)-1β, and IL-10 [44,45]. In **chapter 4**, we show that MS donors with microglia nodules have a more exacerbated pathology than MS donors without microglia nodules, as they have a higher reactive site load, higher lesion load, higher proportion of active lesions, and lower proportion of inactive and remyelinated lesions. Therefore, microglia nodules are pathologically relevant. The question then remains whether microglia nodules are forming in a response to Wallerian degeneration due to damage caused by pathology or are themselves instigators of MS lesions. Microglia nodules are not restricted to MS, since these are also found in relation to Wallerian degeneration in brain donors with traumatic brain injury, ischemia, or stroke [37,42], where microglia nodules line up around complement-opsonized axons similar as in MS [34,35,42]. Therefore, differences between microglia nodules in MS and stroke should elucidate MS-specific characteristics of microglial nodules and their possible contribution to MS lesion formation. Using RNA sequencing, we show in **chapter 4** that although microglia nodules in MS share some commonalities with microglia nodules in stroke, there are many differentially expressed genes that are indicative for lesion formation in MS. Excitingly, microglia nodules in MS, and not in stroke, express genes that have previously been associated with MS lesion pathology and lipid metabolism, possibly indicating demyelination. In **chapter 4**, we show that microglia nodule have indeed phagocytosed oxidized phospholipids and encapsulate partially demyelinated axons, forming 'mini-lesions'.



**Lymphocytes are involved in progression of microglia nodules into lesions**

There must be fate-determining factors which determine whether a microglia nodule will progress into an MS lesion, or if it will resolve. One of these factors could be interaction with cells of the adaptive immune system. In **chapter 4**, we show that microglia nodules in MS are in a more inflammatory environment, as there are B cells, immunoglobulin (Ig) producing B-lineage antibody secreting cells and activated T cells in close proximity to microglia nodules in MS and not

in stroke. Ig produced by B cells can break the immune-tolerance of microglia [46], which indicates that these microglia nodules in MS are perhaps easier to activate through pro-inflammatory cytokines. Furthermore, phagocytosis of oxidized phospholipids, together with activation by pro-inflammatory cytokines, can lead to a hypermetabolic and hyperinflammatory phenotype. Indeed, gene expression indicates that microglia nodules in MS are under metabolic stress, and the mitochondria network of microglia nodules in MS is hyperfused, which is indicative of hypermetabolism. Lastly, the association of microglia nodules with C1qB combined with the presence of Ig leads to formation of the membrane attack complex, which can lead to osmolysis of the tissue. Therefore, presence of pro-inflammatory cytokine-secreting T cells and Ig-producing B-cell blasts makes a microglia nodule in MS more prone to lesion formation.

## LESION PROGRESSION

Molecular pathways underlying disease progression of MS are not yet fully understood. Consequently, there are no suitable biomarkers currently available that can monitor lesion formation, smouldering lesion expansion, remyelination, or scar formation. Therefore, predicting the disease course of people with MS is challenging. Although the overlap is substantial, people with MS are commonly categorized based on dominant clinical descriptors as relapsing-remitting (acute attacks followed by recovery), primary progressive (gradual worsening from onset), and secondary progressive (relapsing-remitting at onset but gradual worsening later in the disease course) [47]. These clinical entities are challenged by recent views that people with relapsing-remitting MS also show progression independent of relapses [48], and a substantial part of people with primary-progressive MS also show relapses [49]. Although several mechanisms contribute cumulatively to disability progression, expansion of white matter lesions has been demonstrated as a relevant correlate of disability progression. On MRI, lesion evolution can be monitored with conventional techniques, such as T2-weighted and gadolinium-enhanced T1-weighted sequences, over time within patients. Lesions can shrink over time, reflecting noninflammatory processes, such as regeneration and repair, become larger over time, or turn into chronic black holes, correlating with permanent demyelination and severe axonal loss [50,51]. In this thesis, we aimed to understand the molecular mechanisms underlying lesion de- and remyelination, to create a better understanding of disease progression.

### Concurrent pathophysiological mechanisms occur simultaneously in MS

Acknowledging the limitations as discussed above, clinical characterisation and treatment selection could be improved by stratification based on disease-

driving pathophysiological mechanisms rather than the traditional clinical descriptors [52]. Therefore, to understand disease progression in MS, all known pathology throughout the CNS should be taken into account. In **chapter 5**, we performed unbiased dimension reduction considering all pathological and clinical parameters known of individual people with MS at the NBB. We show that MS pathology is characterized by three distinct dimensions that are not correlated to each other, that are driven by lesion activity, microglia morphology, cortical pathology, nodules, and infiltrating lymphocytes. These concurrent pathophysiological mechanisms together influence disease progression. The dimensions disentangled MS pathology into 1) microglia activation with ongoing demyelination, 2) lesion formation and microglia activation without demyelination, and 3) loss of lesion activity and scar formation.

**Cortical pathology is associated with WM pathology and disease progression**

Cortical lesions, and particularly leukocortical lesions and intracortical lesions but less so subpial cortical lesions, are associated with subcortical demyelinating and inflammatory lesion activity [53]. In line with this, interestingly, in **chapter 2**, we show that expression of check-point molecule CD200 in the GM was positively correlated with the expression of CD200 in the WM. Accordingly, the WM pathology was also more severe in MS donors with lower CD200 expression in the GM. This indicates that mechanisms of lesion initiation in the GM and the WM may have donor-specific similarities. In **chapter 5**, we show that cortical pathology is associated with all three dimensions of pathology related to disease progression. The cortical lesion rate is positively correlated to dimension 1, which is associated with microglia activity and ongoing demyelination, and to dimension 3, which is associated with loss of lesion activity and scar formation. Interestingly, dimension 3 is mainly associated with subpial lesions, which are, in contrast to other cortical lesion types, indeed not correlated with WM lesion activity [53].



Similarly to CD200, CD47 is also a check-point molecule, which is mainly expressed by neurons and to a lesser extent by oligodendrocytes. Binding of CD47 to its receptor, SIRPα, keeps microglia in a more homeostatic state. Previously, loss of CD47 has been implied in the uncontrolled internalization of myelin, and has been hypothesized to boost myelin uptake and promote demyelination [54]. In **chapter 2**, we show that in contrast to CD200, CD47 expression was similar in MS NAGM and control GM, however CD47 expression was lower in cortical peri-lesion regions and in cortical lesions compared to the NAGM. Previously, this was also found in the peri-lesion region of mixed lesions in the WM, where it was hypothesized to be involved in expansion of lesions. We hypothesize that CD47 is similarly involved in the expansion of GM lesions.

**Foamy microglia morphology is associated with degeneration and smouldering lesion expansion**

Reflecting on the dimensional reduction analysis, the dimension associated with foamy microglia in lesions associates with fastest accumulation of disability. In line with this, previously we have shown that the proportion of active and mixed lesions in the CNS correlates with a faster disability accumulation in MS [53]. Interestingly, the microglia/macrophage activity score is positively correlated with the lesion load and the proportion of active lesions. This indicates that foamy microglia in active and mixed lesions may be associated with lesion progression. In **chapter 5**, we show that the microglia/macrophage activity score is positively correlated with dimension 1, which was associated with microglia activation with ongoing demyelination, but negatively with dimension 2 and 3, which were associated with ramified microglia activation without demyelination and with loss of lesion activity, respectively. This indicates a biological difference between active and mixed lesions with ramified microglia compared to those with foamy microglia. Accordingly, in **chapter 6**, we show that only the proportion of active and mixed lesions with foamy microglia positively correlate with the neurofilament light chain levels in the cerebrospinal fluid (CSF), and not the proportion of those with ramified microglia. This indicates that active and mixed lesions with foamy microglia are associated with more acute axonal stress than those with ramified microglia. Indeed, with immunohistochemistry, we show that that acute axonal damage is most prevalent in active lesions with foamy microglia and the border of mixed lesions with foamy microglia and not in those with ramified microglia. Interestingly, although uptake of myelin debris by microglia can induce an anti-inflammatory phenotype that is beneficial to repair, excessive lipid uptake and loss of lipid efflux may drive foamy microglia towards a more pro-inflammatory phenotype that limits remyelination [54,55]. Possibly, lesions with foamy microglia are more degenerative than those with ramified microglia. In **chapter 7,** we show that, compared to mixed lesions with ramified microglia, the border and peri-lesion region of those with foamy microglia have a higher expression of genes that indicate degeneration. Lesions with foamy microglia have a disturbed iron metabolism, increased antigen presentation and Ig production, more oxidative stress, and more destabilization of microtubules. Additionally, the higher number of oligodendrocytes with enrichment of immune-related pathways, immune-oligodendrocytes, in lesions with foamy microglia may perpetuate sustained demyelinating activity, as these are cytotoxic targets [56]. As the gene expression in the peri-lesion region of mixed lesions with foamy microglia shows similarities with the border of these lesions with foamy microglia, we hypothesize that these lesions are expanding.

**Lymphocytes contribute to demyelinating activity**

Only few lymphocytes populate the non-diseased human brain [57,58]. In MS NAWM, the number of T and B cells is higher compared to control WM, and there is a further enrichment of T and B cells in MS lesions [57,59,60]. B-cell presence in lesions is associated with a more severe clinical MS, higher proportion of mixed lesions and T-cell clustering [61]. Most lymphocytes are peri-vascular, although some are found in the parenchyma [62,63]. In MS, some B cells develop into antibody-secreting cells, and are responsible for intrathecal and local immunoglobulin (Ig) production [57,62]. This is in line with the presence of oligoclonal bands in the CSF of people with MS [64]. Recently, spatial transcriptomics has shown that there may be a higher number of B cells in the MS brain than previously believed. These B cells lack the commonly used B cell marker CD20, and highly express CD79a and CD38, implying their development into Ig producing cells [62]. This is of special interest, as Ig can break the immune tolerance of microglia, making them more prone to activation by cytokines [46]. Additionally, Ig can activate the complement cascade, ultimately leading to formation of the membrane attack complex [65]. In **chapter 4**, we show that activated T cells secreting cytokines and Ig-producing B cells may be involved in progression of a nodule into an MS lesion. Accordingly, in **chapter 5**, we show that perivascular and parenchymal T cells and plasma cells in the brain stem as well as presence of cuffing is associated with a higher score on dimension 1, indicative of microglia activation and ongoing demyelination throughout the CNS and with clinically more severe MS. We additionally show that absence of cuffing is associated with a higher score on dimension 3, indicating loss of demyelinating activity and scar formation. Strikingly, in **chapter 7**, we show that especially in mixed lesions with foamy microglia Ig is produced by plasma blasts. We propose that mixed lesions with foamy microglia are expanding and are degenerative based on their gene expression profile and presence of acute axonal damage. Together, this indicates that CNS-resident populations of T and B lymphocytes are associated with both initiation of demyelination and lesion formation, as well as lesion expansion and ongoing demyelination through sustained microglia activation.



## LESION REPAIR AND REMYELINATION

Remyelination can be extensive in MS despite having a long disease course [53,66]. It is thought that many active and some mixed lesions have the potential to remyelinate, which means that not all active and mixed lesions have equal remyelinating potential [67].

**Axon stability is important for regeneration**

In **chapter 5,** we show that dimension 1 is negatively correlated with lesions with ramified microglia, and positively correlated acute axonal damage. In line with this, dimension 3, associated with loss of microglia activation, is associated with lower levels of acute axonal damage. In **chapter 6**, we show that mixed lesions with ramified microglia are associated with less acute axonal damage than those lesions with foamy microglia. Accordingly, in **chapter 7**, we show that in the border and peri-lesion region of mixed lesions with ramified microglia, there is higher expression of genes associated with synaptic functioning, cytoskeleton organisation, neurite outgrowth, and stability of the microtubule network, compared to those with foamy microglia. In contrast, in lesions with foamy microglia, there is higher expression of genes associated with repulsion of axonal growth. Therefore, ramified microglia may support axon regeneration, and the environment of these ramified lesions compared to foamy lesions may be more permissive to regeneration and remyelination. Taken together, this indicates that the morphology of microglia in these lesions could be an indicator for their remyelinating potential.

**Preservation of myelin stability and more remyelination in mixed lesions with ramified microglia**

In **chapter 7**, we show that in the border of mixed lesions with ramified microglia, there is a higher expression of genes that are associated with myelin stability, myelin ensheatment, and remyelination, compared to the border of mixed lesions with foamy microglia. On a protein level, we show that there is a comparable number of $SOX10^{+}QKI^{+}$ and $SOX10^{+}ABCA2^{+}$ oligodendrocytes in the border of mixed lesions with ramified microglia compared to the NAWM, and a loss of these oligodendrocytes in the border of mixed lesions with foamy microglia. This indicates that in these lesions with foamy microglia, there is a loss of myelin integrity and stability. As there is no difference in the number of total oligodendrocytes, it is likely that the myelin in the border of mixed lesions with foamy microglia has lost integrity, therefore insulating the axons less efficiently, but is still present. As myelin has inhibitory effects on the ability of oligodendrocyte progenitor cells to differentiate into mature remyelinating oligodendrocytes, and therefore clearance of instable myelin in the border of mixed lesions with foamy microglia is an essential step for efficient remyelination [68–70].

## GENETIC SUSCEPTIBILITY AND PATHOLOGY

Lastly, genetic constitution of individuals could also contribute to differences in disease progression and lesion expansion. From twin and familial clustering studies is has become clear that genetics play a role in MS. The theory of common disease-common variant indicates that diseases with high prevalence in a population, such as MS, are caused by several small, frequently occurring, genetic variations. This implies that many single-nucleotide polymorphisms (SNPs) will each have a small effect toward the disease [71,72].

**rs3135388 is associated with microglia activation without demyelination**
To date, over 200 SNPs have been associated with increased risk of MS. Most of these associated loci are related to immunological pathways, affecting B cells, T cells, natural-killer cells, myeloid cells and microglia [73,74]. In **chapter 5** we found that the polygenetic risk score, which is an estimate of an individual's genetic liability to develop MS, is associated with dimension 2 of disease progression, that was associated with microglia activation without demyelination. This dimension is considered to reflect initiation of lesion formation due to the association with microglia nodules. This association is driven by the rs3135388 SNP. This tagging SNP of the HLA-DRB1*15:01 allele, confers a greatly increased susceptibility to develop MS [75,76].

**rs10191329 is associated with exacerbated pathology**
Intriguingly, none of the SNPs associated with increased risk of onset of MS have been found to be associated with clinical MS severity [77]. Lately, the International Multiple Sclerosis Genetics Consortium and the MultipleMS Consortium identified rs10191329 as a SNP associated with earlier age of disability accumulation [78]. In **chapter 8**, we show that homozygous rs10191329 SNP carriers have a higher cortical lesion rate and a higher lesion load. In **chapter 5**, we show that homozygous carriers of rs10191329 all score high on dimension 1, associated with microglia activation and ongoing demyelination and with a faster accumulation of disability. Accordingly, in **chapter 9**, we show that homozygous rs10191329 carriers compared to non-carriers have a higher proportion of active and mixed lesions with foamy microglia. Furthermore, we show that homozygous rs10191329 carriers have a decreased neuronal density in the NAGM and have more acute axonal stress in the NAWM. WM lesions of homozygous rs10191329 carriers have a higher number of T cells than non-carriers. With nuclear RNA sequencing of oligodendrocytes and neurons we identified mitochondrial changes in homozygous risk carriers compared to homozygous non-risk carriers, which may be indicative of stressed cells. Collectively, these findings consistently indicate that homozygous rs10191329

carriers have a more severe pathology showing more lesions with higher levels of acute tissue damage.

The rs10191329 SNP is located in the *DYSF-ZNF638* locus [75]. A causal relationship between MS progression and the gene products of this locus remains to be show. Dysferlin is a mediator of plasma membrane repair in response to membrane damage [79]. We show that it is mainly expressed by oligodendrocytes in the WM and by neurons in the GM. The number of dysferlin$^+$ cells in the NAWM and NAGM is increased in homozygous rs10191329 carriers compared to non-carriers, which may be associated with the increased acute axonal damage. ZNF638 is a factor implicated in viral transcriptional silencing in association with the human silencing hub complex [80]. Similar to dysferlin, we here show that ZNF638 is also mainly expressed by oligodendrocytes in the WM and by neurons in the GM. The increased number of ZNF638$^+$ cells in the NAWM and NAGM may imply a failure to silence viral DNA, possibly due to alternative splicing.

## SUMMARY

Data presented in this thesis indicates that loss of homeostasis of microglia and decompaction of myelin sheaths precede lesion formation, and that microglia nodules are the first starting point of MS lesions. Different pathophysiological processes are simultaneously occurring in people with MS, which combined with the genetic make-up are indicative for the clinical and pathological progression of the patient. Lastly, especially lesions containing foamy microglia, and less so those containing ramified microglia, are degenerative, with ongoing demyelination triggered by Ig-producing plasma blasts. Lesions containing ramified microglia, on the other hand, may hold the key to regeneration and remyelination.

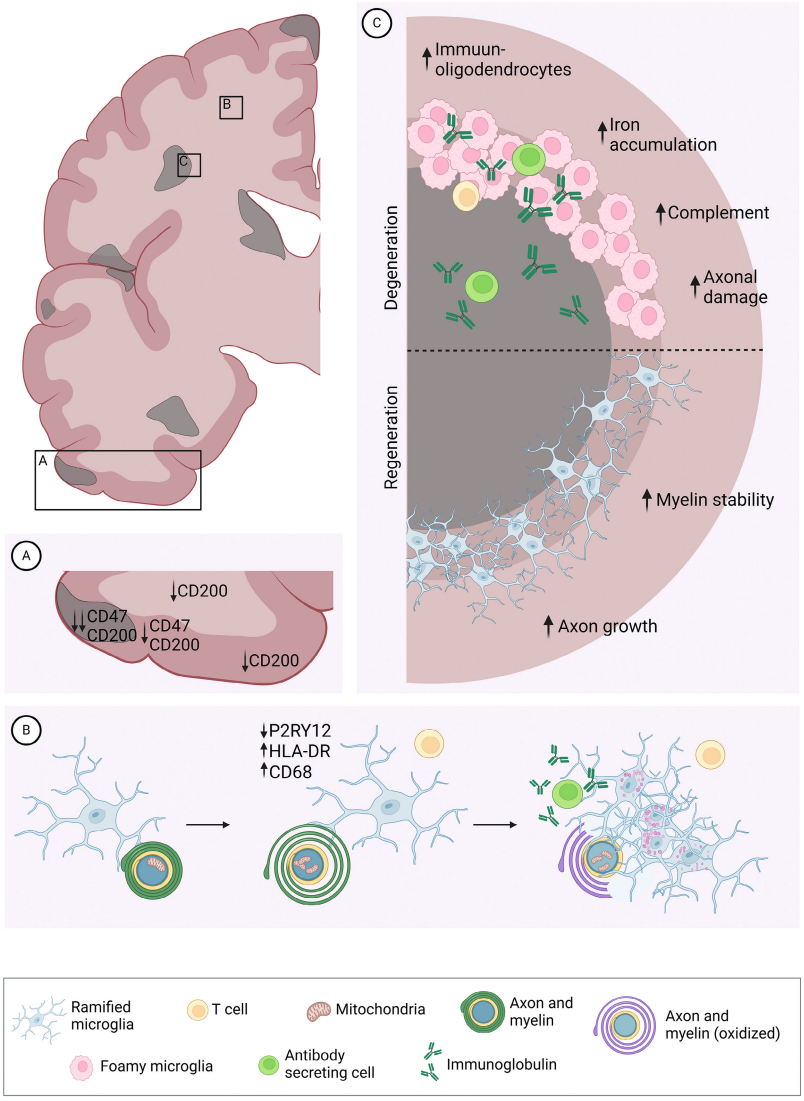


**Figure 1: Summary of the findings of this thesis.** A) In normal-appearing white and grey matter, CD200 expression is decreased. In grey matter lesions and peri-lesion regions, CD47 and CD200 expression is decreased. B) In the normal-appearing white matter there are more T cells and activated microglia which is correlated to less compact wrapping of the myelin and an increase of axonal mitochondria. Microglia nodules form, clear up oxidized phospholipids, and are activated by T cells and by immunoglobulin produced by antibody secreting cells, leading to 'mini-lesions'. C) Mixed active/inactive lesions with foamy microglia are likely expanding and are characterized by complement activation, immunoglobulin production, immune-oligodendrocyte destruction, and axonal damage. Contrastingly, those with ramified microglia are likely remyelinating or becoming inactive and are characterized by higher myelin stability and axonal growth.

## FUTURE DIRECTIONS

As usually in science, our findings have led to a multitude of new questions. Future research addressing these questions can validate, strengthen, and deepen our knowledge on the role that microglia and neuro-axonal communication have in initiation of lesion formation, expansion and repair. In this section, I would like to elaborate on some interesting future directions we can take from here. Excitingly, potential therapeutic targets have come from the studies in this thesis, some of which I want to highlight in this section.

In the first part of this thesis, pathways involved in initiation of lesion formation were discussed. CD200 emerged as an interesting mechanism to dampen microglia activation and to prevent loss of homeostasis. However, the mechanism driving the reduction of CD200 in MS remains unclear. As the decreased expression in the NAGM is limited to the first two cortical layers, those that are closest to the meninges, perhaps soluble factors in the CSF or in the serum are mediating this expression of CD200. Investigating the expression of CD200 *in vitro* in neuronal cells, such as SY-SH5Y cells, before and after incubation with CSF, cytokines, and Ig, would be of interest. Next, *in vitro* studies should study the effect of loss of neuronal CD200 on microglia in a co-culture of neuronal cells with microglia, by studying their cytokine secretion and potency to phagocytose myelin. Increasing the expression of CD200 in the same co-culture should then decrease the inflammation and their phagocytic potency. If CD200 upregulation dampens microglia activation, this may also rescue the disorganisation of the paranode and juxtaparanode domain [21].

The tubular mitochondria in microglia nodules in MS imply hypermetabolism and hyperinflammation. We have proposed that the activation of microglia nodules by phagocytosis of oxidized phospholipids together with the activation by cytokines has led to a hypermetabolic and hyperinflammatory state. This needs to be functionally validated, e.g. through metabolic measurements with a Seahorse analysis of microglia that have phagocytosed oxidized lipids and have been activated through pro-inflammatory cytokines. If they are indeed hypermetabolic, removal of one of the activators should prevent the microglia from becoming hypermetabolic and hyperinflammatory through this pathway. In that case, oxidative species and oxidized lipids are interesting targets. Superoxide dismutase (SOD) is an antioxidant that converts the superoxide generating hydrogen peroxide, which then is catalysed by glutathione (GSH) into water [81]. In some MS lesions, the expression of SOD is increased, likely reflecting a protective response [82]. Perhaps, general upregulation of SOD or GSH through viral vectors can successfully catch some of the oxidative species before the myelin is oxidized. The Keap1-Nrf2 pathway is activated by oxidative

stress to activate transcription of antioxidant genes [83]. Upregulation of Nrf2 may therefore also be an interesting therapeutic target to prevent oxidative stress and damage. Alternatively, antibodies targeted against oxidized phospholipids, such as E06, may prevent the phagocytosis of the myelin. However, inhibiting phagocytosis of damaged myelin may be more detrimental than beneficial, as this will likely inhibit remyelination [68]. The hypermetabolism of microglia nodules itself may present an interesting therapeutic target. In the hypermetabolic state, both oxidative phosphorylation as well as glycolysis are maximally utilized, which leads to longevity of the cell, inflammation, and production of oxidative species. It is possible to inhibit oxidative phosphorylation by inhibiting complexes of the mitochondrial electron transport chain (ETC). Metformin, a treatment for diabetes type 2, is an example of a therapeutic target that can block the first complex of the ETC and reduce the production of oxidative species, which may have a beneficial effect [84,85]. In the third part of this thesis, gene expression analysis of oligodendrocytes and neurons of homozygous carriers of the progression risk SNP rs10191329 and homozygous non-risk carriers indicated mitochondrial changes which may imply cellular stress. Similarly to the microglial nodules, a Seahorse analysis on isolated oligodendrocytes and neurons of risk carriers and non-risk carriers or on CRISPR-cas9 gene edited cell-lines will shed more light on the functional implications of the increased mitochondrial gene expression.

In the second part of this thesis, pathways involved in lesion expansion and lesion repair were discussed. Here, CD47 emerged as an interesting target to halt lesion expansion. As this is also the case for WM mixed lesions thought to be expanding [12], targeting CD47 may be beneficial for both WM and GM. Similar to CD200, functional tests are still needed to gain a better understanding of the molecular mechanism of CD47, and how down- or upregulation of this check-point molecule influences microglia activity, inflammation, and phagocytic propensity.

Iron dysregulation has been described in multiple sclerosis pathology, although it's exact role in disease progression is not yet clear [86]. If iron in the border of mixed lesions has accumulated in microglia, this may lead to microglial dysfunction and ultimately ferroptosis [87]. Ferritin is an iron storage protein that sequesters ferrous iron, playing an important antioxidant role in cells [88]. We here show that there is a higher expression of ferritin in the rim and peri-lesion region of mixed lesions with foamy microglia, accompanied by a higher density of ferritin$^{+}$ microglia in these regions. This is indicative of more prominent iron dysregulation in mixed lesions with foamy microglia than those with ramified microglia, both in the border and the peri-lesion region. Further studies are necessary to understand what cells are accumulating iron in MS pathology,

and what the functional effect is. Iron chelators such as desferrioxamine (DFO) suppress ferroptosis by reducing the availability of iron, and may be an interesting therapeutic target [89]. Alternatively, blocking nuclear receptor coactivator 4 (NCOA4) through compound 9a, should prevent the delivery of iron-bound ferritin to autophagosomes for lysosomal degradation and ferrous iron release [90].

A common mechanism of disease progression in both the first and second part of this thesis is Ig. Ig are found near microglia nodules, where they may be involved in breaking the immune tolerance of microglia and activating the complement cascade. Furthermore, Ig production is more prevalent in mixed lesions with foamy microglia than in those with ramified microglia, and depending on the target of the Ig produced this may promote ongoing demyelination. The opsonized structures were heterogenic between donors, and this may translate into a different pathological or clinical development of MS. Therefore, it would be interesting to study the target of Ig found intrathecal, and to see if the same targets are opsonized in the brain. B cells are a well-known target for therapeutic intervention. Anti-CD20-mediated B-cell depletion, through rituximab, ocrelizumab, or ofatumumab, has a high level of success in limiting new events in relapsing MS. However, CD20 is not expressed on plasma cells, therefore immunoglobulin levels remain above the normal range after treatment [91]. Our data indicates that anti-CD79a-mediated B-cell depletion may be a more promising avenue. However, such monoclonal antibodies have poor blood-brain barrier penetrance [92], and effects within the brain may therefore be limited. Alternatively, Bruton tyrosine kinase (BTK) inhibitors are CNS-penetrant, and can target the maturation, survival, migration and activation of B cells and microglia. BTK inhibitors may therefore be a promising therapeutic approach, and are currently undergoing clinical trials [93].

We show that in lesions that are likely not expanding, there is more myelin stability and maintenance, and more axonal health, compared to lesions that are likely expanding. Genes involved in these processes that were higher expressed in the border of mixed lesions with ramified microglia compared to the border of mixed lesions with foamy microglia may provide interesting therapeutic targets to promote regeneration and remyelination, and inhibit lesion expansion. Among these genes are *QKI*, *ABCA2*, *APOD, BCAS1,* and *BOK*. Functional implications of up- or downregulation of these genes needs to be tested *in vitro* and *ex vivo*, before being tested *in vivo*.

Lastly, in the studies described in this thesis, we have capitalized on recent exciting revolutions in transcriptomics techniques that have now reached unprecedented resolution and sensitivity. In addition, we applied high- and ultra-resolution

microscopy. We have focused on optimizing protocols to apply these techniques on post-mortem human brain tissue. We adapted the protocol for cryo-tissue, and achieved high-resolution immunofluorescence visualization using super-resolution confocal microscopy and semi-automatic quantification with Imaris software. Possibly, future immunofluorescent studies may benefit from the use of multispectral light-emitting diodes (mLEDs) to minimize autofluorescence [94]. We successfully visualized and quantitatively characterized the axon-myelin unit at an ultrastructural level using transmission electron microscopy (EM). For future studies, scanning EM and 3D reconstruction of consecutive images could uncover additional interesting structures in the human brain [95]. Cryo-EM may reduce some fixation artefacts [96], and correlative-light-EM will facilitate the identification and characterization of specific interactions and regions of interest [97]. Lastly, we performed transcriptome-wide spatial transcriptomics at single-cell resolution. Various platforms are now commercially available, each with its own advantages and limitations. Some platforms offer genome-wide analysis, while others are probe-based approaches. StereoSeq (BGI) and Visium (10X Genomics) are genome-wide, whereas MERFISH (Vizgen), ISS (Cartana), and GeoMX DSP (Nanostring Technologies) are panel-based. The capturing area also varies. While most platforms offer a broad range of (customizable) chip sizes, those of Visium are limited to 6.5 x 6.5 mm, although each slide contains multiple chips, allowing multiple regions of interest to be sequenced per slide, which is cost-effective. The resolution varies significantly between platforms. Of the genome-wide platforms, StereoSeq offers the highest resolution, with capture sports of 200 nm. Visium on the other hand, has capture spots of 55 µm, and the recently launched Visium HD as capture spots of 2 x 2 µm. Because of its subcellular resolution, StereoSeq requires binning multiple spots based on an ssDNA image to achieve single-cell resolution, which poses bioinformatic challenges, whereas Visium will encompass multiple cells within a single spot. Results of both Visium and Visium HD are dependent on cellular density. Among the panel-based platforms, MERFISH provides single-molecule resolution, ISS offers single-cell resolution, and GeoMX DSP can achieve resolution as low as 10 µm. For our spatial transcriptomics project, we required discovery driven genome-wide analysis of large regions with varying cellular densities, therefore StereoSeq was the optimal choice. However, depending on the specific research question and tissue selection, other platforms might be more appropriate for other research questions. Continuous technological advancements in spatial transcriptomics hold significant promise for the future.

"Whereof one cannot speak, thereof one must be silent."
*Ludwig Wittgenstein*

## REFERENCES


1. Lassmann, H., Van Horssen, J. & Mahad, D. Progressive multiple sclerosis: Pathology and pathogenesis. *Nat. Rev. Neurol.* 8, 647–656 (2012).
2. Miller, D. H., Johnson, G., Tofts, P. S., Macmanus, D. & McDonald, W. I. Precise relaxation time measurements of normal-appearing white matter in inflammatory central nervous system disease. *Magn. Reson. Med.* 11, 331–336 (1989).
3. De Groot, C. J. A. *et al.* Post-mortem MRI-guided sampling of multiple sclerosis brain lesions: Increased yield of active demyelinating and (p)reactive lesions. *Brain* 124, 1635–1645 (2001).
4. Moll, N. M. *et al.* Multiple sclerosis normal-appearing white matter: Pathology-imaging correlations. *Ann. Neurol.* 70, 764–773 (2011).
5. Elliott, C. *et al.* Abnormalities in normal-appearing white matter from which multiple sclerosis lesions arise. *Brain Commun.* 3, (2021).
6. van der Poel, M. *et al.* Transcriptional profiling of human microglia reveals grey–white matter heterogeneity and multiple sclerosis-associated changes. *Nat. Commun.* 10, 1–13 (2019).
7. Hammond, T. R. *et al.* Single-Cell RNA Sequencing of Microglia throughout the Mouse Lifespan and in the Injured Brain Reveals Complex Cell-State Changes. *Immunity* 50, 253-271.e6 (2019).
8. Masuda, T. *et al.* Spatial and temporal heterogeneity of mouse and human microglia at single-cell resolution. *Nature* 566, 388–392 (2019).
9. Paolicelli, R. C. *et al.* Microglia states and nomenclature: A field at its crossroads. *Neuron* 110, 3458–3483 (2022).
10. Zrzavy, T. *et al.* Loss of 'homeostatic' microglia and patterns of their activation in multiple sclerosis. *Brain* 140, 1900–1913 (2017).
11. Koning, N., Swaab, D. F., Hoek, R. M. & Huitinga, I. Distribution of the immune inhibitory molecules CD200 and CD200R in the normal central nervous system and multiple sclerosis lesions suggests neuron-glia and glia-glia interactions. *J. Neuropathol. Exp. Neurol.* 68, 159–167 (2009).
12. Koning, N., Bö, L., Hoek, R. M. & Huitinga, I. Downregulation of macrophage inhibitory molecules in multiple sclerosis lesions. *Ann. Neurol.* 62, 504–514 (2007).
13. Valente, T., Serratosa, J., Perpiñá, U., Saura, J. & Solà, C. Alterations in CD200-CD200R1 system during EAE already manifest at presymptomatic stages. *Front. Cell. Neurosci.* 11, 1–15 (2017).
14. Meuth, S. G. *et al.* CNS inflammation and neuronal degeneration is aggravated by impaired CD200-CD200R-mediated macrophage silencing. *J. Neuroimmunol.* 194, 62–69 (2008).
15. Hoek, R. H. *et al.* Down-regulation of the macrophage lineage through interaction with OX2 (CD200). *Science (80-. ).* 290, 1768–1771 (2000).
16. Lassmann, H. Pathogenic mechanisms associated with different clinical courses of multiple sclerosis. *Front. Immunol.* 10, 1–14 (2019).
17. van Olst, L. *et al.* Meningeal inflammation in multiple sclerosis induces phenotypic changes in cortical microglia that differentially associate with neurodegeneration. *Acta Neuropathol.* 141, 881–899 (2021).
18. Hendrickx, D. A. E., Schuurman, K. G., van Draanen, M., Hamann, J. & Huitinga, I. Enhanced uptake of multiple sclerosis-derived myelin by THP-1 macrophages and primary human microglia. *J. Neuroinflammation* 11, 1–11 (2014).

19. Teo, W. *et al.* Nile Red fluorescence spectroscopy reports early physicochemical changes in myelin with high sensitivity. *Proc. Natl. Acad. Sci. U. S. A.* 118, 1–11 (2021).
20. Wheeler, D., Bandaru, V. V. R., Calabresi, P. A., Nath, A. & Haughey, N. J. A defect of sphingolipid metabolism modifies the properties of normal appearing white matter in multiple sclerosis. *Brain* 131, 3092–3102 (2008).
21. Gallego-Delgado, P. *et al. Neuroinflammation in the normal-appearing white matter (NAWM) of the multiple sclerosis brain causes abnormalities at the nodes of Ranvier. PLoS Biology* vol. 18 (2020).
22. Moscatelli, E. A. & Isaacson, E. Gas liquid chromatographic analysis of sphingosine bases in sphingolipids of human normal and multiple sclerosis cerebral white matter. *Lipids* 4, 550–555 (1969).
23. Caprariello, A. V. *et al.* Biochemically altered myelin triggers autoimmune demyelination. *Proc. Natl. Acad. Sci. U. S. A.* 115, 5528–5533 (2018).
24. Waxman, S. *Multiple Sclerosis as A Neuronal Disease. Multiple Sclerosis as A Neuronal Disease* (Elsevier Inc., 2005). doi:10.1016/B978-0-12-738761-1.X5000-7.
25. Wang, B. *et al.* Mitochondrial Behavior in Axon Degeneration and Regeneration. *Front. Aging Neurosci.* 13, 1–17 (2021).
26. Youle, R. J. & Van Der Bliek, A. M. Mitochondrial Fission, Fusion, and Stress. *Science (80-. ).* 337, 1062–1065 (2012).
27. Gottlieb, R. A. *et al.* At the heart of mitochondrial quality control: many roads to the top. *Cell. Mol. Life Sci.* 78, 3791–3801 (2021).
28. Licht-Mayer, S. *et al.* Enhanced axonal response of mitochondria to demyelination offers neuroprotection: implications for multiple sclerosis. *Acta Neuropathol.* 140, 143–167 (2020).
29. Rosenkranz, S. C. *et al.* Enhancing mitochondrial activity in neurons protects against neurodegeneration in a mouse model of multiple sclerosis. *Elife* 10, 1–60 (2021).
30. Kozin, M. S., Kulakova, O. G. & Favorova, O. O. Involvement of Mitochondria in Neurodegeneration. *Biochemistry* 83, 1002-1021. (2018).
31. Haider, L. *et al.* Oxidative damage in multiple sclerosis lesions. *Brain* 134, 1914–1924 (2011).
32. Sanders, V., Conrad, A. J. & Tourtellotte, W. W. On classification of post-mortem multiple sclerosis plaques for neuroscientists. *J. Neuroimmunol.* 46, 207–216 (1993).
33. Li, H., Newcombe, J., Groome, N. P. & Cuzner, M. L. Characterization and distribution of phagocytic macrophages in multiple sclerosis plaques. *Neuropathol. Appl. Neurobiol.* 19, 214–223 (1993).
34. Prineas, J. W. *et al.* Immunopathology of secondary-progressive multiple sclerosis. *Ann. Neurol.* 50, 646–657 (2001).
35. Barnett, M. H., Parratt, J. D. E., Cho, E. S. & Prineas, J. W. Immunoglobulins and complement in postmortem multiple sclerosis tissue. *Ann. Neurol.* 65, 32–46 (2009).
36. van Noort, J. M. *et al.* Preactive multiple sclerosis lesions offer novel clues for neuroprotective therapeutic strategies. *CNS Neurol. Disord. Drug Targets* 10, 68–81 (2011).
37. Singh, S. *et al.* Microglial nodules in early multiple sclerosis white matter are associated with degenerating axons. *Acta Neuropathol.* 125, 595–608 (2013).

38. Bsibsi, M. *et al.* Alpha-B-crystallin induces an immune-regulatory and antiviral microglial response in preactive multiple sclerosis lesions. *J. Neuropathol. Exp. Neurol.* 72, 970–979 (2013).
39. Sato, F. *et al.* 'Microglial nodules' and 'newly forming lesions' may be a Janus face of early MS lesions; implications from virus-induced demyelination, the Inside-Out model. *BMC Neurol.* 15, 1–6 (2015).
40. Hendrickx, D. A. E., van Eden, C. G., Schuurman, K. G., Hamann, J. & Huitinga, I. Staining of HLA-DR, Iba1 and CD68 in human microglia reveals partially overlapping expression depending on cellular morphology and pathology. *J. Neuroimmunol.* 309, 12–22 (2017).
41. Prineas, J. W. & Parratt, J. D. E. Multiple Sclerosis: Microglia, Monocytes, and Macrophage-Mediated Demyelination. *J. Neuropathol. Exp. Neurol.* 80, 975–996 (2021).
42. Michailidou, I. *et al.* Complement C3 on microglial clusters in multiple sclerosis occur in chronic but not acute disease: Implication for disease pathogenesis. *Glia* 65, 264–277 (2017).
43. Hendrickx, D. A. E. *et al.* Selective upregulation of scavenger receptors in and around demyelinating areas in multiple sclerosis. *J. Neuropathol. Exp. Neurol.* 72, 106–118 (2013).
44. Burm, S. M. *et al.* Expression of IL-1β in rhesus EAE and MS lesions is mainly induced in the CNS itself. *J. Neuroinflammation* 13, (2016).
45. Horssen, J. Van *et al.* Clusters of activated microglia in normal-appearing white matter show signs of innate immune activation. *J. Neuroinflammation* 9, (2012).
46. van der Poel, M., Hoepel, W., Hamann, J., Huitinga, I. & Dunnen, J. den. IgG Immune Complexes Break Immune Tolerance of Human Microglia. *J. Immunol.* 205, 2511–2518 (2020).
47. Lublin, F. D. *et al.* Defining the clinical course of multiple sclerosis, The 2013 revisions. *Neurology* 83, 278–286 (2014).
48. Cagol, A. *et al.* Association of brain atrophy with disease progression independent of relapse activity in patients with relapsing multiple sclerosis. *JAMA Neurol* 79, 682–692 (2022).
49. Blok, K. M. *et al.* Disease activity in primary progressive multiple sclerosis: a systematic review and meta-analysis. *Front. Neurol.* 14, (2023).
50. Hemond, C. C. & Bakshi, R. Magnetic resonance imaging in multiple sclerosis. *Cold Spring Harb. Perspect. Med.* 8, 1–21 (2018).
51. Rovira, A., Auger, C. & Alonso, J. Magnetic resonance monitoring of lesion evolution in multiple sclerosis. *Ther. Adv. Neurol. Disord.* 6, 298–310 (2013).
52. Kuhlmann, T. *et al.* Multiple sclerosis progression: time for a new mechanism-driven framework. *Lancet Neurol.* 22, 78–88 (2023).
53. Luchetti, S. *et al.* Progressive multiple sclerosis patients show substantial lesion activity that correlates with clinical disease severity and sex: a retrospective autopsy cohort analysis. *Acta Neuropathol.* 135, 511–528 (2018).
54. Grajchen, E., Hendriks, J. J. A. & Bogie, J. F. J. The physiology of foamy phagocytes in multiple sclerosis. *Acta Neuropathol. Commun.* 6, 124 (2018).
55. Cantuti-Castelvetri, L. *et al.* Defective cholesterol clearance limits remyelination in the aged central nervous system. *Science (80-. ).* 359, 684–688 (2018).
56. Kirby, L. *et al.* Oligodendrocyte precursor cells present antigen and are cytotoxic targets in inflammatory demyelination. *Nat. Commun.* 10, 1–20 (2019).
57. Bogers, L. *et al.* Selective emergence of antibody-secreting cells in the multiple sclerosis brain. *eBioMedicine* 89, 104465 (2023).

58. Smolders, J. *et al.* Tissue-resident memory T cells populate the human brain. *Nat. Commun.* 9, 1–14 (2018).
59. van Langelaar, J., Rijvers, L., Smolders, J. & van Luijn, M. M. B and T Cells Driving Multiple Sclerosis: Identity, Mechanisms and Potential Triggers. *Front. Immunol.* 11, 1–12 (2020).
60. Hsiao, C. C. *et al.* White matter lesions in multiple sclerosis are enriched for CD20dim CD8+ tissue-resident memory T cells. *Eur. J. Immunol.* 51, 483–486 (2021).
61. Fransen, N. L. *et al.* Absence of B Cells in Brainstem and White Matter Lesions Associates With Less Severe Disease and Absence of Oligoclonal Bands in MS. *Neurol. Neuroimmunol. NeuroInflammation* 8, 1–11 (2021).
62. Absinta, M. *et al.* A lymphocyte–microglia–astrocyte axis in chronic active multiple sclerosis. *Nature* 597, 709–714 (2021).
63. Hsiao, C. C. *et al.* Osteopontin associates with brain TRM-cell transcriptome and compartmentalization in donors with and without multiple sclerosis. *iScience* 26, (2023).
64. Ziemssen, T., Akgün, K. & Brück, W. Biomarkers in multiple sclerosis. *J. Neuroinflammation* 9, 1–11 (2019).
65. Ramaglia, V. *et al.* The membrane attack complex of the complement system is essential for rapid Wallerian degeneration. *J. Neurosci.* 27, 7663–7672 (2007).
66. Patani, R., Balaratnam, M., Vora, A. & Reynolds, R. Remyelination can be extensive in multiple sclerosis despite a long disease course. *Neuropathol. Appl. Neurobiol.* 33, 277–287 (2007).
67. Heß, K. *et al.* Lesion stage-dependent causes for impaired remyelination in MS. *Acta Neuropathol.* 140, 359–375 (2020).
68. Plemel, J. R., Manesh, S. B., Sparling, J. S. & Tetzlaff, W. Myelin inhibits oligodendroglial maturation and regulates oligodendrocytic transcription factor expression. *Glia* 61, 1471–1487 (2013).
69. Kotter, M. R., Zhao, C., Van Rooijen, N. & Franklin, R. J. M. Macrophage-depletion induced impairment of experimental CNS remyelination is associated with a reduced oligodendrocyte progenitor cell response and altered growth factor expression. *Neurobiol. Dis.* 18, 166–175 (2005).
70. Kotter, M. R., Li, W. W., Zhao, C. & Franklin, R. J. M. Myelin impairs CNS remyelination by inhibiting oligodendrocyte precursor cell differentiation. *J. Neurosci.* 26, 328–332 (2006).
71. Patsopoulos, N. A. Genetics of multiple sclerosis: An overview and new directions. *Cold Spring Harb. Perspect. Med.* 8, 1–11 (2018).
72. Sawcer, S., Franklin, R. J. M. & Ban, M. Multiple sclerosis genetics. *Lancet Neurol.* 13, 700–709 (2014).
73. Nourbakhsh, B. & Mowry, E. M. Multiple sclerosis risk factors and pathogenesis. *Contin. Lifelong Learn. Neurol.* 25, 596–610 (2019).
74. Patsopoulos, N. A. *et al.* Multiple sclerosis genomic map implicates peripheral immune cells and microglia in susceptibility. *Science (80-. ).* 365, 7188 (2019).
75. Hafler, D. A. *et al.* Risk Alleles for Multiple Sclerosis Identified by a Genomewide Study. *N. Engl. J. Med.* 357, 861–862 (2007).
76. De Bakker, P. I. W. *et al.* A high-resolution HLA and SNP haplotype map for disease association studies in the extended human MHC. *Nat. Genet.* 38, 1166–1172 (2006).
77. George, M. F. *et al.* Multiple sclerosis risk loci and disease severity in 7,125 individuals from 10 studies. *Neurol. Genet.* 2, 1–11 (2016).

78. Harroud, A. *et al.* Locus for severity implicates CNS resilience in progression of multiple sclerosis. *Nature* 619, 323–331 (2023).
79. Glover, L. & Brown, R. H. Dysferlin in membrane trafficking and patch repair. *Traffic* 8, 785–794 (2007).
80. Zhu, Y., Wang, G. Z., Cingöz, O. & Goff, S. P. NP220 mediates silencing of unintegrated retroviral DNA. *Nature* 564, 278–282 (2018).
81. Malekmohammad, K., Sewell, R. D. E. & Rafieian-Kopaei, M. Antioxidants and atherosclerosis: Mechanistic aspects. *Biomolecules* 9, 1–19 (2019).
82. Moezzi, D. *et al.* Expression of antioxidant enzymes in lesions of multiple sclerosis and its models. *Sci. Rep.* 12, 1–13 (2022).
83. Kasai, S., Shimizu, S., Tatara, Y., Mimura, J. & Itoh, K. Regulation of Nrf2 by mitochondrial reactive oxygen species in physiology and pathology. *Biomolecules* 10, (2020).
84. Peruzzotti-Jametti, L., Willis, C. M., Hamel, R., Krzak, G. & Pluchino, S. Metabolic Control of Smoldering Neuroinflammation. *Front. Immunol.* 12, 1–16 (2021).
85. Peruzzotti-Jametti, L. *et al.* Mitochondrial complex I activity in microglia sustains neuroinflammation. *Nature* (2024) doi:10.1038/s41586-024-07167-9.
86. Popescu, B. F. *et al.* Pathogenic implications of distinct patterns of iron and zinc in chronic MS lesions. *Acta Neuropathol.* 134, 45–64 (2017).
87. Kao, J. K. *et al.* Chronic iron overload results in impaired bacterial killing of THP-1 derived macrophage through the inhibition of lysosomal acidification. *PLoS One* 11, 1–16 (2016).
88. Lassmann, H. & Van Horssen, J. The molecular basis of neurodegeneration in multiple sclerosis. *FEBS Lett.* 585, 3715–3723 (2011).
89. Li, Z. *et al.* Iron Neurotoxicity and Protection by Deferoxamine in Intracerebral Hemorrhage. *Front. Mol. Neurosci.* 15, 1–6 (2022).
90. Fang, Y. *et al.* Inhibiting Ferroptosis through Disrupting the NCOA4-FTH1 Interaction: A New Mechanism of Action. *ACS Cent. Sci.* 7, 1–10 (2021).
91. Hauser, Stephen, L. *et al.* B-Cell Depletion with Rituximab in Relapsing–Remitting Multiple Sclerosis. *N. Engl. J. Med.* 358, 676–88 (2008).
92. Kouhi, A. *et al.* Brain disposition of antibody-based therapeutics: Dogma, approaches and perspectives. *Int. J. Mol. Sci.* 22, 1–24 (2021).
93. Krämer, J., Bar-Or, A., Turner, T. J. & Wiendl, H. Bruton tyrosine kinase inhibitors for multiple sclerosis. *Nat. Rev. Neurol. 2023 195* 19, 289–304 (2023).
94. Adeniyi, P. A. *et al.* Multispectral LEDs Eliminate Lipofuscin-Associated Autofluorescence for Immunohistochemistry and CD44 Variant Detection by in Situ Hybridization in Aging Human, non-Human Primate, and Murine Brain. doi:10.1177/17590914221123138.
95. Shapson-Coe, A. *et al.* A petavoxel fragment of human cerebral cortex reconstructed at nanoscale resolution. *Science* 384, eadk4858 (2024).
96. Stewart, P. L. Cryo-electron microscopy and cryo-electron tomography of nanoparticles. *Wiley Interdiscip. Rev. Nanomedicine Nanobiotechnology* 9, 1–16 (2017).
97. De Boer, P., Hoogenboom, J. P. & Giepmans, B. N. G. Correlated light and electron microscopy: ultrastructure lights up! *Nat. Methods 2015 126* 12, 503–513 (2015).

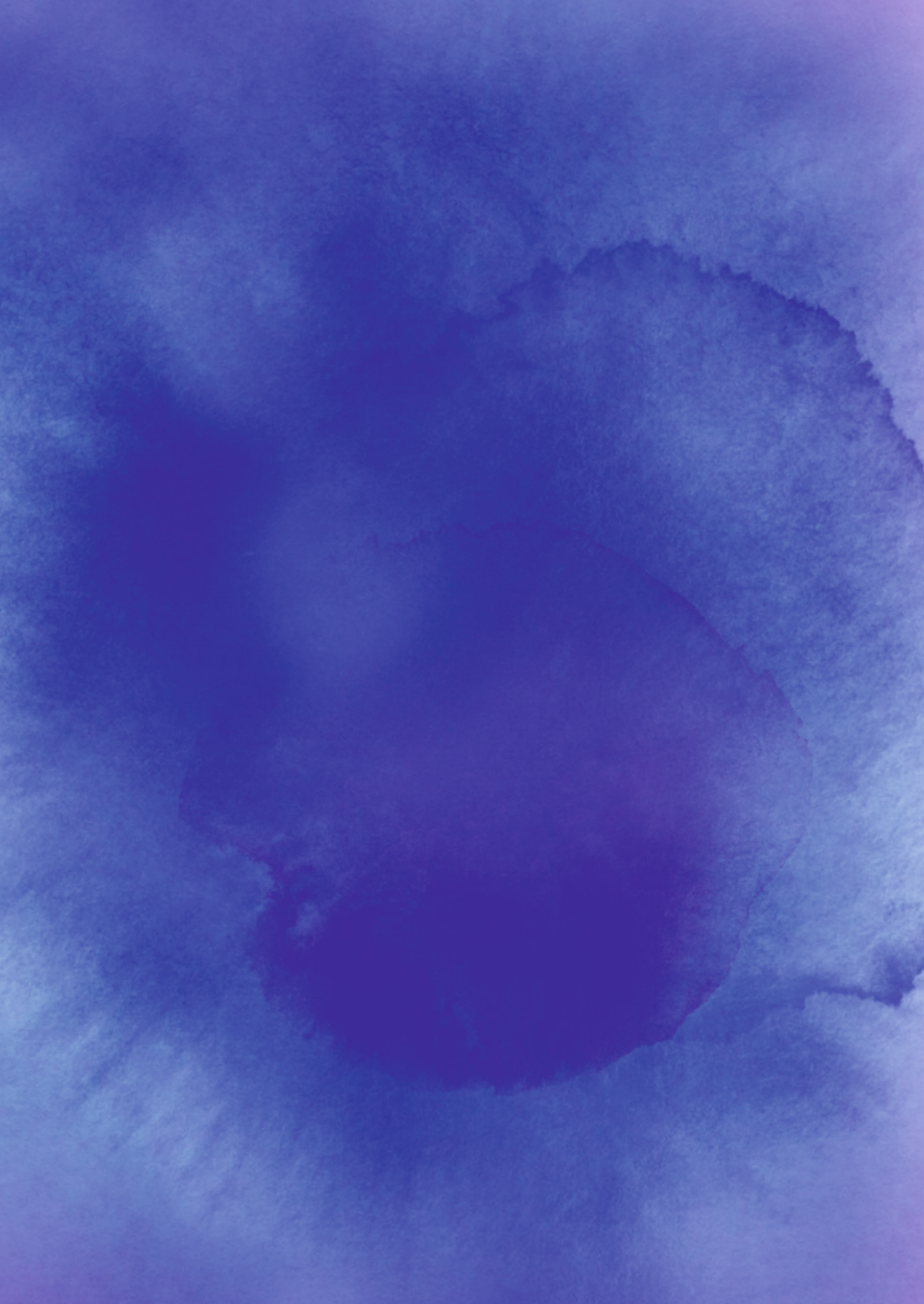

# CHAPTER 11

# Appendices

# ENGLISH SUMMARY

## PROGRESSION OF MULTIPLE SCLEROSIS: THE ROLE OF MICROGLIA AND NEURONS

Multiple sclerosis (MS) is a neuroinflammatory disorder, in which focal, demyelinating lesions occur throughout the central nervous system (CNS). Due to a lack of comprehensive understanding of the molecular mechanisms of lesion formation and lesion progression, there is a lack of effective biomarkers to track disease progression. This is an unmet clinical need for therapeutics that halt or reverse disease progression. This thesis aims to elucidate pathological mechanisms driving MS progression, with a particular focus on the roles of microglia and neurons. In **part 1**, we focus on lesion formation. As new lesions arise from the normal-appearing tissue, we investigate changes that occur in this seemingly normal tissue prior to apparent lesion formation. By understanding these early changes, we aim to identify triggers that initiate the development of new lesions and to identify molecular pathways that are associated with lesion formation. **In part 2**, we focus on pathological heterogeneity and lesion dynamics. We compare mixed lesions with ramified microglia to mixed lesions with foamy microglia, to unravel molecular pathways involved in lesion expansion and failure of remyelination. **In part 3**, we focus on genetic susceptibility for disease progression. We compare MS relevant pathology of homozygous carriers for the risk single nucleotide polymorphism (SNP) rs10191329 with homozygous non-risk carriers, to biologically validate the SNP and to elucidate mechanisms driving disease progression.

### Part 1: Loss of microglia homeostasis can lead to initiation of lesion formation

CD200 and CD47 are checkpoint molecules expressed by neurons and oligodendrocytes that keep microglia in a homeostatic state. In **chapter 2,** we show that CD200 expression compared to control grey matter (GM) was lower in normal-appearing GM (NAGM) in MS, and that CD200 and CD47 expression was lower in peri-lesion grey matter and in grey matter lesions. Downregulation could imply that the microglia are less inhibited and more prone to become reactive. Thus, CD200 may play a role in lesion formation, whereas both CD200 and CD47 may play a role in lesion expansion. We then correlated CD200 expression with pathology throughout the CNS. CD200 was negatively correlated with cortical lesion rate and with the proportion of active and mixed active/inactive lesions, and positively correlated with the proportion of inactive lesions. Together, this suggests that CD200 is indeed associated with lesion formation as well as with the ongoing demyelinating activity of lesions.

In **chapter 3,** we characterized the axon-myelin unit in normal-appearing white matter (NAWM) on the ultrastructural level. We found that the paranodes and juxtaparanodes were elongated in MS NAWM compared to control white matter (WM), and that these regions were overlapping. With electron microscopy, we show that the myelin was wrapped less compact. Together, this may result in a higher axonal energy demand to generate axon potentials. Indeed, we show that the axonal mitochondria density was higher in NAWM compared to control WM. This can lead to pathological production of reactive oxygen species (ROS). This ROS can oxidize myelin, which may contribute to initiation of demyelination. As the ultrastructural alterations were correlated to the density of activated or phagocytic microglia and to the density of activated T cells, it is likely that local inflammation contributes to these early alterations to the axon-myelin unit.

In **chapter 4,** we identified mechanisms of lesion formation by profiling microglia nodules in the (NA)WM in MS and stroke. We show that microglia nodules in MS had a similar gene expression as actively demyelinating MS lesions. Microglia nodules in MS compared to in stroke more often resided in an inflammatory environment, as they were in close contact with activated T cells and immunoglobulin producing B cells. Microglia nodules in MS were associated with early demyelination, as 1) they had often phagocytosed oxidized phospholipids, 2) their gene expression indicated that they are involved in lipid metabolism, and 3) some microglia nodules encapsulated partially demyelinated axons. Co-stimulation of microglia nodules in MS by oxidized phospholipids and either proinflammatory cytokines or immunoglobulin may result in a hypermetabolic and hyperinflammatory phenotype. The gene expression profile of microglia nodules in MS and the fusion of the mitochondrial network together indeed indicate that the microglia nodules may be hypermetabolic and hyperinflammatory, which can contribute to the progression of a microglia nodules in MS into a full MS lesion.

Taken together, data presented in the first part of this thesis indicates that in the normal-appearing tissue, loss of homeostasis of microglia, likely due to a loss of CD200, and decompaction of myelin sheaths precede lesion formation, and that microglia nodules are the first starting point of MS lesions.



**Part 2: Lesions with foamy microglia are expanding and lesions with ramified microglia are regenerative**

In **chapter 5,** we performed exploratory factor analysis on quantitative and qualitative neuropathology data. We identified three independent dimensions of MS pathology that were validated with clinical, genetic, and neuropathological data. The first dimension was associated with higher proportions of active and mixed lesions, B- and T-cell presence, neuroaxonal damage, and a more

severe disease. This first dimension likely represents demyelination and immune cell activity associated with pathological and clinical progression. The second dimension was associated with a high proportion of active lesions, ramified microglia, reactive sites, the presence of nodules, and with genetic MS risk variants. This second dimension likely represents microglia activity and lesion formation initiation. The third dimension was associated with a higher proportion of mixed and inactive lesions, a lower proportion of remyelinated lesions, low involvement of the adaptive immune system, and low levels of acute axonal damage. This third dimension likely represents loss of lesion activity and scar formation. Together, our findings highlight the intricate interplay between multiple pathological characteristics and their contribution to disease progression.

In **chapter 6,** we explored the pathological correlate of the biomarker neurofilament light chain (NfL). As NfL is a major component of the neuronal cytoskeleton, the level of NfL in the CSF is indicative of the level of acute neuro-axonal damage. As expected, we found that the level of NfL was positively correlated to the degree of axonal loss and acute axonal stress in the normal-appearing white matter of the pyramid tract. We furthermore found that the level of NfL was positively correlated with the proportion of active and of mixed lesions with foamy microglia, and not to those with ramified microglia. In line with this, we showed with immunohistochemistry that there was a higher level of acute axonal stress (measured with $APP^{+}$ axonal fragments and bulbs) in active and mixed lesions with foamy microglia compared to those with ramified microglia. Together, our data indicates that lesions with foamy microglia are associated with more axonal damage and stress than lesions with ramified microglia, which may have implications for MS lesion dynamics.

In **chapter 7,** we performed spatial transcriptomics on mixed lesions with ramified microglia and on mixed lesions with foamy microglia. We identified distinct cellular and molecular mechanisms of lesion expansion and failure of remyelination. Mixed lesions with foamy microglia were characterized by enrichment of lymphocytes and immune-oligodendrocytes, immunoglobulin production, complement activation, iron dysregulation, and demyelination. Conversely, mixed lesions with ramified microglia were associated with axonal regeneration and growth, myelin stability, and remyelination. Our data has shed light on the cellular and molecular mechanisms driving lesion expansion and failure of repair in MS.

Taken together, in the second part of this thesis, we have highlighted the complex interplay between pathological characteristics in the MS brain, and we have identified cellular and molecular pathways of lesion dynamics contributing to lesion expansion and failure of remyelination.

**Part 3: Genetic susceptibility for clinical severity is associated with more severe pathology**

In the third part of this thesis, we aimed to biologically validate the severity SNP rs10191329 in the *DYSF-ZNF638* locus recently identified by the International Multiple Sclerosis Genetics Consortium and to identify possible mechanisms underlying disease progression in homozygous risk carriers.

The SNP rs10191329 is the first known SNP to be associated with a more severe clinical disease in MS. Homozygous risk carriers have a shorter time to requiring a walking aid compared to homozygous non-risk carriers and heterozygous risk carriers. In **chapter 8,** we found that homozygous carriership of SNP rs10191329 was associated with increased brainstem and cortical pathology. Therefore, our data validate the biological relevance of the risk SNP rs10191329.

In **chapter 9,** we found that homozygous risk carriers compared to homozygous non-risk carriers for the risk SNP rs10191329 had a higher proportion of active and mixed lesions with specifically foamy microglia, a higher abundance of lesional T cells, and more acute axonal stress and neuronal loss. As rs10191329 is in the *DYSF-ZNF638* locus, it is possible that dysferlin and ZNF638 play a role in disease progression in MS. In homozygous risk carriers we found an increased density of $DYSF^+$ cells in the normal-appearing grey matter and of $ZNF638^+$ oligodendrocytes in the normal-appearing white matter. Neurons and oligodendrocytes had higher mitochondrial gene expression, implying more cellular stress, in homozygous risk carriers compared to homozygous non-risk carriers. Our findings indicate that homozygous risk carriers have an increased susceptibility to tissue damage.

Taken together, in the third part of this thesis, we have biologically validated the severity SNP rs10191329, and our data implies involvement of ZNF638 and dysferlin in MS disease progression.



## CONCLUSION

In conclusion, this thesis elucidates the critical roles of microglia and neurons in the progression of MS. By investigating lesion formation, pathological heterogeneity, and genetic susceptibility, we have identified key molecular triggers and pathways involved in MS pathology. This research reveals the importance of microglia homeostasis and compact myelin, the dynamics of lesion expansion, and the impact of genetic risk factors on disease severity. These insights contribute to a deeper understanding of MS progression and may guide the development of new biomarkers and therapeutic strategies to better manage and treat people with MS.

# NEDERLANDSE SAMENVATTING

## PROGRESSIE VAN MULTIPELE SCLEROSE: DE ROL VAN MICROGLIA EN NEURONEN

Multipele sclerose (MS) is een neuro-inflammatoire aandoening, waarbij er demyeliniserende laesies ontstaan in het centrale zenuwstelsel. Vanwege een tekort aan kennis van de moleculaire mechanismen achter laesie formatie en laesie progressie, is er ook een tekort aan toepasselijke biomarkers om ziekte progressie te monitoren, en zijn er geen therapieën beschikbaar die ziekte progressie tegengaan of kunnen omkeren. Het doel van dit proefschrift is om pathologische mechanismen die ziekte progressie drijven te ontmaskeren, specifiek gericht op de rol van microglia en neuronen. In **deel 1** richten we ons op laesie formatie. Gezien nieuwe laesies uit het normaal-ogende weefsel ontstaan, onderzoeken we veranderingen die in het normaal-ogende weefsel zijn ontstaan voordat er laesies zijn gevormd. Door deze vroege veranderingen in het weefsel in kaart te brengen, kunnen we onderzoeken wat mogelijk de aanleidingen van laesie formatie zijn, en kunnen we moleculaire mechanismes die geassocieerd zijn met laesie formatie identificeren. In **deel 2** onderzoeken we pathologische heterogeniteit en laesie transitie. Microglia zijn zeer dynamische cellen, die snel op stimuli kunnen reageren. Geactiveerde microglia hebben een spectrum aan morfologie die ze kunnen aannemen, met aan het ene uiteinde een vertakte, ramified morfologie, en aan het andere uiteinde van het spectrum een ronde, foamy morfologie waarbij de microglia lipiden hebben opgenomen. Om de moleculaire mechanismen te ontrafelen die betrokken zijn bij laesie uitbreiding en het falen van remyelinisatie, vergelijken we laesies met ramified microglia met laesies met foamy microglia,. In **deel 3** richten we ons op de genetische predispositie voor ziekte progressie. Onlangs is gevonden dat een homozygote mutatie (SNP) in het rs10101329 locus is geassocieerd met snellere klinische ziekte progressie. In dit deel van het proefschrift vergelijken wij MS relevante pathologie van homozygote risico dragers voor de SNP rs10191329 met homozygote non-risico dragers om deze SNP biologisch te valideren en om mechanismen achter ziekte progressie te ontdekken.

### Deel 1: Verlies van microglia homeostase kan leiden tot initiatie van laesie formatie

CD200 en CD47 zijn beide checkpoint moleculen die door neuronen en oligodendrocyten tot expressie worden gebracht om microglia in een homeostatische staat te houden. In **hoofdstuk 2** laten we zien dat CD200 expressie lager is in MS normaal-ogende grijze stof vergeleken met controle grijze stof, en dat vergeleken met MS normaal-ogende grijze stof expressie

van CD200 en CD47 lager is in de peri-laesie grijze stof en in grijze stof laesies. Lagere expressie van deze moleculen kan impliceren dat de microglia minder geïnhibeerd zijn en daardoor makkelijker te activeren zijn. CD200 zou daarom een rol kunnen spelen in laesie formatie, en CD200 en CD47 zouden beiden een rol kunnen spelen in laesie expansie. CD200 is negatief gecorreleerd met de hoeveelheid corticale laesies en met de proportie van actieve en gemixte laesies in de witte stof, en positief gecorreleerd met de proportie inactieve laesies in de witte stof. Samen suggereert dit dat CD200 inderdaad is geassocieerd met laesie formatie en met voortdurende demyeliniserende activiteit van laesies.

In **hoofdstuk 3** hebben we de axon-myeline eenheid in de MS normaal-ogende witte stof gekarakteriseerd. We hebben gevonden dat de paranodale en juxtaparanodale regio's langer zijn in MS normaal-ogende witte stof vergeleken met controle witte stof, en dat deze regio's meer overlap hebben. Met elektronenmicroscopie hebben we laten zien dat de myeline minder compact om de axonen gewikkeld zit. Samen zou dit kunnen betekenen dat er een hogere energie nodig is voor het axon om een actiepotentiaal te genereren. We laten zien dat er inderdaad een hogere dichtheid is van axonale mitochondria in MS normaal-ogende witte stof dan in controle witte stof. Dit zou kunnen leiden tot pathologische hoeveelheden vrije zuurstof radicalen, die myeline kunnen oxideren wat weer kan bijdragen aan initiatie tot demyelinisatie. Aangezien de ultra-structurele alteraties zijn gecorreleerd met de dichtheid van geactiveerde of phagocyterende microglia en met de dichtheid van T cellen, is het mogelijk dat lokale inflammatie bijdraagt aan deze vroege alteraties van de axon-myeline eenheid.

In **hoofdstuk 4** hebben we mechanismes van laesie formatie geïdentificeerd door clusters van microglia, of nodules, te profileren in de (normaal-ogende) witte stof in MS en na beroerte. We laten zien dat de genexpressie van microglia nodules vergelijkbaar is met die van actief demyeliniserende laesies. Microglia nodules in MS vergeleken microglia nodules na een beroerte zijn vaker gesitueerd in een inflammatoire omgeving, aangezien ze in nabij contact zijn met geactiveerde T cellen en met immunoglobuline producerende B cellen. Microglia nodules in MS zijn geassocieerd met vroege demyelinisatie, omdat 1) ze vaak geoxideerde fosfolipiden hebben gefagocyteerd, 2) hun gen expressie impliceert dat ze lipiden metaboliseerden, en 3) sommige microglia nodules om gedeeltelijk gedemyeliniseerde axonen heen gewikkeld zitten. Co-stimulatie van microglia nodules in MS door pro-inflammatoire cytokines of immunoglobuline en geoxideerde fosfolipiden zou kunnen resulteren in een hyper metabool en hyper inflammatoir fenotype. Het gen expressie profiel van microglia nodules en de fusie van het mitochondriale netwerk indiceren samen dat inderdaad de microglia nodules in MS hyper metabool en hyper

inflammatoir zouden kunnen zijn, wat zou kunnen bijdragen aan de progressie van microglia nodules naar MS laesies.

Tezamen tonen de data in het eerste deel van dit proefschrift aan dat voorafgaand aan laesie formatie in MS het normaal-ogend weefsel niet erg normaal is. Verlies van homeostase van microglia, mogelijk door een verlies van CD200 expressie, en het minder compact wikkelen van myeline om axonen heen dragen bij aan laesie formatie, en microglia nodules zijn het eerste begin punt van MS laesies.

**Deel 2: Laesies met foamy microglia breiden uit en laesies met ramified microglia zijn regeneratief**

In **hoofdstuk 5** hebben we een factor analyse uitgevoerd op kwantitatieve en kwalitatieve neuropathologische data. We vonden drie onafhankelijke dimensies van MS pathologie, en hebben deze gevalideerd met klinische, genetische, en neuropathologische data. Dimensie 1 associeert met een hogere proportie van actieve en gemixte laesies, B en T cel aanwezigheid, neuro-axonale dichtheid, en een ernstiger klinisch beloop. Deze dimensie reflecteert waarschijnlijk demyelinisatie en immuun cel activiteit, geassocieerd met pathologische en klinische progressie van MS. Dimensie 2 associeert met een hogere proportie van actieve laesies, ramified microglia, reactieve sites, aanwezigheid van microglia nodules, en genetische MS risico varianten. Deze dimensie representeert waarschijnlijk microglia activiteit en initiatie van laesie formatie. Dimensie 3 associeert met een hoger aantal gemixte en inactieve laesies, lagere proportie geremyeliniseerde laesies, weinig B en T cel aanwezigheid, en weinig acute axonale schade. Deze dimensie reflecteert waarschijnlijk verlies van laesie activiteit. Samen belichten onze bevindingen de complexe wisselwerking tussen pathologische karakteristieken en hun relatie tot ziekte progressie.

In **hoofdstuk 6** hebben we onderzocht wat het pathologische correlaat van de biomarker neurofilament light chain (NfL) is. NfL is een onderdeel is van het neuronale cytoskelet, dus de hoeveelheid NfL in het cerebrospinale vloeistof is een indicator van neuro-axonale schade in het brein. We vonden we dat de hoeveelheid NfL positief correleert aan de hoeveelheid axonaal verlies en acute axonale stress in MS normaal-ogende witte stof. We vonden verder dat de hoeveelheid NfL positief correleert met de proportie actieve en gemixte laesies met foamy microglia, en niet met die met ramified microglia. In lijn hiermee lieten we zien dat er op eiwit-niveau ook meer acute axonale stress (gemeten met $APP^+$ axonale fragmenten en bulbs) in actieve en gemixte laesies met foamy microglia is vergeleken met die met ramified microglia. Tezamen laat onze data zien dat laesies met foamy microglia meer geassocieerd zijn met axonale schade

en stress dan laesies met ramified microglia, wat mogelijk implicaties heeft voor MS laesie dynamiek.

In **hoofdstuk 7** hebben we spatiële transcriptomics uitgevoerd op gemixte laesies met ramified microglia en op gemixte laesies met foamy microglia. We hebben verschillende cellulaire en moleculaire mechanismes geïdentificeerd van laesie expansie en gebrek aan remyelinisatie. Gemixte laesies met foamy microglia zijn gekarakteriseerd door een toename aan lymfocyten en immuun-oligodendrocyten, immunoglobuline productie, complement activatie, ijzer dysregulatie en demyelinisatie. Daartegenover zijn gemixte laesies met ramified microglia geassocieerd met axonale groei, myeline stabiliteit, en remyelinisatie. Onze data heeft inzicht gegeven in de cellulaire en moleculaire mechanismen die laesie-expansie en falen van herstel bij MS aandrijven.

Concluderend, in het tweede deel van dit proefschrift onderzochten we complexe samenwerking tussen pathologische karakteristieken in het MS brein. We identificeerden cellulaire en moleculaire mechanismes van laesie dynamiek die bijdragen aan laesie expansie en remyelinisatie.

**Deel 3: Genetische predispositie voor klinische progressie is geassocieerd met verergerde pathologie**

In het derde deel van dit proefschrift hadden we het doel om de SNP geassocieerd met versnelde klinische progressie rs10191329 in de *DYSF-ZNF638* locus, welke recentelijk is ontdekt door de International Multiple Sclerosis Genetics Consortium biologisch te valideren. Daarnaast wilden we mogelijke mechanismes onderliggend aan ziekteprogressie in homozygote dragers identificeren.

De SNP rs10191329 is de eerste SNP die geassocieerd wordt een versneld ziektebeloop in MS. In **hoofdstuk 8** laten we zien dat homozygote dragerschap van de SNP rs10191329 is geassocieerd met een toename aan pathologie in de hersenstam en de cortex. Hiermee hebben we de biologische relevantie van de risico SNP rs10191329 gevalideerd.

In **hoofdstuk 9** hebben we gevonden dat homozygote risico dragers vergeleken met homozygote niet risico dragers voor rs10191329 een hogere proportie hadden van actieve en gemixte laesies met foamy microglia, meer T cellen hebben in laesies, en meer acute axonale stress en neuronaal verlies hebben. Aangezien rs10191329 in de DYSF-ZNF638 locus ligt, is het mogelijk dat dysferline en ZNF638 een rol spelen in ziekte progressie in MS. In homozygote risico dragers hebben we een hogere dichtheid gevonden van DYSF+ cellen in de normaal-ogende grijze stof en van ZNF638+ oligodendrocyten in de

normaal-ogende witte stof. Neuronen en oligodendrocyten hebben hogere genexpressie voor mitochondriale genen, wat impliceert dat er meer cellulaire stress is in homozygote risico dragers vergeleken met homozygote non-risico dragers. Samen impliceert dit dat homozygote risico dragers gevoeliger zijn voor weefsel schade.

Samengevat, in het derde deel van dit proefschrift hebben we de klinische progressie SNP rs10191329 biologisch gevalideerd. Onze data impliceert dat ZNF638 en dysferline een rol kunnen spelen in MS ziekte progressie.

## CONCLUSIE

In conclusie, dit proefschrift heeft belangrijke mechanismes geïdentificeerd waarmee microglia en neuronen bijdragen aan de progressie van MS. Door laesie formatie, pathologische heterogeniteit, en genetische predispositie te onderzoeken, hebben we belangrijke moleculaire veroorzakers en mechanismes gevonden die een rol spelen in MS pathologie. Dit onderzoek belicht het belang van microglia homeostase en compacte myeline, de dynamiek van laesie expansie, en de invloed van van genetische risico factoren op ziekteprogressie. Deze inzichten dragen bij aan een beter begrip van MS progressie, wat mogelijk kan leiden tot de ontwikkeling van nieuwe biomarkers en therapeutische interventies om mensen met MS beter te behandelen.

# AUTHOR CONTRIBUTIONS

Chapter 2

| Name | Location | Contribution |
|---|---|---|
| Aletta M.R. van den Bosch | Neuroimmunology Research Group, Netherlands Institute for Neuroscience, Amsterdam, The Netherlands | Study concept and design; acquisition of data; analysis and interpretation of data; drafting and revising the manuscript |
| Dennis Wever | Neuroimmunology Research Group, Netherlands Institute for Neuroscience, Amsterdam, The Netherlands | Acquisition of data; revising the manuscript |
| Pleun Schonewille | Neuroimmunology Research Group, Netherlands Institute for Neuroscience, Amsterdam, The Netherlands | Acquisition of data; analysis and interpretation of data; revising the manuscript |
| Sabine L. Schuller | Neuroimmunology Research Group, Netherlands Institute for Neuroscience, Amsterdam, The Netherlands | Acquisition of data; analysis and interpretation of data; revising the manuscript |
| Joost Smolders | Neuroimmunology Research Group, Netherlands Institute for Neuroscience, Amsterdam, The Netherlands<br>MS Center ErasMS, Departments of Neurology and Immunology, Erasmus Medical Center, Rotterdam, The Netherlands | Study concept and design; interpretation of data; revising the manuscript |
| Jörg Hamann | Neuroimmunology Research Group, Netherlands Institute for Neuroscience, Amsterdam, The Netherlands<br>Amsterdam Institute for immunology and Infectious Diseases, Amsterdam University Medical Center, Amsterdam, The Netherlands | Study concept and design; interpretation of data; revising the manuscript |
| Inge Huitinga | Neuroimmunology Research Group, Netherlands Institute for Neuroscience, Amsterdam, The Netherlands<br>Swammerdam Institute for Life Sciences, University of Amsterdam, Amsterdam, The Netherlands | Study concept and design; interpretation of data; revising the manuscript |

Chapter 3

| Name | Location | Contribution |
|---|---|---|
| Aletta M.R. van den Bosch | Neuroimmunology Research Group, Netherlands Institute for Neuroscience, Amsterdam, The Netherlands | Study concept and design; acquisition of data; analysis and interpretation of data; drafting and revising the manuscript |
| Sophie Hümmert | Department of Neurogenetics, Max Planck Institute for Multidisciplinary Sciences, Göttingen, Germany | Study concept and design; acquisition of data; analysis and interpretation of data; revising the manuscript |
| Anna Steyer | Department of Neurogenetics, Max Planck Institute for Multidisciplinary Sciences, Göttingen, Germany | Study concept and design; revising the manuscript |
| Torben Ruhwedel | Department of Neurogenetics, Max Planck Institute for Multidisciplinary Sciences, Göttingen, Germany | Acquisition of data; analysis of data; revising the manuscript |
| Jörg Hamann | Neuroimmunology Research Group, Netherlands Institute for Neuroscience, Amsterdam, The Netherlands<br>Amsterdam Institute for immunology and Infectious Diseases, Amsterdam University Medical Center, Amsterdam, The Netherlands | Interpretation of data; revising the manuscript |
| Joost Smolders | Neuroimmunology Research Group, Netherlands Institute for Neuroscience, Amsterdam, The Netherlands<br>MS Center ErasMS, Departments of Neurology and Immunology, Erasmus Medical Center, Rotterdam, The Netherlands | Interpretation of data; revising the manuscript |
| Klaus-Armin Nave | Department of Neurogenetics, Max Planck Institute for Multidisciplinary Sciences, Göttingen, Germany | Study concept and design; interpretation of data; revising the manuscript |
| Christine Stadelmann | Department of Neuropathology, University Medical Center Göttingen, Göttingen, Germany | Study concept and design; acquisition of data; interpretation of data; revising the manuscript |

Chapter 3 *(continued)*

| Name | Location | Contribution |
|---|---|---|
| Maarten H.P. Kole | Department of Axonal Signaling, Netherlands Institute for Neuroscience, Royal Netherlands Academy for Arts and Sciences, Amsterdam, The Netherlands Cell Biology, Neurobiology and Biophysics, Department of Biology, Faculty of Science, University of Utrecht, Utrecht, The Netherlands | Study concept and design; interpretation of data; revising the manuscript |
| Wiebke Möbius # | Department of Neurogenetics, Max Planck Institute for Multidisciplinary Sciences, Göttingen, Germany | Study concept and design; interpretation of data; revising the manuscript |
| Inge Huitinga # | Neuroimmunology Research Group, Netherlands Institute for Neuroscience, Amsterdam, The Netherlands Swammerdam Institute for Life Sciences, University of Amsterdam, Amsterdam, The Netherlands | Study concept and design; interpretation of data; revising the manuscript |

*# = equal contributions*

Chapter 4

| Name | Location | Contribution |
|---|---|---|
| Aletta M.R. van den Bosch | Neuroimmunology Research Group, Netherlands Institute for Neuroscience, Amsterdam, The Netherlands | Study concept and design; acquisition of data; analysis and interpretation of data; drafting and revising the manuscript |
| Marlijn van der Poel | Neuroimmunology Research Group, Netherlands Institute for Neuroscience, Amsterdam, The Netherlands | Study concept and design; acquisition of data; analysis and interpretation of data; drafting and revising the manuscript |
| Nina L. Fransen | Neuroimmunology Research Group, Netherlands Institute for Neuroscience, Amsterdam, The Netherlands | Acquisition of data; analysis and interpretation of data; revising the manuscript |
| Maria C.J. Vincenten | Neuroimmunology Research Group, Netherlands Institute for Neuroscience, Amsterdam, The Netherlands | Acquisition of data; revising the manuscript |
| Anneleen M. Bobeldijk | Neuroimmunology Research Group, Netherlands Institute for Neuroscience, Amsterdam, The Netherlands | Acquisition of data; revising the manuscript |
| Aldo Jongejan | Department of Epidemiology and Data Science, Amsterdam Public Health Research Institute, Amsterdam University Medical Centers, Amsterdam, The Netherlands | Analysis of data; drafting and revising the manuscript |
| Hendrik J. Engelenburg | Neuroimmunology Research Group, Netherlands Institute for Neuroscience, Amsterdam, The Netherlands | Acquisition of data; revising the manuscript |
| Perry D. Moerland | Department of Epidemiology and Data Science, Amsterdam Public Health Research Institute, Amsterdam University Medical Centers, Amsterdam, The Netherlands | Analysis of data; drafting and revising the manuscript |
| Joost Smolders | Neuroimmunology Research Group, Netherlands Institute for Neuroscience, Amsterdam, The Netherlands<br>MS Center ErasMS, Departments of Neurology and Immunology, Erasmus Medical Center, Rotterdam, The Netherlands | Study concept and design; interpretation of data; revising the manuscript |

Chapter 4 *(continued)*

| Name | Location | Contribution |
|---|---|---|
| Inge Huitinga | Neuroimmunology Research Group, Netherlands Institute for Neuroscience, Amsterdam, The Netherlands<br>Swammerdam Institute for Life Sciences, University of Amsterdam, Amsterdam, The Netherlands | Study concept and design; interpretation of data; revising the manuscript |
| Jörg Hamann | Neuroimmunology Research Group, Netherlands Institute for Neuroscience, Amsterdam, The Netherlands<br>Amsterdam Institute for immunology and Infectious Diseases, Amsterdam University Medical Center, Amsterdam, The Netherlands | Study concept and design; interpretation of data; revising the manuscript |

Chapter 5

| Name | Location | Contribution |
|---|---|---|
| Alyse de Boer | Department of Biomedical Sciences of Cells and Systems, Section Molecular Neurobiology, University of Groningen, University Medical Center Groningen, Groningen, The Netherlands | Study concept and design; acquisition of data; analysis and interpretation of data; drafting and revising the manuscript |
| Aletta M.R. van den Bosch | Neuroimmunology Research Group, Netherlands Institute for Neuroscience, Amsterdam, The Netherlands | Acquisition of data; analysis and interpretation of data; drafting and revising the manuscript |
| Nienke J. Mekkes | Department of Biomedical Sciences of Cells and Systems, Section Molecular Neurobiology, University of Groningen, University Medical Center Groningen, Groningen, The Netherlands<br>Machine Learning Lab, Data Science Center in Health, University of Groningen, University Medical Center Groningen, The Netherlands | Analysis and interpretation of data; drafting and revising the manuscript |
| Nina L. Fransen | Neuroimmunology Research Group, Netherlands Institute for Neuroscience, Amsterdam, The Netherlands | Acquisition of data; revising the manuscript |
| Ekaterina Dagkesamanskaia | Department of Biomedical Sciences of Cells and Systems, Section Molecular Neurobiology, University of Groningen, University Medical Center Groningen, Groningen, The Netherlands<br>Machine Learning Lab, Data Science Center in Health, University of Groningen, University Medical Center Groningen, The Netherlands | Analysis and interpretation of data; drafting and revising the manuscript |
| Eric Hoekstra | Department of Biomedical Sciences of Cells and Systems, Section Molecular Neurobiology, University of Groningen, University Medical Center Groningen, Groningen, The Netherlands | Interpretation of data; revising the manuscript |

Chapter 5 *(continued)*

| Name | Location | Contribution |
|---|---|---|
| Joost Smolders | Neuroimmunology Research Group, Netherlands Institute for Neuroscience, Amsterdam, The Netherlands<br>MS Center ErasMS, Departments of Neurology and Immunology, Erasmus Medical Center, Rotterdam, The Netherlands | Interpretation of data; drafting and revising the manuscript |
| Jörg Hamann | Neuroimmunology Research Group, Netherlands Institute for Neuroscience, Amsterdam, The Netherlands<br>Amsterdam Institute for immunology and Infectious Diseases, Amsterdam University Medical Center, Amsterdam, The Netherlands | Interpretation of data; revising the manuscript |
| Inge Huitinga | Neuroimmunology Research Group, Netherlands Institute for Neuroscience, Amsterdam, The Netherlands<br>Swammerdam Institute for Life Sciences, University of Amsterdam, Amsterdam, The Netherlands<br>The Netherlands Brain Bank, Netherlands Institute for Neuroscience, Amsterdam, The Netherlands | Study concept and design; interpretation of data; revising the manuscript |
| Inge R. Holtman | Department of Biomedical Sciences of Cells and Systems, Section Molecular Neurobiology, University of Groningen, University Medical Center Groningen, Groningen, The Netherlands<br>The Netherlands Brain Bank, Netherlands Institute for Neuroscience, Amsterdam, The Netherlands | Study concept and design; interpretation of data; drafting and revising the manuscript |

Chapter 6

| Name | Location | Contribution |
|---|---|---|
| Aletta M.R. van den Bosch * | Neuroimmunology Research Group, Netherlands Institute for Neuroscience, Amsterdam, The Netherlands | Study concept and design; acquisition of data; analysis and interpretation of data; drafting and revising the manuscript |
| Nina L. Fransen * | Neuroimmunology Research Group, Netherlands Institute for Neuroscience, Amsterdam, The Netherlands | Study concept and design; acquisition of data; analysis and interpretation of data; drafting and revising the manuscript |
| Matthew R.J. Mason | Neuroimmunology Research Group, Netherlands Institute for Neuroscience, Amsterdam, The Netherlands | Analysis of data; revising the manuscript |
| Annemieke Rozemuller | Department of Pathology, Amsterdam UMC, Amsterdam, The Netherlands | Interpretation of data; revising the manuscript |
| Charlotte E. Teunissen | Neurochemistry lab, Department of Clinical Chemistry, Amsterdam Neuroscience, Amsterdam UMC, Vrije Universiteit, Amsterdam, The Netherlands | Analysis of data; revising the manuscript |
| Joost Smolders | Neuroimmunology Research Group, Netherlands Institute for Neuroscience, Amsterdam, The Netherlands<br>MS Center ErasMS, Departments of Neurology and Immunology, Erasmus Medical Center, Rotterdam, The Netherlands | Study concept and design; interpretation of data; revising the manuscript |
| Inge Huitinga | Neuroimmunology Research Group, Netherlands Institute for Neuroscience, Amsterdam, The Netherlands<br>Swammerdam Institute for Life Sciences, University of Amsterdam, Amsterdam, The Netherlands | Study concept and design; interpretation of data; revising the manuscript |

** = equal contributions*

Chapter 7

| Name | Location | Contribution |
|---|---|---|
| Aletta M.R. van den Bosch * | Neuroimmunology Research Group, Netherlands Institute for Neuroscience, Amsterdam, The Netherlands | Study concept and design; acquisition of data; analysis and interpretation of data; drafting and revising the manuscript |
| Jia H. Khoo * | BGI Research, Riga, Latvia | Study concept and design; acquisition of data; analysis of data; drafting and revising the manuscript |
| Zhigang Lu | BGI Research, Riga, Latvia | Analysis and interpretation of data; drafting and revising the manuscript |
| Dennis Wever | Neuroimmunology Research Group, Netherlands Institute for Neuroscience, Amsterdam, The Netherlands | Acquisition of data; revising the manuscript |
| Li Pu | BGI Research, Riga, Latvia | Acquisition of data; revising the manuscript |
| Bart Eggen | Department of Neuroscience, Section Medical Physiology, University Medical Center Groningen, Groningen, The Netherlands | Interpretation of data; revising the manuscript |
| Joost Smolders | Neuroimmunology Research Group, Netherlands Institute for Neuroscience, Amsterdam, The Netherlands<br>MS Center ErasMS, Departments of Neurology and Immunology, Erasmus Medical Center, Rotterdam, The Netherlands | Study concept and design; interpretation of data; revising the manuscript |
| Jörg Hamann | Neuroimmunology Research Group, Netherlands Institute for Neuroscience, Amsterdam, The Netherlands<br>Amsterdam Institute for immunology and Infectious Diseases, Amsterdam University Medical Center, Amsterdam, The Netherlands | Study concept and design; interpretation of data; revising the manuscript |
| Zhouchun Shang # | BGI Research, Riga, Latvia | Revising the manuscript |
| Jan Mulder # | Department of Neuroscience, Karolinska Institute, Stockholm, Sweden | Study concept and design; interpretation of data; revising the manuscript |

Chapter 7 *(continued)*

| Name | Location | Contribution |
|---|---|---|
| Inge Huitinga # | Neuroimmunology Research Group, Netherlands Institute for Neuroscience, Amsterdam, The Netherlands Swammerdam Institute for Life Sciences, University of Amsterdam, Amsterdam, The Netherlands | Study concept and design; interpretation of data; revising the manuscript |

** or # = equal contributions*

Chapter 8

| Name | Location | Contribution |
|---|---|---|
| Aletta M.R. van den Bosch * | Neuroimmunology Research Group, Netherlands Institute for Neuroscience, Amsterdam, The Netherlands | Study concept and design; acquisition of data; analysis and interpretation of data; drafting and revising the manuscript |
| Hendrik J. Engelenburg * | Neuroimmunology Research Group, Netherlands Institute for Neuroscience, Amsterdam, The Netherlands | Study concept and design; acquisition of data; analysis and interpretation of data; drafting and revising the manuscript |
| Dennis Wever | Neuroimmunology Research Group, Netherlands Institute for Neuroscience, Amsterdam, The Netherlands | Acquisition of data; revising the manuscript |
| Adil Harroud | UCSF Weill Institute for Neurosciences, Department of Neurology, University of California, San Francisco, CA, USA<br>The Neuro (Montreal Neurological Institute and Hospital), Department of Neurology and Neurosurgery, McGill University, Montreal, Quebec, Canada | Study concept and design; interpretation of data; drafting and revising the manuscript |
| Jörg Hamann | Neuroimmunology Research Group, Netherlands Institute for Neuroscience, Amsterdam, The Netherlands<br>Amsterdam Institute for immunology and Infectious Diseases, Amsterdam University Medical Center, Amsterdam, The Netherlands | Study concept and design; interpretation of data; revising the manuscript |
| Inge Huitinga | Neuroimmunology Research Group, Netherlands Institute for Neuroscience, Amsterdam, The Netherlands<br>Swammerdam Institute for Life Sciences, University of Amsterdam, Amsterdam, The Netherlands | Study concept and design; interpretation of data; revising the manuscript |
| Joost Smolders | Neuroimmunology Research Group, Netherlands Institute for Neuroscience, Amsterdam, The Netherlands<br>MS Center ErasMS, Departments of Neurology and Immunology, Erasmus Medical Center, Rotterdam, The Netherlands | Study concept and design; interpretation of data; revising the manuscript |

** = equal contributions*

Chapter 9

| Name | Location | Contribution |
|---|---|---|
| Hendrik J. Engelenburg | Neuroimmunology Research Group, Netherlands Institute for Neuroscience, Amsterdam, The Netherlands | Study concept and design; acquisition of data; analysis and interpretation of data; drafting and revising the manuscript |
| Aletta M.R. van den Bosch | Neuroimmunology Research Group, Netherlands Institute for Neuroscience, Amsterdam, The Netherlands | Study concept and design; acquisition of data; analysis and interpretation of data; drafting and revising the manuscript |
| J.Q. Alida Chen | Neuroimmunology Research Group, Netherlands Institute for Neuroscience, Amsterdam, The Netherlands | Acquisition of data; analysis and interpretation of data; revising the manuscript |
| Cheng-Chih Hsiao | Neuroimmunology Research Group, Netherlands Institute for Neuroscience, Amsterdam, The Netherlands | Interpretation of data; revising the manuscript |
| Inge Huitinga | Neuroimmunology Research Group, Netherlands Institute for Neuroscience, Amsterdam, The Netherlands<br>Swammerdam Institute for Life Sciences, University of Amsterdam, Amsterdam, The Netherlands | Study concept and design; interpretation of data; revising the manuscript |
| Jörg Hamann | Neuroimmunology Research Group, Netherlands Institute for Neuroscience, Amsterdam, The Netherlands<br>Amsterdam Institute for immunology and Infectious Diseases, Amsterdam University Medical Center, Amsterdam, The Netherlands | Study concept and design; interpretation of data; revising the manuscript |
| Joost Smolders | Neuroimmunology Research Group, Netherlands Institute for Neuroscience, Amsterdam, The Netherlands<br>MS Center ErasMS, Departments of Neurology and Immunology, Erasmus Medical Center, Rotterdam, The Netherlands | Study concept and design; interpretation of data; revising the manuscript |

# CURRICULUM VITAE

**PhD training**

| | Year |
|---|---|
| **Courses** | |
| Introduction course ONWAR | 2020 |
| Neurodegenerative diseases (ONWAR) | 2021 |
| Molecular biology and genetics (ONWAR) | 2021 |
| Summer School Cajal: Glial cells in health and disease, Bordeaux | 2023 |
| **Seminars, workshops and masterclasses** | |
| Annual ONWAR meetings | 2021-2023 |
| Swammerdam lectures ONWAR | 2020-2024 |
| Masterclass with Beth Stevens | 2021 |
| **Oral presentations** | |
| ACTRIMS, online: Neurofilament light chain levels correlate with lesion activity and axonal damage in MS | 2021 |
| MS Research days, online: Profiling microglial nodules in MS reveals likely involvement in MS lesion formation | 2021 |
| Neuroscience symposium NIN, Amsterdam: Ultrastructural alterations in MS normal appearing white matter and implications for lesion formation | 2022 |
| MS Research days, Rotterdam: Ultrastructural alterations in the normal appearing white matter in MS correlate with activated microglia and lymphocytes | 2022 |
| GliaNed, Amsterdam: The axon-myelin unit in human optic nerve shows ultrastructural alterations in MS that correlate with inflammation | 2022 |
| IMSGC meeting, Amsterdam: Testing two SNPs associated with MS severity in the MS cohort of the Netherlands Brain Bank | 2022 |
| Omics analyses of brain function and brain disease, Amsterdam: Regenerative and degenerative properties of mixed active/inactive lesions in post-mortem human MS tissue | 2023 |
| Microglia, Groningen: Spatial transcriptomics reveals mechanisms of degeneration and regeneration in multiple sclerosis | 2024 |
| Neuroscience symposium NIN, Amsterdam: Spatial transcriptomics reveals mechanisms of degeneration and regeneration in multiple sclerosis | 2024 |
| Dutch Neuroscience Meeting, Tiel (invited): Oligodendrocyte and myelin alterations in MS: implications for MS lesions formation and expansion | 2024 |

**PhD training** *(continued)*

| | Year |
|---|---|
| **Poster presentations** | |
| GLIA, online: Profiling microglia nodules in MS: possible implications for MS lesion formation | 2021 |
| Gordon research conference, Lucca: Ultrastructural alterations in the normal appearing white matter in MS correlate with activated microglia and lymphocytes | 2022 |
| ECTRIMS, Amsterdam: Ultrastructural alterations in the normal appearing white matter in MS correlate with activated microglia and lymphocytes | 2022 |
| GLIA, Berlin: Profiling of MS microglia nodules reveals enriched propensity for lesion formation | 2023 |
| MS Research days, Leuven: Spatial transcriptomics reveals mechanisms of degeneration and regeneration in multiple sclerosis lesions | 2024 |
| **Other** | |
| Visiting the department of Neurogenetics, Max Planck Institute for Multdisciplinary Sciences, Göttingen: collaboration with Wiebke Möbius | 2021 |
| Visiting the department of Neuroscience, Karolinska Institute, Stockholm: collaboration with Jan Mulder | 2022 |
| Organising the annual ONWAR meeting, Woudschoten | 2021-2022 |
| **Teaching** | |
| Sylvia Korhorn (supervision master thesis) | 2020 |
| Jolinde van Bergen (supervision master thesis) | 2021 |
| Sabine Schuller (supervision master internship) | 2021 |
| Pleun Schonewille (supervision master internship) | 2022 |
| Dunya Selemangel (supervision master internship) | 2023 |
| **Parameters of esteem** | |
| Best poster presentation, ONWAR | 2021 |
| ECTRIMS abstract grant | 2021 |
| Aspasia travel grant, to visit the Max Planck institute in Göttingen | 2021 |
| Best poster presentation, Gordon research conference | 2022 |
| Figure selected for the cover of Annals of Neurology | 2023 |
| Auxilium MarMar grant, to participate in the Cajal summerschool | 2023 |
| GLIA travel grant | 2023 |
| Best oral presentation, ONWAR | 2023 |
| Rogier Hintzen Talent Award | 2023 |

## LIST OF PUBLICATIONS

Engelenburg HJ, **van den Bosch AMR**, Chen A, Hasiao C, Melief M, Huitinga I, Hamann J, Smolders J. The progression-associated genetic variant in the DYSF-ZNF638 locus associates with increased neuronal loss and inflammation in multiple sclerosis. *In submission.*

Blok KM, Klein Kranenbarg RAM, Ananth K, Engelenburg JH, **van den Bosch AMR**, Giannini L, de Beukelaar J, Seelaar H, Huitinga I, Green A, Wokke B, Abdelhak A, Smolders J. Multifaceted biomarkers suggest a similar profile of CNS pathology in relapsing and progressive multiple sclerosis. *In submission.*

Klotz L, Smolders J, Lehto J, Matilainen M, Lutje L, Buchholz L, Albrecht S, Walter C, Varghese J, Thomas C, **van den Bosch AMR**, Airas L, Huitinga I, Kuhlmann T. Broad rim lesions are a novel pathological and imaging biomarker for rapid disease progression in multiple sclerosis. *In revision.*

**Van den Bosch AMR**, Wever D, Schonewille P, Schuller SL, Smolders J, Hamann J, Huitinga I. Cortical CD200-CD200R and CD47-SIRPα expression is associated with multiple sclerosis pathology. Brain Communications, 2024, Aug; 6(4): Doi: 10.1093/braincomms/fcae264. PMID: 39175944.

De Boer A, **van den Bosch AMR**, Mekkes NJ, Fransen N, Dagkesamanskaia K, Hoekstra E, Hamann J, Smolders J, Huitinga I, Holtman IR. Disentangling the heterogeneity of multiple sclerosis through identification of independent neuropathological dimensions. Acta Neuropathologica, 2024, May; 147(90). Doi: 10.1007/s00401-024-02742-w. PMID: 38771530.

Peruzzotti-Jametti L, Willis C, Hamel R, Krzak G, Reisz J, Prag H, Wu V, Xiang Y, **van den Bosch AMR**, Nicaise A, Roth L, Bates G, Huang H, Vincent A, Frezza C, Ciscomi C, Marioni J, D'Alessandro A, Takats Z, Murphy M, Pluchino S. Mitochondrial complex I activity in microglia sustains neuroinflammation. Nature, 2024, March 13. Doi: 10.1038/s41586-024-07167-9. PMID: 38480879.

**Van den Bosch AMR**, van der Poel M, Fransen N, Vincenten MCJ, Bobeldijk A, Jongejan A, Moerland P, Hamann J, Huitinga I. Profiling of microglia nodules in multiple sclerosis reveals propensity for lesion formation. Nature Communications, 2024, Feb; 1667(15). Doi: 10.1038/s41467-024-46068-3. PMID: 38396116.

International Multiple Sclerosis Genetics Consortium, MultipleMS consortium. Locus for severity implicates CNS resilience in progression of multiple sclerosis. Nature, 2023, June 28. Doi: 10.1038/s41586-023-06250-x. PMID: 37380766.

**van den Bosch AMR**, Hümmert S, Steyer A, Ruhwedel T, Hamann J, Smolders J, Nave KA, Stadelmann C, Kole MHP, Möbius W, Huitinga I. Ultrastructural axon-myelin unit alterations in multiple sclerosis correlate with inflammation. Annals of Neuroly, 2023 Apr; 93(4):856-870. Doi: 10.1002/ana.26585. PMID: 36565265.

**van den Bosch AMR**, Fransen N, Mason M, Rozemuller AJ, Teunissen C, Smolders J, Huitinga I. Neurofilament light chain levels in multiple sclerosis correlate with lesions containing foamy macrophages and with acute axonal damage. Neurology Neuroimmunology Neuroinflammation, 2022 Mar 3;9(3):e1154. doi: 10.1212/NXI.0000000000001154. PMID: 35241571.

Jarvis LB, Rainbow DB, Coppard V, Howlett SK, Georgieva Z, Davies JL, Mullay HK, Hester J, Ashmore T, **van den Bosch AMR**, Grist JT, Coles AJ, Mousa HS, Pluchino S, Mahbubani KT, Griffin JL, Saeb-Parsy K, Issa F, Peruzzotti-Jametti L, Wicker LS, Jones JL. Therapeutically expanded human regulatory T-cells are super-suppressive due to HIF1A induced expression of CD73. Communications Biology, 2021 Oct 14;4(1):1186. doi: 10.1038/s42003-021-02721-x. PMID: 34650224.

Peruzzotti-Jametti L, Bernstock JD, Willis CM, Manferrari G, Rogall R, Fernandez-Vizarra E, Williamson JC, Braga A, **van den Bosch AMR**, Leonardi T, Krzak G, Kittel Á, Benincá C, Vicario N, Tan S, Bastos C, Bicci I, Iraci N, Smith JA, Peacock B, Muller KH, Lehner PJ, Buzas EI, Faria N, Zeviani M, Frezza C, Brisson A, Matheson NJ, Viscomi C, Pluchino S. Neural stem cells traffic functional mitochondria via extracellular vesicles. PLoS Biology, 2021 Apr 7;19(4):e3001166. doi: 10.1371/journal.pbio.3001166. PMID: 33826607.

Hsiao CC, Fransen NL, **van den Bosch AMR**, Brandwijk KIM, Huitinga I, Hamann J, Smolders J. White matter lesions in multiple sclerosis are enriched for CD20dim CD8+ tissue-resident memory T cells. European Journal of Immunology, 2021 Feb;51(2):483-486. doi: 10.1002/eji.202048665. PMID: 32949467.

Bernstock JD, Peruzzotti-Jametti L, Leonardi T, Vicario N, Ye D, Lee YJ, Maric D, Johnson KR, Mou Y, **van den Bosch AMR**, Winterbone M, Friedman GK, Franklin RJM, Hallenbeck JM, Pluchino S. SUMOylation promotes survival and integration of neural stem cell grafts in ischemic stroke. EBioMedicine. 2019 Apr;42:214-224. doi: 10.1016/j.ebiom.2019.03.035. PMID: 30905846.

van Montfort SJT, van Dellen E, **van den Bosch AMR**, Otte WM, Schutte MJL, Choi SH, Chung TS, Kyeong S, Slooter AJC, Kim JJ. Resting-state fMRI reveals network disintegration during delirium. NeuroImage Clinical, 2018 Jun 19;20:35-41. doi: 10.1016/j.nicl.2018.06.024. PMID: 29998059.

# DANKWOORD

Dat was het dan, we zijn aangekomen op het meest gelezen hoofdstuk van het proefschrift: het dankwoord! Ik ben enorm dankbaar voor iedereen die mij de afgelopen jaren heeft bijgestaan. Alles wat in dit proefschrift staat is mede mogelijk gemaakt door de steun die ik van vrienden, familie en collega's heb gekregen. Dankzij hen kan ik echt met veel plezier en trots terugkijken op de afgelopen jaren.

Allereerst **Inge**, *onze* professor. In 2017 kwam ik stage lopen in jouw onderzoeksgroep. Hier werd ik door jouw enthousiasme en je kennis over het humane brein continue geprikkeld, en leerde ik al gauw hoe leuk onderzoek doen is. Bedankt voor het vertrouwen dat je in mij had om een PhD te komen doen. Bedankt voor je steun, ook in persoonlijke situaties, en bedankt dat je zorgzaam over de onderzoeksgroep waakt. Ik kijk altijd uit naar onze meetings, en dan vooral naar de brainstorm sessies waar we alle kanten op vliegen. Je hebt me geleerd om naar het grotere plaatje te kijken en om conceptueel na te denken, en je hebt me het zelfvertrouwen gegeven om met mijn eigen ideeën aan de slag te gaan.

**Jörg**, wat was het fijn om met jou samen te werken, en wat ben ik blij en vereerd dat je mijn copromotor bent. Je oog voor detail, vlijmscherpe inhoudelijke vragen, en constructieve feedback, hebben mij enorm geholpen. Je hebt me strategisch leren nadenken. De structuur en daarmee rust die je hebt gebracht aan mijn promotietraject was voor mij ontzettend fijn en belangrijk. Zonder jou was mijn promotie traject zeker een heel stuk chaotischer geweest.

**Joost**, het is altijd een feestje op vrijdag, als je jouw NIN-dag hebt, om te kunnen sparren over iedereens data. Je vermogen om eerdere bevindingen aan elkaar te koppelen is bewonderingswaardig. Dankzij je enthousiasme komen je geliefde T en B cellen toch een aantal keer voor in dit proefschrift! Bedankt voor het vertrouwen om me te betrekken bij je samenwerkingen, voor je kritische vragen, en voor je onuitputtelijke interesse in mijn onderzoek.

De leden van de oppositie, **Prof. Lucassen**, **Prof. Uitdehaag**, **Prof. van der Valk**, **Prof. Kole**, **Dr. Mulder** and **Dr. Absinta**, bedankt voor de tijd om mijn proefschrift te lezen en te beoordelen, thank you for reading and evaluating my thesis. Prof. Kole, Maarten, bedankt voor de fijne samenwerking en voor het delen van je kennis over axonen en het actiepotentiaal. Dr. Mulder, Jan, bedankt voor je gastvrijheid om in je lab mee te mogen draaien voor een paar weken, om het spatial transcriptomics project op te zetten.

De **hersendonoren** van de Nederlandse Hersenbank en hun nabestaanden wil ik graag bedanken. Zonder hun vertrouwen in onderzoek en zonder hun donatie zouden geen van deze onderzoeken mogelijk zijn geweest.

Aan alle (oud) groepsleden van de NeuroImmunologie groep, **Jeen, Alida, Dennis, Niamh, Andy, Lukas, Felipe, Matthew, Karel, Marlijn, Nina, Manon, Jackelien,** bedankt voor het delen van al jullie kennis, voor de leuke discussies, de prettige samenwerkingen, en natuurlijk voor jullie gezelligheid! Bedankt dat jullie mijn geklaag en geklier hebben doorstaan, en voor de vele snack-loopjes naar het AMC. Thank you all for sharing your knowledge with me, for the fun discussions, the pleasant collaborations, and of course for all the gezelligheid! Thank you for putting up with me, and for all the snack-walks to the AMC. **Jeen**, wat ontzettend leuk om niet alleen tijdens onze stage maar ook tijdens onze PhD naast elkaar te zitten, en wat bijzonder dat je naast me wil staan tijdens mijn promotie als mijn paranimf. Ik heb ontzettend veel aan je steun gehad tijdens dit traject, heel erg bedankt! **Alida**, mijn AA teamgenoot! Helaas waren onze gezamenlijke meetings maar van korte duur, maar ik vond het ontzettend leuk om te zien hoe je steeds beter op je plek bent gekomen, en je project echt eigen hebt gemaakt. Bedankt voor het opladen in de zon met me, zowel op het NiN als in Lucca, en voor al je pasta-recept inspiratie. Heel veel succes met al je projecten! **Dennis**, het was erg leuk om je zo te zien groeien binnen onze groep, van junior technician naar lab manager. Bedankt dat je ons (meestal) veilig weet te houden, en voor al je geweldig vermakelijke verhalen. **Hsiao**, **Andy**, good luck on your quest around the world! **Niamh**, I am so happy you decided to join our group after we met in Lucca! Thank you for livening up our discussions, for proof-reading my texts, and for all the wine we have drank together already. Much more of that to come! **Lukas**, bedankt voor je heerlijke humor, en heel veel succes met het verder opzetten van je project. Ik kijk er erg naar uit om te zien wat je allemaal gaat ontdekken in de broad rim lesions! **Felipe,** you have only been in our group for a short time, but you have already been a great person to have on our team! Good luck with your ME project, I am looking forward to your findings. **Matthew**, thank you for your valuable input in my projects, and for guiding me in my statistics. Your experience and knowledge will be greatly missed in our lab. **Karel**, bedankt voor je interessante en vaak indrukwekkende verhalen uit de kliniek. **Marlijn** en **Nina**, bedankt voor jullie vertrouwen om jullie opgestarte projecten naar een goed einde te kunnen brengen. Door jullie kon ik met een vliegende start aan mijn promotietraject beginnen. **Manon**, onze talloze uren achter de LDM waren niet voor niks, bedankt voor al je hulp! **Jackelien**, bedankt voor onze openhartige gesprekken, en voor het vermaak als ik het even niet zag zitten. Ik hoop nog veel updates over je kinderen en kippen te krijgen, en ik hoop dat je binnenkort ook geitjes kan verwelkomen.

Aan iedereen van de hersenbank, het obductieteam, sectie assistenten, en neuropathologen, heel erg bedankt voor jullie inzet, dag en nacht. In het bijzonder aan **Michiel, Danae, Paul, Isabell, Leanne, Mignon, Marja, Minke, An, Petra, Ashley, Marylin,** en **Vanessa** bedankt voor jullie inzet om hersenonderzoek mogelijk te maken, voor alle taart momenten, en voor het delen van jullie kennis over het humane brein. Zonder jullie zou dit hele proefschrift niet mogelijk zijn geweest. **Danae**, bedankt voor je gezelligheid, en voor al je hulp bij de MS karakterisatie. Het was erg fijn om altijd even binnen te kunnen komen vallen met een wild verhaal, voor wat afleiding, of voor een gezamenlijk klaag-moment. **Isabell** en **Michiel**, bedankt voor jullie hulp met MS weefsel uitgifte en het uitpluizen van aanvragen. Jullie houden de boel op orde!

Aan iedereen van het NIN, maar in het bijzonder **Luuk, Amber, Giorgia, Sarah, Daan, Viktor, Paul** en **Kieran**, bedankt voor de gezelligheid, het delen van frustraties en voor de karaoke avonden. Dat er nog veel mogen volgen! Thank you for all the fun times, for sharing frustrations, and for karaoke nights. I hope that there will be many more to follow! **Roeland**, **Joris** en **Joop**, bedankt voor de talloze uren hulp en vermaak bij de microscopen.

Aan de studenten die ik heb mogen begeleiden tijdens hun stages, **Sabine, Pleun, Dunya**, bedankt voor jullie directe en indirecte bijdragen aan dit proefschrift. Ik vond het ontzettend leuk om te zien hoe enthousiast jullie waren over jullie projecten, en om jullie steeds zelfstandiger te zien worden in het lab en meer zelfvertrouwen te zien krijgen in jullie experimenten. Ik hoop dat jullie hebben kunnen zien hoe leuk werken in een lab kan zijn.

I have had the luck to be able to work with great people during my PhD from other institutes. **Wiebke,** thank you for hosting me in Göttingen, to learn about the beauty of electron microscopy, and thank you for welcoming me in your home (and for letting me meet your chickens). I have enjoyed our talks and discussions, thank you for the pleasant collaboration. I look forward to seeing you again at conferences. **Sophie**, I have enjoyed our collaboration together. Thank you for showing me around the lab and Göttingen. Good luck with your PhD! **Jia**, we have managed to find common ground in completely different areas of expertise, which has made the spatial transcriptomics project a success. I have greatly enjoyed working together and getting to know you. All the luck in the rest of your career, wherever that may take you! **Rianne Gorter**, bedankt voor de leuke online meetings over onze samenwerking in spe, en bedankt voor je bemoedigende woorden. Succes in Calgary! **Alyse**, we hebben samen wat moois kunnen maken van een enorm chaotische MS-Dbase. Bedankt voor deze prettige samenwerking.

**Rianne** en **Annabel**, wat heb ik een ongelofelijk geluk om jullie als vriendinnen te hebben. Ik weet dat ik altijd bij jullie terecht kan, maakt niet uit waarvoor, en jullie hebben vaak eerder door dan ik als ik iets nodig heb. Heel erg bedankt dat jullie er zijn. **Ria**, er waren tijden in onze studie dat we gemiddeld 12 uur per dag samen waren (ja dit hadden we uitgerekend). Je was er vanaf het begin van de studie bij, en ik vind het heel bijzonder dat je nu bij mijn verdediging ook erbij bent als mijn paranimf. Laten we nog vaak Zatte drinken bij het Badhuis! **An**, het maakt niet uit waar ik je voor bel, je bent altijd overal voor in, en daardoor hebben we de leukste spontane avonden uit gehad, films gezien, wedstrijden gerend, en vakanties gehad. Bedankt voor je enthousiasme en je luisterende oor! Ik vind het echt heel gaaf om te zien dat je je zo inzet voor wat je belangrijk vindt. Bedankt dat je me hierin soms mee neemt en me op een andere manier naar situaties leert kijken, door jou is de wereld een betere plek. Laten we nog vaak een van onze 4 recepten maken!

**Kimberley**, Kim, ik ben zo blij dat we de afgelopen jaren elkaar zo veel beter hebben leren kennen. Het is heerlijk om te zien hoe heerlijk jezelf je bent. En wat is het leuk om te zien hoeveel energie jij uit je werk kan halen! Je verdient de wereld, je bent een prachtig mens. Bedankt dat je mijn cheerleader bent, en dat ik bij jou zowel kan komen ontladen als opladen.

**Stascha, Rachelle, Maite,** en **Lisa,** bedankt voor alle etentjes, fietstochten, dansjes, drankjes en koffie-dates. Door jullie waren de afgelopen jaren een heel stuk vrolijker en gezelliger! **Julia, Alies, Caroline, Charlotte, Iris, Sophia, Roosje,** oftewel de *BB's***,** bedankt voor de leuke borrels, etentjes en kleding-ruil! Ik vind het erg leuk om te zien hoe iedereen sinds het begin van de studententijd is gegroeid, en om te zien waar iedereen terecht is gekomen.

**Kara, Michelle, Manon, Stefanie, Freya** en **Karlijn**, wauw wat hebben wij veel meegemaakt met z'n allen. Het is zo bijzonder dat we er nog altijd voor elkaar zijn, ondanks dat onze levens sinds de middelbare school zulke andere wegen op zijn gegaan. We hebben samen gelachen en gehuild, en lief en leed gedeeld, en ik weet dat we dat zullen blijven doen. Bedankt dat we altijd tijd maken voor elkaar.

**Jurriena**, mijn eerste vriendin in Amsterdam! Bedankt dat je er al die jaren voor me bent geweest. We zijn samen volwassen geworden, en ik geniet ervan om je nu in je nieuwe rol als moeder te zien groeien. Je doet het fantastisch, bedankt dat je er altijd voor me bent.

**Tessa,** ik ben ontzettend bij dat wij samen veel te vroeg in de ochtend in een roeiboot zijn gestapt in Cambridge, en dat hier zo'n mooie vriendschap uit is

gekomen. Onder andere onze avonturen samen, vele brunches, en onze fijne avondjes kletsen onder het genot van een kaasplank, zorgen ervoor dat ik met veel plezier terug denk aan deze tijd. Toch mooi dat we 010 en 020 afwisselen. Ik kijk er naar uit om Guatemala met je te gaan ontdekken!

**Regan**, thank you for making me feel welcome in Cambridge. You kept me sane, both in and out of the lab, and made my internship unforgettable. I'm happy I will get to return the favor now that you will be moving to Amsterdam! **Clay**, it was so much fun to see you fall in love with this beautiful city, thank you for letting me show you around. Your positive energy and your stories always cheer me up. Succes met je Nederlandse lessen.

**Ysanne,** ondanks dat we blijkbaar samen hebben gestudeerd, hadden we toch het NIN nodig om elkaar tegen te komen. Ik ben blij met jou als vriendin, en ik vind het heel leuk dat ik nooit helemaal (of helemaal niet) kan voorspellen hoe onze avonden lopen. Laten we dit vaak blijven doen!

**Jolanda**, **Lara,** en **Sascha,** bedankt dat jullie me altijd welkom hebben laten voelen, en me helemaal opgenomen hebben in jullie familie. Het betekent heel veel voor me dat ik gelijk meegenomen werd in tradities en weekendjes weg. **Renee, Margriet, Senna,** en **Ties,** het is altijd gezellig bij jullie, bedankt dat jullie altijd geïnteresseerd zijn in waar ik mee bezig ben.

**Oma**, ik denk dat de vele uren die ik met u en opa in de keuken heb doorgebracht mij de basis heeft gegeven om nu met zo veel plezier in het lab te werken. Wat is het heerlijk om bij u langs te kunnen fietsen, en uren te kunnen kletsen over alles en nog wat. Uw liefde en openhartigheid naar iedereen in uw omgeving is bewonderingswaardig. Bedankt dat u en opa het belang hiervan aan ons hebben meegegeven.

**Oscar**, mijn grote broer, en **Nienke,** wat fijn dat ik soms wat bij jullie wat kan afkijken hoe ik dingen moet aanpakken. Bedankt dat jullie er voor me zijn. Het is heel leuk om te zien hoe jullie het leven als gezin uitpluizen, met de lieve **Isa** en **Hugo**. Ik kijk er naar uit om ze verder op te zien groeien.

**Charlotte**, ik ben heel erg blij met jou als zus. Fijn dat je tegenwoordig dichterbij woont (in ieder geval hetzelfde continent). Ik vind het erg bijzonder dat je de kaft van dit proefschrift hebt ontworpen. Bedankt dat ik altijd welkom ben, en weet dat je dat ook altijd bij mij bent. Ik vind het leuk dat we steeds meer naar elkaar toe zijn gegroeid! Bedankt dat je er altijd voor me bent.

**Pap** en **Mam**, ik kan jullie niet genoeg bedanken. Door jullie heb ik geleerd wat het betekent om door te zetten, om creativiteit te omarmen, om mezelf te vertrouwen en om nieuwsgierig te blijven. Ik vind het leuk dat ik een beetje in jullie voetsporen heb kunnen stappen, en ook heb kunnen zien hoe interessant en spannend biologie is. Doordat ik weet dat ik altijd op jullie terug kan vallen als het mis gaat, heb ik grote stappen durven te zetten. Heel erg bedankt!

En dan als laatste, **Sam**. Je hebt me de afgelopen jaren stabiliteit gegeven. Je zorgt ervoor dat ik altijd zal blijven lachen, ongeacht hoe de dingen lopen (of hoe slecht je grap is). Ik weet dat je me steunt en er voor me bent, bedankt dat je dit zo duidelijk maakt. Ik heb van jou geleerd hoe mooi het kan zijn om af en toe even te stil te blijven staan om ergens van te genieten, in plaats van steeds maar te blijven rennen. Ik kijk er naar uit om samen de wereld verder te ontdekken. Ik hou van je.

***"Just smile and wave."*** – Skipper the Penguin.

## ABOUT THE AUTHOR

Aletta Marthe Roswitha van den Bosch was born on October 9th in 1995 in Boxmeer, the Netherlands. After obtaining her Gymnasium degree at het Elzendaalcollege in Boxmeer in 2013, she began studying Psychobiology at the University of Amsterdam. Intrigued by fundamental neuroscience and pathophysiological mechanisms involved in brain disorders, she started the research master's program Neurobiology: Pathophysiology and Psychopharmacology at the University of Amsterdam in 2017.

During her master's degree, she performed internships focusing on multiple sclerosis (MS) at the NeuroImmunology group at the Netherlands institute of Neuroscience and the PluchinoLab at the University of Cambridge. There, she delved into MS pathology, neuro-immunology, and cellular metabolism, sparking her passion to continue research on MS in her PhD.

In 2020, she began her PhD at the NeuroImmunology group at the Netherlands institute of Neuroscience, under the supervision of Prof. Inge Huitinga, Dr. Jörg Hamann and Dr. Joost Smolders. Here, she explored the intricate pathophysiological mechanisms of disease progression in MS, focusing on microglia and neurons. During her PhD, she participated in a number of international collaborations. She visited the Karolinska institute in Stockholm to perform experiments, and she obtained funding to visit the Max Planck institute in Göttingen and to participate in the Cajal summer school on glial cells in health and disease in Bordeaux. In 2022, she received the Best Poster Presentation Award at the Gordon Research Conference in Lucca, and in 2023 she was honered with the Rogier Hintzen Talent Award.

Aletta lives in Amsterdam with Sam Scheeren.